SWANSEA UNIVERSITY

DOCTORAL THESIS

Materials Coatings and Enhanced Characterisation for Alkaline Water-Splitting Devices

Author:
William J. F. GANNON

Supervisor:
Dr. Charles W. DUNNILL

Swansea University
Prifysgol Abertawe

A thesis submitted in fulfillment of the requirements for the degree of Doctor of Philosophy

in the

Energy Safety Research Institute
College of Engineering

June 2020

Declaration of Authorship

I, William J. F. GANNON, declare that this thesis titled, "Materials Coatings and Enhanced Characterisation for Alkaline Water-Splitting Devices" and the work presented in it are my own. I confirm that:

- This work was done wholly or mainly while in candidature for a research degree at this University.
- Where any part of this thesis has previously been submitted for a degree or any other qualification at this University or any other institution, this has been clearly stated.
- Where I have consulted the published work of others, this is always clearly attributed.
- Where I have quoted from the work of others, the source is always given. With the exception of such quotations, this thesis is entirely my own work.
- I have acknowledged all main sources of help.
- Where the thesis is based on work done by myself jointly with others, I have made clear exactly what was done by others and what I have contributed myself.

Signed:

Date:

SWANSEA UNIVERSITY

Abstract

Energy Safety Research Institute
College of Engineering

Doctor of Philosophy

Materials Coatings and Enhanced Characterisation for Alkaline Water-Splitting Devices

by William J. F. GANNON

A number of material coatings were investigated, specifically for 316-grade stainless steel electrodes, for use with alkaline water-splitting electrolysis. The aim was to enhance longevity, particularly with respect to the highly intermittent usage that is typical of renewable energy generation, and to increase activity. Long-term experiments were conducted over many thousands of cycles of on-off accelerated ageing at constant current density. The effects of ageing were analysed using chronopotentiometry, cyclic voltammetry (CV), electrochemical impedance spectroscopy (EIS), scanning electron microscopy, energy dispersive x-ray spectroscopy, x-ray photoelectron spectroscopy and gas chromatography. It was found that titanium nitride did not have high activity for the hydrogen evolution reaction (HER), and underwent rapid oxidation and destruction if used as an anode. A new version of electrodeposited Raney nickel was developed that demonstrated improved activity, including an overpotential for the HER at $10\,\mathrm{mA\,cm^{-2}}$ of just 28 mV. As a bifunctional catalyst it demonstrated an overpotential at $10\,\mathrm{mA\,cm^{-2}}$ of just 319 mV, making it the second most active catalyst known, and certainly the simplest to deposit. This activity was traced to the increased electrochemical surface area of the coating, which was higher as deposited, and increased by up to a factor of three after ageing. During surface-area measurements, an apparent anomaly was discovered between results obtained for the same electrode via EIS and CV. New methods of equivalent circuit fitting to transient waveforms were developed, and the anomaly was explained by time-domain simulations of the constant-phase element representation of the double-layer capacitance. A zero-gap electrolyser was constructed in order to investigate its performance, and it was found that woven stainless-steel mesh could operate as a gas-separation membrane.

Acknowledgements

I would like to thank my supervisor Dr. Charlie Dunnill, for having so many great ideas, and for being a patient sounding board for my own.

I would like to thank Prof. Trystan Watson, who remembered our conversation and gave me the name of a potential supervisor.

I would like to thank Swansea University, for the funding which made all of this possible. I hope I am worthy of their investment.

Finally, I would like to thank my wife Fiona, who knew exactly what she was letting herself in for…

Contents

List of Figures

List of Tables

List of Abbreviations

316SS	**316**-grade **S**tainless-**S**teel
AEM	**A**nion **E**xchange **M**embrane
APXPS	near **A**tmospheric **P**ressure version of XPS
CE	**C**ounter **E**lectrode
CP	**C**hrono**p**otentiometry
CPE	**C**onstant **P**hase **E**lement
CV	**C**yclic **V**oltammetry
DFT	**D**ensity **F**unctional **T**heory also, **D**iscrete **F**ourier **T**ransform
ECSA	**E**lectro**c**hemical **S**urface **A**rea
EDX	**E**nergy **D**ispersive **X**-ray Spectroscopy
EIS	**E**lectrochemical **I**mpedance **S**pectroscopy
FGE	**F**inite-**G**ap **E**lectrolyser
FWHM	**F**ull **W**idth **H**alf **M**aximum
GC	**G**as **C**hromatograph(y)
HER	**H**ydrogen **E**volution **R**eaction
ID	**I**nternal **D**iameter
LEDC	**L**ess **E**conomically **D**eveloped **C**ountries
LFL	**L**ower **F**lammability **L**imit
LSP	**L**inear **S**weep **P**otentiometry
MEA	**M**embrane **E**lectrode **A**ssembly
MFC	**M**ass **F**low **C**ontroller
MWB	**M**odified **W**att's **B**ath
NHE	**N**ormal **H**ydrogen **E**lectrode
OEC	**O**xygen **E**volving **C**omplex
OER	**O**xygen **E**volution **R**eaction
PAR	**P**assive **A**utocatalytic **R**ecombiner
PEM	**P**roton **E**xchange **M**embrane
PEMFC	**P**roton **E**xchange **M**embrane **F**uel-**C**ell
PVD	**P**hysical **V**apour **D**eposition
RE	**R**enewable **E**nergy also, **R**eference **E**lectrode

RHE	**R**eversible **H**ydrogen **E**lectrode
SCE	**S**tandard **C**alomel **E**lectrode
SEM	**S**canning **E**lectron **M**icroscopy
SHE	**S**tandard **H**ydrogen **E**lectrode
tpi	**t**hreads **p**er **i**nch
UFL	**U**pper **F**lammability **L**imit
WE	**W**orking **E**lectrode
XPS	**X**-ray **P**hotoelectron **S**pectroscopy
ZGE	**Z**ero-**G**ap **E**lectrolyser

Physical Constants

Faraday constant	$F = 96\,485.3415\,\mathrm{C\,mol^{-1}}$
Universal gas constant	$R = 8.314\,472\,\mathrm{m^2\,kg\,s^{-2}\,K^{-1}\,mol^{-1}}$
Euler constant	$e = 2.718\,281\,828$
Avogadro's constant	$N_A = 6.022\,140\,76 \times 10^{23}\,\mathrm{mol^{-1}}$
Boltzmann constant	$k_B = 1.380\,650\,3 \times 10^{-23}\,\mathrm{m^2\,kg\,s^{-2}\,K^{-1}}$

Chapter 1

Introduction and Theory

Are you willing to be sponged out,
erased, cancelled, made nothing?
Are you willing to be made
nothing?
dipped into oblivion?

If not, you will never really change.

D.H.Lawrence

Now that climate change is underway it is, at least from the point of view of a single human lifespan, impossible to stop. The momentum of its myriad processes is such that its timescales are measured in centuries, if not thousands of years. Even if at some point in the future technology is invented which can reduce atmospheric CO_2 to pre-industrial levels, that momentum will be very hard to reverse. This is because the Earth's climate can silently cross 'Tipping Points' whereupon it is flipped into a new mode of operation, for example via the loss of Arctic sea-ice, with each tipping point potentially leading to more tipping points in a phenomenon known as 'Tipping Cascades' [1]. It is also non-linear, with effects that are already in-line with absolute worst-case predictions of just 20 years ago. Given that the current set of 'gold-standard' predictions by the United Nations Intergovernmental Panel on Climate Change (IPCC) are based on simplified and relatively linear models, this calls into question whether we can rely on them at all. As our ability to measure what the climate is doing improves to levels of exquisite precision, so too does our ability to pull at the threads of the most complex system ever studied, and discover its inherent positive feedback loops. It may not be long before humanity discovers that prior to industrialisation, the Earth was in reality a climate change time-bomb waiting for the fuse to be lit.

The possibility of Tipping Cascades can explain how rapid warming events have occurred at various times in Earth's history, particularly the Paleocene-Eocene Thermal Maximum (PETM), which is regarded as the best analogue for a rapid and massive carbon release, and thus best able to predict what changes planet Earth is about to undergo [2]. With

uncanny similarity, approximately 55 million years ago, this warming event has been attributed to the rapid release of 2 trillion tonnes of carbon in the form of methane, and led to global warming of at least 5 °C [3]. Given predictions of a 10% increase in anthropogenic CO_2 emissions by 2040, rather than any form of decrease, and given the normal range of human behaviour, it is quite reasonable to conclude that global warming of 4 °C is already an inevitability. This is, in fact, the IPCC's median projection for the year 2100 if no significant changes are made, and this is in spite of the fact that the IPCC is employing a simplified model that does not take into account any tipping points.

Despite the apparent futility of the situation, every effort must nevertheless be made to minimise humanity's dependence on fossil fuel. There have never been more options available, more technologies at our disposal, or more evidence to guide us. Human behaviour too can experience tipping points of its own, particularly in response to that most powerful of emotions: fear. It is possible that widespread fear of the coronavirus, and the wholesale changes to society that were enacted in just a few weeks, could be one of the most important lesson of recent times. If our ever-changing climate succeeds in eliciting the same levels of emotion, then anything becomes possible.

1.1 Thesis Structure

This thesis has seven chapters, which obviously should be read in order. However, chapters 4 and 5 constitute a parallel path, as shown in Figure 1.1.

To summarise:
Chapter 1: covers the theoretical basics of electrochemistry, specifically as regards electrolysis and catalysis, which are the two areas most pertinent to water-splitting.
Chapter 2: covers the electrical and analytical methods employed in the testing and characterisation of electrodes, as well as the mechanical methods relevant to practical electrolysers.
Chapter 3: presents several analytical methods which have been taken to a new and advanced level, and thereby constitutes the first of the results chapters.
Chapter 4: presents an assessment of the performance of a non-catalytic TiN electrode coating, to see whether it can extend the lifetime of 316-grade stainless-steel.
Chapter 5: builds on this work by investigating a new catalytic coating based on Raney nickel.
Chapter 6: brings together the ideas presented in chapters 2, 3 and 5 to design, build, test, characterise and model a zero-gap electrolyser.
Chapter 7: summarises the most important findings of all of the research work, and how it may guide future work.

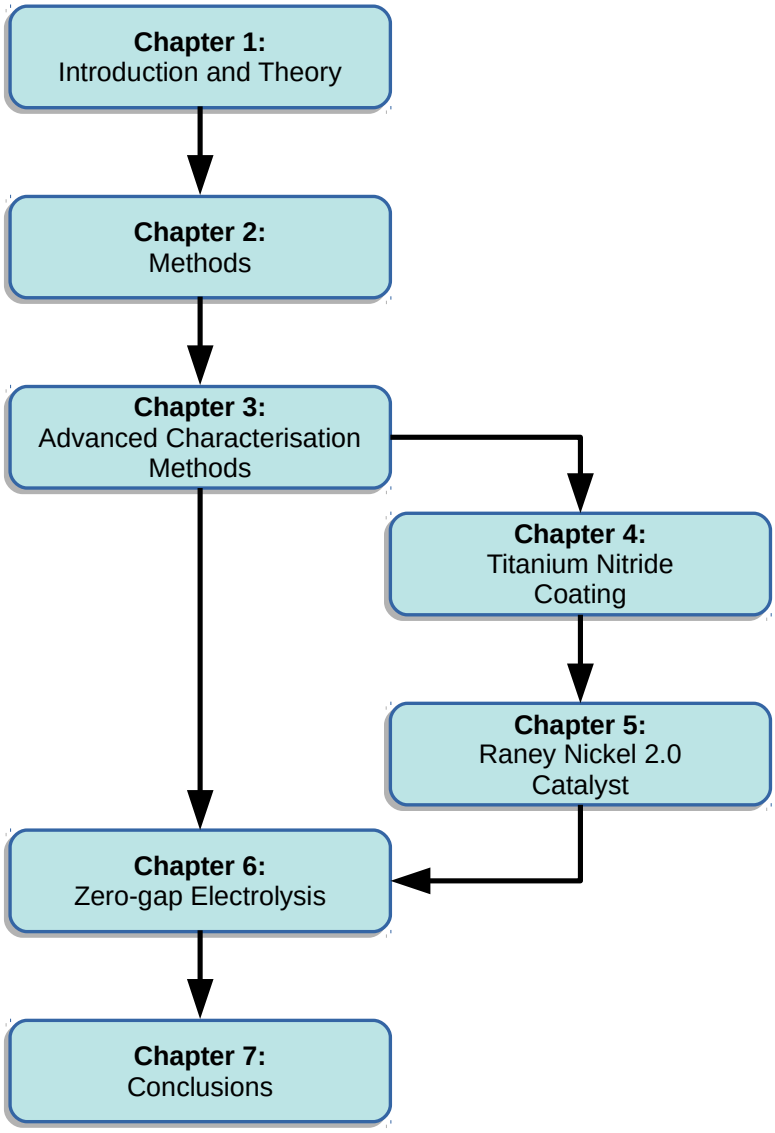

Figure 1.1: Thesis structure

1.2 The Energy Landscape

In its Annual Energy Report for 2019, British Petroleum (BP) projected that Renewable Energy (RE) will be the world's largest single source of power within the next two decades [4]. RE generation is expected to grow at 7.1% per year during this period, eventually displacing coal as the single largest source of energy by the year 2040. Such growth would see RE advancing from 1% of global energy supply to 10% in just 25 years, which would be "far quicker than any fuel has ever penetrated the energy system in history". This compares with 45 years for oil to achieve the same level of growth, and more than 50 years for gas. The report goes on to state that if government policies and technological changes drive a faster transition to a low-carbon economy, this period could be reduced to just 15 years.

Despite these advances, BP envisage that carbon emissions will nevertheless increase by

10% by 2040, largely due to a projected expansion in global energy demand of 30%. The reasons for this are simple: there are many people, companies and countries in the world that have few other sources of income, other than to continue to mine for fossil fuel. Until they can avail themselves of alternative sources of revenue, fossilised energy will not stay in the ground of its own accord. Furthermore, it is foreseen that even if political efforts were to genuinely reduce fossil-fuel consumption, fuel-producing countries would increase production in a bid to sustain profits [5]. Almost exactly this scenario was observed as a result of the coronavirus outbreak of 2020. As worldwide demand for oil collapsed, Russian refusals to cut production prompted Saudi Arabia to *increase* production. As both sides tried to stimulate demand, the price of oil instantly fell by a further 30%, triggering the brief suspension of all trading in US stocks and shares. One month later, as a result of contractual obligations by traders to buy oil even though they had nowhere to store it, the price of oil fell to *minus* $37 a barrel, as those with spare storage capacity discovered they could be paid simply to take delivery of it.

Against this background of entrenched fossil-fuel interests must be considered the practicalities of energy distribution. Since renewable energy has at present little practical scope for large-scale conversion into liquid, its primary distribution method remains electrical. This has led many to call for the electrification of everything, particularly transport and heating, a viewpoint which has aligned with the interests of proponents of carbon capture. This is because it is clearly impossible to capture the gas from millions of flues and exhausts, but it may be possible to do so from a few large, centralised power stations.

However, it remains a matter of active research whether conventional electricity grids can cope with *both* the demands of electrified transport and heating *and* renewable generation, which by its nature is intrinsically decentralised. One particular issue of concern is grid stability, which is the maintenance of both generators and consumers in proper synchrony, and it is conceded that the collective dynamics of power grids are still not fully understood. In realistic simulations of the UK power grid, Rohden *et al.* found that 'decentralised grids become more sensitive to dynamical perturbations', but 'more robust to topological failures' [6].

Despite this optimistic conclusion, decentralised power grids can nevertheless face significant practical hurdles, one of which is Braess' Paradox. This phenomenon, first postulated in 1968 as a result of observations of traffic flow, states that the *addition* of a link to a network can make the resultant flow through the network *worse*. This behaviour has been ascribed to motorists acting in their own interests, rather than the interests of all, but it has since been discovered in electrical power grids, and even for small numbers of electrons [7]. Since an electron cannot be accused of being selfish, this means that the paradox must be a much more universal law than was first realised. Crucially for renewable energy, the chances of encountering the paradox in a power grid are increased the more distributed the

generation becomes [8]. This picture is supported by the intriguing story behind a recent UK power outage.

UK August 2019 Power Outage: The consequences of grid instability were highlighted on the 9th of August 2019 in the UK, when a lightning strike triggered a sequence of events resulting in blackouts across much of mainland Britain. In addition to the loss of power to 1.15 million customers, other consequences included a loss of signalling on the London Underground, and trains refusing to restart due to a software problem. Four hospitals were deprived of power, only two of which managed to successfully switch to backup generators.

For reasons which are still not entirely understood, the strike caused the sudden, simultaneous and erroneous disconnection of two medium-sized generators, namely the gas-fired power station at Little Barford, and the Hornsea offshore wind farm in the North Sea. The sudden combined loss of more than 1 GW of generation caused a reduction of the mains frequency below 49.5 Hz, at which point, like a house of cards, other forms of generation disconnected for safety reasons. Subsequent to this the frequency fell below 49 Hz, which resulted in automatic Low Frequency Demand Disconnection, which ultimately deprived customers of power.

In the resulting investigation Ofgem (the regulator for the UK gas and electricity market) allocated the largest fines to Little Barford and Hornsea, but of perhaps greater significance in its report is its identification of the role of Distributed Generation (DG) in the outage [9]. This is defined as "electricity generating plant that is connected to a distribution network rather than the transmission network". It is generally of small capacity (less than 100 MW), and also not generally licensed. The report concludes:

> Our lower bound for total estimated DG lost across the event is 1300 MW, and the loss could be as high as 1500 MW. There is a significant possibility that this volume is in excess of the transmission connected generation lost during the event. This underscores the changes that Great Britain's electricity system is facing and the importance of understanding the role of DG in the energy mix and the control of the electricity system.

In other words, it is Ofgem's conclusion that so much unlicensed DG has already been added that the ability of the network to respond to relatively innocuous events such as a lightning strike has already been compromised. Therefore, in order for the roll out of DG to continue, it is going to have to prove to the regulator that it can be more of a help than a hindrance. In any event, DG is certain to face much tighter regulation and licensing.

Therefore, whilst grid stability problems continue to be an issue, hydrogen offers a potential and completely independent outlet for renewable energy. In many ways, it is hard to see how a truly zero-carbon country would be able to operate without it.

1.2.1 The Role of Hydrogen

Hydrogen is the simplest element in the periodic table and has the potential to store significant amounts of energy per unit weight. When reacted with oxygen to form water (either by straightforward combustion, or chemical conversion in a fuel cell) only 11% of the total mass of the combustion product needs to be transported, the rest being supplied by the atmosphere. Compare this to 23% for diesel combustion and 32% for ethanol combustion, in theory at least hydrogen can provide a weight-efficient solution.

In practice hydrogen is let down by its volumetric efficiency, at least when compared to liquid hydrocarbon fuels. Even when liquefied (at temperatures below 33 K) the density reaches just $71\,\mathrm{g\,l^{-1}}$ (one fourteenth that of water), and the resulting energy density of $10\,\mathrm{MJ\,l^{-1}}$ is just 25-30% that of Gasoline/Diesel. Nevertheless, it compares well with batteries where even the latest lithium ion technology, which currently achieves a density of about $2.4\,\mathrm{MJ\,l^{-1}}$ [10], constitutes less than half the $6\,\mathrm{MJ\,l^{-1}}$ achieved by hydrogen when compressed to 700 bar. However, possibly the greatest benefit of hydrogen is its versatility. No other energy storage medium can be burnt to provide heat, transported by pipeline, stored in simple containers, and converted directly into electricity.

In addition, the prospect of combining renewably generated hydrogen with sources of carbon (e.g. CO_2 or biomass) into hydrocarbon fuels is a useful bonus, especially in the short to medium term, because of their compatibility with existing technologies (e.g. boilers or internal combustion engines). If successful, this could help renewable energy to tap into the vast markets of transportation and heating. For example, it may be some time before we see a battery-powered commercial airliner, but the Fischer Tropsch process is already certified to generate aviation fuel from a mixture of hydrogen and carbon-monoxide [11]. In the field of Enhanced Biomass to Liquid (EBtL), the addition of extra energy into the system in the form of hydrogen can theoretically lead to dramatic improvements in yield, up from 180 kg of diesel per tonne of dry biomass to 590 kg [12].

As regards sources of biomass, there is an interesting case to be made for cultivated seaweed. First generation sources of biomass (i.e. sugars and vegetable oils) as well as second generation sources (i.e. agricultural waste and non-food crops) can be heavily compromised as regards their life-cycle emissions, with corn stover achieving a staggering 42 kg of carbon debt per litre of bioethanol produced [13]. This is not to mention other contentious issues related to land-use change, such as biodiversity loss and social injustice. Seaweed farming on the other hand can actually enhance the offshore ecosystem, helps soak up excess marine nutrients from fish-farms and agricultural run-off, requires no irrigation with fresh water, no fertilisation, and its low or virtually non-existent lignin content means it is less costly to process. It is also highly productive, with Gelidium amansii producing a dry mass yield of up to $66\,\mathrm{t\,ha^{-1}}$ per annum, three times as much as the nearest land-based alternative, sugar cane [14].

Regardless of the final use for renewable hydrogen, the rôle of the catalyst is of paramount importance in achieving high efficiency. The act of splitting water is thermodynamically steeply uphill, and the energy losses can be significant. With commercial equipment, a typical round-trip from electricity to hydrogen (via electrolysis) and back to electricity (via fuel-cell) in a unitised regenerative fuel-cell involves an efficiency of just 40-45% [15]. This needs to improve, as does the unfortunate dependence of the industry on rare-earth elements such as Pt, Ru and Ir. Therefore the need for efficient catalysts remains as critical as ever, whether they are for use in a standard cell design [16] or a more advanced zero-gap design [17].

A 2019 study by the Ifo Institute in Münich has confirmed many of the serious reservations that surround the large-scale roll-out of battery-powered electric vehicles [5]. Using figures from a Swedish study [18] that analyses the lifetime CO_2 emissions of lithium-ion batteries throughout mining, refining and recycling, plus the general energy mix of the German electricity supply, the authors compared two specific models of vehicle, namely a Tesla Model 3 and a Mercedes C220d. In all respects, the diesel vehicle emitted less CO_2, largely due to the astonishing 11 to 14 t of CO_2 emitted during the production and recycling of the 75 kW h battery. The study assumed an average 10-year life for each battery, plus an annual mileage of 15 000 km.

In addition to this, a large increase in the number of electric vehicles being charged would necessitate ambitious levels of increase in green energy production simply to maintain the current energy mix. Coupled with the continuing phase-out of nuclear generation, to move just half of German road traffic to green energy would require the current 29,000 wind turbines to be increased by more than 60,000, assuming turbines of a similar size. Instead, the authors foresee a political incentive for the relaxation of emissions allowances, which would permit much more coal-powered generation to make up the shortfall. Thus, switching from diesel engines to electric motors would, depending on the type of battery production, increase CO_2 emissions by two-thirds, if not more a factor of two. In the short-term, the authors point out that genuine CO_2 emission reduction can be realised by powering existing vehicle engines with natural gas. However hydrogen, and only it, is the ideal complement to wind and solar power when renewable electricity reaches a market share in excess of 30%, leading to energy-rich, seasonal peaks that are not otherwise exploitable.

Hydrogen as a Feedstock At present the total industrial consumption of hydrogen is in excess of 50 million tonnes per annum [19]. Some of this is produced as a by-product of other processes, for example the Chlor-Alkali process, which is used to produced chlorine from the electrolysis of brine. Hydrogen can also be used to enable carbon-dioxide captured from industrial processes to be recycled, for example in the form of methanol, which itself can be used directly with fuel-cells. An example of this is to be found at the George Olah

plant in Iceland, which combines hydrogen from electrolysis with CO_2 from a geothermal power-plant to produce 5 million litres of methanol per year.

In 2009 the European Union brought into force its Renewable Energy Directive, which mandated that 20% of the energy consumed within the union be renewable, mirroring a similar US biofuel mandate dating from 2007. This, according to the CEO of the Malaysian Palm Oil Council, "created an unprecedented market for the uptake of palm oil", with EU biofuel usage tripling between 2011 and 2014, and palm oil's share of that increasing five-fold. Given that in many developing nations "palm oil is synonymous with poverty eradication" (Teresa Kok, Malaysian Minister of Primary Industries, 2018) it is no surprise that large areas of virgin tropical rainforest were subsequently cleared to make way for highly profitable plantations. These forests are, however, some of the most carbon-rich in the world, and when that carbon is released, the end result is a significant net *contribution* to global warming. According to the BBC Documentary 'Climate Change - The Facts', deforestation accounts for fully one third of all current CO_2 emissions. Although measures have since been taken to propose limits on biofuel crops tied to deforestation, much of the damage has already been done, and it serves to highlight the interconnectedness of global systems, and the way in which good intentions can backfire.

The effects of climate change are on the one hand too slow to notice, but on the other shockingly rapid:

- In Europe the winter of 2019 went down as the first to witness the complete failure of the German Eiswein harvest, a variety of wine that requires temperatures of $-7\,^{\circ}\mathrm{C}$ or colder. For the first time the winter was so mild that this temperature was not achieved in *any* German wine region. Behind this story is an even more startling statistic, that the winter was $3.4\,^{\circ}\mathrm{C}$ hotter than the average for the years 1981 to 2010, and $1.4\,^{\circ}\mathrm{C}$ hotter than the previous record, which was set in 2015 [20].

- In Australia the two hottest summers on record occurred in the last two years (2018 and 2019) and were accompanied by the 'Black Summer', where the annual bushfire season burned out of control, and consumed an area of land 50% larger than England. More than 1 billion animals died.

- Similarly, according to a 2018 report by the European Academies Science Advisory Council (EASAC) the number of storms worldwide has *doubled* between 1980 and 2016; droughts, forest-fires and extreme temperatures have more than doubled; floods and other 'hydrological events' have quadrupled, as shown in Figure 1.2 [21].

It is almost inconceivable that such changes have occurred in much less than a single lifetime.

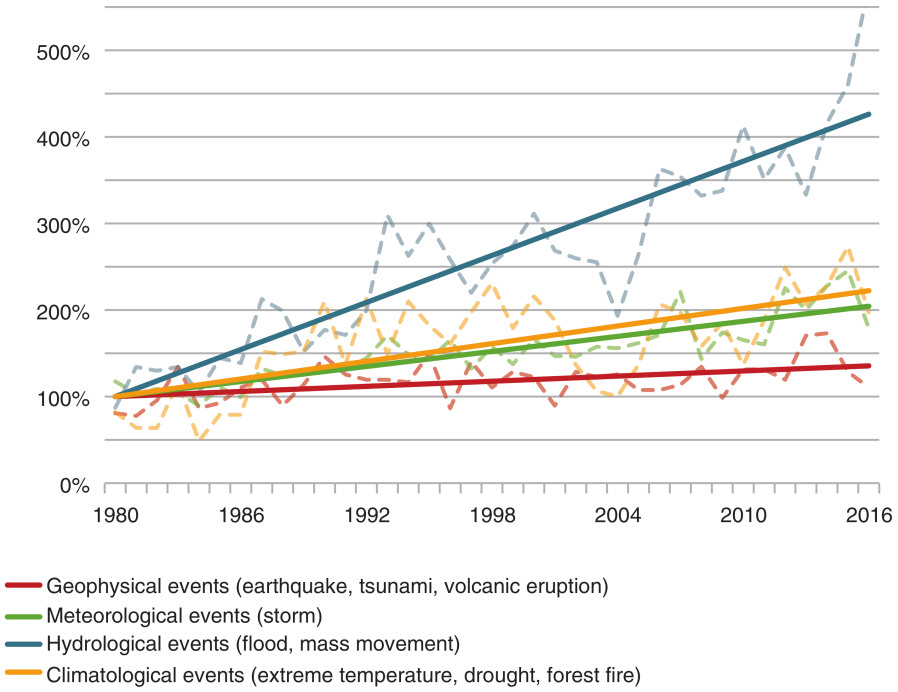

Figure 1.2: Trends in different types of natural catastrophe worldwide 1980-2016 (1980 levels set at 100%). MunichRe NatCatSERVICE.

1.2.2 Energy Storage

Hydrogen has perhaps its greatest contribution to make towards reducing carbon dioxide emissions as a means of storing excess renewable electricity. For example, in the UK it is reported that wind farm owners were paid £125 million in 2018 to leave wind turbines standing idle, because more electrical wind energy was available than could successfully be fed into the grid.[1] This certainly indicates that a market is available.

It is also reported that for just one wind farm in Spain, with a nominal installed capacity of 48.8 MW, the total excess energy in one year that could not be sold to the grid amounted to nearly 250 GW h [22]. According to a relatively simple calculation, this would be enough to run 37,000 hydrogen-powered cars, assuming each car consumes 2.3 kg of hydrogen per week, which is sufficient to achieve the average UK mileage per car.[2] Assuming a nominal retail value of £10 per kilo of H_2, this would equate to a potential *additional* income of £44m per annum. This highlights the high value that can be obtained for energy when delivered to the wheels of a motor vehicle.

Although extrapolation of such figures is at best illustrative, it is worth noting that the Dogger Bank wind farm, due for completion in 2025, will have an installed capacity of

[1] https://ref.org.uk/ref-blog/348-constraint-payments-to-wind-farms-in-2018 (viewed April 2020)

[2] Assuming 55 kW h kg^{-1} of H_2 (source https://en.wikipedia.org/wiki/Hydrogen_economy), 100 km kg^{-1} of H_2 (source https://www.hyundai.co.uk/new-cars/nexo) and 12 160 km per car per annum (source https://www.gov.uk/government/statistical-data-sets/nts09-vehicle-mileage-and-occupancy)

4.8 GW, and the whole Dogger Bank site is reported to have a potential realisable capacity of 110 GW. Assuming a typical *capacity factor* of 40% (i.e. the average output of the site relative to its rated capacity) this single site could in theory supply all of the electricity for the UK.

In practice, although there is an economic case to store surplus electricity as hydrogen, the case to transform it back into electricity can be much weaker. This is because it entails *both* additional capital expenditure for fuel-cells, *and* a reduction in round-trip efficiency. A combined electrolyser/fuel-cell can reduce expenditure, but in practice only at the expense of yet further reduced round-trip efficiency. In conjunction with the comparatively low value of electricity, it can make more sense to seek direct uses for the hydrogen itself. To assess this, a brief survey was conducted of eight potential energy markets, as presented in Table 1.1.

Market	**Price**	**CO_2 Output**	**Utilisation Efficiency**	**Adjusted Price**	**Adjusted CO_2 Output**
	p per kWh	kge per kWh		p per kWh	kge per kWh
Elec consumer	18	0.28	100%	18	0.28
Elec wholesale	5.0	0.28	100%	5.0	0.28
Gas consumer	3.5	0.18	90%	3.9	0.20
Gas wholesale	1.7	0.18	90%	1.9	0.20
Petrol	13.8	0.23	20%	69	1.17
Diesel	13.2	0.24	30%	44	0.82
Jet fuel	4.2	0.25	100%	4.2	0.25
Shipping	3.7	0.26	50%	7.4	0.53

Table 1.1: Price of energy per kW h in various markets. The utilisation efficiency describes the useful energy output obtainable on a like for like basis with a hydrogen-derived alternative. kge = kilogram of CO_2 climate warming equivalent. Prices quoted are typical UK average prior to the coronavirus pandemic.

The table shows that if hydrogen is converted into electricity and sold directly to a domestic consumer, then it could raise 18p per kW h. However, if sold on the wholesale market, then the price is just 5p per kW h. The situation is similar for the consumer and wholesale gas markets, but the cost is divided by the efficiency of a typical condensing boiler, which is about 90%. The efficiency of shipping appears high at 50%, but this is in fact a typical efficiency figure for the very largest two-stroke marine diesel engines operating at almost constant rpm. The utilisation efficiency of jet-fuel is listed as 100% because the hydrogen-derived alternative is also jet-fuel, albeit synthetic. The various methods required for hydrogen to compete in each market are as listed in Table 1.2.

The table shows that if hydrogen competes with petrol via the use of a vehicle fitted with a fuel-cell with 50% efficiency, then a price of 35p could in theory be raised for each kW h of hydrogen. This is the highest financial reward available, and demonstrates why the petrol motor vehicle currently constitutes the most attractive market for hydrogen. By comparison, the low price of jet-fuel, coupled with the low efficiency of the Fischer-Tropsch

Market	Method	Utilisation Efficiency	Competition Price	Price Available	CO_2 Avoided
			p per kWh	p per kWh	kge per kWh
Petrol	Fuel-cell	50%	69	35	0.58
Diesel	Fuel-cell	50%	44	22	0.41
Elec Consumer	Fuel-cell	50%	18	9	0.14
Shipping	Engine	50%	7.4	3.7	0.26
Gas Consumer	Boiler	90%	3.9	3.5	0.18
Elec Wholesale	Fuel-cell	50%	5.0	2.5	0.14
Gas Wholesale	Boiler	90%	1.9	1.7	0.18
Jet Fuel	Fischer Tropsch	23%*	4.2	1.0	0.06

Table 1.2: Price available for hydrogen energy by market sector, based on existing competition. The 'Method' column shows what equipment would be required for hydrogen to compete in each market sector, followed by the efficiency of that equipment. Based on the 'Competition Price' and 'Adjusted CO_2 Output' (from Table 1.1) this permits the 'Price Available' and 'CO_2 Avoided' to be calculated. kge = kilogram of CO_2 climate warming equivalent. * = estimated

method means that a price of only 1p per kW h is available should that hydrogen be used to help power aircraft. Note that the 23% efficiency of the Fischer-Tropsch process for the synthesis of jet-fuel is an estimate. In addition to significant heat input, the process also requires a suitable source of carbon, either in the form of air-captured CO_2 or biomass, prior to refining.

The tables also show the total CO_2 emitted per net kW h (Table 1.1), as well as the amount of CO_2 avoided per kW h of hydrogen (Table 1.2). Thus, each kW h of hydrogen used to power a motor vehicle that replaces a petrol vehicle could avoid the release of 0.58 kg of CO_2 equivalent into the atmosphere. This gives an idea of how much *carbon subsidy* might be required in each sector to help make hydrogen competitive. Thus, for example if the actual production price of hydrogen were 5p per kW h, then in the shipping sector a subsidy/tax of $(5 - 3.7)/0.26 = 5$p per kg of emitted CO_2 or equivalent would be required to equalise costs.

1.2.3 Hydrogen Safety

At the Laporte Industries factory in Ilford, Essex in April 1975, an explosion occurred in an electrolyser, as a result of which extensive damage was caused. Four operators were injured, of whom one later died, and the incident became one of the first to be investigated in detail by the newly-formed Health and Safety Executive. Their conclusion was that the explosion was caused by the accidental mixing of hydrogen and oxygen, followed by its subsequent ignition. The report went on to mention that the blocking of feed tubes by sludge was a 'perennial problem'.

It is possible to speculate that the sort of long and narrow feed tubes that would be prone to blocking were in fact an attempt by the designers to reduce leakage currents, since this was a common strategy within the industry. However, simulations confirm that such a system is consequently sensitive to blockages, which ironically serve to dramatically *increase* leakage currents, and thereby go on to produce the kind of fatal gas-mixing which resulted in the explosion [23]. It is important to note that blockages can occur not just as a result of sludge, but also as a result of bubbles and air-locks in the system. The task then of producing an electrolyser design which is invulnerable to excessive gas-mixing under *all* circumstances is potentially quite complex.

Many systems involving hydrogen operate at 99.999% purity, a level which is described as 'fuel-cell grade' [24]. This is difficult, if not impossible, to achieve with basic electrolysis equipment because of the ease with which dissolved gas can diffuse across the membrane. However, this figure has little to do with safety, but instead is one that is inherited from industry, where the majority of hydrogen is derived from the steam-reformation of methane, or other hydrocarbons such as methanol. Critically, this means that the contaminants in the hydrogen are chiefly CO_2 and CO, not oxygen, and it is known that CO is extremely detrimental to the operation of PEMFCs [25].

This is due to surface-coverage of CO, which adheres preferentially to the Pt surface at the anode of the PEMFC. It does this not just because it bonds more strongly to platinum than does hydrogen, and is therefore thermodynamically more difficult to remove, but also because it is kinetically 15 times more likely to adhere during collisions. Thus at concentrations of CO as low as 25 ppm (which is a purity of 99.975 %), a 50% reduction in fuel-cell output voltage could be observed at 800 $\mathrm{mA\,cm^{-2}}$ [25]. Since power is proportional to voltage squared, this constitutes a 75% reduction in peak power output. Should this fuel-cell be the sole source of motive power for a car or train, such a loss could render the vehicle unusable. Thus, from an operational point of view, 'five-nines' hydrogen purity is a guarantee of PEMFC availability. The good news is that the poisoning of even the most badly degraded fuel-cell can be reversed after open-circuit operation for a few hours in pure hydrogen.

In any case, it implies that a hydrogen stream that is carbon-free can be used with fuel-cells at much lower levels of purity. In fact, since oxygen contamination will combine with hydrogen inside the fuel-cell to produce water, it can be beneficial, and help the PEMFC to remain hydrated in situations where it might otherwise dehydrate. Despite this, there are of course limits to how much hydrogen and oxygen should be allowed to mix, and consequently it is important to understand the unique properties of hydrogen. To quote from M.S. Butler *et al.* (2009) [26]:

> Hydrogen is an unusual fuel. It has a high leak propensity and wide flammability limits, 4–75% by volume. Among all fuels, hydrogen has the lowest molecular weight, the lowest quenching distance (0.51 mm), the smallest ignition energy in

air (28 mJ), the lowest auto-ignition temperature by a heated air jet (640 °C), the highest laminar burning velocity in air (2.91 m s^{-1}), and the highest heat of combustion (119.9 kJ g^{-1}). Hydrogen flames are the dimmest of any fuel. Hydrogen embrittles and attacks metals more than any other fuel.

The flammability and detonation properties of hydrogen, as presented in Table 1.3, are in large part dictated by its high mobility [27]. As the lightest element, its molecules travel faster than those of any other gas at any given temperature and pressure. This means that it is able to continue burning at concentrations and flow-rates lower than any other fuel, since the high-speed of the combustible molecules means they can come into contact with the next oxygen molecule sufficiently quickly to sustain combustion. For example, in experiments with extremely low flow-rates, Butler *et al.* were able sustain hydrogen flames of such small size that they could only be seen using a digital camera with a 30 s exposure [26].

Mixture	**Flammability**		**Detonability**	
	Lower	*Upper*	*Lower*	*Upper*
Hydrogen in Air	4 vol%	75 vol%	18.3 vol%	58.9 vol%
Hydrogen in Oxygen	4 vol%	94 vol%	15 vol%	90 vol%

Table 1.3: Flammability and detonability limits for mixtures of hydrogen in air and oxygen at 1 atmosphere [26–28]

This also indirectly explains why the lower flammability limit (LFL) of H_2 is the same in air as it is in pure oxygen. With 21% O_2 (in air) and just 4% H_2, the O_2 is already in excess, so adding more O_2 has little effect on the kinetics, and the LFL is not reduced. By contrast, the LFL is reduced if the *pressure* of the mixture is raised, because it increases the concentration of H_2 molecules per unit volume [29]. The low number of O_2 molecules required per combustible molecule (i.e. 0.5) means that each combustion reaction proceeds rapidly, even in comparison with the simplest (saturated) hydrocarbon CH_4, which requires four times as much O_2. The combination of high molecule velocity and rapid combustion leads to a flame velocity which is *eight times* higher than for natural gas/air or propane/air mixtures [30].

It is accepted that above 560 °C (i.e. inside flames) the reaction of molecular hydrogen with molecular oxygen proceeds first via the production of atomic hydrogen, such that the activation energy is dominated by the breaking of just one H-H bond: [31, 32]

$$H_2 + O_2 \longrightarrow H + HO_2 \tag{1.1}$$

which helps explain why hydrogen also has the lowest ignition energy in air of any fuel [26]. The amount (as low as 20 µJ) is described as the same as a single grain of sand travelling at 4 m s^{-1}, and means that hydrogen can be ignited by innocuous amounts of friction, such as 'cracking' open the valve on a hydrogen cylinder to clear the outlet of dust [33].

The combination of these factors would appear to make hydrogen a very dangerous fuel, but the same properties which make it so effective at igniting and burning also make it very quick to escape. It is not an easy gas to confine, not only because of the speed with which it can move, but also because in comparison with all other fuels it is by far the most buoyant. Therefore, in ventilated conditions it is difficult to ignite large quantities of it, and even harder to detonate [19, 30]. In deliberate deflagration experiments inside a vented metal enclosure, Hooker *et al.* measured overpressures of at most 50 mbar from mixtures up to 14% H_2 in air. Pressures were observed to be higher for the sort of stratified hydrogen distributions which would be expected in practice, but only slightly [34]. For comparison, the pressure required to rupture 50% of eardrums has been reported as approximately 1 bar [35].

If hydrogen does burn, it does not generate toxic chemicals or smoke, which are known to create the largest share of hazards from fire [28]. Similarly, although hydrogen burns at temperatures similar to if not greater than hydrocarbons, the absence of soot in the flame means it does not radiate anywhere near as much heat at infra-red wavelengths [19, 36]. Small leaks tend to be on fire already, and accepted practice is for them to be located using a piece of paper on a stick [33]. A balanced conclusion is therefore that the dangers of hydrogen are no greater than for most other fuels (e.g. natural gas or petrol), but they are different [28, 30]. Hence it will take time for both industry and the public to become as familiar with the risks as they are with those of more conventional alternatives.

1.3 Electrolysis

Just like any other chemical reaction, electrolysis is governed by some of the most fundamental principles of chemistry. This section shall describe four of the most important.

1.3.1 The Arrhenius Equation

The Arrhenius equation expresses the empirical observation of the exponential dependence of the rate of almost any chemical reaction on temperature:

$$k = A \exp\left(-\frac{E_A}{k_B T}\right) \tag{1.2}$$

where k is the net forward rate of the reaction, A is a constant, E_A is the activation energy of the reaction, k_B is the Boltzmann constant, and T is the temperature. This relationship arises because the likelihood of individual reactant molecules possessing sufficient energy to overcome the activation barrier increases exponentially with temperature.

Ultimately this arises from Fermi-Dirac statistics, which includes the Fermi function:

$$F(E) = \frac{1}{1 + \exp\left(\frac{E-\mu}{k_B T}\right)} \tag{1.3}$$

where μ is the chemical potential. This equation applies to all matter, but particularly to solids, where the density of states is such that the Pauli exclusion principle comes into effect, broadening the discrete energy levels available to the system into energy bands.

This function can simplify to produce the Boltzmann equation if $E - \mu \gg k_B T$, or in other words if the temperature is much less than $\frac{E-\mu}{k_B}$, where the expression $E - \mu$ is comparable to the activation energy E_A. From the Boltzman equation, the distribution of molecular velocities at any given temperature can be derived, as given by the Maxwell-Boltzmann equation:

$$f(v, T) = \left(\frac{m}{2\pi k_B T}\right)^{3/2} 4\pi v^2 \exp\left(-\frac{mv^2}{k_B T}\right) \tag{1.4}$$

where $f(v, T)$ is the probability density at temperature T of finding a molecule with velocity v, where m is the mass of a molecule. This produces a distribution of molecular velocities as shown in Figure 1.3, where the dashed vertical line represents a hypothetical minimum required velocity to permit a chemical reaction to proceed.

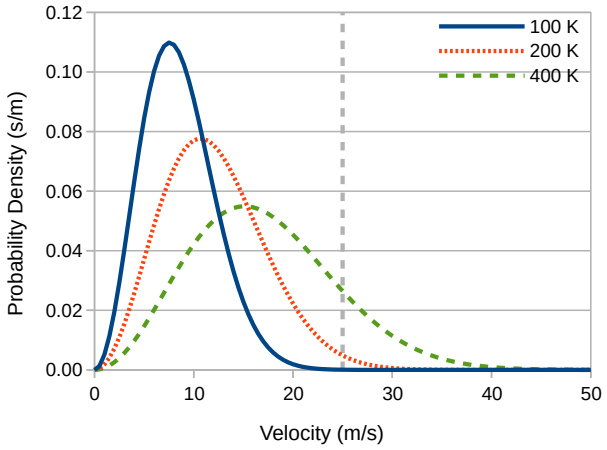

Figure 1.3: Maxwell-Boltzmann distribution of molecular velocities at three different temperatures. The dashed vertical line represents a minimum required velocity to permit a hypothetical chemical reaction to proceed.

Since velocity and energy are related, the likelihood that an energy barrier E_A will be surmounted at temperature T can be calculated by integrating Equation 1.4 between limits:

$$F(V) = \int_V^\infty f(v,T)dv \tag{1.5}$$

$$= 4\pi \left(\frac{m}{2\pi k_B T}\right)^{3/2} \int_V^\infty v^2 \exp\left(\frac{-mv^2}{2k_B T}\right) dv \tag{1.6}$$

where $F(V)$ is the total fraction of molecules that have a velocity V *or higher*. The limit integral of a Gaussian function of the form $\exp(-x^2)$ does not lend itself to analysis, but is simple to investigate numerically, with the results as presented in Figure 1.4.

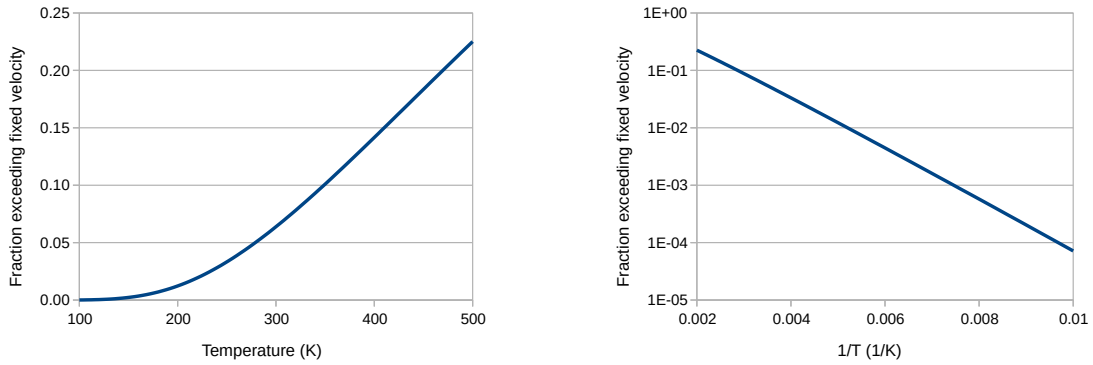

(a) Numerical Integral

(b) Redrawn as Arrhenius plot

Figure 1.4: Results of a numerical limit integral of the Maxwell-Boltzmann equation, to identify the fraction of molecules exceeding a fixed velocity as a function of temperature.

The numerical analysis confirms that the fraction exceeding the fixed velocity does indeed appear to be an exponential function of T. This is further confirmed by redrawing Figure 1.4a as an Arrhenius plot, as shown in Figure 1.4b, where the straightness of the line is proof that the relationship is of the form:

$$F(V) \propto \exp\left(\frac{b}{T}\right) \tag{1.7}$$

This relationship is a simplification, and it is clear that it will not continue indefinitely since the fraction of molecules cannot exceed 1. Inspection of Figure 1.3 reveals this will begin to occur at temperatures where the peak of the distribution approaches the dashed vertical line. This is another way of saying that the Arrhenius equation only applies at temperatures where $k_B T \ll E_A$, which is the same condition required for the simplification of the Fermi function.

Close inspection of the line in Figure 1.4b reveals that it is not in fact perfectly straight.

However, its slope at low temperatures (against natural logarithm) can be confirmed to approach a value given by:

$$slope \rightarrow \frac{½mV^2}{k_B} \tag{1.8}$$

thereby confirming, for the benefit of this analysis, that:

$$E_A = ½mV^2 \tag{1.9}$$

i.e. that the activation energy is equal to the kinetic energy of the molecules at the target velocity V.

This approach therefore reveals how the empirical observation of an exponential relationship between the rate of a chemical reaction and temperature can be tied back to the fundamental quantum physics of particles obeying the Pauli exclusion principle. This is the bedrock of chemistry, and emergent properties such as the Arrhenius equation provide profound insights into the physical forces at work.

The man after whom the equation is named was Professor Svante Arrhenius, a Swedish scientist who was awarded the Nobel prize in chemistry in 1903 for his ionic theory. This proposed that solid crystalline salts could dissociate into ions when dissolved, without the need for an external electric current, thereby contradicting the greatest authority of his day, Michael Faraday. Among his other achievements was to be the first to use modern physical chemistry to assess the effect of CO_2 emissions on global climate change via the greenhouse effect. However, based on the rate of such emissions at the end of the 19th century, his calculations indicated that it would take 2,000 years to reach present day levels.

In an extraordinary coincidence, one of Arrhenius' direct descendants is called Svante Thunberg, christened in honour of his illustrious forebear and father to a girl called Greta, who is now the world's most famous climate change activist. It is therefore fitting that the person doing most to raise awareness of the greenhouse effect is a descendent of the first person to calculate its impact.

1.3.2 The Nernst Equation

The Nernst equation expresses how the potential across an electrolytic cell is related to the electrochemical reactions occurring within it *at equilibrium*:

$$E_{cell} = E^{\ominus}_{cell} - 2.303\frac{RT}{zF}\log_{10}\left(\frac{a_{red}}{a_{ox}}\right) \tag{1.10}$$

where $E^{\ominus}_{cell}$ is the *standard cell potential*, z is the number of electrons involved in the redox reaction, and a_{red} and a_{ox} are the *activities* of the reduced and oxidised species respectively.

It is only at equilibrium that the potential of the electrode is just positive enough to encourage the reduced species in solution to undergo oxidation at exactly the same rate as the electrode is just negative enough to encourage the oxidised species to undergo reduction. It is also the only situation under which the electrode potential becomes a direct function of the bulk concentrations of the products and reactants.

The equation can be extended to include multiple products and reactants, and separated into half-reactions at each electrode. The activities can also be converted into concentrations by dividing by the respective *activity coefficients* γ_{red} and γ_{ox}, producing:

$$E_{cell} = E^{\ominus}_{cell} - 2.303\frac{RT}{zF}\log_{10}\left(\frac{C_{red}}{C_{ox}} \cdot \frac{\gamma_{ox}}{\gamma_{red}}\right) \tag{1.11}$$

$$\text{therefore} \qquad E_{cell} = E^{\ominus'}_{cell} - 2.303\frac{RT}{zF}\log_{10}\left(\frac{C_{red}}{C_{ox}}\right) \tag{1.12}$$

where C_{red} and C_{ox} are the concentrations of the reduced and oxidised species, and $E^{\ominus}_{cell}$ is subsequently adjusted to become the *formal potential* $E^{\ominus'}_{cell}$. At low concentrations the difference between the two is slight.

The rate of change of potential with concentration is given by $2.303RT/zF$, which at room temperature (25 °C) and $z = 1$ is equal to 59 mV. This becomes of crucial importance in the determination of the standard potentials of the water-splitting reactions:

$$2\,H_2O \longrightarrow O_2(g) + 4\,H^+ + 4\,e^-$$
$$4\,H^+ + 4\,e^- \longrightarrow 2\,H_2(g)$$

since

$$E_{ox} = E^{\ominus'}_{ox} - 2.303\frac{RT}{4F}\log_{10}\frac{[p_{H_2O}]^2}{[p_{O_2}][H^+]^4}$$
$$E_{red} = E^{\ominus'}_{red} - 2.303\frac{RT}{4F}\log_{10}\frac{[p_{H_2}]^2}{[H^+]^4}$$

where $[x]$ is a shorthand notation for 'concentration of x', and p_x is the partial pressure of species x, which in most cases will be unity. The formal potential of hydrogen reduction $E^{\ominus'}_{red}$ is 0 V, and that for oxygen evolution $E^{\ominus'}_{ox}$ is 1.23 V, therefore the equations simplify to:

$$E_{ox} = 1.23 - 0.059 \times \text{pH V}$$
$$E_{red} = 0 - 0.059 \times \text{pH V}$$

since $¼\log\frac{1}{x^4} = -\log x$, and $\text{pH} = -\log_{10}[H^+]$. Therefore, at a typical level of pH found in alkaline electrolysis of 14, say, the water-splitting reactions run at potentials of -0.828 V and 0.402 V. This is based on the assumption that the electrolyte (NaOH or KOH) fully

dissociates, and that the resultant concentration of H^+ ions really is 1×10^{-14} M. At this level, one litre of water would 'only' contain 300 billion H^+ ions.

In reality, it is possible that some of the NaOH could have reacted during storage with atmospheric CO_2, thereby producing $NaHCO_3$. Consequently it is not advisable to rely on chemicals that are several years old for accurate measurements, especially if powdered. Far worse though is that the pK_a value of NaOH is only 13.8, which means that its pK_b value (the equivalent value for basic dissociation) in water is 0.2. This means that:

$$pK_b = -\log_{10} K_b = 0.2$$

$$\text{where} \qquad K_b = \frac{[Na^+][OH^-]}{[NaOH]} = 10^{-0.2} = 0.63$$

$$\text{therefore} \qquad [Na^+][OH^-] = K_b[NaOH]$$

where K_b is the equilibrium constant of basic dissociation. If it is declared that the starting concentration of NaOH is m, and the number of moles that dissociate is x, this means that:

$$x^2 = K_b(m - x)$$

where it has been assumed that the concentration of sodium and hydroxide ions remains equal. This generates a quadratic equation in x, which when solved produces the results presented in Figure 1.5.

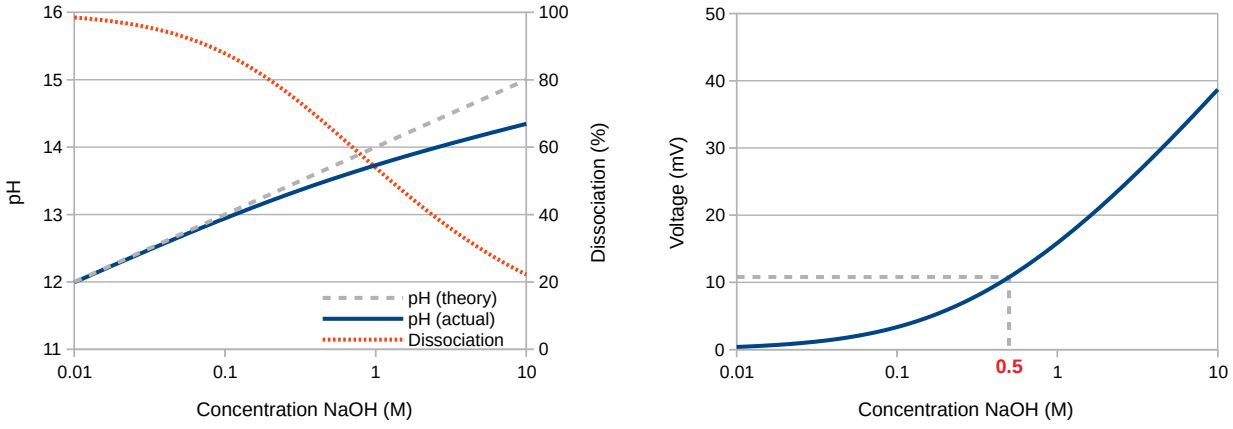

(a) pH error and dissociation

(b) Reaction standard potential error

Figure 1.5: Plot of the pH and reaction standard potential errors that arise due to incomplete dissociation of NaOH, based on a pK_a value of 13.8.

These results contradict much of the accepted wisdom that NaOH is a 'strong base', and therefore fully dissociates even at concentrations up to and beyond 1 M. In fact, at a concentration of 1 M, only 54% of the NaOH dissociates, which results in a pH of only 13.74 instead of 14. If subsequent calculations are based on the assumption that a pH of 14 has

been achieved, this will result in an error of 16 mV. For KOH the situation is even worse, since its pK_a is only 13.5, and the error at 1 M concentration is 22 mV.

Despite this, to the knowledge of the author, no such correction is made to any of the hydrogen or oxygen overpotentials published in the literature, the majority of which use 1 M KOH as an accepted baseline for comparison. However, a very similar argument based on the reduced activity of H_2O has been proposed by Colli *et al.* [37]. The effect of lower-than-expected pH is to push all overpotentials downwards, i.e. hydrogen evolution overpotentials will become more negative (therefore worse) and oxygen evolution overpotentials will become less positive (therefore better).

Since the majority of chronopotentiometry experiments for this thesis were performed in 0.5 M NaOH, the error is as given by the dashed grey line in Figure 1.5b, specifically 11 mV. Although it is possible to correct for such pH errors, this would in fact make them harder to compare with other results published in the literature.

1.3.3 The Butler-Volmer Equation

Where the Nernst equation makes no allowance for any deviation from equilibrium, the Butler-Volmer equation takes into account the kinetics at the electrode surface to determine how much net current flows for any given electrode potential. In this way a graph of current *versus* potential can be plotted. The Arrhenius equation provides the basis for the kinetics, since not only does it indicate that the reaction rate is an exponential function of $1/T$, it also indicates that it is an exponential function of E_A. Note that the derivation here presented differs slightly from others encountered in the literature (for example Brett [38]) in that it emphasises its similarity to that for the Brønsted-Evans-Polanyi Model (see next section).

Ordinarily, the activation energy E_A would be measured in terms of the enthalpy of the transition state $\Delta H^\ddagger$. However, since $\Delta G = \Delta H - T\Delta S$ it is possible to rewrite the Arrhenius equation as:

$$k = A \exp\left(\frac{\Delta G^\ddagger + T\Delta S^\ddagger}{RT}\right)$$

$$\text{therefore} \qquad k = A \exp\left(\frac{\Delta G^\ddagger}{RT}\right) \exp\left(\frac{\Delta S^\ddagger}{R}\right) = A' \exp\left(\frac{\Delta G^\ddagger}{RT}\right) \tag{1.13}$$

The rate of reaction is therefore just as much an exponential function of the Gibbs free energy as it is of enthalpy, although this inevitably demands that the entropy change ΔS is constant within the temperature range of interest.

The physical model on which the Butler-Volmer equation is based is as presented in Figure 1.6. This model has been drawn with the electrode on the right, with its Gibbs energy

dictated by the electrode potential. The electrolyte bulk is on the left, with Gibbs energy independent of electrode potential, and for this analysis defined as zero. The electrode is both a source and sink of electrons, therefore for alkaline electrolysis where all charged species are negative, any that travel from right to left have gained an electron (reduction), and any that travel from left to right will lose one (oxidation).

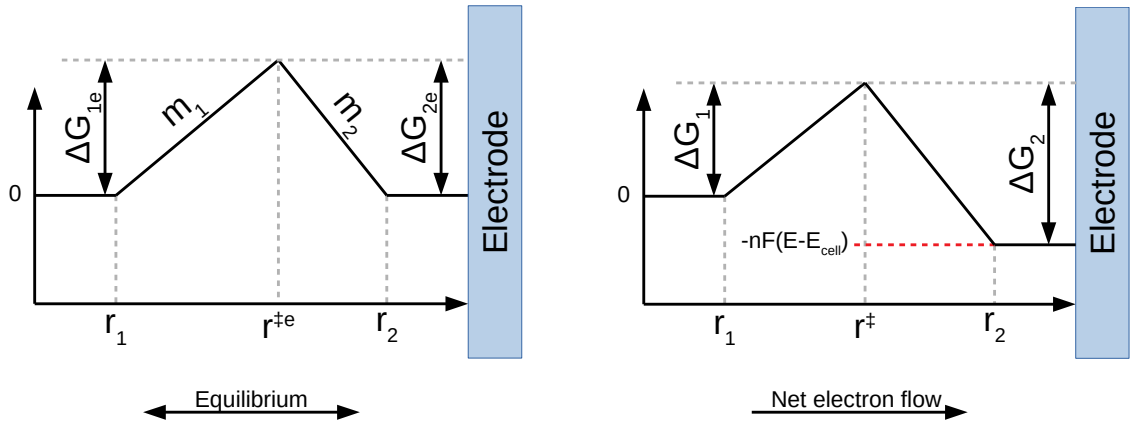

(a) $E = E_{cell}$ (b) $E = E$

Figure 1.6: Depiction of Gibbs energy *versus* reaction coordinate for a redox reaction at an electrode surface. The electrode is at the right, with Gibbs energy dictated by the electrode potential. The electrolyte bulk is on the left, with Gibbs energy independent of electrode potential.

At equilibrium the electrode potential equals the Nernst potential E_{cell}, and the rate of the oxidation and reduction reactions will be equal. For this to be the case, the energy barrier for oxidation and reduction must also be equal, i.e. $\Delta G_{1e} = \Delta G_{2e}$. Therefore,

$$\begin{aligned} \Delta G_{1e} &= m1(r^{\ddagger e} - r_1) \\ \Delta G_{1e} - m_2(r_2 - r^{\ddagger e}) &= 0 \end{aligned}$$

where $r^{\ddagger e}$ is the reaction coordinate of the intermediate at equilibrium. Rearranging these equations to elimate $r^{\ddagger e}$ produces:

$$\begin{aligned} \Delta G_{1e} - m_2\left[r_2 - (\Delta G_{1e}/m1 + r_1)\right] &= 0 \\ \Delta G_{1e}(1 + m_2/m_1) - m_2(r_2 - r_1) &= 0 \\ \text{therefore} \qquad \Delta G_{1e} &= \left(\frac{m_1}{m_1 + m_2}\right) m_2(r_2 - r_1) \end{aligned} \tag{1.14}$$

As the electrode potential E changes, the Gibbs free energy at the electrode will change by $-nF(E - E_{cell})$. This will alter the position of $r^{\ddagger}$, as well as the sizes of both ΔG_1 and ΔG_2, such that a net flow of electrons will occur, and therefore a net current in the opposite

direction. Repeating the equations above produces:

$$\Delta G_1 = \left(\frac{m_1}{m_1 + m_2}\right)\left[-nF(E - E_{cell}) + m_2(r_2 - r_1)\right] \tag{1.15}$$

Subtracting Equation 1.15 from Equation 1.14 produces:

$$\Delta G_{1e} - \Delta G_1 = \alpha_1 nF(E - E_{cell})$$
$$\text{where} \qquad \alpha_1 = \left(\frac{m_1}{m_1 + m_2}\right)$$

Thus, since $E - E_{cell}$ is equal to the overpotential η, the height of the energy barrier to oxidation is reduced by $\alpha_1 nF\eta$. As a sanity check, it is good to confirm that raising the potential of an electrode does indeed increase the rate of oxidation, which it does. By a similar argument, the barrier to reduction is increased, therefore:

$$\Delta G_2 - \Delta G_{2e} = \alpha_2 nF(E - E_{cell})$$
$$\text{where} \qquad \alpha_2 = \left(\frac{m_2}{m_1 + m_2}\right)$$

By convention, the parameters α_1 and α_2 are replaced by α and $(1 - \alpha)$, since they add up to unity. If it is declared that:

$$\Delta G_{1e} - \Delta G_1 = \Delta G^{\ddagger 1}$$
$$\Delta G_{2e} - \Delta G_2 = \Delta G^{\ddagger 2}$$

then substitution into equation 1.13 produces:

$$k_1 = A' \exp\left(\frac{\alpha nF\eta}{RT}\right)$$
$$k_2 = A' \exp\left(-\frac{(1-\alpha)nF\eta}{RT}\right)$$

The net current is proportional to the difference between the two rate constants multiplied by their own local reactant concentrations C_1 (oxidation) and C_2 (reduction):

$$i = nF\left[k_1 C_1 - k_2 C_2\right]$$
$$i = nFA'\left[C_1 \exp\left(\frac{\alpha nF\eta}{RT}\right) - C_2 \exp\left(-\frac{(1-\alpha)nF\eta}{RT}\right)\right] \tag{1.16}$$

This is the standard method of expressing the Butler-Volmer equation, and implicit in its construction is the possibility that the local concentration of the reactant species C_1 and C_2

will be different to their values in the electrolyte bulk. This will occur whenever the electrode potential is sufficiently positive or negative of the Nernst potential that limitations of mass transport come into effect. The maximum current will then tend towards the *diffusion-limited current*.

Also implicit is that the rate at which the net current responds to changes of overpotential (i.e. $di/d\eta$) is proportional to A'. This is known as the *exchange current*, and is a measure of electrode activity. It can be increased either by reducing the size of the energy barrier in either direction, which is to say through better catalysis, or by increasing the surface area of the electrode. In the absence of mass transport limitations, the two approaches are indistinguishable.

At values of η sufficiently positive or negative for one of the exponential terms to be ignored, the relationship simplifies to that of the *Tafel equation*, for example if η is positive, Equation 1.16 can be rearranged as:

$$\begin{aligned} & \eta = \frac{RT}{\alpha nF} \ln\left(\frac{i}{nFA'C_1}\right) \\ \text{therefore} \quad & \eta = b\log(j) + c \\ \text{where} \quad & b = \ln(10)\frac{RT}{\alpha nF} \end{aligned} \tag{1.17}$$

and j is the current density. It can thus be seen immediately that the Tafel slope b is proportional to absolute temperature.

1.3.4 The Brønsted-Evans-Polanyi Model

Although from Density Functional Theory (DFT) calculations a figure can be obtained for the onset potential at which an electrochemical reaction will begin to proceed, this is not a binary process, and some current density is observed at potentials well below this. The higher the surface area for the material, the higher such currents will be. In experiments performed at low current densities (or on rotating electrodes) so as to permit diffusion effects to be ignored, the rate of reaction will in general be determined by the Arrhenius equation:

$$k = Ae^{\left(\frac{-E_A}{RT}\right)} \tag{1.18}$$

where k is the reaction rate coefficient, R the universal gas constant, and T the temperature in Kelvin. E_A and A refer to the activation energy and the frequency factor respectively, and can be determined from an Arrhenius plot, whereby $log(j)$ is plotted against $1/T$. This is based on the assumption that j will be proportional to k, which is a good assumption under gas-evolving conditions. The activation energy E_A has in fact two components, one from the thermodynamics (as simulated by DFT) and one from the kinetics (the barrier between

steps that must be overcome). According to the Brønsted-Evans-Polanyi model these are related [39], such that:

$$E_A = E_0 + \alpha \Delta H \tag{1.19}$$

where ΔH is the change in enthalpy (for this reaction step), and α specifies the position of the reaction intermediate along the reaction coordinate, such that $0 < \alpha < 1$. This principle is predicated on the over-simplification that bond energy is a linear function of bond length, as shown schematically in Figure 1.7.

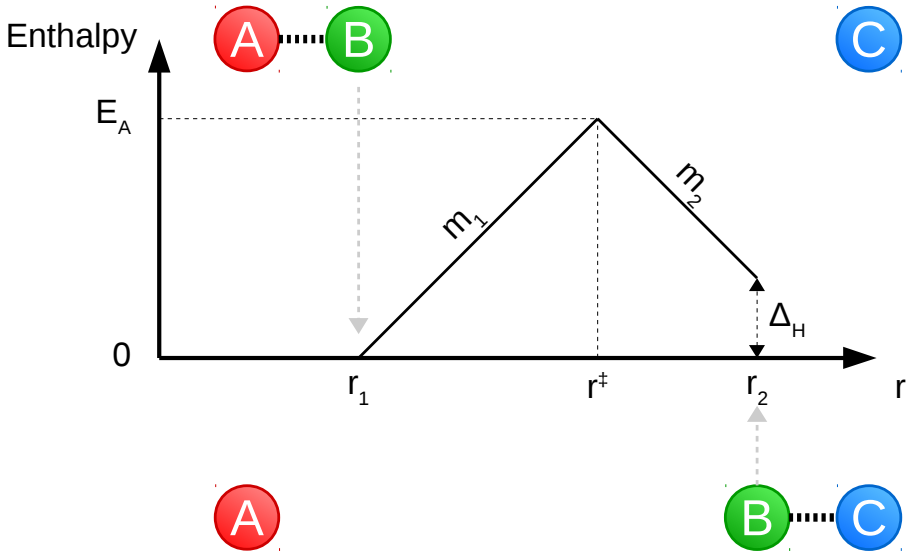

Figure 1.7: Diagram of the concepts behind the Brønsted-Evans-Polanyi principle, which is a simplified scheme for the enthalpy involved in breaking bond A-B and making bond B-C

The diagram is a representation of the chemical reaction:

$$\mathrm{AB} + \mathrm{C} \longrightarrow \mathrm{A} + \mathrm{BC} \tag{1.20}$$

Thus the reaction proceeds by the breaking of bond A-B, and the simultaneous making of bond B-C. It is assumed that the distance A-C remains constant throughout, and the reaction coordinate can therefore be described solely in terms of the position of atom B, which shall be called r. The rate of change of enthalpy with distance for each bond is m_1 and m_2, and at the transition point $r = r^{\ddagger}$ and the enthalpy $H = E_A$, the activation energy. Since the reaction starts, by convention, at zero enthalpy, it can be stated that:

$$E_A = m_1(r^{\ddagger} - r_1) \tag{1.21}$$

$$\text{and} \qquad \Delta H = E_A - m_2(r_2 - r^{\ddagger}) \tag{1.22}$$

By rearranging Equation 1.21 and inserting into Equation 1.22, $r^{\ddagger}$ can eliminated, producing:

$$\begin{aligned}\Delta H &= E_A - m_2[r_2 - (E_A/m_1 + r_1)] \\ &= E_A\,(1 + m_2/m_1) + m_2(r_2 - r_1)\end{aligned}$$

therefore:

$$E_A = \frac{m_1}{m_1 + m_2}\,[\Delta H + m_2(r_2 - r_1)] \tag{1.23}$$

which is the same as Equation 1.19 so long as:

$$E_0 = \frac{m_1 m_2}{m_2 + m_1}(r_2 - r_1)$$

$$\text{and} \qquad \alpha = \frac{m_1}{m_1 + m_2}$$

Thus, if the rate of change of enthalpy with r for bond A-B is the same as for bond B-C, i.e. such that $m_1 = m_2$, then α will equal 0.5.

One surprising aspect of the Brønsted-Evans-Polanyi principle is that it makes observably correct predictions even though no attempt has been made to correctly model the variation of enthalpy with bond length. It may therefore be concluded that correct modelling is not necessary, since whatever errors there are cancel out. Another is that it has found application to many families of chemical reactions, extending far beyond ones that obey the scheme laid out in Equation 1.20. It therefore provides a powerful insight into the fundamental forces of nature that lie behind ordinary chemical reactions.

Ordinarily the value of ΔH for any chemical reaction would be fixed, but in electrochemistry, so long as electron transfer occurs, its value can be altered by changing the electrode potential. This is because the electrons will gain or lose energy as they transition between differing electric potentials. Expressing this formally:

$$\Delta H = \Delta G_0 + T\Delta S - nUeN_A \tag{1.24}$$

where ΔG_0 is the change in Gibbs free energy for the reaction, n is the number of electrons transferred in the overall chemical reaction, U is the electrode potential, e is the charge on an electron, and N_A is Avogadro's constant. Thus, since ΔH can be altered by changing the electrode potential, so in turn can the activation energy, and it is by this means that electrical energy can be used to power chemical reactions, which would otherwise occur extremely slowly. Since the term eN_A can be replaced by the Faraday constant F, Equations 1.19 and 1.24 can be combined to obtain:

$$E_A = E_0 + \alpha\,(\Delta G_0 + T\Delta S - nUF) \tag{1.25}$$

If it is stated that $j \propto k$, and Equation 1.25 is substituted into Equation 1.18, the full expression is obtained:

$$j = A' exp\left[\frac{-E_0 - \alpha\left(\Delta G_0 + T\Delta S - nUF\right)}{RT}\right] \tag{1.26}$$

This can be rearranged in the form:

$$ln(j) = k_1\left(1/T\right) + k_2\left(U/T\right) + k_3 \tag{1.27}$$

$$\text{where} \quad k_1 = \frac{-\left(E_0 + \alpha\Delta G_0\right)}{R}$$

$$k_2 = \frac{\alpha nF}{R}$$

$$k_3 = ln(A') - \frac{\alpha\Delta S}{R}$$

Equation 1.27 can be regarded as a mathematical model, which predicts that the current density (and therefore the rate of reaction) should consist of three components: one is invariant, one varies only with temperature, and one varies with both temperature and electric potential. The values k_1, k_2 and k_3 are constants, the values of which depend on fundamental properties of the reaction. In fact, by rearranging the equation as:

$$U = \frac{T}{k_2}\ln(j) - \frac{k_1}{k_2} - \frac{k_3}{k_2}T \tag{1.28}$$

$$\text{therefore} \quad \eta = b\log(j) + c_1 + c_2T \tag{1.29}$$

the model can be seen to be a slightly more advanced version of the Tafel equation (Equation 1.17 on page 23). The Tafel slope b is still proportional to temperature, but the Tafel offset c has been separated into two components, one of which describes its variation with temperature.

Unlike any of these models, the model presented here only applies to a three-electrode cell *after* iR-correction, and thus only describes a single over-potential. It is also derived solely from theory, rather than empirical observation, and therefore represents an idealised version of this behaviour.

Differentiating Equation 1.27 with respect to $1/T$ produces:

$$\frac{dln(j)}{d(1/T)} = k_1 + k_2U \tag{1.30}$$

Since an Arrhenius plot is a plot of $\ln(j)$ against $(1/T)$, this indicates that the slope of the Arrhenius plot should equal zero when:

$$U = \frac{E_0 + \alpha\Delta G_0}{\alpha nF} \tag{1.31}$$

Note the above equations also imply that the slope of the Arrhenius plot could become positive, i.e. such that the rate of reaction *decreases* with increasing temperature. This is non-physical, since it would imply a negative activation energy, so Equation 1.31 defines a maximum value for U beyond which the above equations cease to apply.

Differentiating Equation 1.30 with respect to U yields:

$$\frac{dK}{dU} = k_2, \text{ where } K = \frac{dln(j)}{d(1/T)} \tag{1.32}$$

which reveals how the slope of the Arrhenius plot should vary with electrode potential. However, since differentiation is a process that increases signal noise, this may be unreliable in practice. More reliable is to differentiate Equation 1.27 with respect to U, yielding:

$$\frac{dln(j)}{dU} = k_2/T = \frac{\alpha nF}{RT} = \frac{2.303}{\text{Tafel slope}} \tag{1.33}$$

This is confirmation that at sufficiently high current densities, the Tafel slope is equal to $2.303RT/\alpha nF$. It also confirms that the α from the Brønsted-Evans-Polanyi principle is the same α as that from the Butler-Volmer theory. This provides a method of measuring alpha, which will be attempted experimentally in Section 3.2 on Page 79.

1.4 Catalysis

Catalysis is the process by which the rate of a chemical reaction is increased by the introduction of a substance that is not itself consumed in the reaction. The catalyst achieves this either by lowering the activation energy barrier of the straightforward reaction directly, or by introducing a new reaction mechanism, often involving extra steps that collectively reduce the energy requirements. Surfaces are inherently useful for such a process, since they offer a place where otherwise unstable intermediates, such as adsorbed species, can be stored and presented.

In nature catalysts are called enzymes, and there is much to be learned from them, particularly in terms of the precise choice and arrangement of atoms within the reaction centre. It is perhaps for this reason that biological enzymes tend to be much more specific than those that are produced by conventional laboratory methods. A prime example of this is the oxygen evolving complex (OEC) at the heart of photosynthesis, which is comprised of four manganese atoms and one calcium atom. These atoms simultaneously store energy from sunshine in the form of oxidising equivalents *and* collectively bind two water molecules in the right orientation to permit the two oxygen atoms to be brought together [40], although the precise mechanism by which this is done is still not understood.

Perhaps most astonishing is the way in which the external energy source of sunshine is brought to bear by photosynthesis on to what is essentially homogeneous catalysis. Although it would be tempting to attempt to combine a liquid catalyst into a standard electrolytic cell, this would leave the electrodes with no way to power the electrochemical reactions, since the catalyst and the electrodes would not be in physical contact.

Photosynthesis also has this problem, since the location where each photon is absorbed is random, and certainly unlikely to be a direct hit right onto the active site. Instead the energy of the photon is absorbed as an *exciton*, which is the combination of an excited electron and the hole from which it came. The electron and hole can remain bound to each other because they are attracted by electrostatic forces, and can travel extensively within an extended structure made of chlorophyll called an 'antenna'.

It would appear that the chances of an exciton reaching the OEC by pure chance are extremely slim, and this is correct. However, by the laws of quantum mechanics which govern all matter, the exciton does not exist in just one place, but instead as a *superposition* of all the possible places it could go. In one of these possibilities, the exciton reaches the active site and is absorbed, and it is this that causes the quantum superposition to collapse *as if* the exciton had travelled there and nowhere else. It is only in this way that the plant can harvest enough light to stay alive. This is the remarkable mechanism that nature has discovered, and until such time as chemists are able to achieve similar levels of excellence, they will never be able to claim complete mastery of their subject.

1.4.1 Reaction Mechanisms (HER and OER)

For the hydrogen evolution reaction (HER) it is generally accepted that the reaction mechanisms in alkaline solution are a combination of steps involving the formation of adsorbed hydrogen, according to the Volmer, Heyrovsky and Tafel reactions [41]:

$$\mathrm{M} + \mathrm{H_2O} + \mathrm{e^-} \longrightarrow \mathrm{MH_{ads}} + \mathrm{OH^-} \qquad \text{(Volmer)}$$

$$\mathrm{MH_{ads}} + \mathrm{H_2O} + \mathrm{e^-} \longrightarrow \mathrm{H_2} + \mathrm{M} + \mathrm{OH^-} \qquad \text{(Heyrovsky)}$$

$$2\,\mathrm{MH_{ads}} \longrightarrow 2\,\mathrm{M} + \mathrm{H_2} \qquad \text{(Tafel)}$$

where M stands for any suitable active site on the electrode. This combination of mechanisms gives rise to various characteristic Tafel slopes, which is the rate at which the iR-corrected current density increases exponentially with voltage [42]. If the Volmer reaction is the rate-determining step, then a uniform 120 mV dec^{-1} Tafel slope will be observed. Where the Tafel reaction is the rate-determining step, the Tafel slope would start at 30 mV dec^{-1}, then become infinite, since the Tafel reaction does not involve electron transfer, and therefore its rate is independent of electrode potential. In practice it is more likely that the Heyrovsky

step is rate-determining, and we observe a Tafel slope that transitions from 40 mV dec^{-1} at low current densities to 120 mV dec^{-1} at higher current densities. The physical explanation for this transition is that as the current density increases, the surface coverage of adsorbed hydrogen also increases, with the change of slope occurring when the percentage coverage begins to exceed 50% [42].

For the oxygen evolution reaction (OER) the situation is not so simple, since it is a 4-electron process:

$$4\,OH^- \longrightarrow O_2 + 2\,H_2O + 4\,e^- \tag{1.34}$$

This is highly unlikely to proceed in a single step, and instead can be rewritten as four separate steps, each consuming one OH^- ion, and releasing one electron: [43]

$$OH^- \longrightarrow HO_{ads} + e^- \quad \text{(Step 1)} \tag{1.35}$$

$$HO_{ads} + OH^- \longrightarrow H_2O + O_{ads} + e^- \quad \text{(Step 2)} \tag{1.36}$$

$$O_{ads} + OH^- \longrightarrow HOO_{ads} + e^- \quad \text{(Step 3)} \tag{1.37}$$

$$HOO_{ads} + OH^- \longrightarrow H_2O + O_2 + e^- \quad \text{(Step 4)} \tag{1.38}$$

It should be noted that the above mechanism is only one possibility. There are others, most notably the Krasil'shchkov path, which avoids the HOO_{ads} species in favour of the combination of two O_{ads} species to yield an O_2 molecule [44]. Just like the Tafel step for HER, since this doesn't involve an electron transfer it is quite likely that it will give way to a mechanism that does involve electron transfer as the current density increases. Nevertheless it highlights the fact that the existence of the HOO_{ads} species shouldn't be taken for granted in every situation.

More interesting perhaps is evidence that the mechanism can change with pH. In experiments with highly purified iron-free nickel and electrolyte, Diaz-Morales *et al.* observed that the OER mechanism changes to a more efficient regime above pH 11 [45]. The explanation given is that the normally uncharged OH_{ads} or OOH_{ads} species can deprotonate if the pKa value of the proton is less than the pH of the electrolyte. The H^+ proton and the OH^- of the electrolyte combine to form H_2O, leaving behind a charged species on the surface of the catalyst, which quickly undergoes further reactions leading to the release of O_2. Identical pH-dependent deprotonation steps have been observed on Fe-containing Ni [46] and manganese oxide [47].

It is important to note that this mechanism change is associated with an increase in activity towards oxygen evolution, and as such it therefore presents us with a possible route for escaping the limitations of the fully concerted electron-transfer mechanism outlined above. Similarly, Grimaud *et al.* have shown with perovskites and isotopic labelling that lattice oxygen itself can participate in the chemical reactions leading to oxygen evolution [48], and it is perhaps enlightening that the same effect has been observed with IrO_2 [49] and RuO_2 [50].

Whilst this raises concerns regarding the long-term stability of such catalysts [51], these mechanism changes are again associated with an increase in activity towards oxygen evolution, and as such offer great potential if the stability issues can be controlled.

1.4.2 DFT Simulation and the Energy Staircase

Density Function Theory (DFT) is a powerful method in Computational Chemistry that can be used to calculate the ground-state of molecules and condensed matter, that is the lowest energy state it can adopt in the absence of any excitation or thermal energy. In electrochemistry it has the revolutionary property that it can be used to help predict the electrode potentials at which various reactions start to become feasible, and thus permit rational electrode design and simulation [52, 53].

Every reaction at an electrode involves a change in energy, and that energy is itself composed of various components: the Gibbs Free Energy (G), the Zero Point Energy (ZPE) plus the product of Temperature (T) and Entropy (S). There are also additional energy changes involved with charged species (e.g. e^-, H^+, OH^-) which can be calculated as the product of their charge, and the change in potential through which they are moving. Since we are only concerned with relative changes in energy, we can write [54]:

$$\Delta G = \Delta E_{DFT} + \Delta ZPE - T\Delta S + \Delta E_{charge} \tag{1.39}$$

where the ZPE is that which is left over *even after* the substance has been cooled to absolute zero, and is a consequence of the uncertainty principle from quantum mechanics. It is generally small, but can also be calculated from DFT simulations. The importance of the Gibbs Free Energy stems from the fact that it describes the *feasibility* of any given reaction, which can proceed even if ΔE is positive (i.e. an endothermic reaction). Entropy is particularly relevant to water-splitting since there is a pronounced phase change involved in gas evolution.

Consider the situation depicted by Figure 1.8. The upper dotted blue line shows the increases in Gibbs Energy as the OER reaction described in Equations 1.35 to 1.38 proceeds from start to finish. It is notable that Step 3 has the largest change in energy, and Step 4 the smallest. The solid blue line shows the associated jumps in enthalpy (at zero volts). Now Step 4 is the largest, since it involves the biggest jump in entropy associated with the evolution of gaseous O_2. This step will therefore be highly endothermic. Nevertheless, it will still be able to proceed so long as it is able to draw thermal energy from the inefficiencies of the previous steps.

The lower dotted orange line shows the situation where the anode has a potential of 1.6 V. Here the energy gain of each step is reduced because an electron is being removed into the electrode, which has a positive potential, therefore the electron has energy eU. After Step 2

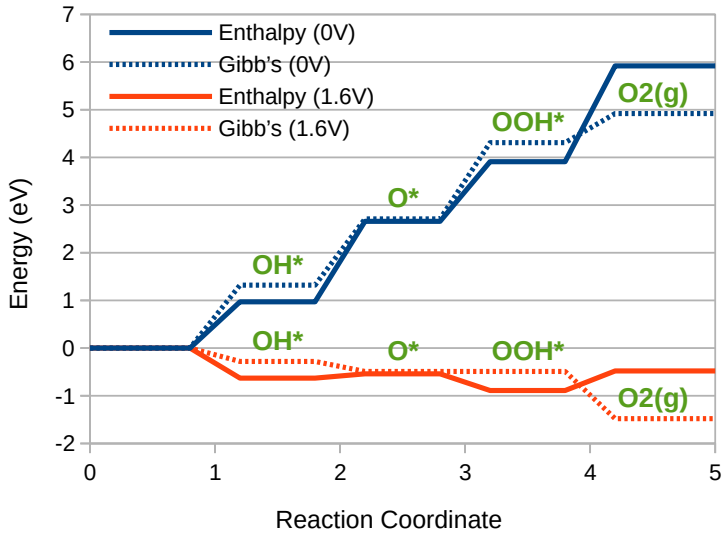

Figure 1.8: The steps in enthalpy and Gibbs free energy during a hypothetical 4-step oxygen evolution reaction.

there are two electrons in the electrode, which have energy $2eU$, and so forth. It is therefore possible to predict that at an electrode potential of 1.6 V (for the above diagram), all steps (in Gibbs free energy) are either flat or downhill, and the reaction is now able to proceed. Note that the total enthalpy is also slightly downhill, which it will be for all electrode potentials above 1.48 V, since this constitutes the thermoneutral voltage.

1.4.3 Scaling Relationships

One of the most important insights to come out of the field of *ab initio* Density Functional Theory (DFT) simulations in recent years is that the ground-state energies of various reaction intermediates appear to be related [39, 52]. We obtain on metallic (111) surfaces:

$$\Delta G(OH_{ads}) \approx 0.50 \times \Delta G(O_{ads}) + 0.05\text{eV} \tag{1.40}$$

$$\Delta G(OOH_{ads}) \approx 0.53 \times \Delta G(O_{ads}) + 3.18\text{eV} \tag{1.41}$$

and on oxide surfaces:

$$\Delta G(OH_{ads}) \approx 0.61 \times \Delta G(O_{ads}) - 0.58\text{eV} \tag{1.42}$$

$$\Delta G(OOH_{ads}) \approx 0.64 \times \Delta G(O_{ads}) + 2.40\text{eV} \tag{1.43}$$

This seems fairly intuitive, since the adsorbed species feature similar chemical bonds, both to the electrode surface and internally. However, the implications for the thermodynamics are far-reaching [39]. Since, regardless of the material, we see roughly a 3.2 eV energy difference between the ground-state of OOH_{ads} and OH_{ads}, this should place a theoretical

limit on the overpotential that is seen for OER of about 0.37 V [43, 52]. This will occur when the jumps in binding energy are as equalised as they can be which, using the above equations for oxides, will occur when $\Delta G(O_{ads}) \approx 2.43\,\text{eV}$. It is therefore good confirmation that theoretical work by Calle-Vallejo *et al.* correlating the number of outer electrons with binding energies places the closest match to this figure at 2.49 eV on nickel oxide, and second closest on cobalt oxide, as shown in Figure 1.9, which has been adapted from this work [55].

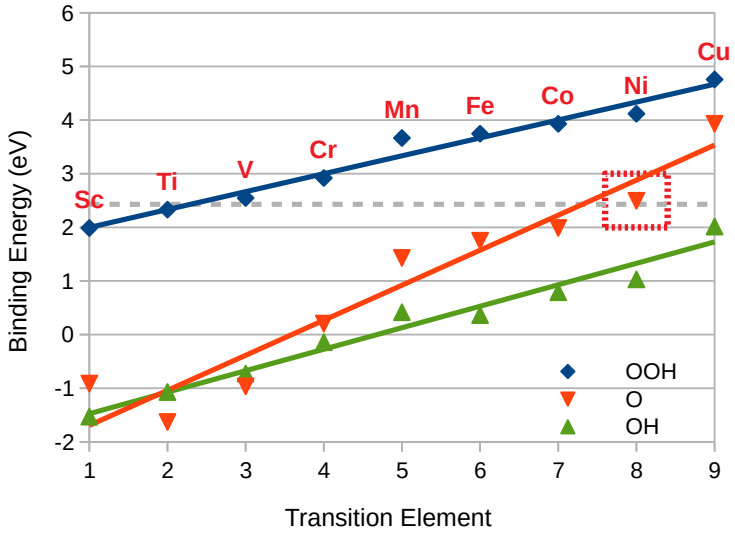

Figure 1.9: Variation of the binding energies of three adsorbed species across the first row transition elements. The most equal jumps in energy will occur where $\Delta G(O_{ads}) \approx 2.43\,\text{eV}$, which is indicated by the horizontal dashed grey line. The element that falls closest to this (for oxides) is nickel, as indicated by the dotted red box.

Nevertheless, it should be stressed that this will only apply if the reaction proceeds according to four-step mechanism outlined above. There is plenty of evidence that this is not always the case [47], but determining the precise mechanism at work on any given catalyst is challenging the limits of analytical chemistry. It will also only apply if the catalyst remains as nickel oxide, and there is good evidence that it is instead transformed into NiOOH [56]. In contrast to NiO, the binding energies on the NiOOH surface are no longer at the top of the volcano plot, and there is therefore scope for dopant atoms to be introduced so as to fine tune the binding energies via ligand effects .

Nevertheless, a sound theoretical understanding of the processes at work is vital if breakthroughs are to be made. To this end DFT research work continues with the goal of discovering how to modify the active sites to be more three-dimensional [57] or indeed more molecular [58]. It is the belief, based both on simulation and experimental work, that the activity of surface bridge sites can be optimised independently of the activity of the more conventional surface sites, and thereby provide the required number of degrees of freedom needed to permit full catalytic optimisation.

1.4.4 Mixtures and synergy

A lot of research has been conducted into mixtures of transition elements, and in many cases it has been observed that a mixture of transition-metal oxides out-performs any of the individual metal oxides on their own. Such synergistic effects have been observed for many such mixtures, including Ni-Fe [59], Ni-Co [60], [61], Ni-Co-Fe [62], Ni-Cu [63], Cu-Fe-Mo [64], Fe-Ni-Mo [65], Mn-Cr [66], Fe-Mo [67], Cu-Co [68] and Fe-Co-W [69]. In addition similar effects have been observed in other materials, such as Ni-Co Phosphide [70], Ni-Fe Nitride [71] and Ni-Fe Selenide [72].

Interestingly, the same effect has been observed for ultra-thin layers (i.e. down to one mono-layer) of cobalt oxide on gold, an effect which is attributed to the gold enhancing the oxidation of cobalt to Co^{IV} [73]. It is this form of cobalt that is the active site for oxygen evolution, since it is so electrophillic that it is believed to be able to promote O-OH bond formation, and the rôle of the gold is to provide an electron sink that encourages the cobalt into this oxidation state at a lower electrode potential than would otherwise be the case, thereby enhancing efficiency. This is in agreement with a study on iridium oxide nanoparticles by Sanchez Casalongue *et al.* who successfully employed synchroton-based APXPS to identify a characteristic change from Ir^{IV} to Ir^{V} that was only observed during OER [74]. They conclude that this lends support to an OER mechanism involving adsorbed OOH groups, with the theory being that the ionisation shift helps to lower the free-energy required to jump from $OH^- + O_{ads}$ to $OOH_{ads} + e^-$, thereby allowing OER to proceed at a lower potential.

Yet another material that demonstrates this effect is a ternary mixture of iron, cobalt and tungsten (FeCoW) [69], where the addition of tungsten was predicted from DFT to achieve a smoother energy staircase. It is perhaps significant that throughout the entire transition metal block, the two most electronegative elements are gold and tungsten. Other electronegative candidates (on the Pauling scale, and excluding group 7) are nitrogen, sulphur, selenium and carbon, so it is surely no coincidence that these also feature prominently in the field of oxygen evolution electrocatalysis.

The explanation for all of these results is elusive, with some explanations centring on electronic properties of the materials, such as 'the d-band model' for metallic surfaces [75]. In this model the binding energy between the transition metal surface and the adsorbate species is explained by the formation of both bonding and antibonding states between the adsorbate valance states and the metal d-states. The model goes on to predict that the higher the metal d-states and the antibonding states above them fall relative to the Fermi level, the less likely the antibonding states are to be occupied, and therefore the stronger the bond. Thus Au, Ag and Cu, with mostly complete d-shells, form bonds which are too weak to be catalytically useful, whereas the left third of the transition block tend to form bonds which are too strong.

This model has been extended in recent years to encompass transition metal oxide surfaces by focussing on the band-filling of e_g spin states, along with the covalency of metal-oxygen bonds [76]. The theory states that because e_g states of 3d orbitals form σ bonds, in contrast to the π bonds of t_{2g} states, they are more able to transfer electrons to oxygen-based adsorbates, thereby forming stronger bonds. For the same reason the transition metal-oxygen bonds will also involve more electron transfer, and will therefore be more covalent in nature. The peak of this situation occurs when the e_g occupancy is close to unity, after which point the bonds tend to become too strong.

Early Oxidation: It is quite possible that all of these materials are highlighting the same two general principles at work, namely that a) two similar materials will transfer electrons between them, thereby breaking symmetry and promoting early oxidation, and b) two dissimilar materials will promote early oxidation if one of them is sufficiently electronegative. In both cases, early oxidation of the transition metal sites at the catalyst surface enhances the efficiency of the oxygen evolution reaction.

Another potential route towards early oxidation might be to incorporate a photo-sensitive material as a cocatalyst, as has been achieved with the synthesis of alkyl aryl ethers [77]. The real challenge for electrochemistry is to be able to simulate and predict these effects, and thereby achieve optimum results.

Perhaps the simplest explanation involves heterogeneous adjacent sites [78, 79]. For example, in an Fe-Co catalyst this would occur at any sites wherever Fe and Co occur as neighbours at the surface of the crystal lattice. The oxygen evolution reaction is free to proceed independently on each of these sites, until both are in possession of an adsorbed oxygen atom, i.e. Fe=O and Co=O. At this point an O-O bond can form directly between the two oxygen atoms, leading to the release of O_2 gas. Most importantly, DFT calculations indicate that the overpotential of oxygen evolution by such a mechanism on Fe-Co neighbours is lower than for either Fe-Fe or Co-Co. Thus, *any* mixture of Fe and Co is a better catalyst than either of the elements on their own.

One reason this theory fails to provide an adequate explanation is that it requires the Krasil'shchkov mechanism to predominate. As mentioned in Section 1.4.1 on page 28, this direction oxygen recombination step does not involve electron transfer, and would therefore result in an infinite Tafel slope. Since this does not happen, this cannot be the dominant mechanism at high current densities, and since catalyst synergy is observed at all current densities, this cannot be the full explanation.

However, that does not mean that it cannot form the basis of an explanation that can work for all mechanisms. It is also certainly able to explain how the improvement can be so rapid with just small amounts of contamination, since a single Fe atom could have multiple heterogeneous neighbours (or *vice versa*) depending on the precise lattice arrangement.

It should also be noted that not all mixtures are equally easy to generate, or as stable. Carbon in particular is expected to experience strong corrosion at practical oxygen evolving potentials, and indeed if it is doing so, it may well be contributing to misleading results [44]. Other elements, such as tungsten, tend to crystallise out and form microscopic particles, thereby raising a question mark over whether their potential can be reliably harnessed long-term [69].

1.4.5 State of the art

Hydrogen Evolution: A limited survey of recently published results for earth-abundant hydrogen evolution catalysts is as presented in Table 1.4.[3]

Lead Author(s)	Year	Catalyst	Substrate	Electrolyte	Tafel slope mV dec^{-1}	Overpotential mV
Wang Mingyong [80]	2015	NiMo	Cu	10 wt% NaOH	137	12
Zhang Jian [81]	2017	MoNi 4 /MoO 2	NF	1 M KOH	30	21
W. Gannon [82]	2019	**Raney2**	**316SS**	1 M KOH	50	28
R. Solmaz [83]	2017	NiZn-Au	Cu/Ni	1 M KOH	66	31
Wang Yuhang [84]	2014	3D NiMo	Cu foam	1 M NaOH		34
Zhang Tao [85]	2018	Ni_5P_4@$NiCo_2O_4$	NF	1 M KOH	27	35
Chen Weiwu [86]	2019	S-NiP	NF	1 M KOH	44	48
Xiang Rui [87]	2019	**PtC**	NF	1 M KOH	53	48
Gao M. [88]	2017	Ni-Mo MS	Cu	1 M KOH	49	63
Men Yana [89]	2019	Ni−Co_2P	CC	1 M KOH	68	65
Huang Yichao [90]	2019	1T-MoS_2	CFP	1 M KOH	52	66
Herraiz-Cardona [91]	2012	Ni	Cu foam	30 wt% KOH	103	68
Xiang Rui [87]	2019	Co@CoMoO 4	NF	1 M KOH	85	73
Liu Caichi [92]	2020	Ni_2P−$NiSe_2$	CC	1 M KOH	72.6	88
Shi Zhangping [93]	2016	nano MoC	GCE	1 M KOH	50	99
Liang Hai-Wei [94]	2015	CoNx	C	1 M KOH	75	111
Zhu Yanping [95]	2019	$CoSe_{1.26}P_{1.42}$	CC	1 M KOH	90	120
Lai Feili [96]	2019	Fe−$NiCo_2O_4$@HNCP	GCE	1 M KOH	47	143
Farjana Haque [97]	2019	2D Crys-AMO	NF	0.1 M KOH	50	153
Zhu Wenxin [98]	2016	NiS−MS	Ni foam	1 M KOH	83	158
Feng Yi [99]	2016	Ni-Co-P-300	not known	1 M KOH	61	169
Xing Zhicai [100]	2016	Ni_3N	NF	1 M KOH	109	177

Table 1.4: Recent achievements in earth-abundant hydrogen evolution catalysis. All overpotentials quoted at 20 mA cm^{-2}. Catalyst PtC is noble-metal, and included for comparison purposes only. The figures for 'Raney2' are as presented in Figure 5.34a on page 196.

The table shows that the overpotential, at least at 20 mA cm^{-2}, can be almost arbitrarily small. As a result, some authors only quote the overpotential at 100 mA cm^{-2}, by which point hydrogen evolution is very well established. Therefore, the table has been generated

[3] Abbreviations: CC: carbon cloth; CCH: cobaltous carbonate hydroxide; CFP: carbon fibre paper; CNT: carbon nanotubes; DO: derived oxide; FTO: fluorine-doped tin oxide; GCE: glassy carbon electrode; LDH: layered double hydroxide; MNA: mesoporous nanorod array; MS: microsphere; NA: nanorod array; NF: nickel foam; NP: nanoplates; NR: nanorods; NrGO: nitrogenated reduced graphene oxide; NSh: nanosheets; Nst: nanostructures; NA: nanowire arrays;

by taking measurements from published diagrams, so as to establish a common baseline. Many papers also offer a well-known commercial catalyst called 'PtC' (platinum on carbon) as a baseline for comparison, therefore it has been included in the table, even though it is not earth-abundant. It is heartening to note that 7 of the catalysts are able to outperform it, including the Raney2 catalyst presented in Chapter 5 of this thesis (see page 181).

Oxygen Evolution: A limited survey of recently published results for earth-abundant oxygen evolution catalysts is as presented in Table 1.5.

Lead Author(s)	Year	Catalyst	Substrate	Electrolyte	Tafel slope mV dec^{-1}	Overpotential mV
Bo Zhang [69]	2016	Gelled FeCoW	Au-plated NF	1 M KOH		191
Xiang Xu [101]	2016	$Ni_xFe_{1-x}Se_2$ – DO	NF	1 M KOH	28	195
Lu Xunyu, Zhao Chuan [102]	2015	NiFe NSh	NF	1 M KOH	28	215
Chi Jun [103]	2018	FeOOH/NiFe	CCH NA	1 M KOH		220
Feng Yan [71]	2017	NiFe-N NSh	CC	1 M KOH	26	224
Liu Rong [104]	2017	CoFe LDH NSh	NF	1 M KOH	36	232
Nai Jianwei [105]	2017	Ni-Fe-Se disks	GCE	1 M KOH	26	240
Lu Xue Feng [106]	2017	$CoFe_2O_4$/C NRA	NF	1 M KOH	45	240
Wang Zhaoyang [72]	2016	NiFeSe NSh	CC	1 M KOH	47	229
Gong Ming [107]	2013	NiFe-LDH	CNT	1 M KOH	31	247
Lu Zhiyi [108]	2014	NiFe-LDH NP	Nickel	1 M KOH	43	250
Zhang Huabin [109]	2019	FeCoP nanoboxes	CFP	1 M KOH	31	269
Rodney Smith [62]	2013	$Fe_{40\%}Ni_{60\%}$	FTO	0.1 M KOH	34	284
Xu You [110]	2017	Ni@NC-800	NF	1 M KOH	45	285
S. Anantharaj [111]	2017	CoP NSt	GC	1 M KOH	70	287
Yun-Pei Zhu [112]	2015	CoP-MNA	NF	1 M KOH	65	290
W. Gannon [82]	2019	**Raney2**	**316SS**	1 M KOH	38	291
Wang Huaping [113]	2019	$LaFexNi_{1-x}O_3$ NR	GCE	1 M KOH	50	302
Zhang Huabin [114]	2019	HCM@Ni-N	Carbon	1 M KOH	76	304
Fang Song, Xile Hu [115]	2014	CoMn LDH	GC	1 M KOH	43	324
Guang Liu [116]	2016	$NiFe_2O_4$ NR	GC	1 M KOH	44	342
S. Bikkarolla [117]	2015	$CuCo_2O_4$	NrGO	1 M KOH	64	360
Jing Jiang [118]	2014	NiCo-LDH NSh	NF	0.1 M KOH	113	420

Table 1.5: Recent achievements in earth-abundant oxygen evolution catalysis. All overpotentials quoted at 10 mA cm^{-2}. The figures for 'Raney2' are as presented in Figure 5.34b on page 196.

Although it can be difficult to make direct comparisons between catalysts, a picture has been emerging over recent years of the limits to which transition metals can be taken. At present this looks to be an overpotential of about 200 mV at a current density of 10 mA cm^{-2}. This current density is chosen because it is the most widely quoted figure, and because it is described as the most significant for solar fuel synthesis [119]. However, it is not the most significant figure for a commercial electrolyser, which needs to attain figures about two orders of magnitude higher. As an illustration of what is possible, figures of 100 mA cm^{-2} at an overpotential of 277 mV are quoted for the NiFeSe catalyst, whereas the NiFe-N catalyst has achieved 360 mA cm^{-2} at an overpotential of 255 mV, fully 220 mV less than the equivalent figure measured for IrO_2. At such current levels, diffusion and bubble effects are

likely to become ever more dominant, which is perhaps why at such current densities, talk of catalytic performance should in fact give way to whole system performance.

It should be stressed that for all of the nickel-iron materials listed in Table 1.5, the basic activity of the material is likely to be essentially invariant, and that variations in performance can primarily be ascribed to differences in effective surface area and porosity. It is for this reason that many studies in the literature only quote relative changes in overpotential, achieved by changing one aspect of the experiment. Even so, many aspects of the deposition and subsequent operation can have a significant impact on the effective surface area, such as cracking and flaking, and as such if these can be regarded as intrinsic properties of the catalyst, then there is no need to correct for them.

As previously mentioned, the developers of the FeCoW catalyst discovered that any annealing of their catalyst had a destructive effect on its catalytic ability. This they ascribed to the phase separation of the ternary catalyst into discrete crystalline particles of Fe_3O_4, Co_3O_4 and $CoWO_4$. Keeping all the elements of the catalyst in close proximity is key to its performance, and no doubt the performance of many other catalysts in this field, and it is a good example that highlights the key conflict between crystallinity, with its lower activity but higher stability, and amorphousness.

During in-situ observations performed by Arno Bergmann *et al.* on crystalline Co_3O_4, the catalyst was observed to undergo a reversible amorphisation at oxygen-evolving potentials. Upon subsequent removal of the anodic potential, the material reverted to the more stable crystalline state [120]. There are many putative benefits to an amorphous electrocatalyst: namely that the structural irregularities permit flexibility as regards the participation of multiple metal centres, and also enables the increased build up of oxidation equivalents, that provide the necessary electrochemical energy to drive energetic chemical reactions at reduced electrode potentials. The authors speculate that such amorphisation may neatly explain the observed OER activity of several other crystalline oxide materials, with the implication being that no crystalline oxide material can be catalytically active without some electropotential-induced, and presumably amorphous, surface structural change. That is not to say, however, that there is no benefit to the underlying crystallinity, which the authors propose can help prevent long-term dissolution of the metal cations.

As regards realistic long-term performance, the typical situation is that very little attention is given beyond sustaining a constant current density for a few tens of hours. Perhaps this is not surprising because according to Frydendal *et al.* it is simply not possible to obtain a meaningful stability estimation purely from electrochemical measurements [121]. Instead they recommend the monitoring of mass losses using an electrochemical quartz crystal microbalance (EQCM) and/or inductively coupled plasma mass spectrometry (ICP–MS). Certainly their finding that as a fraction of total system current, corrosion currents are at least 4 orders of magnitude lower, means that they are very difficult to measure, even though they

constitute an irreplaceable loss of catalyst (or substrate) material.

Nickel cathodes in particular have a reputation for coping badly with intermittent operation, to the extent that commercial nickel-based alkaline electrolysers commonly stipulate a minimum operational limit of 20% of rated electrical power [122]. This can have a huge impact on system efficiency, with the net result that one realistic study, which used off-the-shelf components and included all of the losses due to start-up, shutdown and idling, ended up producing a round-trip efficiency for electrical storage of just 13.5% [123].

On a final note, it is perhaps worth pointing out that humankind still has some way to go to catch up with nature and the photosystem II (PSII) complex, which achieves water-splitting at an overpotential of just 160 mV in an electrolyte of pH 6.5 [47]. The view is that in electrolytes of intermediate pH our present range of catalysts, and manganese in particular since that is at the heart of PSII, does not have the capability to control both electrons and protons at the same time, leading to unwanted competitor reactions that hinder the desired water-splitting reaction. This lead the researchers to add bases with a variety of pKa values to their experiment, such that the combination of the manganese and the base could perform a favourable internal proton transfer, and thus appear externally as a better catalyst [124]. If applied correctly, this lesson could be of use in many other situations, not just in artificial photosynthesis.

Chapter 2

Methods

> At the moment it is *our* ongoing emissions that are driving global temperatures up, but if we cross tipping-points that could spiral *beyond* our control.
>
> *David Attenborough*

2.1 Electrical Methods

The acquisition of repeatable and reliable electrochemical measurements is of crucial importantance to any electrochemistry research. Within the literature many papers have been written that attempt to standardise the benchmarking of electrocatalysts, and much inspiration was taken from these, particularly Stevens *et al.* [125]. However, it is often the case that few photographs exist of the researchers' actual experimental equipment.

Of those that do exist, it is clear that some researchers have chosen to use a beaker [125], others glassware [119, 126, 127], and some PTFE [128]. Many others refer to PTFE, but only from the text [121, 129–134]. Laboratory-grade ground glassware is specialised and expensive, and sadly unavailable within budget. An early attempt was made at using a beaker, but it was quickly realised that there were too many variables to control, such as the positioning of each electrode and the volume of electrolyte, and achieving repeatability would take great care.

It was also felt that much benefit could be gained by making proper use of the efforts of previous researchers within the department, most notably George Passas who, with Charles Dunnill, developed the original electrolysis cell based on laser-cut components [16]. In place of PTFE the cell makes use of acrylic, which due to its low melting point is particularly amenable to laser-cutting, and has extremely high resistance to alkaline conditions. It also has the added benefit of being transparent, which permits direct observation of conditions inside the cell. Most importantly, the cell holds the electrodes in precisely defined positions

relative to the electrolyte, which is itself also precisely defined and electrically insulated. Mechanical drawings of the electrolysis cell are as presented in Figure 2.1, with the physical appearance as presented in Figure 2.2.

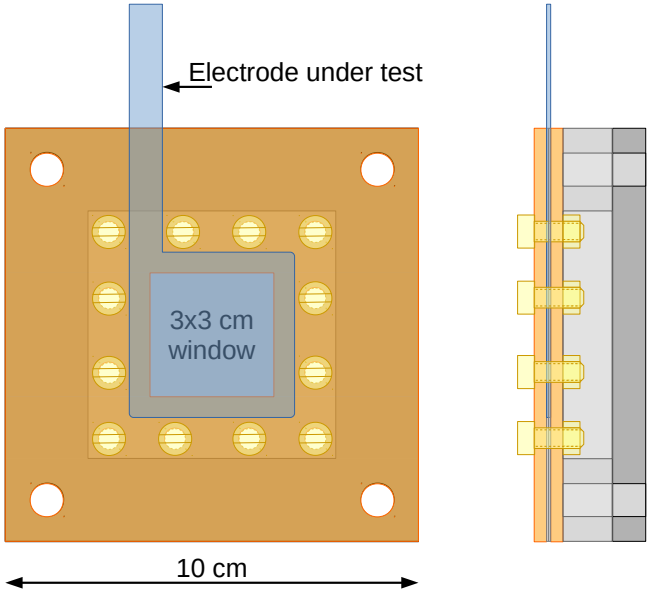

(a) Electrode mount

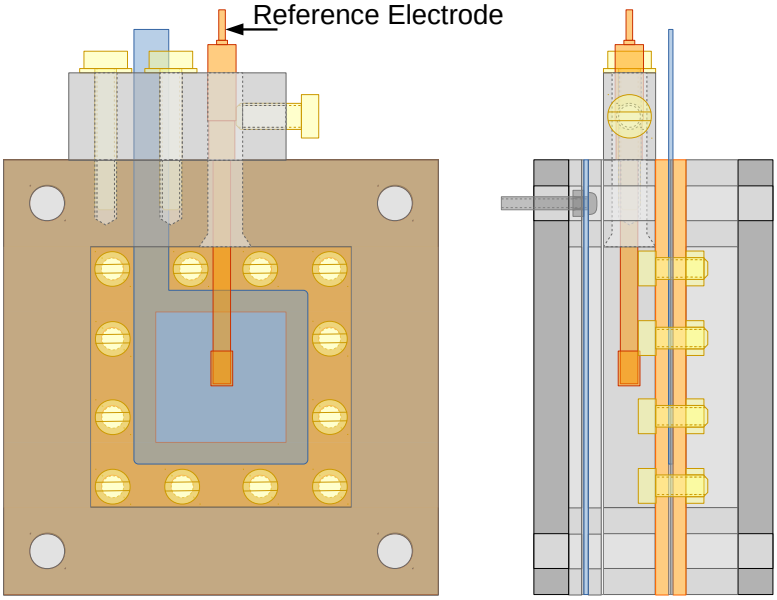

(b) Assembly drawing

Figure 2.1: Mechanical drawings of the cell used for electrochemical measurements.

The counter-electrode was 316-grade stainless-steel (316SS), which is in contrast to the consensus view that the counter-electrode should be a large area of platinum. In theory, it should not matter which material is used, since the potentiostat will simply compensate for any variation in kinetics. In any case, a large area of platinum was also out of budget, so

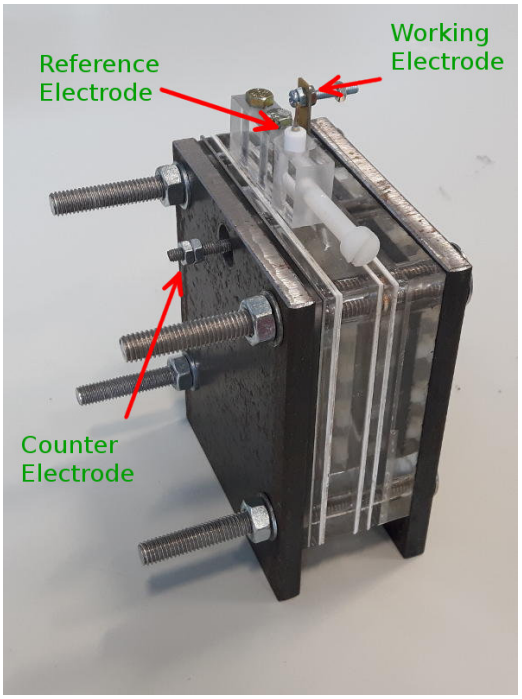

Figure 2.2: Photograph of electrochemical characterisation cell.

a brief experiment was conducted with a Pt sputter-coated counter-electrode. However, it was quickly realised that the threat of Pt contamination far outweighed any putative benefit, particularly for any measurements of HER overpotential. Therefore the Pt-coated counter electrode was not used again.

The drawings show the final version of the electrode mount. Initially the working electrode (as based on the inherited designs) was 10 cm × 10 cm, with a 3 cm × 3 cm exposed window. However, such a size precluded much (non-destructive) characterisation, particularly inside the scanning electron microscope (SEM). Therefore a new design was produced which made use of the engraving function of the laser-cutter to accommodate an L-shaped electrode, a shape which also permitted four times as many electrodes to be cut from the same amount of stock. This was small enough to fit inside the SEM, and therefore permitted characterisation both before and after experiments, which transformed the possibilities for research. With the addition of a small stylus mark and some relative measurements, it was even possible to image the same regions before and after experiments, for example as shown in Figure 5.29 on page 191. Efforts to prevent the mount leaking met with failure, therefore the chamber behind it was leak-proofed instead, which achieved the same objective.

2.1.1 Cyclic Voltammetry (CV)

CV measures the current flowing in an electrode/electrolyte system as the voltage is swept through a defined range. The voltage is swept at constant rate, and in a cyclical fashion such that repeatable and non-repeatable behaviour can be separated. In general, non-repeatable

behaviour will relate to irreversible chemical changes of either the electrode or electrolyte. Reversible behaviour can relate to faradaic reactions and capacitive current, but the most distinctive features are peaks which are related to ionisation changes, and the voltages at which these occur can shed light on the active species at work.

For example, it is well-known that under alkaline conditions nickel undergoes an ionisation change from +2 ($Ni(OH)_2$) to +3 (NiOOH) at oxygen-evolution potentials, as confirmed in Figure 5.8 on page 174 [44]. Further, as a general rule it can be said that since an anode has a positive voltage and is therefore attractive to electrons, the higher the ionisation state of the metal ions within it, the greater their ability to tear molecules apart, such as water, that come within range. This is borne out by many experimental results (*cf.* 'Early Oxidation' on page 34) as well as by the oxygen evolving complex at the heart of photosynthesis (*cf.* page 27), which can only operate when the four manganese atoms within have accumulated four oxidising equivalents.

For a perfect reversible redox reaction occurring within an ideal system, the shape of the current waveforms produced by cyclic voltammetry can be calculated [38], with the peak current being proportional to the square root of the voltage scan rate. The full width at half maximum (FWHM) is independent of scan rate, and equal to $28.3/n$ mV where n is the number of electrons involved in the redox reaction. In addition, the separation between paired anodic and cathodic peaks is also independent of scan-rate, and equal to $57/n$ mV.

However, two factors detract from this ideal picture, the first being the solution resistance between reference and working electrodes. This resistance reduces the peak current, as well as increasing the peak width and separation. The second is irreversibility of the redox couple, which has the same set of effects. In addition, reversible behaviour can transition to irreversible behaviour as the voltage scan-rate increases. For this reason the interpretation of CV results can require some skill, and numerical analytical techniques are increasingly employed.

2.1.2 Electrochemical Impedance Spectroscopy (EIS)

Impedance is the ratio of voltage over current, but generalised to include not just resistance (symbol Z'), but also capacitance or inductance (collectively termed 'reactance', symbol Z''). As such, in response to a driving sinusoidal voltage, an impedance can produce not just a variation in current magnitude, but also in phase. Collectively, the magnitude and phase can be plotted separately against frequency (as a Bode plot), or the resistance and reactance can be plotted against each other (as a Nyquist plot). Both plots show how the impedance of the system under test varies with frequency, and can therefore reveal information about the various processes at work.

The reason for this is that typically different processes operate at different frequencies. Therefore, just as spectroscopy of the sound made by an orchestra could separate out the behaviour of the double-basses from that of the violins, so too spectroscopy can separate out the various components of an electrochemical system, and therefore the behaviours within it.

For example, the process of diffusion normally operates at the lowest frequency within the system, since diffusion is a slow process, and being a bulk phenomenon does not directly couple with the double-layer capacitance. By contrast, a faradaic process occurring right at the electrode surface is extremely fast, and couples directly with the double-layer capacitance. An adsorption/desorption reaction will be slower, but also occurring right on the electrode surface. Any coupling between resistance and capacitance produces a characteristic semi-circular shape on the Nyquist plot, and often multiple semi-circles can be observed, as different processes come to the fore.

EIS Frequency Limits A practical lower frequency limit for EIS is about 0.1 Hz, below which natural convection currents will disrupt diffusion [135]. It may be possible to extend this lower limit by using a much larger electrolytic cell, but this would involve a lot of inconvenience for very little gain. The upper frequency limit is dominated by the inductance of cables, and frequencies above about 100 kHz would require very careful design. In practice, no signifiant variation in impedance was observed above 10 kHz, so the normal EIS range employed was 0.1 to 10 000 Hz.

2.1.3 Electrochemical Surface Area (ECSA)

Electrochemical Surface Area (ECSA) is a widely accepted method for measuring how much of the surface area of an electrode is accessible to the electrolyte, which due to surface roughness can be many times the geometrical surface area. For example, if an electrode measures 3x3 cm, then it has a geometrical surface area of 9 cm^2, but it may have a roughness factor (RF) of 100, in which case the ECSA will be 900 cm^2.

This can be used to correct the measured electrochemical activity of the electrode to give an indication if its activity is due to catalysis, or due to surface area. Often the presumption is that catalysis is 'better' than surface area, but at the macro-electronic level, larger surface area is indistinguishable from faster kinetics, and faster kinetics can equally be due to better catalysis. Therefore, catalysis and surface area are in fact two entirely equivalent solutions to the same problem, that being to achieve the highest possible current at the lowest possible overpotential.

There are various techniques within the literature to measure the ECSA, for example:

Hydrogen Monolayer Underpotential Deposition: UPD occurs when a material (in this case a hydrogen atom) can be deposited onto a substrate at a lower voltage than it can be deposited onto itself. Thus, once a single monolayer of hydrogen has been deposited, no further deposition can occur, since the hydrogen cannot deposit onto itself. If it can be deduced at which voltages such deposition starts and finishes, then integration of the current will reveal the size of the surface area. Due to surface heterogeneity, it is expected that UDP will occur over a range of voltages as deposition occurs on each type of active site in turn [136].

In practice, it is not clear where the start and stop voltages should be (for example see Figure 2.4 on page 46), and in the absence of a clearly defined region the technique is no different from cyclic voltammetry. This could be one reason that the technique is most commonly encountered in acidic conditions with fuel-cells, not in alkaline conditions with electrolysers.

Capacitance Plot: This is an EIS technique whereby $-1/(\omega Z'')$ is plotted against Z'. The limiting value of this capacitance at low frequency is equal to the sum of the double-layer capacitance plus any faradaic pseudo-capacitance [137]. Since the faradaic processes are potential dependent, the limiting capacitance will thus be a function of the d.c. bias at which the EIS is performed.

In practice, changing the d.c. bias not only changes the capacitance, but also the shape of the capacitance plot, since any curvature on the Nyquist plot is greatly amplified on the capacitance plot. Therefore, the technique is limited to exactly the same range of bias voltages as cyclic voltammetry (see below). This technique also only works if the low frequency impedance is much greater than the limiting impedance at high frequency, such that a horizontal line is produced. Failure to produce a horizontal line within the practicable limits of EIS (see page 43) means that the limiting capacitance can at best be estimated.

An example of a capacitance plot is as shown in Figure 2.3. For comparison, the capacitance measured for this electrode using cyclic-voltammetry (see below) was 0.564 F, which is certainly in agreement with the capacitance plot, but it is impossible to read such a value from the plot.

Cyclic Voltammetry: The measurement protocol published by McCrory *et al.* in a series of 'benchmarking' papers has been used as the basis of that followed in this work [119]. This involves performing cyclic voltammetry on the working electrode over a 100 mV range at varying scan rates, but with a 10 second pause at the end of each sweep. This pause allows any diffusion gradients that may have been created in the electrolyte to disperse. The McCrory procedure is as outlined below.

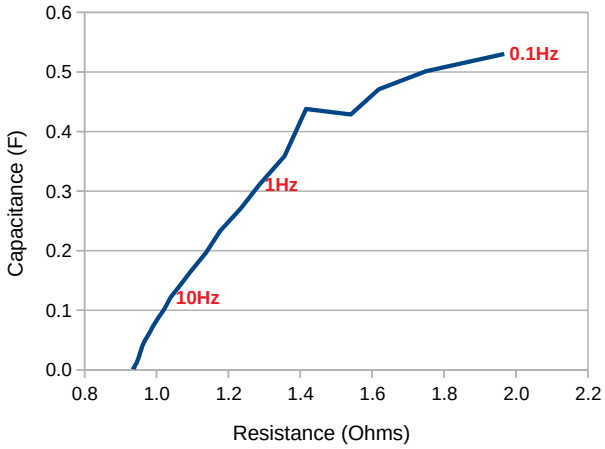

Figure 2.3: Capacitance plot for a Raney Nickel electrode derived from an EIS sweep between 10 kHz and 0.1 Hz.
Bias voltage: 0 V *vs.* Ag/AgCl. Amplitude: 10 mV.

1. Obtain the *open circuit potential* d.c. bias voltage such that the maximum positive and negative currents whilst sweeping the voltage up and down through 100 mV are nearly equal. This shall be called V_{OCP}.

2. Obtain 3 cyclic-voltammograms at 3.3, 6.6 and 10 mV s^{-1} for the 100 mV range around V_{OCP}. Pretreatment shall consist of holding the electrode at V_{OCP} for 120 seconds, and each of the voltammograms shall loop at least three times to allow initial transients to die down.

3. Obtain the anodic and cathodic mid-point currents for the last loop of each of the cyclic-voltammograms.

4. Plot the mid-point currents against sweep-rate. Ideally these will converge on the origin.

5. Obtain the slopes of the anodic and cathodic lines of best-fit. Note that the unit of the slope of current *vs.* sweep rate is capacitance.

6. The double-layer capacitance (C_{DL}) is equal to the average of the above two slopes

ECSA measurements should be conducted in a flat region of the overall voltage/current characteristic, well away from HER and OER, but also in a region that avoids redox peaks. The results of a wide-range linear-sweep for a bi-functional Raney nickel electrode at 1 mV s^{-1} are as shown in Figure 2.4. The current at negative voltages becomes steeply negative, which indicates the onset of hydrogen evolution. At positive voltages the current becomes steeply positive, which indicates oxygen evolution. In the middle the current is

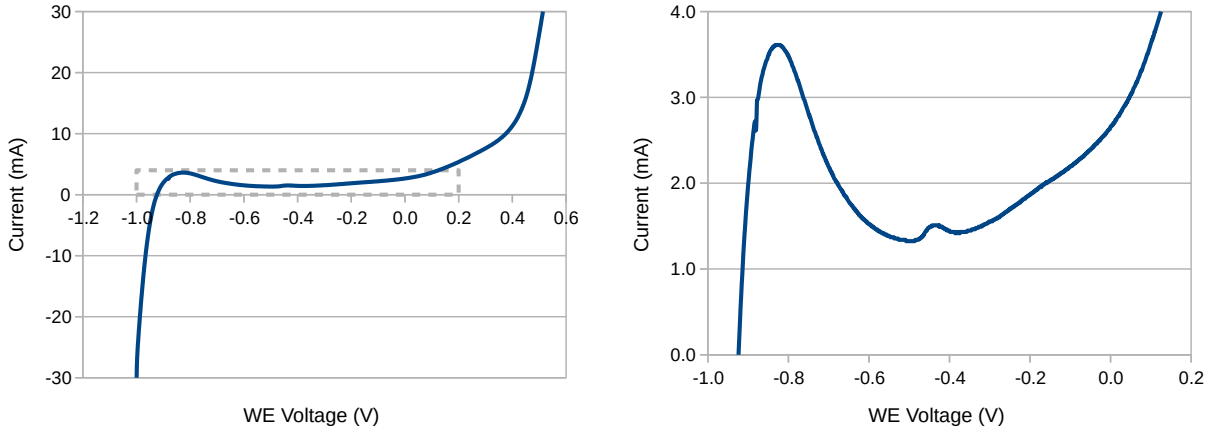

(a) Linear sweep

(b) Detail view of dashed grey box

Figure 2.4: Results of a wide-range linear-sweep for a bi-functional Raney nickel electrode from -1.0 to $0.5\,\mathrm{V}$ *vs.* Ag/AgCl at $1\,\mathrm{mV\,s^{-1}}$.

close to zero, but always remains positive, which is correct because the current is charging the electrode capacitance.

Figure 2.4b presents a closer look at the flat region, as highlighted by the dashed grey box, and reveals the presence of two peaks. The first large peak at $-0.8\,\mathrm{V}$ corresponds to the oxidation of incorporated hydrogen, which can be in the form of adsorbed atoms, or as deeper deposits of hydride. The diffusion of hydride to the surface is as shown in Equation 2.1, and the oxidation of adsorbed hydrogen in Equation 2.2. This can occur directly as the net reaction shown in Equation 2.3.

$$\mathrm{NiH}_x \rightleftharpoons \mathrm{NiH}_{\mathrm{ads}} \tag{2.1}$$

$$\mathrm{NiH}_{\mathrm{ads}} + \mathrm{OH}^- \rightleftharpoons \mathrm{Ni} + \mathrm{H_2O} + \mathrm{e}^- \tag{2.2}$$

Net reaction:

$$\mathrm{NiH}_x + \mathrm{OH}^- \rightleftharpoons \mathrm{Ni} + \mathrm{H_2O} + \mathrm{e}^- \tag{2.3}$$

The depth of the hydride deposits, and their slow diffusion to the surface can cause this peak to be substantially spread out in time. The second smaller peak at $-0.4\,\mathrm{V}$ *vs.* Ag/AgCl corresponds to the oxidation of metallic nickel, as shown in Equation 2.4.

$$\mathrm{Ni}^{2+} + 2\,\mathrm{e}^- \rightleftharpoons \mathrm{Ni\,(s)} \tag{2.4}$$
$$E^0 = -0.25\,\mathrm{V}\ \textit{vs.}\ \mathrm{NHE}$$

The presence of this peak means that the most suitable area for the collection of capacitance data would therefore appear to be between -0.2 to $0.0\,\mathrm{V}$ *vs.* Ag/AgCl. Prior to long-term ageing, this is the typical range that is used.

However, in practice by far the dominating criterion is that the maximum positive and negative currents should be nearly equal. Once an electrode had been used extensively for HER (e.g. for long-term ageing), its open-circuit potential was substantially negative, such that a d.c. bias voltage of -0.5 to $-0.4\,\mathrm{V}$ *vs.* Ag/AgCl would be required to equalise the currents. Similarly, once the electrode had been used extensively for OER, a d.c. bias of 0.3 to $0.4\,\mathrm{V}$ *vs.* Ag/AgCl was required.

The explanation is the build up of relatively large amounts of chemically altered material (e.g. nickel hydride or nickel hydroxide) that cause the electrode to behave as a battery. The long-term ageing process can therefore also be regarded as a battery charging process.

In practice, the cyclic voltammetry procedure failed with electrodes with either very high capacitance, or very low capacitance. Therefore, two new curve-fitting techniques were developed, one analytical and one using gradient-descent. The first was as presented in Section 3.3 on page 86.

2.1.4 Chronopotentiometry

The word chronopotentiometry (CP) means 'to measure voltage over time', with the implication being that since it is the voltage that is being measured, then it is the current that is being controlled. As such, the ultimate aim of CP is to establish a dynamic equilibrium, whereby all transient effects have decayed to zero. Such an equilibrium is completely analogous to that of the Nernst potential, except for non-zero electron flow, and it is important that the electrode potential is just sufficient to sustain the desired current indefinitely. In so doing, an accurate overpotential for the faradaic reaction can be measured.

A plot of the overpotential *versus* the log of the current density is called a Tafel plot, and almost always exhibits a linear section. This linear section arises due to an exponential dependency between the rate of the chemical reaction (i.e. the current) and the activation energy (the voltage), and is thus a pure expression of the Arrhenius equation (see Section 1.3.1 on page 14). The slope of the linear section is called the *Tafel slope*, and its extrapolated intercept with the x-axis (i.e. the current at zero overpotential) is called the *exchange current density*.

In theory at least, the exchange current density would be a revealing and highly-prized characteristic indicating catalytic excellence. In practice it is compromised by small errors in the Tafel slope resulting in large errors in the extrapolation. To quote from Pletcher *et al.* [138]

> The use of exchange current density is avoided because the values in the literature are subject to large errors. In addition to factors such as pretreatments and experimental procedures, the determination of the exchange current density requires extrapolation of current density *vs* potential data over hundreds of millivolts using Tafel slopes that are poorly defined or even 'imaginary'.

The proposed alternative is to compare catalytic overpotential at fixed current density, with a commonly quoted figure being $10\,\mathrm{mA\,cm^{-2}}$. Since this is only two orders of magnitude away from $1\,\mathrm{A\,cm^{-2}}$, this figure is very likely to cover all current densities of the greatest commercial interest.

2.1.5 Faradaic Efficiency

The Faradaic Efficiency of an electrolyser is defined as:

$$\eta_{Faradaic} = \frac{\text{quantity of hydrogen produced}}{\text{quantity of hydrogen expected}} \tag{2.5}$$

Since 2 electrons must pass between the electrodes in order to produce one molecule of hydrogen, and four electrons to produce one molecule of oxygen, it is possible by measuring the total charge passed to predict the total amount of gas that should be produced. The possible side reactions that could compete with gas production include:

- any oxidation half-reaction at the anode that has a *lower* standard electrode potential than +0.401 V SHE
- any reduction half-reaction at the cathode that has a *lower* standard electrode potential than -0.8277 V SHE

Such half-reactions could include:

$$\mathrm{Zn(OH)_4^{2-} + 2\,e^- \rightleftharpoons Zn(s) + 4\,OH^-} \quad \text{(-1.199 V)}$$
$$\mathrm{2\,H_2O + 2\,e^- \rightleftharpoons H_2(g) + 2\,OH^-(aq)} \quad \text{(-0.8277 V)}$$
$$\mathrm{2\,H^+ + 2\,e^- \rightleftharpoons H_2(g)} \quad \text{(+0.000 V)}$$
$$\mathrm{O_2(g) + 2\,H_2O + 4\,e^- \rightleftharpoons 4\,OH^-(aq)} \quad \text{(+0.401 V)}$$
$$\mathrm{O_2(g) + 2\,H^+ + 4\,e^- \rightleftharpoons 2\,H_2O} \quad \text{(+1.229 V)}$$
$$\mathrm{Cl_2(g) + 2\,e^- \rightleftharpoons 2\,Cl^-(aq)} \quad \text{(+1.36 V)}$$

Here $\mathrm{Zn(OH)_4^{2-}}$ or $\mathrm{2\,Cl^-}$ ions could be present in small quantities as a result of impurities present in the electrolyte, or in the feed water used to replenish that which is consumed by the water-splitting reaction. Note that the above *standard electrode potentials* are quoted

for a normalised effective concentration of 1 mol/litre, therefore the Nernst equation would be used to calculate the electrode potential at other concentrations.

Even then, the reaction will not proceed until enough potential has been provided to overcome the reaction kinetics i.e. the *overpotential*, which will be different for each reaction. This explains why in the electrolysis of neutral salt solution at pH 7, it is *chlorine gas* that is evolved at the anode, not oxygen, even though the standard electrode potential for chlorine evolution (+1.36 V) is not lower than for oxygen (+1.229 V). It happens because the overpotential for chlorine evolution is lower, which is confirmation that the oxygen evolution reaction is hampered by its high overpotential.

It also explains why a membrane that prevents the migration of OH^- ions from cathode to anode is required in the industrial Chloralkali process, since otherwise the pH at the anode would rise, and the *desirable* evolution of chlorine would be inhibited. In this case it is not because oxygen gas itself is evolved, but because *both* chloride and hydroxyl ions are consumed by the anode to produce a combination: hypochlorite ions.

In an alkaline electrolyser, the oxidation of contaminating chloride ions to chlorine gas is suppressed by the basic environment, since the standard electrode potential for oxygen evolution is shifted downwards by 59 mV for every unit on the pH scale. It would appear that this must lead to an indefinite accumulation of chloride ions within the electrolyte, but in practice chlorine and oxygen evolution remain in competition via the mechanism of *diffusion*. Since OH^- ions can only reach the anode at a certain rate, there will exist a 'hydroxyl ion limiting current' [139] above which chlorine gas will be produced. Regardless of oxidation state, chlorine is normally to the detriment of all metal components within the electrolyser, including the catalytic coating.

Without such release mechanisms, contaminant ions can accumulate indefinitely within the electrolyte. Therefore any water used to replenish the electrolyte as it is consumed by water-splitting must be as free as possible not just of chloride ions, but also magnesium and calcium. It is for this reason that the water-splitting of sea-water remains a challenging goal in electrochemistry.

Precious metals such as platinum can also be extremely vulnerable to poisoning by foreign metals, via the mechanism of *underpotential deposition* (UPD) [131, 140, 141]. In UPD, a metallic cation in solution is able to electrodeposit itself onto a dissimilar metallic surface (e.g. a platinum cathode) at an electropotential *more positive* than the equilibrium Nernst potential. This is because the Nernst potential does not take into account the possibility of a favourable lattice interaction between the two metals. Such UPD deposits can by definition therefore only occur up to one or two monolayers in thickness, but this is sufficient to completely poison the electrode surface.

Regardless of any contaminant ions present in small quantities, in an experiment passing several thousand coulombs of charge they are likely to be insignificant, since they will either

be quickly consumed, or not consumed at all. A more significant source of ongoing Faradaic losses could be the recombination reaction:

$$H^+ + OH^- \longrightarrow H_2O$$

Even at pH 14, H^+ ions will be present at some level, but in practice the presence of a gas-separation membrane means that the opportunity for H^+ and OH^- ions to meet is limited. It is only through the diffusion of dissolved gases through the membrane that the above reaction can proceed [24]. Since there are very few competing side reactions, a standard electrolyser of sound design should produce a figure that is close to 100%.

However, in practice it is an experimental technique which is prone to several sources of error, as a result of which it would neccessitate great care and accurate equipment to produce a reliable figure. The sources of error in the basic measurement performed for this thesis include:

Atmospheric pressure Without access to a barometer this was obtained from a weather forecast, but could easily be subject to an error of 10 mbar, or about 1%

Measurement of height This was measured using a ruler to the millimetre, or about 1 %

Measurement of internal chamber diameter This was measured using Vernier calipers in several places and averaged. However, the cylindrical tubing is not perfectly circular, and the diameter reading is squared, so the area error will be about 1%

Measurement of current The Ivium potentiostat measures currents to 0.2% accuracy, but this is only at the *full-scale* setting of 10 A. At 2.5 A, the accuracy is about 1%

Escape of hydrogen This is potentially quite likely to occur because hydrogen is recognised to have a 'high leak propensity' [26]. In particular a lot of use was made of low-cost push-fit connectors, which are not expected to have the same leak performance as 'Swagelock' connectors.

The accumulative effect of these errors, even if uncorrelated, means it should not be expected to obtain a result that is more accurate than about 2%. In order to ensure that the electrolyser remained fully saturated with electrolyte, the decision was taken to use small electrical pumps to maintain circulation. The equipment used to perform Faradaic efficiency measurements was therefore as shown schematically in Figure 2.5.

Note that as the two volumes of gas are collected, the height of liquid in the central chamber increases, with the result that the pressure is slightly increased. It is possible to compensate for this effect by taking two further height measurements, Hydrogen h_2 and

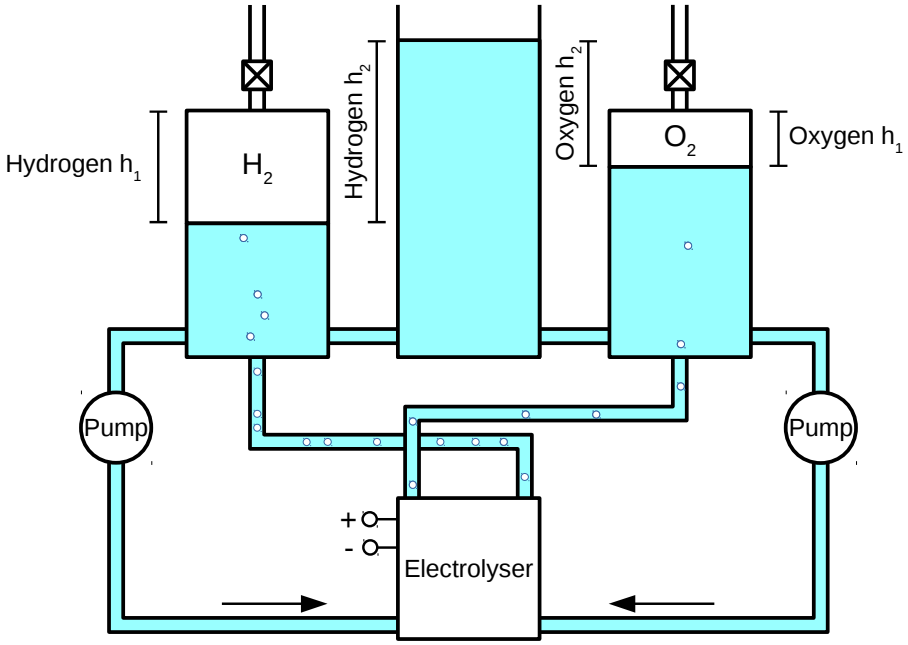

Figure 2.5: Schematic of equipment used to perform Faradaic efficiency measurements

Oxygen h_2, as indicated in the diagram. The number of moles of gas in each chamber therefore becomes:

$$n = \frac{pV}{RT} = \frac{(p_{atm} + h_2\rho g) \cdot (h_1 \pi r^2)}{RT} \tag{2.6}$$

where h_1 is the height of the gas volume, r the internal radius of the gas collecting cylinder, p_{atm} is the atmospheric pressure (in Pa), h_2 is the head height, ρ is the density of the electrolyte, and g, R and T are gravity, the gas constant and temperature.

A reasonably accurate figure can thus be produced within the laboratory using basic equipment. The results of this experiment are as presented in Section 6.5.1 on page 232.

2.2 Analytical Methods

2.2.1 Scanning Electron Microscopy (SEM)

The first electron microscopes developed worked by transmission electron microscopy (TEM), whereby high energy electrons were fired right through the sample directly onto a fluorescent screen. They were quickly able to surpass the capabilities of even the best optical microscopes. This was possible because the de Broglie wavelength of a particle is inversely proportional to its momentum, and since an electron weighs a lot more than a photon, that means it can have a much smaller wavelength. Thus a beam of electrons is able to resolve much finer detail than a beam of light.

A much more practical instrument than a TEM is the scanning electron microscope (SEM), such as the one used for this thesis, the Hitachi TM3030 table-top microscope. A SEM scans a beam of electrons over the sample, and generates images by detecting the signals that bounce back from the surface. This removes the need to fire electrons right through the sample, and means that much lower accelerating voltages can be used. In practice the resolution is limited by aberrations and distortions introduced by the lenses, which are created using magnetic fields. The TM3030 does not quote an absolute resolution figure, but from a typical image taken at 10000× magnification, it appears to be about 50 nm. At such magnification a lot of time is expended getting the image maximally into focus.

The TM3030 offers three observation conditions: 5 kV, 15 kV and 'EDX'. The lower voltage is intended to observe surface features, particularly with non-conductive (biological) samples. The higher voltage produces more sharply defined images, and is suitable for higher magnification. The condition 'EDX' is undefined, and is certainly not restricted to be used with EDX. The manual states that it is "well-suited for observing specimens that do not produce adequate brightness/contrast levels", and this was found to be the case. It is not possible to adjust the aperture, convergence angle or the beam current.

The microscope detects three types of signal that bounce back from the surface, namely secondary electrons (SE), back-scattered electrons (BSE) and energy-dispersive x-rays (EDX, see next section). There are others, most notably cathodoluminescence (CL) and auger electrons (AE), but these are not observed.

Secondary electrons (SE): These are produced by inelastic scattering from conduction or valance electrons within the top few nanometres of the sample. They typically have energies up to 50 eV, which is less than 1% of the incident energy, which highlights how much of the incident energy can be dissipated as heat within the sample. Fortunately, for the highly metallic samples that were analysed this was not a problem.

For steeply sloping surfaces and edges the electron beam enters at a low incident angle. This means that the interaction volume is on average closer the surface, with the result that more electrons escape the sample, and these areas appear brighter. This adds a persuasive three-dimensional appearance to images generated using SE.

Back-scattered electrons (BSE): These are produced by elastic scattering directly from atoms within the sample. Since little energy is lost, these electrons emerge with high energy, and can thus be distinguished from SE. They reveal little of the surface topography of the sample, but instead create contrast based on sample composition, since elastic scattering is more likely from the heavier elements within the sample.

The TM3030 offers three observation modes: BSE, SE and Mix, which allows either BSE or SE to be observed, or a composite image containing both. It was thus simple to see which combination produced the best image.

2.2.2 Energy Dispersive X-ray Spectroscopy (EDX)

It is not surprising that when a sample is bombarded with electrons it is not just electrons which are emitted, but also photons. These photons are emitted principally by two separate mechanisms: luminescence and x-ray fluorescence.

Luminescence: This is caused by the absorption by an atom of a lower energy secondary electron, such that the energy is sufficient only to promote an electron from a valance band orbital into the conduction band. Therefore, no ionisation of the atom occurs. A photon will be emitted when the electron falls back into the valence band, typically of a visible-light wavelength, and with an energy that is determined by the energy gap between the valance and conduction bands. This is the same mechanism by which light is emitted from a cathode-ray tube. When collected by an instrument for diagnostic purposes the technique is called cathodoluminescence, but the TM3030 does not have this function. In any case, it is not applicable to conductors such as metals, since they do not have an energy gap.

X-ray Fluorescence: This is caused by the absorption by an atom of a high-energy electron, either a secondary electron or directly from the electron beam. The energy absorbed is such that an electron is ejected from the atom, thereby ionising the atom. This is inelastic scattering, and the ejected electron is therefore a secondary electron. If the electron is ejected from an inner orbital, then an electron from a higher orbital will fall into the vacancy, and so on. Since the sample is electrically conductive (or steps have been taken to prevent charge build-up) the positively charged atom will combine with an external electron to achieve charge neutrality, and thus the atom will once again return to its ground state.

Each time an electron falls from a higher orbital into a lower one, the energy change is emitted as either a phonon or an x-ray photon. The phonons are dissipated as heat, but the photons are highly descriptive of the atoms present in the sample. This is because the photon energy is equal to the difference in energy between the atomic orbitals, which are highly characteristic to each element. In combination with suitable look-up tables, quantitative analysis can be performed which also identifies the amount of each element in the sample. The penetration depth of a high-energy electron beam into various materials is published on-line, and for 15 keV into iron is about 1 µm[1]. The EDX results in this work therefore give compositional analysis from about the top micron of the electrode material.

[1]Obtained from http://www.globalsino.com/EM/page4795.html (May 2020)

EDX collection and analysis on the TM3030 electron microscope was performed by an Oxford Instruments (Oxford, UK) AZtecOne spectrometer. The device and its software is designed specifically for use with the Hitachi electron microscope. It offers the ability to collect EDX data from selected points on an electron micrograph, such that the composition of different parts of the image can be compared. It also offers the ability to collect data from a general area, such as a rectangle. This would be of particular use with a fragile sample where the sustained focussing of the beam onto a specific point would quickly destroy it.

In practice, EDX can involve a certain amount of subjectivity. The EDX software that accompanies the spectroscope is very good at automating a lot of the analysis procedure, but can leave very obvious peaks unidentified, particularly carbon. It is therefore necessary to double-check each analysis to ensure that it makes sense. Double-clicking a peak brings up a list of candidate elements which can then be manually added or removed from the inventory. The inventory controls how the spectrum is interpreted, and therefore the quantity of each element reported by the software.

However, since each element has a characteristic fingerprint of peaks of specific relative sizes, the manual addition or removal of elements can succeed in improving the fit in one part of the spectrum, but only at the expense of making it worse somewhere else. This explains how the software can get into difficulties. Common-sense is required, such as the exclusion of extremely rare elements that are very unlikely to be in the sample, and the inclusion of those that are likely to be there. Once the reconstructed spectrum is as close as possible to the detected spectrum, and the inventory makes objective sense, then the analysis is complete.

Notation: Within the software, each peak in an EDX spectrum is notated not just with the element from which it was emitted, but also the orbitals that produced it. Electron orbitals come in shells which are labelled K, L, M, N *etc.* in 'x-ray notation', and correspond to the *principal quantum number* in 'quantum notation'. Within each shell are orbitals that are labelled s, p, d, f *etc.* in 'atomic notation'. The mth shell contains m orbitals in order, the nth orbital contains $2n$ electrons, and the orbits are filled in a complicated sequence that minimises energy as the number of protons in the nucleus increases.

In EDX, a peak labelled K1 corresponds to a photon that was emitted by an electron that falls from the L shell to the K shell, i.e. it has fallen by one shell. A peak labelled K2 corresponds to one that has fallen two shells, i.e. from M to K. Similarly, a peak labelled L2 has fallen from N to L. Instead of the numbers 1, 2, 3, the greek characters α, β, γ could be used, or the letters a, b, c. This system therefore implies that the emitted photon energy is dominated by the shells involved, and much less so by the individual orbits. In practice, nearly all peaks are labelled K1, K2 or L1.

2.2.3 X-ray Photoelectron Spectroscopy (XPS)

Instead of using high-energy electrons to eject photons from a sample, XPS works by ejecting electrons from a sample using high-energy photons. The energies of the ejected photoelectrons will be determined by their binding energy within the sample, so long as the incident x-ray photons have an extremely narrow energy range. This is due to the principle of the conservation of energy, such that:

$$E_{electron} = E_{photon} - E_{binding} - \phi \tag{2.7}$$

where $E_{electron}$ is the energy of the detected electron, E_{photon} is the energy of the incident x-ray, $E_{binding}$ is the energy with which the electron was bound within the sample, and ϕ is the *work function* of the material. Thus, $E_{binding}$ can only be calculated from $E_{electron}$ if E_{photon} is constant. By revealing the elecron binding energy, XPS is therefore able to reveal more than just the elemental composition of the sample, but also how those elements are bonded to each other.

The x-rays are generated by firing a beam of electrons at a metallic target, typically aluminium or magnesium. This will, by the same mechanism behind EDX, emit x-ray photons peaked around specific energies. The largest of these peaks is the K1 (or Kα) peak, hence this is called an Al-Kα x-ray source. This source can be used directly to perform XPS, but the spectra will be of poor quality.

The spectra can be improved by bouncing the x-ray beam off a suitable crystal, for example quartz. This will, by the principle of Bragg diffraction, produce a highly monochromatic beam at a specific angle, and is thus known as a monochromator. The crystal can also be shaped to focus the x-rays onto the sample, in a way that lenses cannot. The size of the x-ray spot on the sample can be controlled by the focussing of the electron-beam in the x-ray source, and is typically sub-millimetre.

Since photons do not penetrate very far into the sample, at most 20 nm, XPS is very much a surface characterisation technique when compared with EDX. It is consequently much more sensitive to contamination, and care must be taken to keep samples clean. For example, it is anecdotally reported that a sample of iron was analysed that had been handled, and no iron at all was detected. Should surface contamination be suspected, use can be made of *XPS Depth Profiling*, whereby an ion beam (for example composed of monoatomic argon ions) is used to drill into the sample, and a sequence of XPS spectra are taken at intervals to reveal how the composition changes with depth. This can also reveal how surface chemical changes recede into the bulk, but the estimation of distance is difficult because it depends on a lot of factors.

All XPS experimentation for this thesis was performed by Dr Daniel Jones of Swansea

University, and he is thanked for the high quality of his work and support. The XPS machine was a Kratos Axis Supra using an Al-Kα excitation source with an energy of 1486.6 eV. Incident angle 54.7°. The fitting of peaks to the XPS spectra was performed using CasaXPS, which is a Windows software package.

2.2.4 Gas Chromatography (GC)

GC experiments were performed on an Agilent Technologies 7820A GC System with OpenLAB CDS ChemStation Edition software. The experimental set-up for the GC was as shown in Figure 2.6.

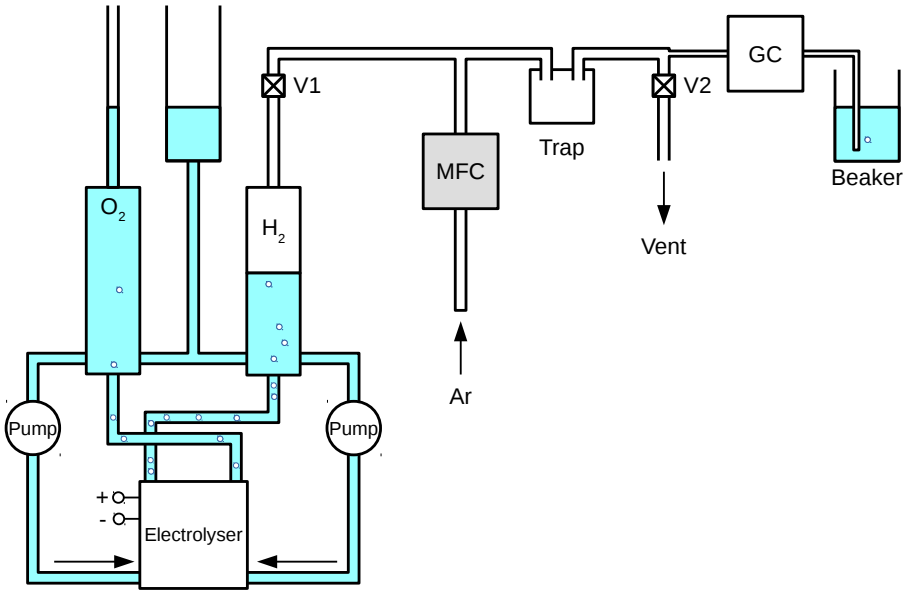

Figure 2.6: Experimental set-up for electrolyser gas-chromatography.

One of the aims was to reduce the total amount of electrolyte in the system to under 500 ml. This was achieved by reducing the diameter of the header and collection tanks, and positioning them such that the bottom of the header tank was higher than the top of the collection tanks. This reduced chemical usage and waste, and made it easier to change the concentration of the electrolyte between runs. The sampling procedure was as specified in Table 2.1.

The rate of argon flow through the Mass Flow Controller (MFC) was configured at $10\,\mathrm{ml\,min^{-1}}$, whereas the rate of gas flow through the GC was much lower at about $1\,\mathrm{ml\,min^{-1}}$. Therefore the argon collected in the H_2 collection tank, and was subsequently used to flush the system in Step 2. Argon was chosen because it is the carrier gas for the GC, which means that the GC can only detect gases *other than* argon. Therefore, should the gas sample be contaminated with argon, although the peak sizes would be reduced, the ratio between them would be unaffected. The trap was to protect the GC from the corrosive alkaline electrolyte, just one drop of which would be enough to cause serious damage.

Step	MFC	V1	V2	Description
1	✓	✓	✗	Switch on MFC, open V1, close V2. Let Ar back up into H_2 collection tank. Check bubbles exit the GC. Wait 10 minutes.
2	✓	✗	✓	Open V2. Close V1 when level reaches top of tank, then close V2. The whole system from V1 to the GC is now flushed with Argon.
3	✗	✗	✗	Switch off MFC.
4	✗	✗	✗	Switch on pumps (optional). Switch on electrolyser and collect predetermined amount of H_2 in collection tank.
5	✗	✓	✓	Open V1. Open V2 until level reaches about 1 cm from top of tank, then close it again.
6	✗	✓	✗	Wait 15 s to allow gas through the final section of tube closest to the GC, then push the start button on the GC.
7	✗	✓	✗	Turn off the electrolyser and the pumps.
8	✗	✓	✓	(Whilst GC running) Open V2 to let the H_2 out until all levels equalise. To take next sample, proceed to step 1.

Table 2.1: Procedure for analysing electrolyser output with the GC.

The amount of gas collected in step 4 was about 100 ml, which was chosen because it was approximately double the total volume of the tubes and trap between V1 and the GC. It was assumed that a factor of two was adequate to flush the system. Although it would be preferable to flush the system through the GC itself, this would take a long time.

As a result, one of the most critical measurements dictating the performance of the system was the volume of the tube between V2 and the point inside the GC where the sample was taken. As depicted in the diagram, this connection was implemented using tubing of a smaller dimension (approximately 1 mm internal diameter) than elsewhere in the system.

Assuming the distance from V2 to the sample point was no more than 30 cm, and that the tubing inside the GC was no larger than 1 mm, this gives a maximum volume of 0.25 ml. At a flow-rate of 1 ml min^{-1} this means the tube would take no more than 15 s to flush, which was the reasoning behind the delay in step 6.

Once the GC start button was pressed, the sample was taken and the rest of the gas in the system could be disposed of. To reduce the amount of time per sample, the GC could perform its run at the same time as the system was flushed with argon for the next sample. In this way the system could take a new sample every 10 minutes, in addition to the current-dependent gas collection time.

Calibration This had previously been performed by PhD student Bertrand Rome, and involved the use of MFCs to produce sample gas streams of known concentrations in argon. For each sample gas, the calibration determined a *Response Factor* (RF), which equates the size of the signal produced to the concentration of the gas. Thus for example if the RF for hydrogen is 0.00852, and for oxygen is 0.06162, this means that the total signal area produced for hydrogen is 7.2 times larger than for oxygen, all other things being equal.

Contamination with Atmospheric Air All GC measurements reported the presence of some N_2. Since this cannot be produced by water-splitting, it was assumed that all nitrogen was due to contamination by air. This could be due to air that was present at system start-up, or air that had leaked in through joints and fittings. Regardless of origin, its presence permits the reported oxygen level to be corrected. This is based on the assumption that air contains 78% nitrogen and 21% oxygen, such that the correct amount of oxygen is given by Equation 2.8.

$$Conc.(O_2)_{corrected} = Conc.(O_2)_{measured} - \frac{21}{78} Conc.(N_2)_{measured} \tag{2.8}$$

2.3 Zero-gap Electrolyser

The concept behind zero-gap electrolysis is that the anode and cathode are brought so close together that they are separated only by the width of the gas-separation membrane/diaphragm, which can be much less than 1 mm. As such, resistive losses in the electrolyte should be reduced near to zero, with the only remaining resistance being that of the membrane.

In practice losses still arise as a result of imperfect mass transport, most notably because the approach path of reactant molecules towards the reaction surfaces, and the escape path of both gaseous *and liquid* product molecules is inevitably constrained by the co-location of an electrically conductive electrode. A choice must therefore be made about how to trade-off the closed structure required for high electrical conductivity, and the open structure required for high mass-transport. Despite such difficulties, great performance gains can be made, and zero-gap remains one of the simplest and most efficient water-splitting schemes known.

2.3.1 Flow-plate

Flow-plates are an integral component of the zero-gap design concept. It is precisely because the electrolyser is constructed such that the electrodes are *in contact* with the gas-separation membranes that higher current densities can be achieved. As a result, gas generation rates can be high, and under maximum load the electrolyser can quickly fill with product gases, at which point mass transport resistance climbs rapidly. A circulation pump solves this problem, but at the expense of an additional electrical load, and additional system complexity.

There are in general two different designs of flow-plate: single channel and multi-channel. A single-channel must of necessity zig-zag across the electrode, and under high-load, the end of the channel will become clogged with evolved gas, even at high electrolyte flow rates [142, 143]. Therefore the flow-plate in this study is a multi-channel design, as shown in Figure 2.7. This presents a lower flow-resistance to the pump, and thus has the

benefit of achieving a higher flow rate for the same electrical power. Nevertheless, it is possible that flow-rates across the active area may not be equal, hence the decision to flow the electrolyte diagonally from corner to corner.

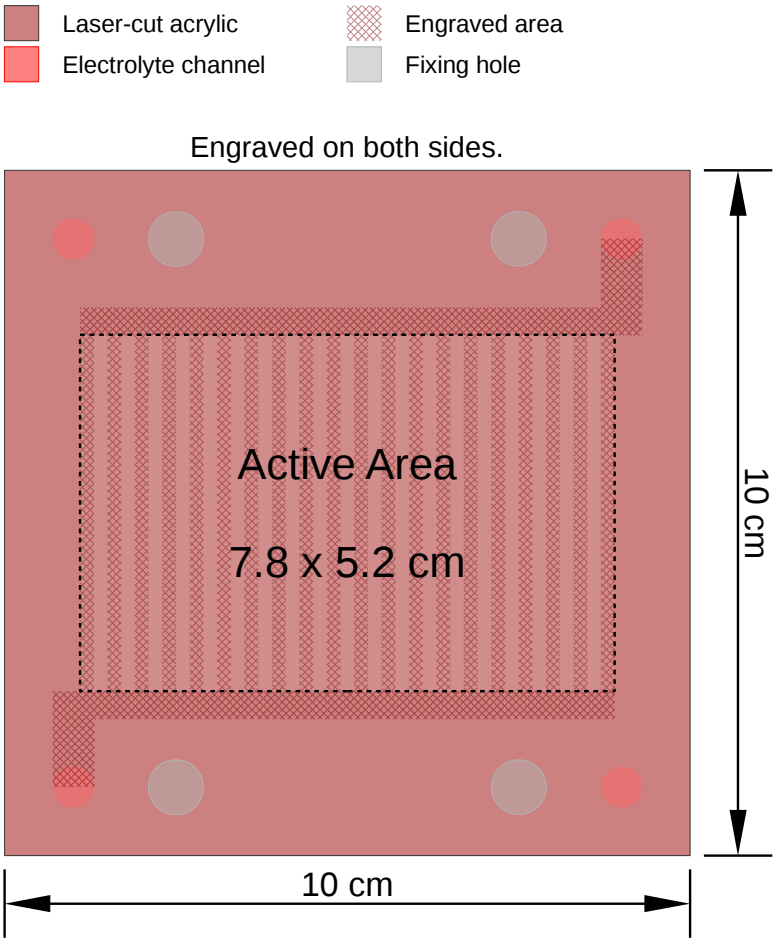

Figure 2.7: Zero-gap electrolyser flow-plate. The electrolyte enters at the bottom left corner and exits at the top-right. The same occurs on the other-side of the plate, such that the opposite pair of channels are utilised, and two separate bodies of electrolyte are maintained within the electrolyser.

The design has not been optimised in terms of channel width, since this was believed to be beyond the scope of that which could be achieved in the time available. Certainly there is an argument to be made that if each of the 20 vertical channels are 2 mm across, then the bottom and top channels should be 40 mm across, so as to achieve the same flow speed. This would be a large waste of space, and in any case the inlet and outlet holes are only 6 mm across. Between the two extremes there therefore exists an optimal trade-off between cost and performance, but this is left as an exercise for future study.

As an aid to permit comparison, the depth of all engraved areas was standardised at 1.5 mm. This was chosen to achieve compatibility with results generated by R. Phillips [143], whose work this thesis aims to extend. It is possible that the channels are a little shallow, and

that a depth of at least 2 mm would achieve better performance. Nevertheless, the optimal choice of channel depth remains another exercise for future study.

The flow-plate is a 4-channel design, such that there exist two electrolyte inlets and two electrolyte outlets. Thus, the flow-plate is able to maintain two separate bodies of electrolyte within the electrolyser, one for oxygen evolution and one for hydrogen evolution. Whether these are combined externally into a single body of electrolyte is a separate system issue, but it is certainly true that if the flow-plate is designed on a 3-channel basis, this option is excluded.

Under high load the electrolyte outlets contain a large number of gas bubbles, in addition to dissolved gas. If this gas-filled electrolyte is able to circulate quickly to the opposite electrode, and thus to the opposing body of electrolyte, then large amounts of gas-mixing will occur. Maintaining electrolyte separation is therefore of great relevance to the purity levels of the product gases, as well as to overall system and downstream safety. Nevertheless, it was observed experimentally that even if two completely separate bodies of electrolyte were maintained, liquid levels equalised relatively quickly due to the passage of electrolyte through the Zirfon membrane.

2.3.2 Electrode Pair Assembly

Each electrode pair in the electrolyser is constructed of five layers, as shown in Figure 2.8. The three silicone gaskets have registration holes which align via the fixing holes. The Zirfon membrane achieves registration by fitting into the cutout in the central gasket, and similarly the electrodes fit into the cutout in the outer pair of gaskets.

The central gasket removes any necessity for the Zirfon membrane to extend to the edge of the electrolyser, or within the vicinity of the electrolyte channels and fixing holes. This achieves two goals:

1. the electrolyte is prevented from leaking out of the electrolyser along the Zirfon membrane

2. the electrodes cannot short-circuit along the fixing holes

It was observed that Zirfon membrane leaks profusely, even under the highest compressive forces, and is therefore ill-suited for use as a gasket. This is because neither of the materials from which it is constructed (zirconium oxide over a woven plastic mesh) are sufficiently elastic. The solution to this problem is to permit the Zirfon to leak, but only into volumes that are themselves leak-proof. The same approach has been used in the design of the electrolytic test-cell.

The second goal is assisted by the use of 8 mm outer diameter (6 mm inner diameter) nylon tubing as a sleeve over the M6 stainless-steel threaded bar that runs through the fixing

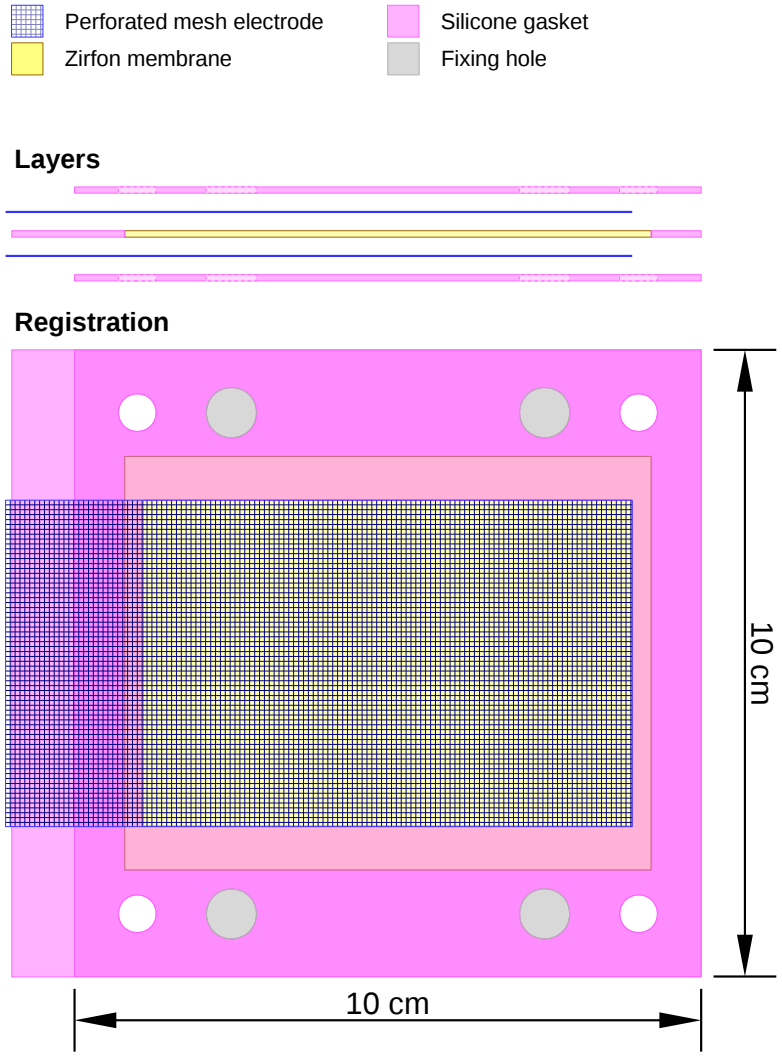

Figure 2.8: Assembly drawing of a zero-gap electrode pair, which is composed of five layers as shown. The layer thicknesses are drawn close to correct scale.

holes. Thus, the threaded bar is fully insulated, and cannot act as an electrical conductor that could short-circuit the stack. Similarly, the Zirfon is sized such that it is at least 3 mm larger than the combination of the electrodes and flow channels, such that the electrodes cannot short-circuit around the edge of the membrane.

The nylon tube sleeving is tough, durable and insulating, and was found to be superior to the heat-shrink sleeving which was previously used for this task. Since the tubing can terminate at any point within the acrylic end-plates, which are 10 mm thick, the length-tolerance required is extremely low, and unaffected by any reduction in width of the stack as the compression nuts are tightened.

2.3.3 Full Assembly

Mechanical drawings of the assembled electrolyser are as shown in Figure 2.9, with the appearance as shown in Figure 6.18 on page 228. Note that the drawing depicts how the design can be extended to produce a 4-electrode *bipolar* stack, with two floating electrodes. Due to time constraints this stack has *not* been constructed, and all measurements have been taken using a *monopolar* version of the design with just two electrodes. Nevertheless, such data can be extrapolated to predict the *electrical* performance of a bipolar design, although it is possible that higher rates of gas-mixing may occur due to parasitic currents.

To test the resistance of the electrolyser to leakage, it was left assembled between experiments for a period totalling 50 days. During this period none of the electrolyte was lost, and there was also none of the white powder that indicates seepage. The leak-proof nature of the design stems from the way in which the edges of the Zirfon membrane have been enclosed by silicone gasket (see previous section) and from the clamping system, which was comprised largely of low-cost mild steel bar.

2.3.4 Clamping

When subjected to compression all structures will deform in accordance with their shape and their Young's Modulus, which is a measure of the stiffness of a solid material. Thus, a steel spring will deform more than a steel bar, even though they are made of the same material, since they have a different shape. Similarly, at the rectangular corners of the electrolyser, the same compressive force leads to greater deformation than halfway along each edge, since at the corners there is more space into which the weak acrylic can expand.

If variations in deformation are allowed to occur then the material is bending, and wherever bending occurs there are bending moments and shear stresses. As a rule of thumb, the maximum shear stress of a material is approximately equal to half its ultimate tensile stress, as is conceptualised graphically by Mohr's Circle. However, for most applications the ultimate yield stress is more applicable, since that governs the point at which the material ceases to maintain its intended shape. For acrylic, this would give a figure of around 25 MPa, which would appear to compare relatively well with that of mild steel at about 125 MPa, but this figure is misleading.

Under continuous load acrylic is vulnerable to stress crazing, which leads to early failure. As a result, in practice the maximum continuous design shear stress of acrylic is reduced to around 5 MPa [2], however this figure is only applicable at room temperature. As a thermoplastic acrylic softens when heated, and with a glass transition temperature as low as just

[2] see https://www.builditsolar.com/References/Glazing/physicalpropertiesAcrylic.pdf

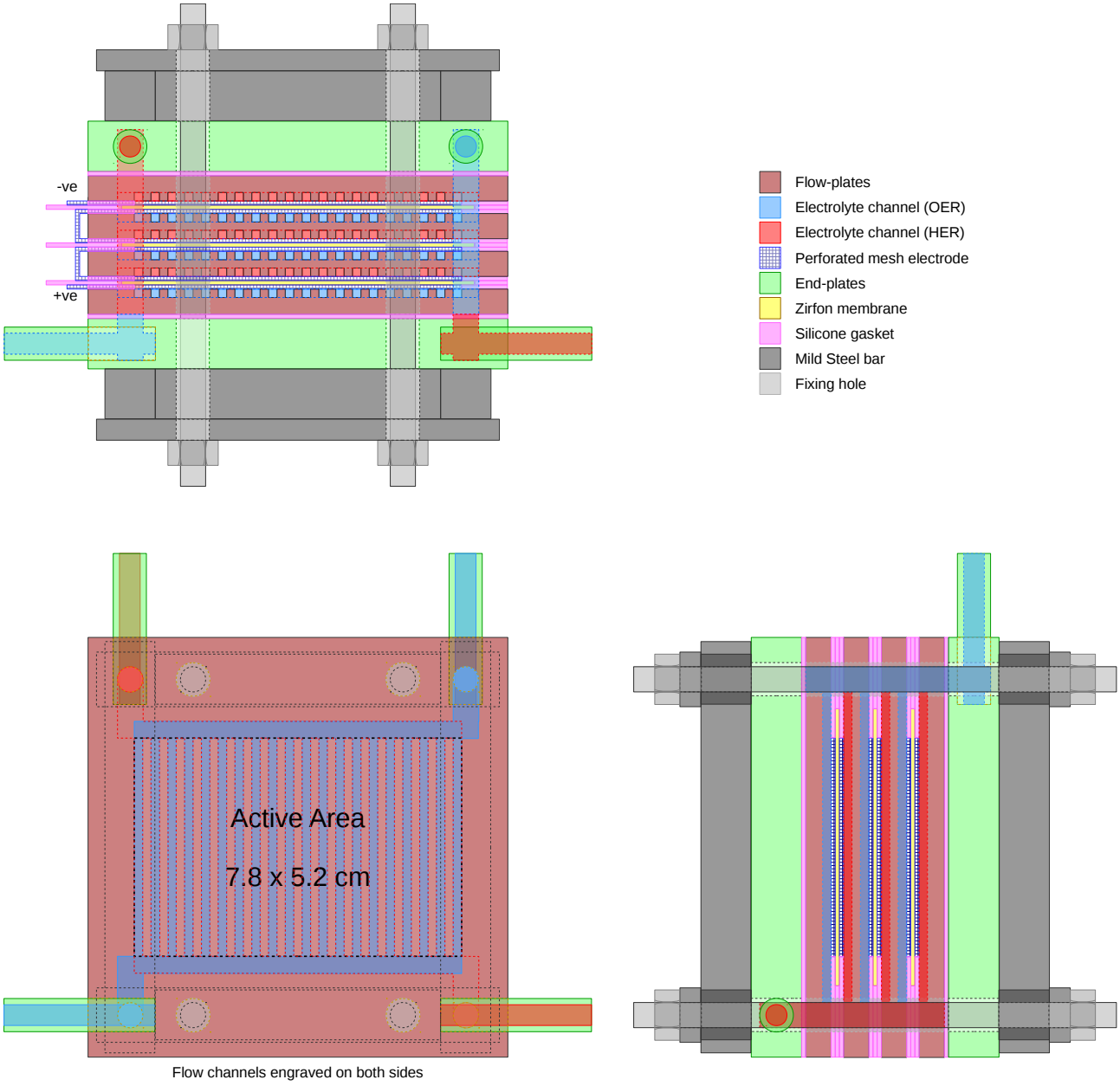

Figure 2.9: Full assembly drawing of a zero-gap electrolyser, extended to include 4 electrodes in a bipolar series arrangement. Note: the narrower components, such as gaskets, membranes and electrodes, have been drawn slightly larger to aid visibility.

85 °C [3], its maximum continuous design temperature is as low as 70 °C [4]. This is well within the range of standard, heated commercial electrolysers, and even an unheated electrolyser will be able to self-heat itself to such an extent that acrylic becomes soft.

It is for these reasons that the clamping forces must be applied to the electrolyser stack with care. The use of mild steel bar spreads the forces along each edge, thus avoiding any

[3] see https://en.wikipedia.org/wiki/Poly(methyl_methacrylate)

[4] see https://omnexus.specialchem.com/polymer-properties/properties/max-continuous-service-temperature

highly localised stresses immediately surrounding each of the fixing holes. Forces are applied directly through the gaskets, and at the sort of modest compressive forces required the steel remains almost completely straight, and consequently the acrylic does not bend.

If the material does not bend, then it is less likely to crack. The compressive force at the corners is automatically reduced, since the displacement is constrained to be equal. This means that the electrolyser will be slightly more likely to leak at the corners, but it is not worth attempting to compensate for this, since it would risk cracking the material.

Off-the-shelf steel bar is low-cost due to its ubiquity, and its consistent thickness means construction tolerances are low. It is also able to clamp the electrolyser with just four fixing holes, which reduces design complexity and assembly/disassembly time. In fact, it may be possible with just two. Upon assembly, it was discovered that the side pieces of steel bar did not need any assembly holes, and were simply slid into place.

Chapter 3

Advanced Characterisation Methods

> However beautiful the strategy, you should occasionally look at the results.
>
> *Sir Winston Churchill*

3.1 Enhanced Gas Collection

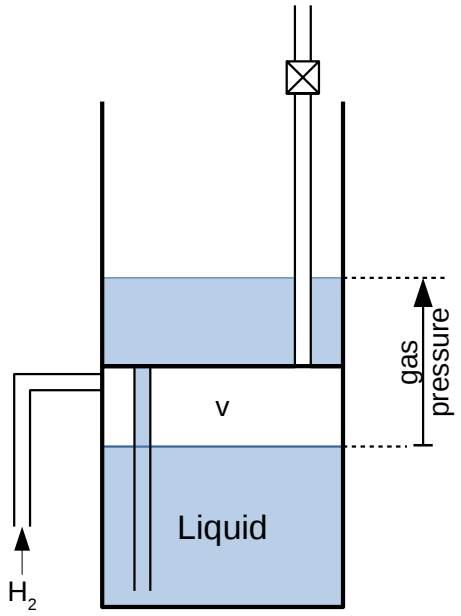

Figure 3.1: Vertical displacement tube, where the pressure of the gas collected is proportional to the height of the arrow

Although a vertical displacement tube, as shown in Figure 3.1, is both simple and elegant, it does have one notable draw-back, that being that as more gas is collected, the greater the pressure under which it is stored. If the pressure increases only for the hydrogen side of the electrolyser, because only hydrogen is stored, this will result in a pressure difference across the gas-separation membrane. Given the normal range of performance of gas-separation

membranes, this will result in a large amount of hydrogen leaking across to the oxygen side. Even if immediately released this is not just wasteful, but there are safety implications.

Therefore it is worth considering gas collectors that operate at constant pressure. The design of a system to do this has been published by Lee *et al.*, but the system employed *permanent* water displacement, and could thus only collect gas once before it had to be manually reset [144].

Another design which is extremely simple is as presented in Figure 3.2. This is based on a piston of mass m sliding in a cylinder, such that the pressure p is at all times given by mg/A, where A is the cross-sectional area of the cylinder.

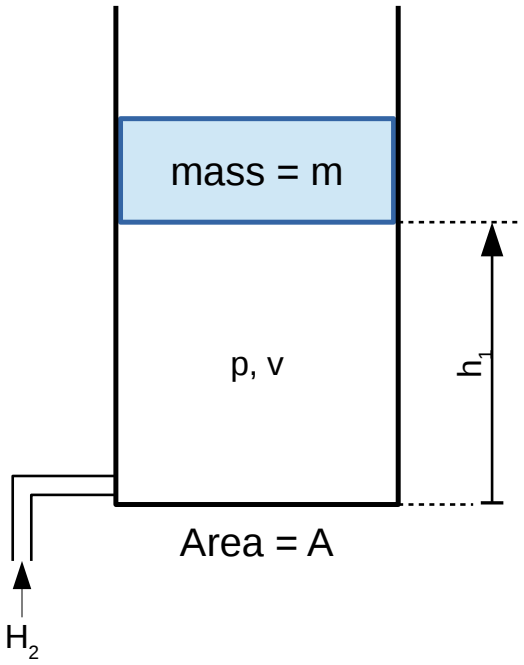

Figure 3.2: Constant pressure gas collector, based on a piston.

Such a design, although simple, has several drawbacks, most notably that if the seal between the piston and the cylinder is not perfect, then gas will escape. Another drawback is that the piston is likely to be subject to *stiction*, which means that it will not move smoothly, and as a result the pressure regulation will not be maintained at a constant level as the collector is filled and emptied.

One way to overcome such drawbacks is to combine the displacement tube and the piston into a single design, as presented in Figure 3.3, where the pressure in the gas collecting chamber is equal to the difference in height of the two surfaces of liquid 1, multiplied by the density of the liquid and the force of gravity g:

$$p = \rho_1 h_1 g \tag{3.1}$$

The pressure can therefore be adjusted by altering the height of the two right-hand chambers relative to the left. For the pressure of the gas to remain constant as it is collected, the height difference h_1 must remain fixed, i.e. such that:

$$\frac{dh_1}{dv} = 0 \tag{3.2}$$

where v is the normalised volume of gas collected.

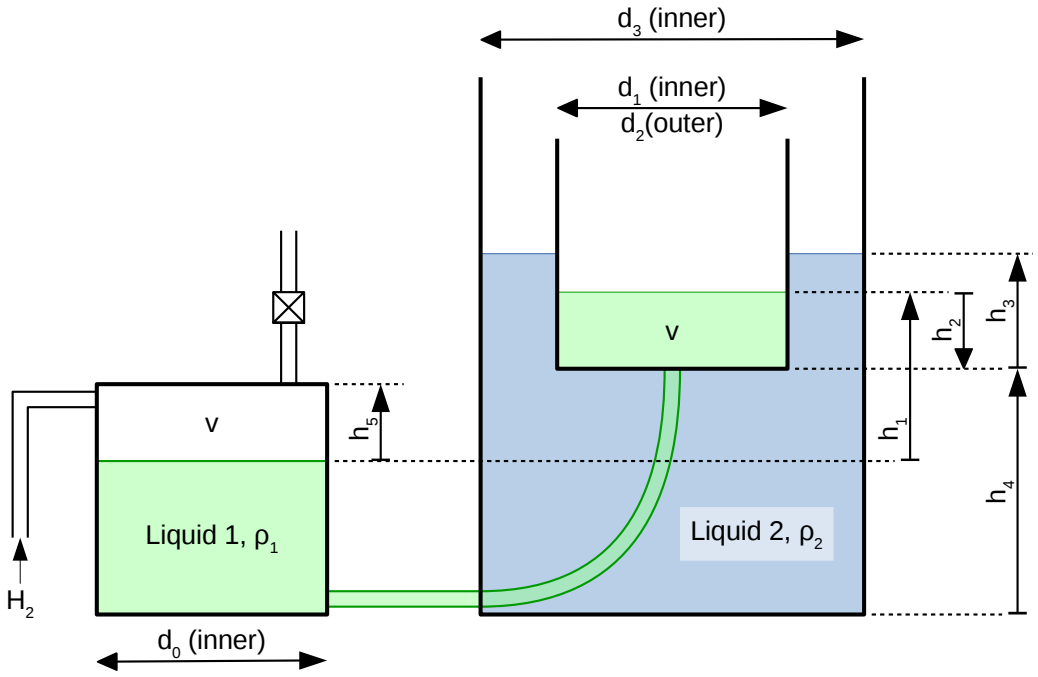

Figure 3.3: Constant pressure gas collector, based on two liquids of different densities

In the following equations, to aid simplicity it has been assumed that the depth of all the vessels in the z-direction (i.e. orthogonal to the page) is equal to 1. Therefore, since the hydrogen gas in the left-hand chamber is collected at constant pressure, it is possible to state that:

$$h_5 d_0 = v \tag{3.3}$$

Similarly, because liquid 1 is incompressible:

$$h_2 d_1 = v \tag{3.4}$$

Using the Archimedes principle, which states that the total weight of the right hand floating vessel is equal to the weight of the fluid it displaces, we can state:

$$\rho_2 h_3 d_2 = W_B + \rho_1 v \tag{3.5}$$

where W_B is the empty weight of the floating vessel. Since the volume of liquid 2 in the right-hand chamber must remain constant, we can state:

$$(d_3 - d_2)h_3 + d_3h_4 = V_3 = \text{constant} \tag{3.6}$$

Finally we can state that the various heights are related, such that:

$$h_4 = H - h_5 + h_1 - h_2 = H - v/d_0 + h_1 - v/d_1 \tag{3.7}$$

where H is equal to the height of the hydrogen collecting vessel, and is constant. Combining all five equations, Equation 3.6 can be rewritten as:

$$(d_3 - d_2)(W_B + \rho_1 v) - \rho_2 d_2 d_3(-H + v/d_0 - h_1 + v/d_1) = constant \tag{3.8}$$

Differentiating this equation with respect to v produces:

$$\rho_1(d_3 - d_2) = \rho_2 d_2 d_3(1/d_0 - dh_1/dv + 1/d_1) \tag{3.9}$$

Therefore, since the constraint for constant pressure is that dh_1/dv is equal to zero, this will occur when:

$$\rho_1 d_0 d_1(d_3 - d_2) = \rho_2 d_2 d_3(d_0 + d_1) \tag{3.10}$$

$$\text{and} \qquad d_3 = \frac{\rho_1 d_0 d_1 d_2}{\rho_1 d_0 d_1 - \rho_2(d_0 + d_1)d_2} \tag{3.11}$$

In order for there to be any solutions for d_3, the denominator of Equation 3.11 must be positive, which occurs when:

$$\rho_1 > d_2 \left(\frac{d_0 + d_1}{d_0 d_1}\right) \rho_2 \tag{3.12}$$

Since (according to Figure 3.3) d_2 must be more than d_1, this immediately confirms that for this design of collector, liquid 1 must be more dense than liquid 2. This stands to reason, since as gas is collected the floating vessel must sink quite rapidly for h_1 to remain constant, which will occur much more easily if liquid 1 is denser than liquid 2.

To reduce the number of variables, we can declare that d_0, d_1 and d_2 are related, such that:

$$d_1 = \alpha d_0$$
$$d_2 = d_1 + \beta d_0$$

It is then possible to plot how the minimum value of ρ_1 varies with α and β, as shown in Figure 3.4.

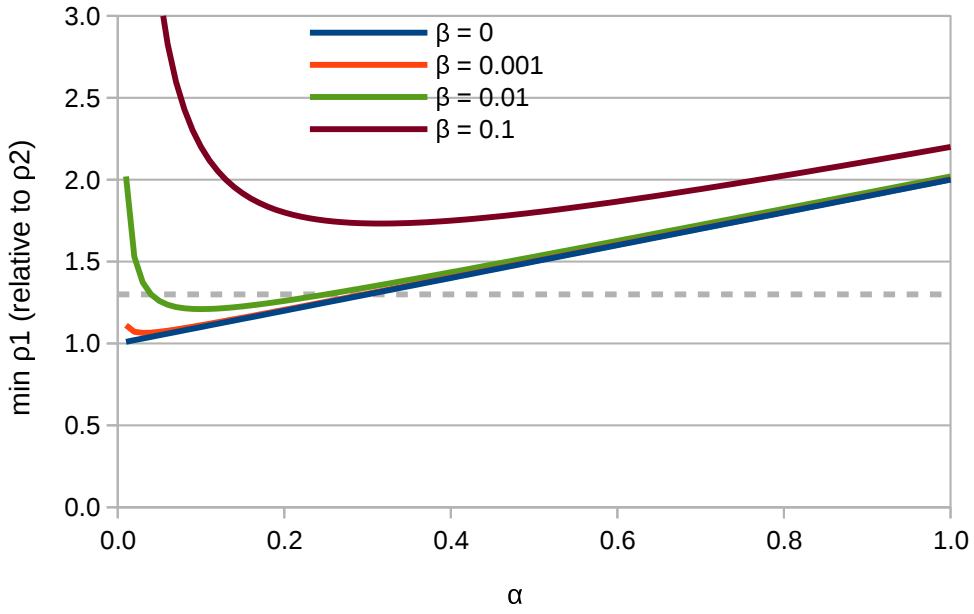

Figure 3.4: Minimum density of liquid 1 as a function of α and β, where $d_1 = \alpha d_0$ and $d_2 = d_1 + \beta d_0$.

Assuming that liquid 2 is water, liquid 1 must therefore be more dense, but for practical reasons also relatively safe. Some liquids that are include brine (saturated, density = 1.23), sodium hydroxide (28 wt%, density = 1.31), and sugar solution (68 brix, density = 1.34). If, as an example, the density of liquid 1 is taken to be 1.3, this produces the horizontal dashed line on Figure 3.4. Assuming that the wall thickness of the collecting vessel can be kept small, this means to have any margin at all above the minimum possible density, α must be approximately 0.1. In other words, the floating vessel must have a cross-sectional area which is about 10% that of the gas collecting tank. This in turns means that h_2 will vary $\sim 10\times$ faster than h_5.

In practice this means that the collecting tank will have to be very wide, and the floating tank very tall, leading to a very inefficient use of space. For example, to collect $1\,\mathrm{m}^3$ of gas would require a design with dimensions similar to those shown in Table 3.1.

Parameter	$\mathbf{d_0}$	$\mathbf{d_1}$	$\mathbf{d_2}$	$\mathbf{d_3}$	$\boldsymbol{\rho_1}$	$\boldsymbol{\rho_2}$	$\mathbf{W_B}$	$\mathbf{V_3}$
Units	m	m	m	m	$\mathrm{kg\,m^{-3}}$	$\mathrm{kg\,m^{-3}}$	kg	$\mathrm{m^3}$
Value	3.00	0.30	0.32	3.28	1300	1000	100	13

Table 3.1: Design exercise for a $1\,\mathrm{m}^3$ constant pressure gas collector based on Figure 3.3.

Given such a design, as the gas is collected the heights h_1 to h_5 will vary as shown in Figure 3.5.

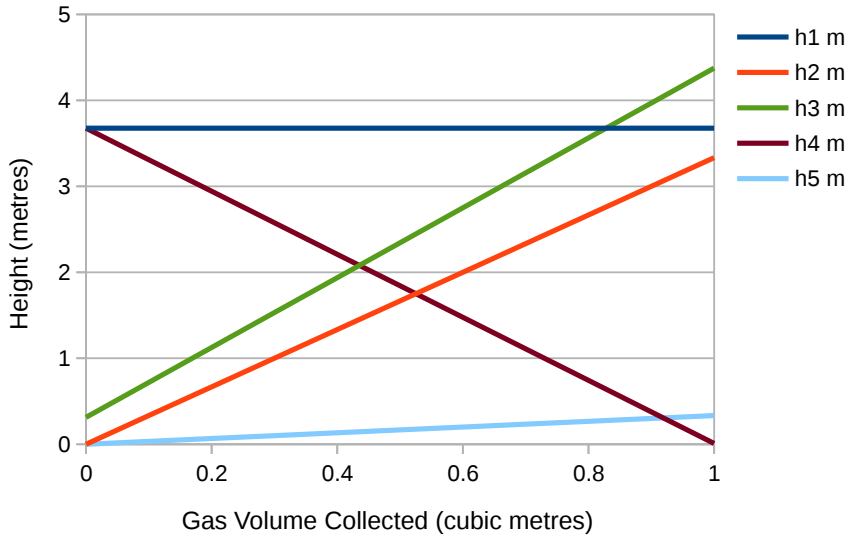

Figure 3.5: Simulation of the variation of heights h_1 to h_5 as a function of volume of gas collected.

Even though the width and height could be reduced by redesigning to take advantage of a third dimension, the inefficiency of the design is clear, since it requires a width of over 3 m, a height of over 4 m, and 13 m^3 of water just to collect 1 m^3 of gas.

3.1.1 Improved Constant Pressure Gas Collector

From the analysis in the previous section, it is clear that one of the limiting factors of the design is that d_1 must be less than d_2, i.e. such that width of the inside of the floating container must be smaller than the width of the outside. Because of this, the density of liquid 1 is constrained to be higher than that of liquid 2, and h_2 is constrained to vary much faster than h_5. It may appear impossible to make the inside bigger than the outside, but the same effect can be achieved by altering the design as shown in Figure 3.6. For simplicity, it has been assumed that the wall-thickness of the floating container is negligible, such that $d_1 = d_2$.

This alters Equation 3.4 such that it becomes:

$$h_2(d_1 + d_4) = v \tag{3.13}$$

and Equation 3.11 becomes:

$$d_3 = \frac{\rho_1 d_0 d_1 (d_1 + d_4)}{\rho_1 d_0 (d_1 + d_4) - \rho_2 d_1 (d_0 + d_1 + d_4)} \tag{3.14}$$

With the improved design, it is possible to declare that both liquids are water, such that

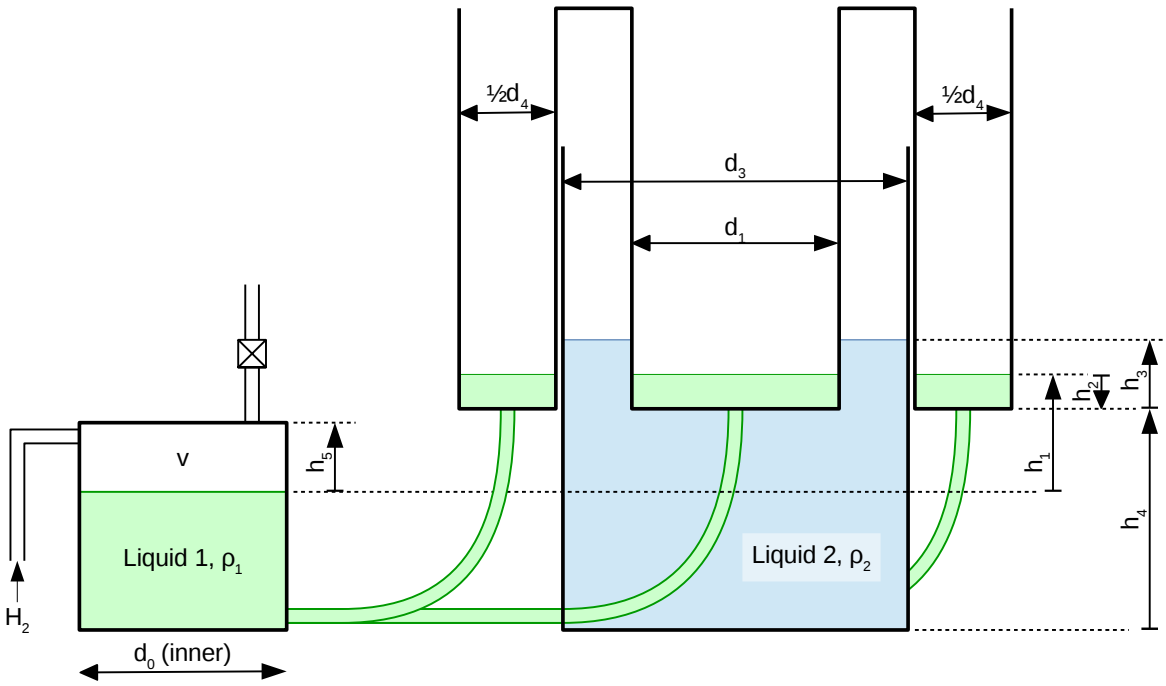

Figure 3.6: Improved design of the constant pressure gas collector.

$\rho_1 = \rho_2$. Also, for convenience, it is possible to apply the constraint that $d_3 + d_4 = d_0$, such that the width of the left and right sections of the collector are equal, and can therefore be stacked one on top of the other. Once this is done, a possible design solution is as shown in Table 3.2.

Parameter	$\mathbf{d_0}$	$\mathbf{d_1}$	$\mathbf{d_3}$	$\mathbf{d_4}$	$\boldsymbol{\rho_1}$	$\boldsymbol{\rho_2}$	$\mathbf{W_B}$	$\mathbf{V_3}$
Units	m	m	m	m	$\mathrm{kg\,m^{-3}}$	$\mathrm{kg\,m^{-3}}$	kg	$\mathrm{m^3}$
Value	2.15	0.50	1.15	1	1000	1000	100	1.5

Table 3.2: Design exercise for a $1\,\mathrm{m^3}$ improved constant pressure gas collector based on Figure 3.6.

For this design, the heights h_1 to h_5 will vary as gas is collected as shown in Figure 3.7. The improved design is therefore able not only to operate with two liquids of equal density, it is also able to reduce the width, height, and volume of liquid required to collect $1\,\mathrm{m^3}$ of gas at constant pressure.

As before, the width can be reduced further by properly including a third dimension into the design. To investigate this, one possible design of floating vessel is considered, as shown in Figure 3.8. This shows the top view of the vessel, with the dimensions d_1 and d_3 corresponding to the matching dimensions in Figure 3.6, and the area A corresponding to d_4, since d_4 can be calculated directly from A using:

$$d_4 = \sqrt{A + d_3^2} \tag{3.15}$$

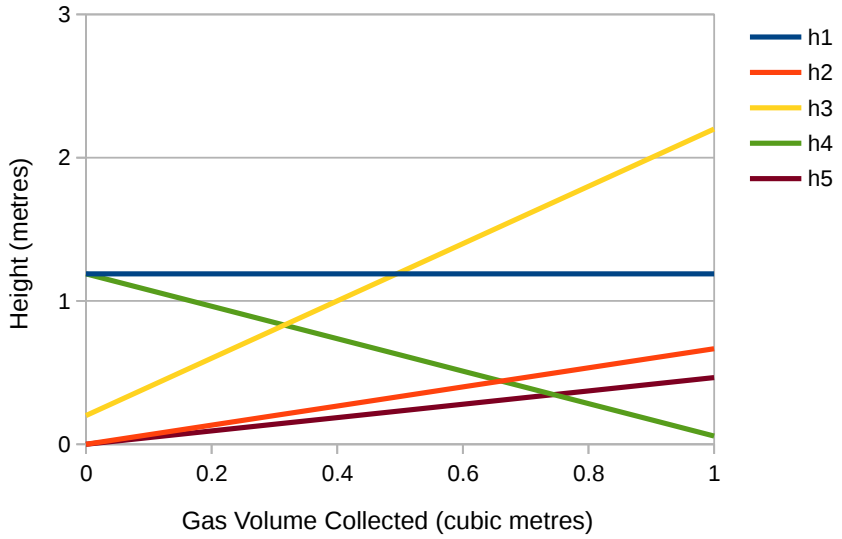

Figure 3.7: Simulation of the variation of heights h_1 to h_5 as a function of gas volume collected for the improved constant pressure gas collector.

The outer annulus and the inner square are connected by flexible tubing, and thus fill with displaced liquid simultaneously to the same level, but only the inner square is floating, and thus supporting the weight. In such a way it is therefore able to emulate the effect of a liquid that is denser than water.

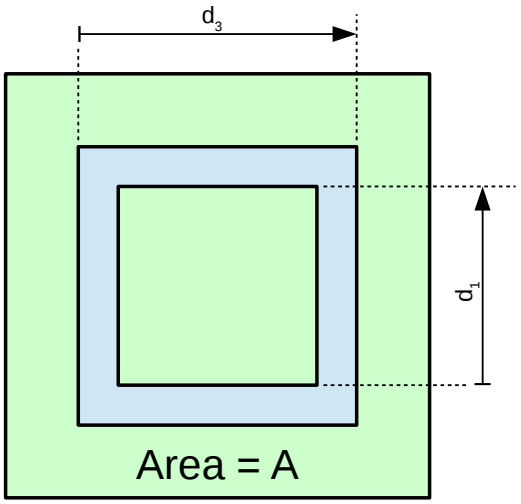

Figure 3.8: Top view of a 3-dimensional constant pressure gas collector as a design example. The labelled dimensions correspond to those in the two-dimensional design shown in Figure 3.7.

As a result of the extra dimension, the equations must be adjusted as follows:

$$\text{Equation 3.3} \rightarrow \quad h_5 d_0^2 = v \tag{3.16}$$

$$\text{Equation 3.4} \rightarrow \quad h_2(A + d_1^2) = v \tag{3.17}$$

$$\text{Equation 3.5} \rightarrow \quad \rho_2 h_3 d_1^2 = W_B + \rho_1 v \tag{3.18}$$

$$\text{Equation 3.6} \rightarrow \quad (d_3^2 - d_1^2)h_3 + d_3^2 h_4 = V_3 = \text{constant} \tag{3.19}$$

$$\text{Equation 3.7} \rightarrow \quad H - v/d_0^2 + h_1 - v/(A + d_1^2) \tag{3.20}$$

Equation 3.19 then becomes:

$$(d_3^2 - d_1^2)(W_B + \rho_1 v) - \rho_2 d_1^2 d_3^2 \left(-H + \frac{v}{d_0^2} - h_1 + \frac{v}{A + d_1^2} \right) = constant \tag{3.21}$$

Differentiating with respect to v, constraining $dh_1/dv = 0$ and multiplying both sides by $d_0^2(A + d_1^2)$ produces:

$$\rho_1 d_0^2 (A + d_1^2)(d_3^2 - d_1^2) = \rho_2 d_1^2 d_3^2 (d_0^2 + A + d_1^2) \tag{3.22}$$

$$\text{therefore} \quad d_3^2 = \frac{\rho_1 d_0^2 d_1^2 (A + d_1^2)}{\rho_1 d_0^2 (A + d_1^2) - \rho_2 d_1^2 (d_0^2 + A + d_1^2)} \tag{3.23}$$

With the addition of a stacking constraint such that $d_0 = \sqrt{A + d_3^2}$, a possible design solution is as shown in Table 3.3.

Parameter	$\mathbf{d_0}$	$\mathbf{d_1}$	$\mathbf{d_3}$	**A**	$\mathbf{d_4}$	$\boldsymbol{\rho_1}$	$\boldsymbol{\rho_2}$	$\mathbf{W_B}$	$\mathbf{V_3}$
Units	m	m	m	m^2	m	$kg\,m^{-3}$	$kg\,m^{-3}$	kg	m^3
Value	1.70	0.80	1.14	1.6	1.70	1000	1000	100	1.2

Table 3.3: Design exercise for a 1 m^3 improved constant pressure gas collector based on Figure 3.8.

For this design, the heights h_1 to h_5 will vary as gas is collected as shown in Figure 3.9. The addition of a third dimension has permitted d_0 and V_3 to each be reduced by 20%, and the maximum liquid height $(h_3 + h_4)$ to be reduced from 2.26 m to 1.77 m.

A scale drawing of the solution presented in Table 3.3 is as shown in Figure 3.10, which is positioned at the point where 0.5 m^3 of gas has been collected. To aid visualisation, the three separate vessels have been coloured black, red and blue.

3.1.2 Stability

It is possible that all of the constant pressure solutions here presented may have problems with stability. If the value of d_3 in Table 3.3 is adjusted to 1.15 m instead of 1.14 m, then

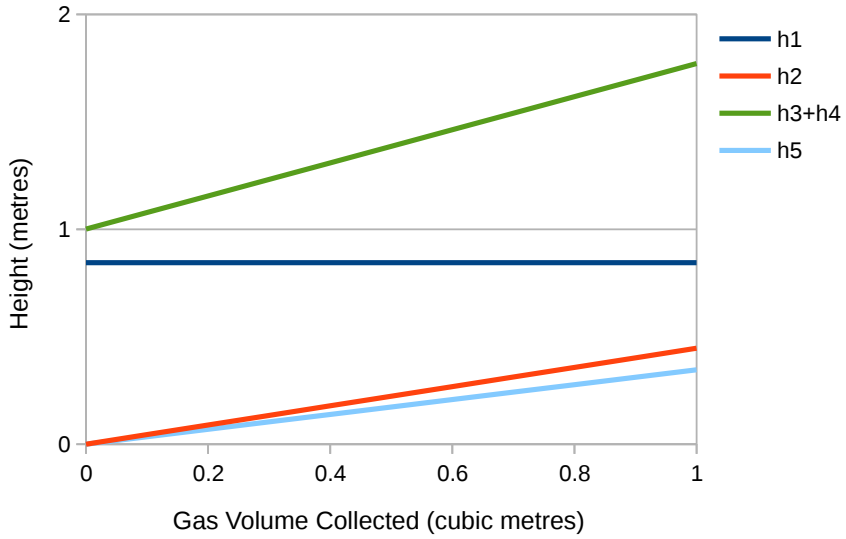

Figure 3.9: Simulation of the variation of heights h_1 to h_5 as a function of gas volume collected for the 3-dimensional constant pressure gas collector shown in Figure 3.8.

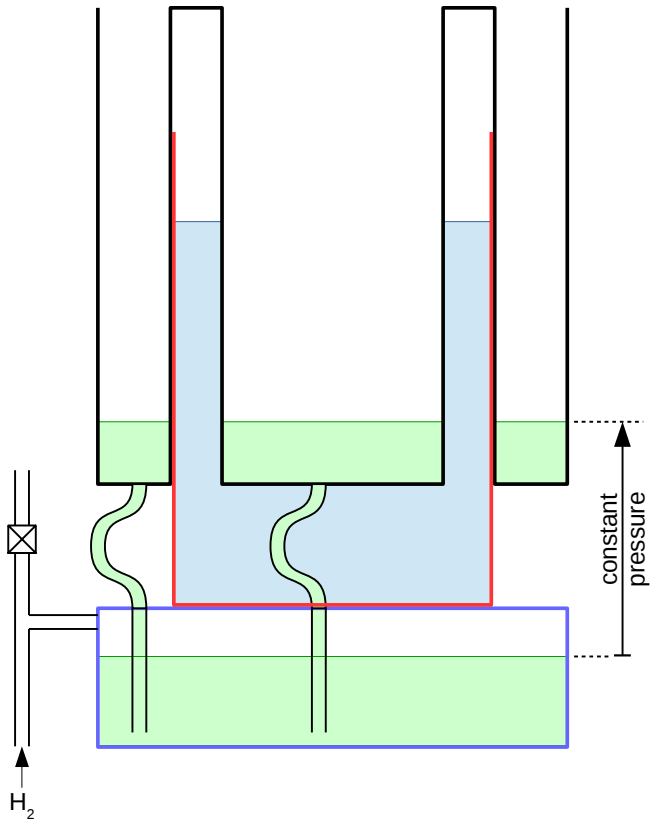

Figure 3.10: Scale drawing of the design solution presented in Table 3.3, at the point where 0.5 m^3 of gas has been collected.

h_1 will *reduce* very slightly as gas is collected, which means that the pressure will decrease. If the collecting chamber is regarded as a spring, this is equivalent to saying that it has a

negative spring constant.

As such, the collecting chamber might be expected to 'burst' due to instability. This is because as the volume of gas collected increases, the pressure resisting further gas entry reduces, therefore more gas enters and the pressure reduces even further, thereby creating positive feedback. To analyse whether this is genuinely the case, it is necessary to consider the total energy of the system.

As an example, consider the system energy of the gas collector presented in Figure 3.2 on page 66. The potential energy of the mass m is given by:

$$E_{mass} = mgh_1 \tag{3.24}$$

If the volume of gas is regarded as a 'gas-spring', then as for all springs its total potential energy is calculated from the integral of force times distance:

$$E_{spring} = \int F(x)dx \tag{3.25}$$

The force F can be calculated from the Ideal Gas Law as:

$$pV = pAh_1 = nRT \tag{3.26}$$

$$pA = -F \quad = \frac{nRT}{h_1} \tag{3.27}$$

where the minus sign appears because in a spring the force acts in the *opposite* direction to displacement. Combining Equations 3.25 and 3.27 produces:

$$E_{spring} = \int \frac{-nRT}{h_1} dh_1 \tag{3.28}$$

$$\text{therefore} \quad E_{spring} = -nRT \ln(h_1) + c \tag{3.29}$$

This equation predicts that $E_{spring} \to +\infty$ as $h_1 \to 0$, and $E_{spring} \to -\infty$ as $h_1 \to \infty$. At some point in between E_{spring} will be zero, based on the value of c, but for a spring made of gas this position is largely arbitrary. The total system energy, in terms of displacement h_1, is thus:

$$E_{system} = E_{mass} + E_{spring} \tag{3.30}$$

$$= mgh_1 - nRT \ln(h_1) + c \tag{3.31}$$

In graphical form this relationship appears as shown in Figure 3.11, for which the values $n = 1\,\text{mol}, T = 293\,\text{K}, m = 1000\,\text{kg}$ and $c = 0$ have been used.

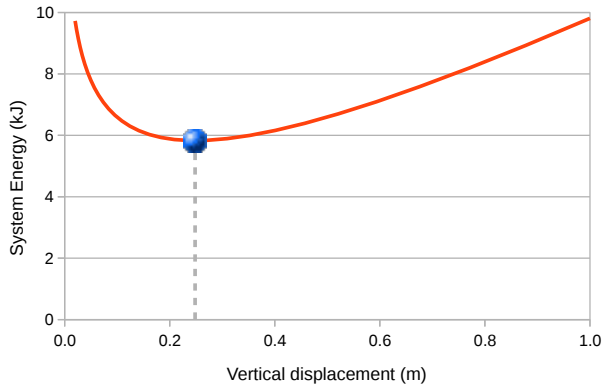

Figure 3.11: Simulation of total system energy *versus* displacement for the mass-spring gas collector shown in Figure 3.2 on page 66.

The lowest system energy will occur when $\frac{dE_{system}}{dh_1} = 0$, specifically:

$$\frac{dE_{system}}{dh_1} = mg - \frac{nRT}{h_1} = 0 \tag{3.32}$$

$$\text{therefore} \quad h_1 = \frac{nRT}{mg} \tag{3.33}$$

Comparison of Equations 3.33 and 3.27 reveals the trivial result that the system adopts the lowest energy configuration when $F = -mg$. However, the same technique can be applied to analyse the stability of any system.

Note that in this example the gas-spring adopts the same height regardless of its cross-sectional area. This is because as the area increases, the pressure imposed by the mass decreases, and the two effects cancel each other out. In practice, since the system is likely to have a maximum pressure limit, the mass chosen would be proportional to the area.

Note also that no allowance has been made for the volume of the pipe leading to the collector. This is because the effect of this pipe is simply to increase the volume of the gas spring, and it is clear from Figure 3.11 that regardless of any additional volume, the system remains stable.

3.1.3 Gas Collector Stability

To calculate the total energy of the two-dimensional gas collector presented in Figure 3.6 on page 71, it is possible to consider the separate contributions of each component:

$$E_{spring} = -nRT\ln(h_5) \tag{3.34}$$
$$E_{beaker} = W_B g h_4 \tag{3.35}$$
$$E_{liquid1} = \rho_1 g\left[h_2(d_1+d_4)(h_4+h_2/2) + (H-h_5)d_0(H-h_5)/2\right] \tag{3.36}$$
$$E_{liquid2} = \rho_2 g\left[h_4 d_3 h_4/2 + h_3(d_3-d_1)(h_4+h_3/2)\right] \tag{3.37}$$
$$E_{system} = E_{spring} + E_{beaker} + E_{liquid1} + E_{liquid2} \tag{3.38}$$

Taking the number of moles of gas n as that which corresponds to a nominal gas volume of 0.5 m^3, these equations permit the total energy of the gas collection system to be plotted against h_5, as shown in Figure 3.12. The dimensions chosen for the collector are those from the design exercise presented in Table 3.2, except that V_3 has been increased to 3 m^3 so that the horizontal axis can be extended to 1 m without generating 'negative energies'. In general, as h_5 increases the two liquids are displaced upwards, and thereby increase in potential energy, whereas the gas-spring deflates and its energy decreases.

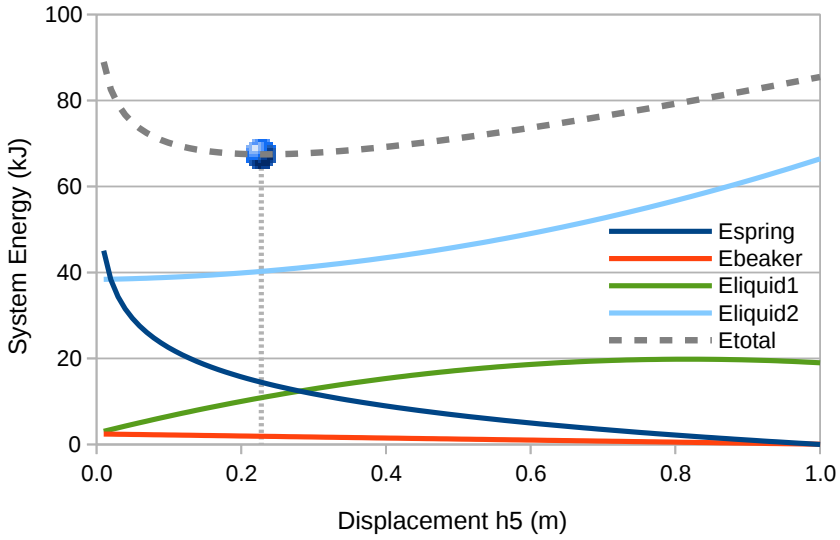

Figure 3.12: Simulation of total system energy versus displacement for the constant pressure gas collector shown in Figure 3.6 on page 71.

As confirmed by simulation, the balance point between the two occurs at the value of h_5 predicted from theory in Figure 3.7. However, unlike the previous analysis, this set of equations permits examination of how the stability of the system would be affected by multiple changes, for example as a result of tolerances, or by changing liquids, temperature, or even the force of gravity. One way to achieve this would be to search for any criteria that would cause the second-order differential of E_{system} with respect to h_5 to become negative, i.e. such

that:

$$\frac{d^2E_{system}}{dh_5} < 0 \tag{3.39}$$

In order to differentiate Equation 3.38 with respect to h_5, an understanding is required of how each of its components varies with respect to h_5. This is relatively straightforward since, with reference to Figure 3.7 on page 72, it is apparent that all of the heights are linearly related. It is therefore possible to conclude that:

$$\frac{dh_2}{dh_5} = \frac{d_0}{d_1 + d_4} \equiv R_2 \tag{3.40}$$

$$\frac{dh_3}{dh_5} = \frac{d_0}{d_1} \equiv R_3 \tag{3.41}$$

$$\frac{dh_4}{dh_5} = -\left(\frac{d_3 - d_1}{d_3}\right)\frac{d_0}{d_1} \equiv R_4 \tag{3.42}$$

$$\tag{3.43}$$

where R_2, R_3 and R_4 will be used as a shorthand to refer to these ratios. The first-order differentials of the four components of Equation 3.38 therefore become:

$$\frac{dE_{spring}}{dh_5} = \frac{-nRT}{h_5} \tag{3.44}$$

$$\frac{dE_{beaker}}{dh_5} = W_B g \frac{dh_4}{dh_5} = W_B g R_4 \tag{3.45}$$

$$\frac{dE_{liquid1}}{dh_5} = \rho_1 g \left[R_2(d_1 + d_4)(R_4 + R_2/2) + (-1)d_0(-1)/2\right] \tag{3.46}$$

$$\frac{dE_{liquid2}}{dh_5} = \rho_2 g \left[R_4 d_3 R_4/2 + R_3(d_3 - d_1)(R_4 + R_3/2)\right] \tag{3.47}$$

Since none of the values R_n, d_n, ρ_n or g are functions of h_5, differentiation again with respect to h_5 produces:

$$\frac{d^2E_{spring}}{dh_5^2} = \frac{nRT}{h_5^2} \tag{3.48}$$

$$\frac{d^2E_{beaker}}{dh_5^2} = 0 \tag{3.49}$$

$$\frac{d^2E_{liquid1}}{dh_5^2} = 0 \tag{3.50}$$

$$\frac{d^2E_{liquid2}}{dh_5^2} = 0 \tag{3.51}$$

$$\text{therefore} \quad \frac{d^2E_{system}}{dh_5^2} = \frac{nRT}{h_5^2} \tag{3.52}$$

Since n, R, T and h_5^2 are all constrained to be positive, this means that $\frac{d^2E_{system}}{dh_5^2}$ is also constrained to be positive, and therefore the system is constrained to be stable for all values of d_n, ρ_n and g. This analysis could easily be extended to cover the three-dimensional gas-collector design presented in Table 3.3, but there seems little requirement to do so.

To the knowledge of the author the designs here presented are new, and constitute the first auto-resetting constant pressure gas collectors based on liquid displacement.

3.2 Enhanced Arrhenius

To investigate whether the predictions of the Brønsted-Evans-Polanyi model (as outlined in Section 1.3.4 on Page 23) can be verified, an experiment was conducted using a 316-grade stainless-steel electrode in 1 M NaOH. The temperature of the electrolyte was controlled by immersing the electrolytic-cell in a water bath, and using a probe inside the cell to verify that the desired temperature had been reached.

Although it would be conceptually neater to vary the temperature at constant potential, experimentally it is easier to vary the potential at constant temperature. The experiment therefore reduces to generating a sequence of Tafel plots at varying temperatures, with the results as presented in Table 3.4 and Figure 3.13.

The Tafel plots can be rearranged as Arrhenius plots by using interpolation to find where each line crosses a specific value of overpotential. Taking an overpotential of 0.3 V, for example, from Figure 3.13 it can be seen to intercept with the Tafel plots for 30 °C, 40 °C, 50 °C and 60 °C. This gives four values of current density, which can thus be plotted against $1/T$ on an Arrhenius plot. Once this procedure is repeated for multiple values of overpotential, the results are as shown in Table 3.5 and Figure 3.14. Note that an Arrhenius plot is plotted

Overpotential	18.6	30	40	50	60	69	Temp °C
Volts	291.6	303	313	323	333	342	Temp K
-4.49	0.309	0.286	0.273	0.241	0.217	0.194	
-4.00	0.320	0.300	0.284	0.257	0.235	0.214	
-3.49	0.334	0.313	0.296	0.270	0.248	0.227	
-3.00	0.351	0.328	0.309	0.283	0.261	0.238	
-2.49	0.372	0.347	0.325	0.298	0.276	0.253	
-2.00	0.396	0.368	0.342	0.315	0.293	0.271	
-1.49	0.427	0.398	0.363	0.336	0.313	0.293	
$\log_{10}$(j) (A cm^{-2})							

Table 3.4: Measurements of overpotential taken at varying values of temperature and current density. The overpotentials have been corrected for iR-losses

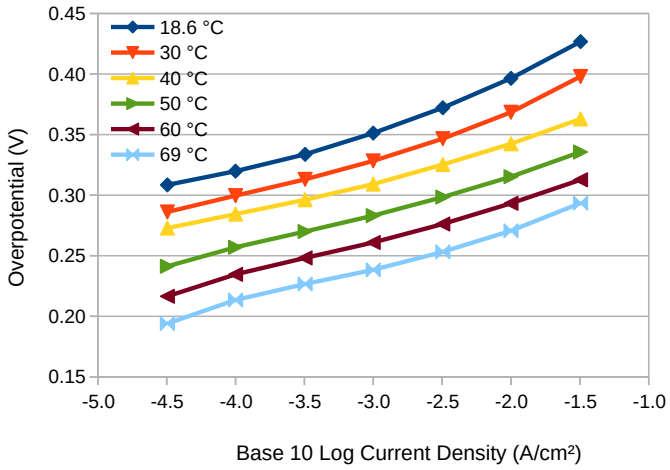

Figure 3.13: Tafel plots, corrected for iR losses, for a 316-grade stainless-steel working electrode in 1 M NaOH at various electrolyte temperatures

using a natural logarithm of the current density, since this produces a slope with the correct units.

	ln(j)	Overpotential (V)						
	A m^{-2}	0.225	0.25	0.275	0.3	0.325	0.35	0.375
0.00343	291.6					0.432	2.222	3.599
0.00330	303				0.032	2.094	3.640	4.862
0.00319	313			-0.927	1.497	3.444	5.034	
0.00310	323		-0.508	1.594	3.570	5.160		
0.00300	333	-0.606	1.326	3.373	5.007			
0.00292	342	1.014	3.214	4.826				
1/T (K^{-1})	T (K)							

Table 3.5: Calculated values of current density at various overpotentials and current density, generated by interpolation from the data in Table 3.4

The most notable feature of an Arrhenius plot is that its slope is equal to $-E_A/R$, where E_A is the apparent activation energy of the chemical reaction under investigation, and R is the gas constant. Using the data from Figure 3.14, it is therefore possible to calculate how E_A varies with overpotential, with the results as presented in Table 3.6. The values for E_A vary

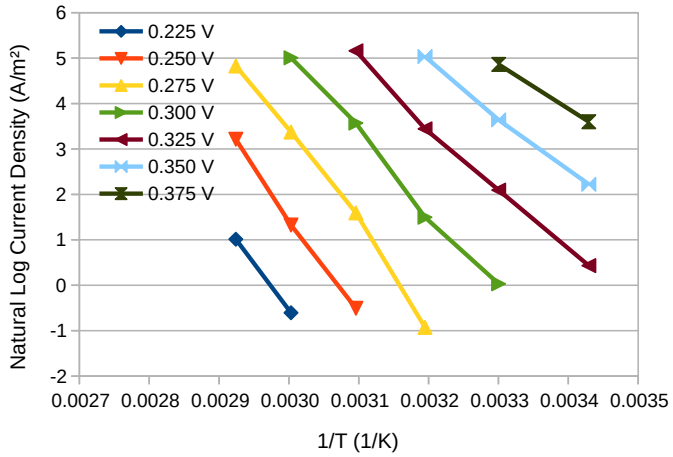

Figure 3.14: The Tafel plots from Figure 3.13 rearranged as Arrhenius plots at various values of overpotential

between about 80 and 180 kJ mol^{-1}, which is higher than typical values for oxygen evolution catalysts in the literature, where figures down to 30 kJ mol^{-1} have been reported [145]. This is not surprising, since this electrode does not feature a catalytic coating.

Overpotential V	**Arrhenius Slope**	E_A **kJ mol^{-1}**
0.225	-20492	170.4
0.250	-21580	179.4
0.275	-21092	175.4
0.300	-17142	142.5
0.325	-13999	116.4
0.350	-11959	99.4
0.375	-9785	81.3

Table 3.6: Arrhenius slopes extracted from Figure 3.14 for various values of overpotential, together with the values of apparent activation energy, E_A, to which these correspond.

It is important to note that the value of E_A calculated from the slope of the Arrhenius plot is only notionally applicable *at absolute zero*. This explains why in Table 3.6 E_A is only a function of overpotential, whereas in Equation 1.25 on Page 25 it is a function of both overpotential *and* temperature. The term $T\Delta S$ is lost because it is proportional to T, and therefore appears as a constant offset on the Arrhenius plot. Despite some noise on the data it is possible to pick out a trend, especially if the results from Table 3.6 are rendered graphically, as in Figure 3.15.

The line of best fit through the data in Figure 3.15 produces a line with slope 83510. When this figure is fed into Equation 1.32 on Page 27, we obtain:

$$\frac{\alpha F}{R} = 83510 \tag{3.53}$$

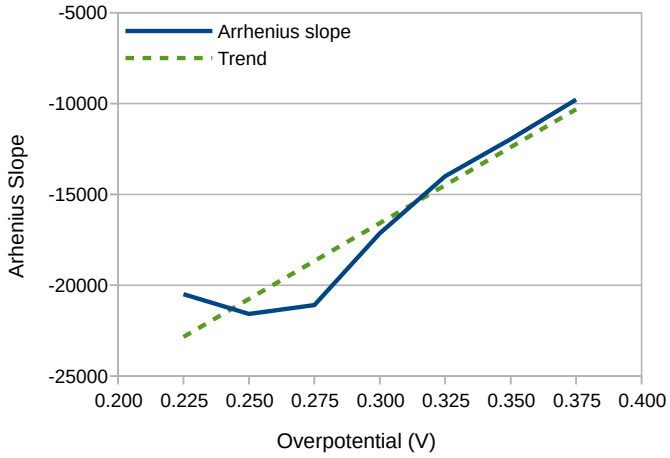

Figure 3.15: The slopes of the Arrhenius plots from Figure 3.14 plotted against overpotential.

therefore

$$\alpha = 7.2 \tag{3.54}$$

This value is clearly wrong, since α describes a reaction coordinate, and it should therefore be between 0 and 1. The explanation for this is that the lines in Figure 3.14 have been affected by the bend in the Tafel plots, especially at the higher values of overpotential. This non-linearity is caused by diffusion effects, which could be eliminated with careful experiment design, and bubble-effects, which cannot. It is therefore not possible to rely on any individual value of the calculated activation energy, and certainly not the rate at which it changes with potential. However, it is possible to perform a 'best-fit' of the mathematical model that was developed in Section 1.3.4 on Page 23. This model states:

$$ln(j) = k_1\,(1/T) + k_2\,(U/T) + k_3 \tag{3.55}$$

It is therefore possible to calculate the values as follows:

1. differentiate $\ln(j)$ with respect to U to determine k_2
2. differentiate $\ln(j)$ with respect $1/T$ to determine k_1
3. use the average value of $\ln(j)$ to determine k_3

This is because:

$$\frac{d\ln(j)}{dU} = \frac{k_2}{T} \tag{3.56}$$

$$\text{and, } \frac{d\ln(j)}{d1/T} = k_1 + k_2 U \tag{3.57}$$

When the first step of this procedure is followed, the results are as shown in Table 3.7. This generates a value of $d\ln(j)/dU$ and k_2 for each row of the table, plus an average value of k_2 that constitutes the best-fit.

ln(j)	Overpotential (V)								
A m^{-2}	0.225	0.25	0.275	0.3	0.325	0.35	0.375	dln(j)/dU	k_2
291.6					0.432	2.222	3.599	63.3	18473
303				0.032	2.094	3.640	4.862	64.1	19434
313			-0.927	1.497	3.444	5.034		79.3	24826
323		-0.508	1.594	3.570	5.160			75.9	24523
333	-0.606	1.326	3.373	5.007				75.5	25156
342	1.014	3.214	4.826					76.2	26077
T (K)								Average(k_2)	23081

Table 3.7: Calculated values of k_2 generated from the data in Table 3.5

The second step of the procedure produces the results shown in Table 3.8. The value of k_1 is calculated using:

$$k_1 = \frac{d\ln(j)}{d(1/T)} - \text{Average}(k_2)U \tag{3.58}$$

	ln(j)	Overpotential (V)								
	A m^{-2}	0.225	0.25	0.275	0.3	0.325	0.35	0.375	dln(j)/dU	k_2
0.00343	291.6					0.432	2.222	3.599	63.3	18473
0.00330	303				0.032	2.094	3.640	4.862	64.1	19434
0.00319	313			-0.927	1.497	3.444	5.034		79.3	24826
0.00310	323		-0.508	1.594	3.570	5.160			75.9	24523
0.00300	333	-0.606	1.326	3.373	5.007				75.5	25156
0.00292	342	1.014	3.214	4.826					76.2	26077
1/T (K^{-1})	T (K)								Average(k_2)	23081

dln(j)/d(1/T)	-20492	-21580	-21092	-17142	-13999	-11959	-9785		
k_1	-25685	-27350	-27439	-24066	-21500	-20037	-18440	Average(k_1)	-23503

Table 3.8: Calculated values of k_1 generated from the data in Table 3.7

The final step of the procedure is to calculate an average value for k_3. For example, the value of k_3 for the sample at 0.3 V overpotential and 313 K is:

$$\begin{aligned} k_3 &= ln(j) - k_1(1/T) - k_2(U/T) \\ &= 1.497 + 23503 \times (1/313) - 23081 \times (0.3/313) \\ &= 54.5 \end{aligned}$$

When this is repeated for all the samples, an average of 54.64 is generated. The three parameters of the model are therefore as summarised in Table 3.9.

Parameter	Value
k_1	-23503
k_2	23081
k_3	54.64

Table 3.9: Best-fit values for the mathematical model in Equation 3.55 to the empirical data from Figure 3.14

When the modelled results are overlayed on the earlier Tafel and Arrhenius plots, the results are as shown in Figures 3.16 and 3.17.

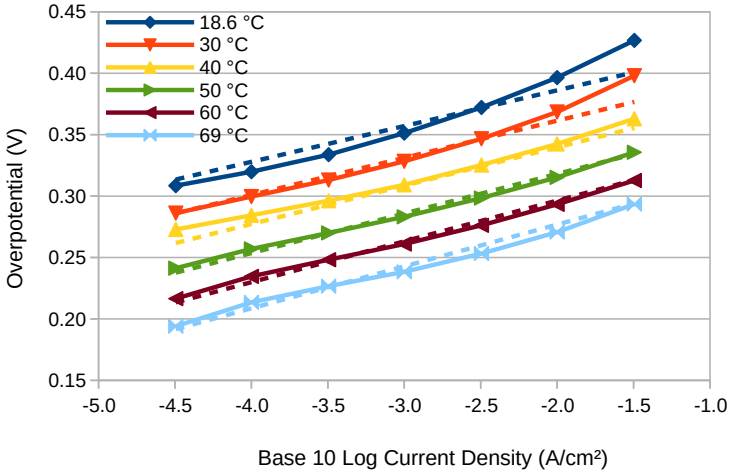

Figure 3.16: Overlay of the modelled Tafel plots (dashed lines) over the empirical data from Figure 3.13

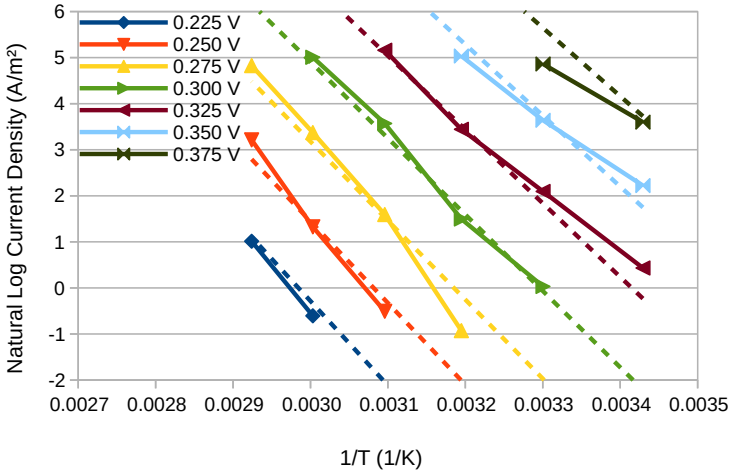

Figure 3.17: Overlay of the modelled Arrhenius plots (dashed lines) over the empirical data from Figure 3.14

Visually, the model is a good fit to the empirical data, but there are several differences. First is that the model predicts perfectly straight Tafel slopes, whereas the empirical data is

curved. This is due to the diffusion and bubble effects, as mentioned on Page 82. Second is that the model predicts much less variation in the slope of the Arrhenius plot, especially at higher overpotentials. This is also explained by diffusion and bubble effects, and serves to underline how the rate of change of the slope of the Arrhenius plot cannot be used to determine the value of α.

When the predictions of the model are analysed in greater detail, the results are as shown in Table 3.10. This table shows derived values for the Tafel slope and Arrhenius slope, and from these values can be derived the activation energy (at absolute zero) and α.

	ln(j)	Overpotential (V)							Tafel Slope	alpha
	A m^{-2}	0.225	0.25	0.275	0.3	0.325	0.35	0.375	mV dec^{-1}	
0.00343	291.6	-8.15	-6.17	-4.19	-2.21	-0.23	1.75	3.73	29.1	0.497
0.00330	303	-5.78	-3.88	-1.98	-0.07	1.83	3.74	5.64	30.2	0.497
0.00319	313	-3.85	-2.01	-0.17	1.68	3.52	5.36	7.21	31.2	0.497
0.00310	323	-2.04	-0.26	1.53	3.32	5.10	6.89	8.68	32.2	0.497
0.00300	333	-0.34	1.39	3.13	4.86	6.59	8.32	10.06	33.2	0.497
0.00292	342	1.11	2.79	4.48	6.17	7.86	9.54	11.23	34.1	0.497
1/T (K^{-1})	T (K)									
Arrhenius Slope		-18309	-17732	-17155	-16578	-16001	-15424	-14847		
E_{A0} (kJ mol^{-1})		152.2	147.4	142.6	137.8	133.0	128.2	123.4		

Table 3.10: Modelled values for the electrode current density as a function of overpotential and temperature, as generated by best-fit.

The table predicts that the underlying Tafel slope is very close to 30 mV dec^{-1} at room temperature, and increases proportionally with the temperature in Kelvin, which is inline with expectations. The activation energy decreases with increasing overpotential, which shows how the application of electrical potential lowers the barrier and permits the oxygen evolution reaction to proceed. The real activation energy remains unknown, since it depends on the change in entropy ΔS of the reaction, which is not a figure that can be determined by this analysis. Nevertheless, the slope of the Arrhenius plot, even though it is only applicable at absolute zero, is a widely reported figure in electrochemistry, and a very useful basis for comparison.

The most important outcome of the analytical modelling is a reliable determination of the value of α, which is equal to 0.497. This is remarkably close to the expected value of 0.5, and thereby constitutes an extremely useful confirmation of the fundamental theory behind electrode chemistry, the oxygen evolution reaction, and the Brønsted-Evans-Polanyi principle. This chapter lays out an accurate method of measuring it empirically, even from data that are far from perfect.

Ultimately Figure 3.13 on page 80 serves to highlight the high degree of correlation between the catalytic performance of the electrode and the temperature of the electrolyte, and this is even *after* the often significant iR losses of the electrolyte have been subtracted. It is

for this reason, and given the almost horizontal nature of the Tafel slope at the anode, i.e. at typically only 30 mV dec^{-1}, that if a choice has to be made between catalytic efficiency or warming the electrolyte, from a system point of view it is far more productive to choose the latter.

3.3 Enhanced ECSA

The ECSA characterisation procedure based on Cyclic Voltammetry (CV), as described on page 44, proved to be useful and reliable with many electrodes. However, the procedure failed with electrodes exhibiting very high levels of capacitance, and therefore a very large RC time-constant. For example, when used with electrodes coated with Raney nickel, the sort of waveforms obtained were as presented in Figure 3.18.

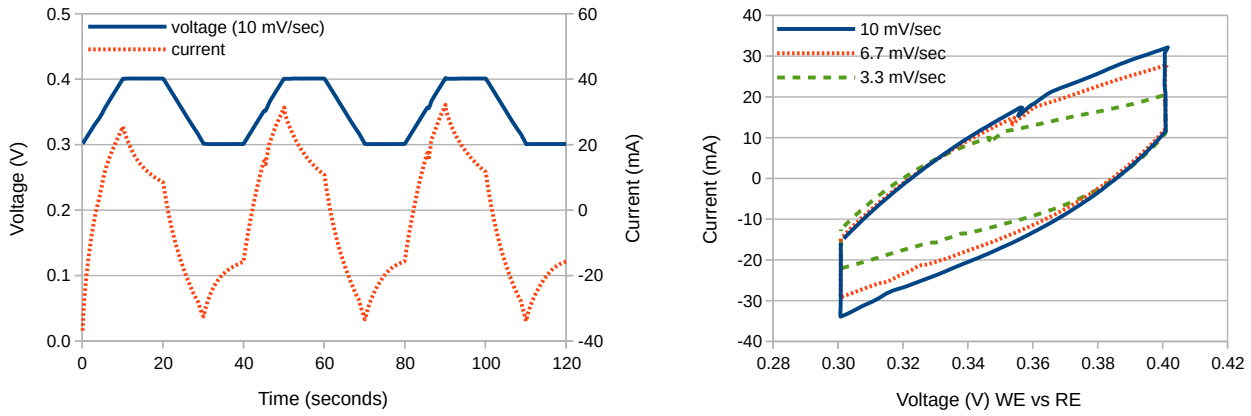

(a) Transient waveform

(b) Redrawn as voltammograms

Figure 3.18: CV waveforms and voltammograms for a Raney 1 electrode exhibiting a high level of capacitance. *(Electrode reference: Paddle #19)*

Even at 3.3 mV s^{-1} the 100 mV window takes 30 s to traverse, which is not enough time for the current to stabilise to an asymptotic value. As a consequence, it is clear from inspection of Figure 3.18b that the mid-point current is no longer a linear function of voltage ramp rate.

In order to provide more time, either the voltage window must be made wider, or the voltage ramped more slowly. However, in this mode, this was the slowest voltage ramp that the Ivium potentiostat could produce. Likewise, the voltage window could not be made much wider without taking the electrode far from open circuit potential, and thus compromising the validity of the measurement. Consequently, the CV ECSA procedure could not be used for this electrode.

Since it was not possible to use the mid-point method to calculate the ECSA value from the waveforms in Figure 3.18b, it was necessary to develop a new procedure, and it was thus proposed to make use of curve-fitting.

3.3.1 Literature

Curve-fitting is a well-known technique within engineering, and relates to any method whereby a mathematical function is fitted to a set of data. Since the function is based on a model, and thereby a set of assumptions, it is able to answer two questions: a) which model parameters best fit the data, and b) how accurate that model is, and therefore the assumptions behind it.

The fitting of an equivalent circuit to frequency-domain data obtained by EIS is absolutely standard within electrochemistry. However, it is far less common to fit an equivalent circuit to time-domain (transient) data. For example, the electrochemistry software Ivium-soft does not offer it as an option. Mathematically, the same information is present, albeit with a different axis, and the two processes are equivalent.

The fitting of a four-component model to CV waveforms obtained from a bilayer lipid membrane was performed by Gu *et al* [146]. Their method was trigonometrical in nature, relying on precise measurements of waveform slopes and intercepts, and would therefore cope poorly with small deviations from the expected curve shapes.

An alternative to frequency-domain fitting called potential-step impedance analysis (PSIA) was developed by Ehrensberger *et al.* [147]. This involves applying a voltage step to the working electrode whilst recording the resulting transient current response. The electrode's frequency-domain response was calculated from the transient response using what was referred to as a 'numerical Laplace transform', but is perhaps more commonly known as a discrete Fourier transform (DFT). However, the technique is still largely trigonometrical, and the calculation of the CPE phase-angle required the capture of a Nyquist plot semi-circle, which many real world systems do not produce clearly, if at all.

The exact same problem of fitting a Randles equivalent circuit to transient waveforms has arisen in the assessment of the corrosion of steel in concrete [148]. The signal applied to the concrete sample was either potentiostatic or coulostatic, and it was observed that the two methods were largely comparable. The authors also chose to perform a numerical Laplace (Fourier) transform to bring the data into the frequency domain.

It appears that the curve-fitting of electrical equivalent circuits to transient waveforms is relatively uncommon, particularly within electrochemistry.

3.3.2 Analytical Solution

In order to perform curve-fitting of an RC network (as shown in Figure 3.19) to the waveforms in Figure 3.18, it is necessary to calculate the response of an RC network to a voltage ramp.

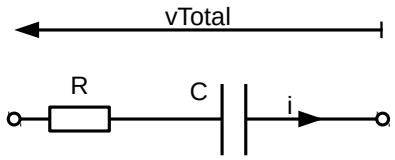

Figure 3.19: Schematic of RC network

This can be performed by expressing the voltage across an RC network as a function of the current i through the resistor R, and the charge Q on the capacitor C, such that:

$$v = iR + Q/C \tag{3.59}$$

Differentiating with respect to time permits dQ/dt to be replaced with i:

$$\frac{dv}{dt} = R\frac{di}{dt} + \frac{1}{C}i \tag{3.60}$$

Rearranging as a linear differential equation in i produces:

$$\frac{di}{dt} + \frac{1}{RC}i = \frac{1}{R}\frac{dv}{dt} \tag{3.61}$$

If an RC network is driven with a voltage ramp then dv/dt is a constant. The solution of a linear differential equation is in general equal to the sum of the solution to the *homogenous equation* (the 'complementary function') and the *inhomogeneous equation* (the 'particular integral'). In this case the homogenous equation is:

$$\frac{di}{dt} + \frac{1}{RC}i = 0 \tag{3.62}$$

to which the solution is (by inspection):

$$i = A\exp\left(\frac{-t}{RC}\right) \tag{3.63}$$

Since *any* solution to the inhomogeneous equation can be used to produce the general solution, it is simplest to opt for the steady-state solution, i.e. such that $di/dt = 0$. Substituting this into Equation 3.61 and rearranging produces:

$$i = C\frac{dv}{dt} \tag{3.64}$$

The general solution is therefore:

$$i = C\frac{dv}{dt} + A\exp\left(\frac{-t}{RC}\right) \tag{3.65}$$

which is equal to the sum of a constant current (the asymptotic value) and an exponential decay. The value of A will depend on the starting conditions, but it can be seen that as t becomes large, the current will always tend towards Cdv/dt. Since the value of C is proportional to the ECSA, this means that the only value that needs to be measured is that of the asymptotic value towards which the current is tending.

However, if the RC constant is large, and the minimum value of dv/dt is limited by the capabilities of the potentiostat, this can place a minimum value on Δt, and thereby a minimum value on Δv. Therefore, the size of voltage window needed to reliably measure the asymptotic value of the electrode current could be larger than the flat region of the electrode response that is available. Under these conditions it will be impossible to make a straightforward measurement of the asymptotic current.

3.3.3 Simulation

In order to visualise how a large RC constant would affect ECSA measurements, simulations were conducted using ngSpice, based on the following schematic:

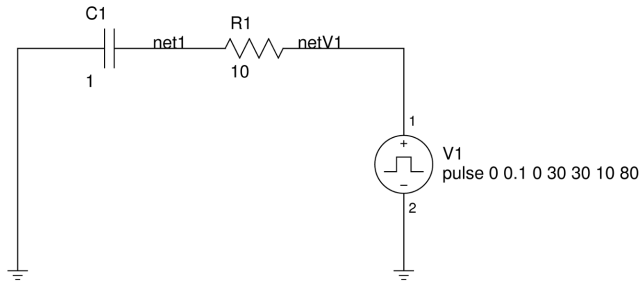

Figure 3.20: Schematic diagram for Spice simulations of ECSA.

Component $C1$ represents the double-layer capacitance C_{DL}, and $R1$ the series resistance of the electrolyte, plus the resistance of the electrodes, wiring and any insulating surface layers on the electrode.[1] The results of the transient simulations for two different values of the RC time constant at a sweep-rate of $10\,\mathrm{mV\,s^{-1}}$ are as shown in Figure 3.21.

When these transient waveforms are plotted as cyclic voltammograms, they appear as shown in Figure 3.22.

[1]The pulse voltage source $V1$ is programmed with the number sequence '0 0.1 0 30 30 10 80', which configures it to cycle between 0 and 0.1 volts, starting at 0 seconds, with upward and downward ramp times of 30 seconds, a 10 second pulse width and a total cycle time of 80 seconds. This corresponds to a sweep rate of $3.33\,\mathrm{mV\,s^{-1}}$, and therefore matches the slowest measurement in Figure 3.18b

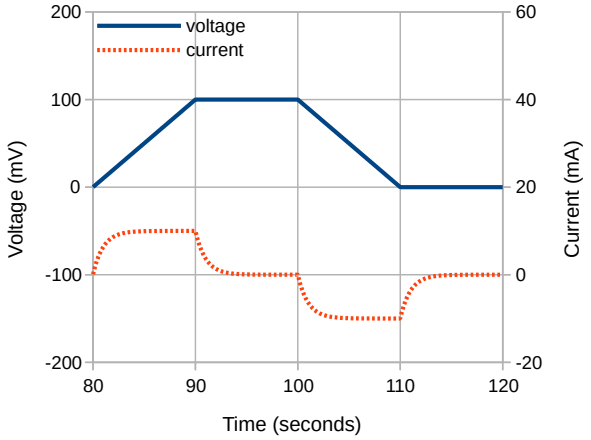

(a) 1 Farad and 1 Ohm

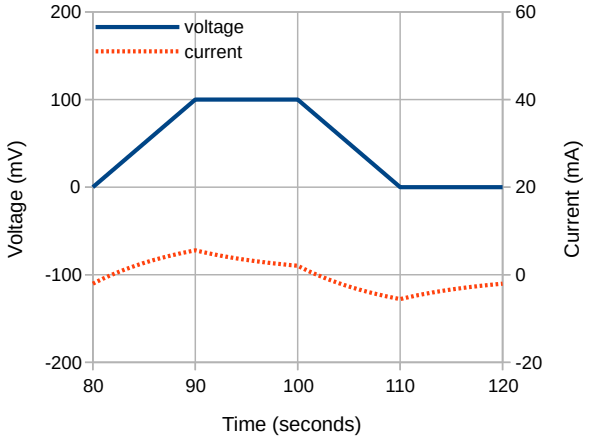

(b) 1 Farad and 10 Ohms

Figure 3.21: Simulated transient waveforms for two values of R and C

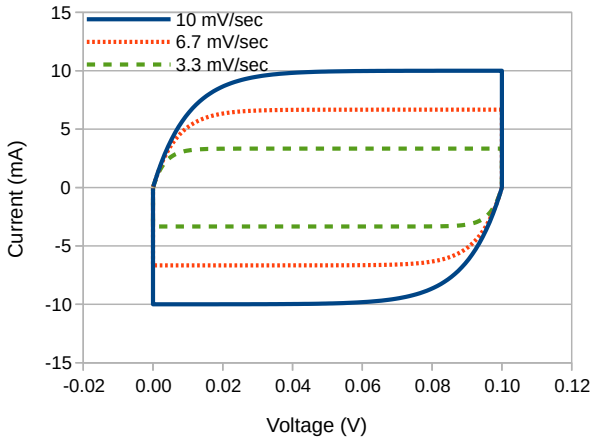

(a) 1 Farad and 1 Ohm

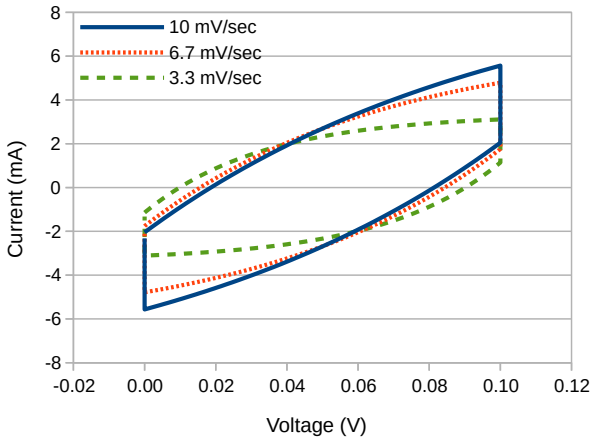

(b) 1 Farad and 10 Ohms

Figure 3.22: Simulated cyclic voltammograms for two values of R and C

The voltammograms in Figure 3.22b bear a striking resemblence to the measured voltammograms in Figure 3.18b on page 86, and therefore support the idea that this electrode was exhibiting a large RC time constant.

From inspection, it is clear that the anodic and cathodic midpoint voltages can no longer be used to determine the ECSA when the RC constant is too high (as on the right), since the midpoint position has become almost invariant of sweep rate. A better candidate might be the maximum and minimum voltages of each sweep, but from inspection it is clear these vary non-linearly. The task therefore of extracting a reliable figure for the double-layer capacitance becomes one that requires some form of curve-fitting.

An alternative approach would be to sweep the voltage at an even slower rate, such that the current has time to stabilise, however $3.33\,\mathrm{mV\,s^{-1}}$ is the minimum sweep rate of which the Ivium potentiostat is capable outside of a narrow voltage range. An equivalent

solution would be to sweep over a larger voltage range, but 100 mV is already quite large in comparison with some values in the literature, and a larger sweep requires a larger flat spot in the current-voltage characteristic.

3.3.4 Curve-fitting

Since the waveforms produced during measurements of ECSA should produce an exponential decay towards a final asymptotic value, it should be possible to calculate what this asymptotic value is, even if the waveform itself does not have enough time to reach it. One way to do this is to subtract many different values of asymptote, and see which value produces the straightest line on a logarithmic plot.

A widely recognised value of the straightness of any dataset is the square of its Pearson coefficient, a value which is commonly referred to as 'r-squared'. This is available in all well-known spreadsheet programs as the function RSQ().

From Equation 3.65 it is known that if the behaviour of the electrode can be modelled as an RC network, then the time-response of the electrode current to a constant voltage ramp can be expressed as:

$$i = C\frac{dv}{dt} - Aexp\left(\frac{-t}{RC}\right) \tag{3.66}$$

which is in the same form, except that constant A has the opposite sign. At $t = 0$, the value of the current is equal to $Cdv/dt - A$, and as time progresses the current tends towards Cdv/dt. If a final asymptotic current value, F, is postulated and the current is subtracted from this (to produce i_F), the equation becomes:

$$i_F = F - C\frac{dv}{dt} + Aexp\left(\frac{-t}{RC}\right) \tag{3.67}$$

If the value of F is correct, such that $F = Cdv/dt$, then only the exponential term will remain, leaving:

$$log(i_F) - log(A) = \frac{-t}{RC} \tag{3.68}$$

Thus, if $log(i_F)$ is plotted against t, a straight line will result. Differentiating this line with respect to time produces:

$$\frac{dlog(i_F)}{dt} = \frac{-1}{RC} \tag{3.69}$$

Thus, the slope of the straightest logarithmic plot determines the RC time constant of the exponential decay. However, since doubling R and halving C produces the same result, the

slope cannot be used to determine them independently. For this the final asymptotic current value can be used, since it is equal to Cdv/dt, hence:

$$C = \frac{\text{final asymptotic value of current}}{\text{rate of change of voltage}} \tag{3.70}$$

and from this the values of both R and C can therefore be calculated.

The first step in applying this procedure to the waveforms measured in Figure 3.18b is therefore to plot the current against time rather than voltage, and then to extract representative segments of the anodic and cathodic waveforms. When this is done, the results are as shown in Figure 3.23. The anodic voltage sweeps are evidently producing artefacts on the current waveform, but from inspection of Figure 3.18b on page 86 these artefacts are clearly also present on the voltage waveform. We may therefore conclude that they are quite possibly due to the internal workings of the potentiostat. In any case, as will become clear, such is the noise-rejection of the analytical technique here described that they have very little impact on the quality of the results produced.

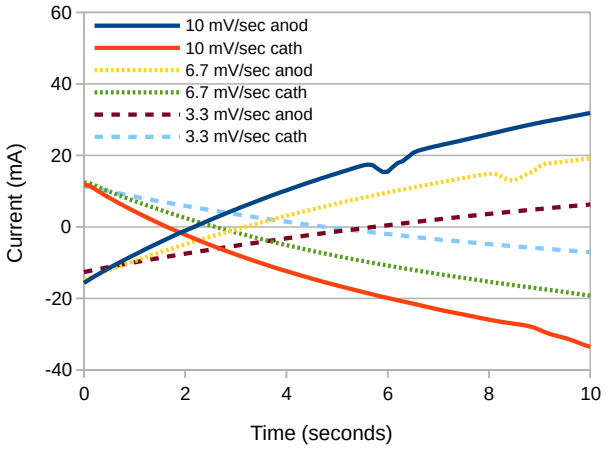

Figure 3.23: Anodic and cathodic ECSA transient current waveforms segments for Paddle 19

Taking the blue '10 mV/sec anod' line in the above figure as an example, it is clear that the line is tending asymptotically towards a current of approximately 50 mA, but it is very difficult to visualise exactly where it is heading. However, it is possible to subtract several different values of asymptotic current, and to plot these on a logarithmic chart, as presented in Figure 3.24a.

From Figure 3.24a it is perhaps not immediately obvious, but the blue line '47.2 mA' has a slight downward curve, whereas the brown line '67.2 mA' has a slight upward curve. Neither line is therefore completely straight, and would consequently have a lower R-squared value than the lines between them. This implies that the asymptotic value of the current to which the blue line in Figure 3.23 is tending is somewhere between 47 and 67 mA.

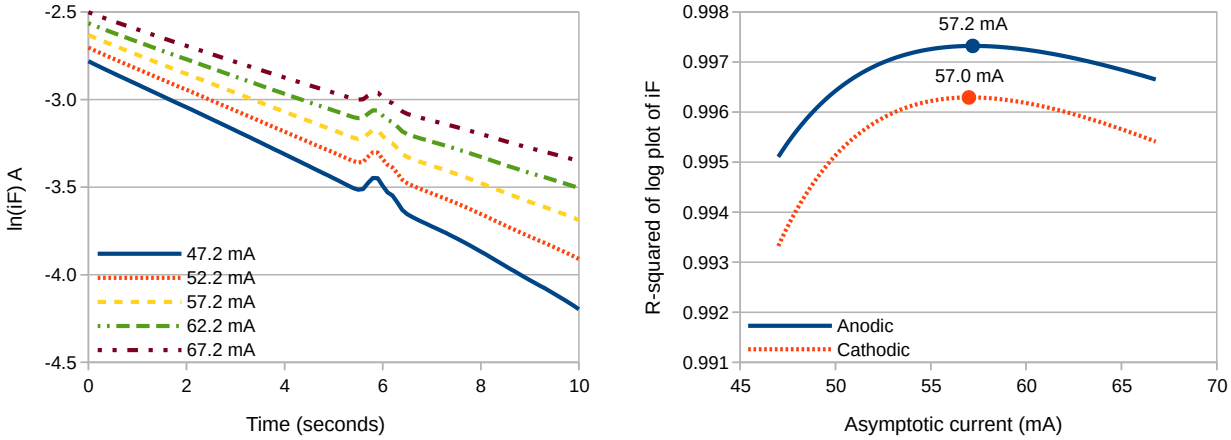

(a) Logplots of i_F *vs* F

(b) Straightness of logplots *vs* F

Figure 3.24: Determination of anodic and cathodic asymptotic currents for Paddle 19, based on the waveforms in Figure 3.23, a) natural logarithmic plots of current i_F for various values of asymptotic current F, b) variation of R-squared of log-plot of i_F versus asymptotic current F for anodic and cathodic waveforms. Voltage ramp rate: 10 mV s^{-1}

Finding the exact asymptotic value of current that will maximise the value of R-squared is a time-consuming procedure to perform using a spreadsheet. Therefore, software was written using the PHP language to perform the calculations, with the results as presented in Figure 3.24b.

The figure shows that the variation of R-squared with asymptotic current value F is a smooth curve and allows the best-fit asymptotic values of 57.2 mA anodic and 57.0 mA cathodic to be extracted. This technique has therefore measured the exponential rate of decay of the waveform to predict the final value of the current to which it is tending. The R-squared value for the cathodic waveform is lower than for the anodic, which is because the waveforms feature artefacts that will limit how straight the lines on the logarithmic plot can be. It is the position of the maximum that is of primary importance.

The asymptotic values permit the slope of the log-plot to be measured, and hence a value for the RC time constant to be determined. When this is done, a value of 9.6 s is produced. This means that every 9.6 s the difference between the electrode current and the final asymptotic current reduces by 63.2%, regardless of starting point. This percentage equates to $(1 - 1/e)$ where e is Euler's number (2.718). As a sanity check, it is possible to test this time-constant against Figure 3.23 on page 92, by observing that at $t = 0$ the current is about -16 mA, and at $t = 9.6$ s it is about 30 mA. Therefore the final value of current should be approximately equal to:

$$-16 + \frac{30 + 16}{0.632} = 56.8\,\text{mA} \tag{3.71}$$

which is correct.

The results of applying this procedure to all six waveforms in Figure 3.23 are as presented in Figure 3.25.

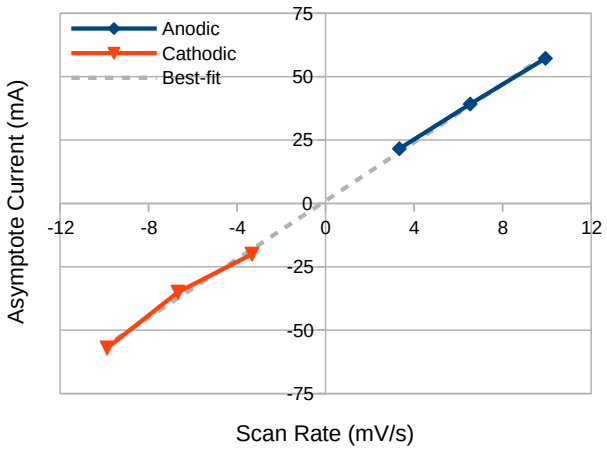

Figure 3.25: Plot of asymptotic current values *versus* scan rate for Paddle 19

The figure shows that this analytical procedure has produced a convincing straight line from the waveforms presented in Figure 3.23 on page 92. This was not possible with the original ECSA procedure, therefore the curve-fitting procedure is an improvement. It confirms that the waveforms are exponential in nature, and that the electrochemical system that is constituted by the electrode at open-circuit potential can therefore be represented as an *RC* network.

Note that there is no requirement for the above line of best-fit to pass through the origin. Indeed it will only do so if the ECSA measurements were performed exactly around the d.c. bias voltage that produces precisely equal positive and negative current waveforms. Often this is not the case, since the Raney Nickel electrode behaves as a combination of supercapacitor and battery, particularly after accelerated ageing. As a result, the d.c. bias voltage is not just non-zero, but can drift significantly between one measurement and the next.

However, it is the slope of the line of best-fit that is of greatest importance, since it is proportional to the ECSA. For this electrode, the value measured is 5.76 A V^{-1}, or 5.76 F. The value of the RC time-constant averaged over all six waveform segments is 10.4 s, therefore the value of R is 1.8 Ω. Consequently, it can be seen that the slow *RC* time-constant exhibited by Paddle 19 is largely due to a high value of capacitance, not resistance. This is reassuring, because it is would be more difficult to explain a high value of resistance, since the resistive properties of the electrolyte are well understood.

As a consistency check, the series resistance can be compared with the value obtained from EIS, which for this electrode was 1.12 Ω. There is therefore a discrepancy of about 50%. The reasons for this are complicated, and arise due to the non-ideal constant-phase behaviour of the double-layer capacitance. This will be explained in greater detail in Section

3.4 on page 110. It can also arise due to a mismatch in the time-constant due to a small amount of transfer resistance, so this will be investigated first.

3.3.5 RCR Network Transient Equivalent Circuit Fitting

The addition of an extra resistor across the double-layer capacitance, corresponding to some form of transfer resistance, produces an equivalent circuit as shown in Figure 3.26a.

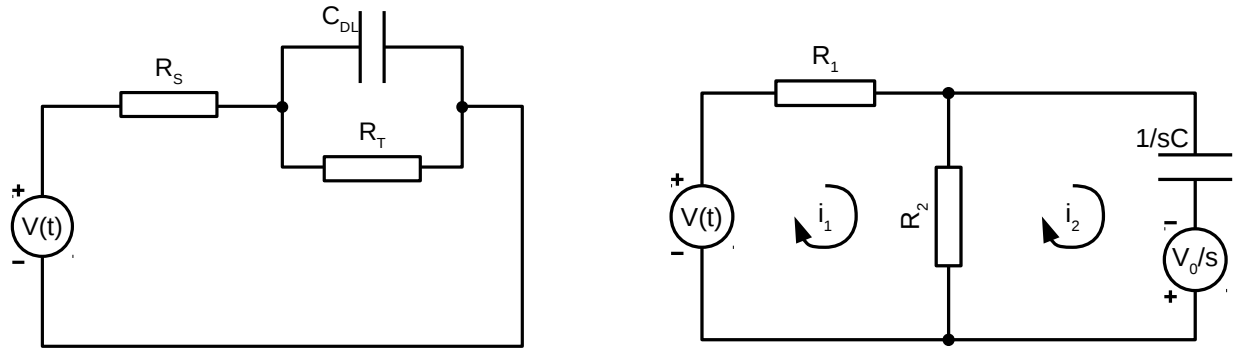

(a) The RCR equivalent circuit

(b) As redrawn in s-domain

Figure 3.26: Equivalent circuit for the electrode/electrolyte interface extended to include transfer resistance R_T

In order to choose which values of R_S, R_T and C_{dl} constitute the 'best-fit' of any given empirical waveform, it would be beneficial to know how these values affect the shape of the waveform produced. One accepted way to achieve this is via Laplace transforms, wherein active components such as capacitors are replaced by their s-domain equivalent circuit, as shown in Figure 3.26b. The result of performing mesh-current analysis on the rearranged circuit are the following two equations:

$$R_1 i_1 + R_2(i_1 - i_2) = V(t) \tag{3.72}$$

$$\frac{i_2}{sC} + R_2(i_2 - i_1) = \frac{V_0}{s} \tag{3.73}$$

Since the function of the driving voltage $V(t)$ is a ramp, this can be expressed in the s-domain as:

$$V(s) = \frac{\beta}{s^2} \tag{3.74}$$

where β is the ramp-rate expressed in volts per second. Assuming that the charge on the capacitor at time $t = 0$ is 0 V, which means that $V_0 = 0$, Equation 3.73 can be rewritten as:

$$i_2\left(\frac{1}{sC} + R_2\right) - R_2 i_1 = 0 \tag{3.75}$$

$$\text{therefore} \qquad i_2 = \left(\frac{s}{s + \frac{1}{R_2C}}\right) i_1 \tag{3.76}$$

Substituting Equation 3.76 in Equation 3.72 produces:

$$(R_1 + R_2)i_1 - R_2\left(\frac{s}{s + \frac{1}{R_2C}}\right) i_1 = \frac{\beta}{s^2} \tag{3.77}$$

$$\text{therefore} \qquad \left[\frac{(R_1 + R_2)\left(s + \frac{1}{R_2C}\right) - sR_2}{\left(s + \frac{1}{R_2C}\right)}\right] i_1 = \frac{\beta}{s^2} \tag{3.78}$$

Dividing both sides by R_1 and rearranging produces:

$$\left(s + \frac{1}{R_2C} + \frac{1}{R_1C}\right) i_1 = \frac{\beta}{R_1}\left(\frac{s + \frac{1}{R_2C}}{s^2}\right) \tag{3.79}$$

$$\text{therefore} \quad i_1(s) = \frac{\beta}{R_1}\left[\frac{s + \frac{1}{R_2C}}{s^2\left(s + \frac{1}{R_{12}C}\right)}\right] \tag{3.80}$$

where $R_{12} = R_1 \parallel R_2$. The inverse Laplace transform of Equation 3.80 will produce the analytical time-domain solution $i_1(t)$. To do this, the denominator must be expanded into its individual terms, such that:

$$\frac{\beta}{R_1}\left[\frac{s + \frac{1}{R_2C}}{s^2\left(s + \frac{1}{R_{12}C}\right)}\right] = \frac{E + Fs}{s^2} + \frac{G}{\left(s + \frac{1}{R_{12}C}\right)} \tag{3.81}$$

$$= \frac{E}{s^2} + \frac{F}{s} + \frac{G}{\left(s + \frac{1}{R_{12}C}\right)} \tag{3.82}$$

where E, F and G are hypothetical constants that will, by the rules of partial fractions, produce the original numerator, i.e. such that:

$$(E + Fs)\left(s + \frac{1}{R_{12}C}\right) + Gs^2 = \frac{\beta}{R_1}\left(s + \frac{1}{R_2C}\right) \tag{3.83}$$

By reference to the selected Laplace functions presented in Table 3.11, it can be seen that the right hand side of Equation 3.82 corresponds to the summation of a ramp, a step and an

exponential decay.

Description	Function in s-domain	Function in time-domain
Ramp	$1/s^2$	$tu(t)$
Step	$1/s$	$u(t)$
Exponential Decay	$1/(s+\alpha)$	$\exp(-\alpha t)u(t)$

Table 3.11: Table of selected Laplace functions and their time-domain equivalents

If E, F and G can successfully combine to produce the numerator, then the terms in units, s and s^2 must agree, which produces three simultaneous solutions:

$$\text{terms in units:} \quad \frac{E}{R_{12}C} = \frac{\beta}{R_1 R_2 C} \tag{3.84}$$

$$\text{terms in } s\text{:} \quad E + \frac{F}{R_{12}C} = \frac{\beta}{R_1} \tag{3.85}$$

$$\text{terms in } s^2\text{:} \quad F + G = 0 \tag{3.86}$$

Rearranging Equation 3.84 produces:

$$E = \frac{\beta R_{12} C}{R_1 R_2 C} = \frac{\beta}{R_1 + R_2} \tag{3.87}$$

which, on substituting into Equation 3.85 produces:

$$\frac{\beta}{R_1 + R_2} + \frac{F}{R_{12}C} = \frac{\beta}{R_1} \tag{3.88}$$

$$F = \beta R_{12} C \left(\frac{1}{R_1} - \frac{1}{R_1 + R_2} \right) \tag{3.89}$$

$$\text{therefore} \quad F = \beta C \left(\frac{R_2}{R_1 + R_2} \right)^2 \tag{3.90}$$

Therefore the full analytical solution of the transient response of the RCR-network shown in Figure 3.26a to a ramp input of slope β in $\mathrm{V\,s^{-1}}$ is:

$$i_1(t) = Etu(t) + Fu(t) + G \exp\left(\frac{-t}{T}\right) u(t) \tag{3.91}$$

$$\text{where} \quad E = \frac{\beta}{R_1 + R_2} \tag{3.92}$$

$$F = \beta C \left(\frac{R_2}{R_1 + R_2} \right)^2 \tag{3.93}$$

$$G = -F \tag{3.94}$$

$$T = (R_1 \parallel R_2) C \tag{3.95}$$

where $u(t)$ is a unit step function at time $t = 0$. This solution can be verified by comparing it to the result of a Spice simulation, as shown in Figure 3.27, where the values $R_1 = 1.5\,\Omega, R_2 = 10\,\Omega, C = 0.5\,\mathrm{F}$ and $\beta = 10\,\mathrm{mV\,s^{-1}}$ have been chosen.

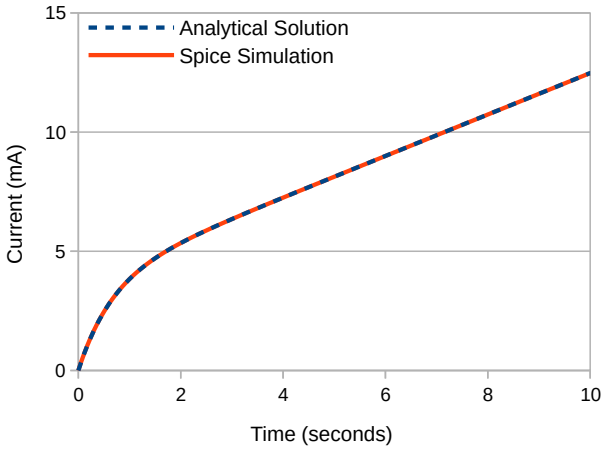

Figure 3.27: Verification against a Spice simulation of the analytical solution for the response of the RCR equivalent circuit to a ramp input.

3.3.6 RCR Analytical Curve-Fitting Method

An example of some empirical measurements that resemble the waveforms produced by an RCR network are as presented in Figure 3.28. These were produced by cyclic voltammetry on a Pt-sputtered 316-grade stainless-steel plate, which exhibited a low value of double-layer capacitance since it had a smooth surface. The low value of double-layer capacitance *appeared* to expose the influence of a parasitic transfer resistance, even though the voltage was not in a region where Faradaic reactions were expected, and as a result the electrode produced waveforms which were too distorted for the conventional ECSA procedure (as described on page 44). In fact, as will be seen in Section 3.4.5 on page 126 no such transfer resistance existed.

In order to fit the analytical solution outlined in the previous section to this waveform a suitable profit function was needed that can be maximised, thereby constituting a 'best-fit' to the data. The analytical solution of the response of an RCR network to a ramp input in Equation 3.91 is the sum of a step function, a ramp function and an exponential. Therefore, the best-fit to empirical data will occur when the subtraction of a step and a ramp produces the 'most exponential' residual. This will occur when the residual signal produces the straightest line on a logarithmic plot, which in practice can be defined as the square of its Pearson coefficient. This is commonly available in spreadsheet programs as the function RSQ().

This definition can be further improved if a section of signal exists where the exponential response of the circuit has diminished, i.e. such that the waveform becomes a straight line.

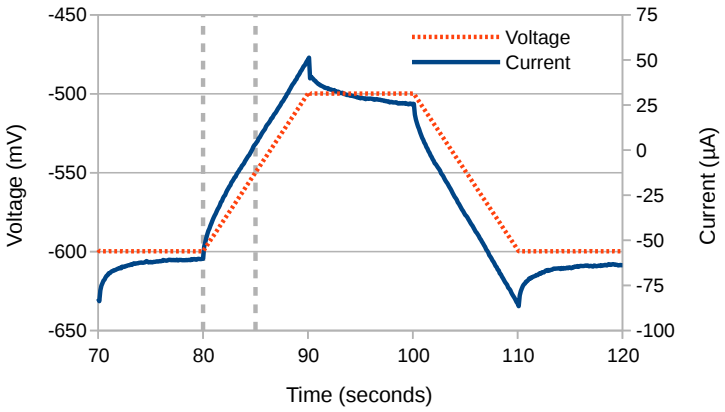

Figure 3.28: Cyclic-voltammetry measurements for a Pt-sputtered 316-grade stainless-steel plate in 0.5 mol NaOH. *(Electrode reference: Paddle #35)*

This permits the ramp response of the circuit to be measured directly. With reference to Figure 3.28, this region occurs between approximately 83 seconds and 90 seconds. Therefore, in order to balance the trade-off between the exponential best-fit and the ramp best-fit, the profit function was calculated using the section of waveform between 80 and 85 seconds, as delimited by the vertical dashed lines.

Once this was performed, the results were as shown in Figure 3.29a. The figure shows the original signal (solid line) which has been normalised to begin at zero amps. From this a ramp function was subtracted, to produce the orange dashed line, which asymptotes towards a horizontal line. This was then subtracted from a proposed asymptotic value to produce the green dotted line, which resembles an exponential decay. If it is, then a plot of the residual current on a logarithmic plot, as shown in Figure 3.29b, will yield a straight line.

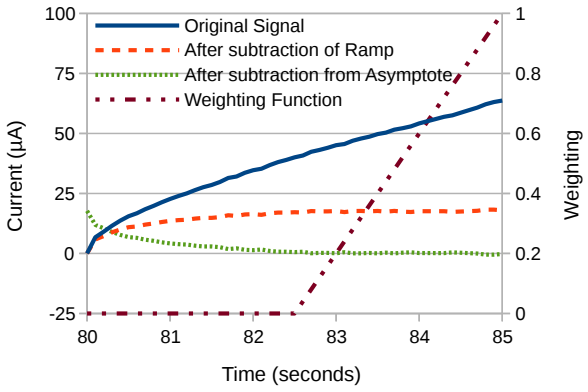

(a) Calculation of residual current

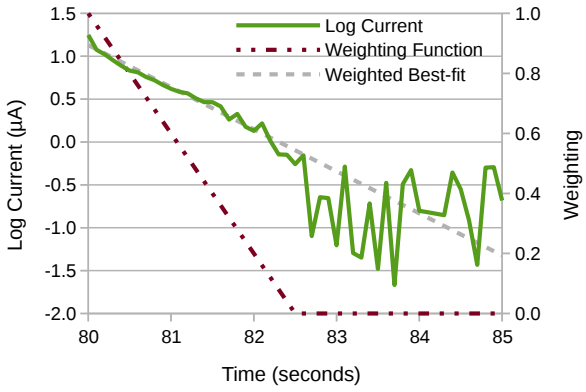

(b) Logplot of residual current

Figure 3.29: Analysis of the section of current waveform from Figure 3.28 between 80 to 85 seconds, a) subtraction of ramp and step to generate residual current, and b) logplot of residual current to find 'most exponential' solution

Nevertheless, it was clear that the right-hand half of the logarithmic plot did not produce

a straight line, because the signal had fallen below the noise floor of the measurement data. For this reason a weighting function was introduced that biased the best-fit towards the beginning of the time window, and not at all after the mid-point. Similarly, a weighting function was introduced which biased the measurement of the ramp-rate towards the end of the time window, and not at all before the mid-point. In this way, maximum advantage was taken of the two different characteristics of the signal that were available, i.e. the first half of the time window which was mostly exponential, and the second half which was mostly linear.

The first component of the profit function can therefore be defined as:

$$I_{flat}(t) = I(t) - I(80) - E(t - 80) \tag{3.96}$$

$$\text{profit}_1 = 1 - k_1 \left(\text{SLOPE}\left[I_{flat} \times W_1(t), t\right]\right)^2 \tag{3.97}$$

where $I(t)$ is the measured current waveform, E is the proposed ramp-rate in $\text{A}\,\text{s}^{-1}$, $W_1(t)$ is the rear-loaded weighting function, SLOPE returns the slope of the line of best-fit, and k_1 is a constant chosen to restrict the profit function to positive values within the chosen range of ramp-rates. The second component of the profit function was defined as:

$$I_{residual}(t) = I_{asymp} - I_{flat}(t) \tag{3.98}$$

$$I_{log}(t) = \log_{10}\left[\text{ABS}(I_{residual})\right] \tag{3.99}$$

$$\text{profit}_2 = \text{RSQ}\left[I_{log} \times W_2(t), t\right] \tag{3.100}$$

where I_{asymp} is the proposed value for the asymptote current, ABS[] returns an absolute value, RSQ[] returns the square of the Pearson coefficient, and $W_2(t)$ is the front-loaded weighting function. The total profit function can then be defined as:

$$\text{profit} = \text{profit}_1 \times \text{profit}_2 \tag{3.101}$$

When plotted as a map over a range of ramp-rates and asymptotic currents, the profit function appeared as presented in Figure 3.30. The map reveals that the function is maximised at a ramp rate of $9.15\,\mu\text{A}\,\text{s}^{-1}$ and an asymptotic current of $17.73\,\mu\text{A}$. The contours also reveal how a trade-off is made between the ideal ramp-rate, which is closer to $8\,\mu\text{A}\,\text{s}^{-1}$, and the 'most exponential' residual current, which occurs at a slightly higher value of ramp-rate.

The profit function is also highly sensitive to asymptotic current to the left of the maximum point. This is because at lower values of proposed asymptotic current, the residual current starts to become negative. As a result the logarithm of the *absolute* current value develops a sharp kink where the residual current changes sign, which greatly decreases the

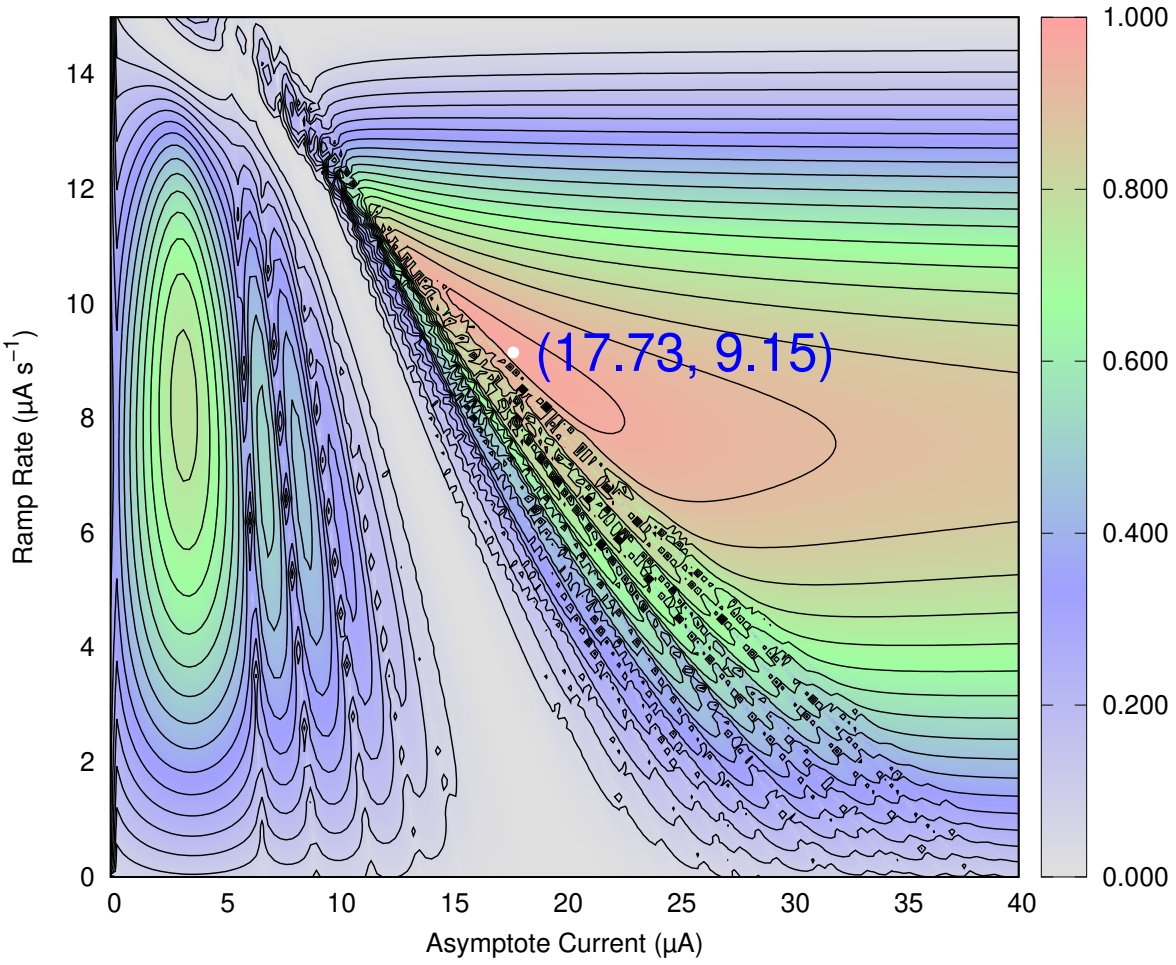

Figure 3.30: Profit function map applied to the section of waveform from Figure 3.28 between 80 and 85 seconds. The function is maximised at a ramp rate of 9.15 µA s^{-1} and an asymptotic current of 17.73 µA.

square of the Pearson coefficient. This is deliberate, and highlights how the ABS() function acts as a mechanism to exclude regions of the solution space that yield negative residual currents.

The slope of the logarithmic plot of the residual current is inversely proportional to the time constant of the exponential component of the transient response, which from Equation 3.91 on page 97 is equal to $(R_1 \parallel R_2)C$. The value of this slope (slope_2) which is shown as the dashed grey line in Figure 3.29b, is related to the time constant such that:

$$(R_1 \parallel R_2)C = \frac{-1}{\ln(10)\text{slope}_2} = T_{12} \tag{3.102}$$

Therefore the full set of best-fit parameters extracted from the RCR network analytical curve-fitting procedure are as presented in Table 3.12.

Parameter	Ramp Rate	Asymptotic Current	Time Constant
Symbol	E	F	T_{12}
Best-fit Value	9.15	17.73	0.885
Units	$\mu A\,s^{-1}$	μA	s

Table 3.12: Best-fit values for the analytical fitting of the RCR equivalent circuit to the current waveform window presented in Figure 3.28.

In order to calculate the values of C, R_1 and R_2 to which these parameters correspond, Equations 3.92, 3.93 and 3.102 must be rewritten, for example as:

$$R_1 + R_2 = \beta / E \tag{3.103}$$

$$\frac{R_2}{R_1 + R_2} = \sqrt{\frac{F}{\beta C}} \tag{3.104}$$

$$(R_1 \parallel R_2)C = \frac{R_1 R_2 C}{R_1 + R_2} = T_{12} \tag{3.105}$$

where T_{12} is the time constant from Table 3.12. Substituting Equations 3.104 into 3.105, and 3.103 into 3.104 produces:

$$R_1 C\sqrt{\frac{F}{\beta C}} = T_{12} \qquad \text{therefore} \qquad R_1 = \frac{T_{12}}{F}\sqrt{\frac{\beta F}{C}} \tag{3.106}$$

$$R_2\frac{E}{\beta} = \sqrt{\frac{F}{\beta C}} \qquad \text{therefore} \qquad R_2 = \frac{1}{E}\sqrt{\frac{\beta F}{C}} \tag{3.107}$$

which can be substituted into Equation 3.103 to produce:

$$\frac{\beta}{E} = \frac{T_{12}}{F}\sqrt{\frac{\beta F}{C}} + \frac{1}{E}\sqrt{\frac{\beta F}{C}} \tag{3.108}$$

$$\sqrt{C} = \frac{E}{\beta}\sqrt{\beta F}\left[\frac{T_{12}}{F} + \frac{1}{E}\right] \tag{3.109}$$

$$\text{therefore} \qquad C = \frac{(ET_{12} + F)^2}{\beta F} \tag{3.110}$$

Once a value for C is calculated using Equation 3.110, values for R_1 and R_2 can be calculated directly using Equations 3.106 and 3.107. Applying these equations to the best-fit parameter values in Table 3.12 produced the values presented in Table 3.13.

To verify that the values in Table 3.13 were a valid equivalent circuit for the electrode, a Spice simulation was conducted as shown in Figure 3.31. The simulation confirmed that the equivalent circuit constituted a good match for the empirical data, but the rate of curvature within the first second was a source for concern. The higher rate of curvature for the empirical data suggested a *lower* value for the double-layer capacitance than had been produced

Element	C_{dl}	R_S	R_T
Value	3766	343.8	743.1
Units	µF	Ω	Ω

Table 3.13: Values of C_{dl}, R_S and R_T corresponding to the best-fit parameters in Table 3.12.

from the RCR analytical curve-fitting method.

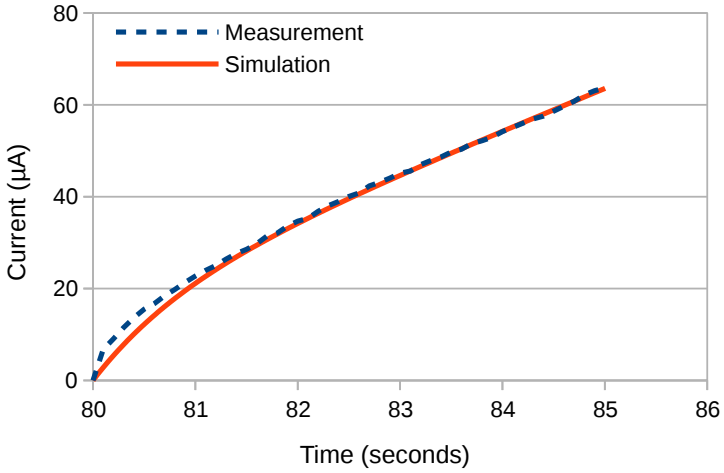

Figure 3.31: Comparison of measurement data and a spice simulation of the analytical best-fit calculated parameters in Table 3.13.

3.3.7 Comparison with EIS data

In Section 3.3.6 on page 98 a Pt-sputtered 316-grade stainless steel flat plate electrode was analysed using Cyclic Voltammetry. The same electrode was also analysed using Electrochemical Impedance Spectroscopy (EIS), and the results analysed using two different equivalent circuit models as shown in Figure 3.32.

The element Q in the RQR Model represents a Constant Phase Element (CPE), and permits the model to achieve a closer fit to the measured data. This is because it is able to reproduce the *flattened semi-circle* that is typically exhibited by electrochemical systems [122, 149–154]. However, it is not clear how much capacitance a CPE represents. In the literature several different methods have been proposed, each based on specific assumptions, and each leading to different values [155–157]. This highlights the fundamental quandary at the heart of the CPE model, which is that although it is able to convincingly fit the frequency-domain response of many electrochemical systems, its physical interpretation remains a matter for debate. The RCR Model is not able to achieve such a close fit to the data, but it does produce a value for the double-layer capacitance directly, and it can be simulated using Spice.

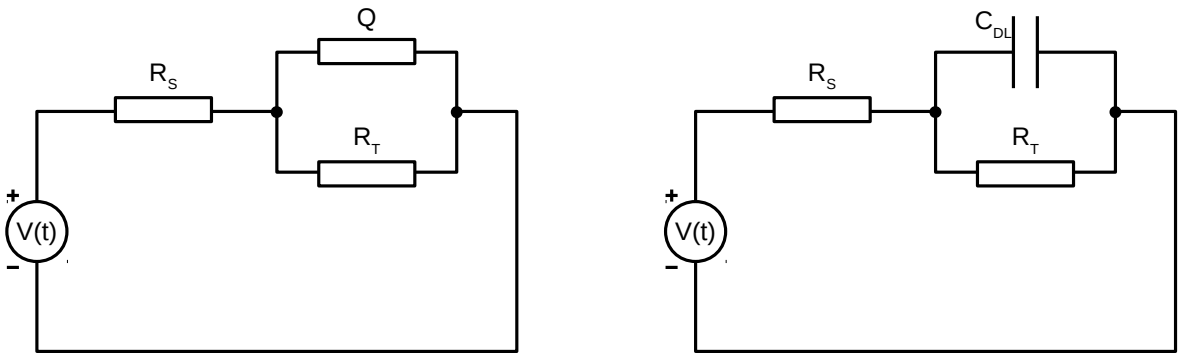

(a) RQR Equivalent Circuit Model

(b) RCR Equivalent Circuit Model

Figure 3.32: EIS equivalent circuit models. The element Q represents a constant phase element (CPE).

Therefore, although the RQR Model is more accurate, the RCR Model is of slightly greater utility.

The fitting of the equivalent circuit models to the measured EIS data was performed using Iviumsoft, the software supplied with the Ivium potentiostat. This resulted in the element values presented in Table 3.14 and the Nyquist plots in Figure 3.33. The element values from Table 3.13 have also been included so that a direct comparison can be made between the RCR equivalent circuits extracted using CV and EIS.

Element	Q	α	C_{dl}	R_S	R_T
Units	μSs^{α}		μF	Ω	Ω
EIS RQR Model	2220	0.89		1.05	560.8
Error	2.1%	2.3%		174%	4.3%
EIS RCR Model			2157	4.69	467.4
Error			2.9%	52%	2.7%
CV RCR Model			3766	343.8	743.1

Table 3.14: Best-fit values for two different equivalent circuit models to the EIS measurements presented in Figure 3.33.

Of greatest concern is that the value of R_S extracted using CV is 343.8 Ω, whereas that extracted using the EIS RCR Model is 4.69 Ω, and that using the more accurate RQR Model is just 1.05 Ω. This is a disparity of more than two orders of magnitude. A Spice simulation reveals there is also a disparity in the transient response of the EIS RCR Model, as shown in Figure 3.34. This disparity will be investigated in Section 3.4 on page 110.

3.3.8 RCR Gradient Descent Curve-Fitting Method

Since the equivalent circuit presented in Figure 3.32b consists of just three components, it can be considered to represent a point in three-dimensional space. If at all such points a cost

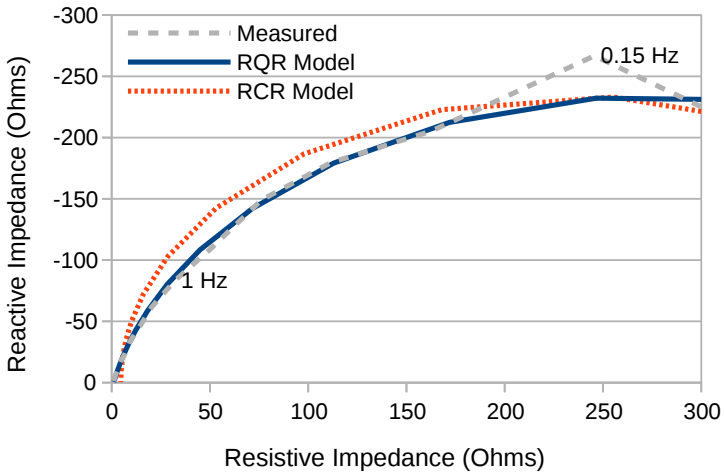

Figure 3.33: Comparative Nyquist plots between the measured data and two different equivalent circuit models for electrode Paddle #35.
Frequency range: 0.1 Hz to 10 kHz; bias voltage: −0.55 V.

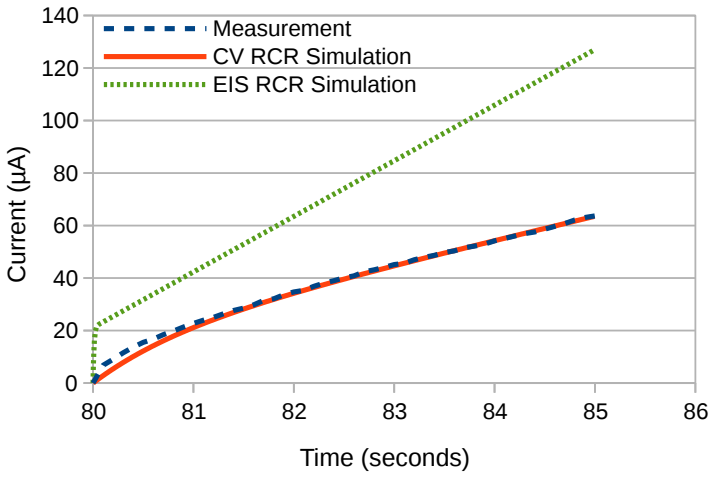

Figure 3.34: Comparison of measurement data and a Spice simulation of the EIS RCR parameters in Table 3.14.

function is defined as the sum of the squares of the difference between the measured waveform and a Spice simulation of the corresponding equivalent circuit, a three-dimensional field is constructed through which standard gradient descent methods can be used to find the optimal equivalent circuit.

This provides an alternative method for transient equivalent circuit fitting to the analytical method presented in Section 3.3.6. This avoids the somewhat arbitrary application of the weighting functions, although it does depend on the descent not getting trapped in localised minima. The existence of such minima depends on the overall shape and consistency of the cost function, which is hard to visualise in 3-dimensions.

In practice it is difficult to restrict the path of the descent to remain exclusively within

the region corresponding to positive values of resistance and capacitance, and although it is possible to perform Spice simulations of negative resistance, it is impossible to simulate negative capacitance. Therefore, as an expedient the descent is performed within 'logspace', whereby the point x is defined as:

$$x_n = \begin{bmatrix} \log_{10}(R_1) \\ \log_{10}(R_2) \\ \log_{10}(C) \end{bmatrix} \tag{3.111}$$

which restricts the values of R_1, R_2 and C to positive values. In addition, it makes it computationally simpler to calculate the gradient of the cost function at, for example, low values of capacitance, which would otherwise be very close to the axis. An analogous space to the (R_1, R_2, C) logspace is one based on (E, F, T) values, for example:

$$z_n = \begin{bmatrix} \log_{10}(E) \\ \log_{10}(F) \\ \log_{10}(T) \end{bmatrix} \tag{3.112}$$

where E, F and T are as defined in Equation 3.91 on page 97, and correspond to the ramp-rate, step-size and exponential decay time-constant respectively. Note there is no no need to include an extra degree of freedom for G, since it is constrained to be equal to $-F$.

This solution space is possible because the location of point x_n can at all times be calculated from the location of point z_n (and the constant β) using Equations 3.106 to 3.110 and *vice versa*. It can be argued that solution space z is more intuitive, since each axis corresponds to an identifiable feature of the waveform. Therefore the effect of progressing in a particular direction in z-space on the resultant waveform can be more easily conceptualised.

Whichever solution space is used, it is possible to define various cost functions F_n of x_n (or z_n), for example:

$$I_{diff}(t) = I_{sim}(x_n, t) - I_{meas}(t) \tag{3.113}$$

$$F_1(x_n) = \log_{10}\left(\text{AVERAGE}\left[I_{diff}^2\right]\right) \tag{3.114}$$

$$F_2(x_n) = \log_{10}\left(\text{AVERAGE}\left[I_{diff}^2 \times \frac{dI_{diff}}{dt}^2\right]\right) \tag{3.115}$$

$$F_3(x_n) = \log_{10}\left(\text{AVERAGE}\left[I_{diff}^2 \times \frac{dI_{diff}}{dt}^2 \times \frac{d^2 I_{diff}}{dt^2}^2\right]\right) \tag{3.116}$$

where $I_{meas}(t)$ is the measured current waveform, and $I_{sim}(x_n, t)$ is the Spice simulation of the equivalent circuit corresponding to the proposed point x_n. The objective of incorporating derivatives of I_{diff} into the cost functions is to potentially improve the fit along sloped and

curved sections of the waveform.

The differential of the cost function, $\nabla F(x_n)$, is defined as:

$$\nabla F(x_n) = \begin{bmatrix} \left[F(x_n + [\delta,0,0]^T) - F(x_n - [\delta,0,0]^T)\right]/2\delta \\ \left[F(x_n + [0,\delta,0]^T) - F(x_n - [0,\delta,0]^T)\right]/2\delta \\ \left[F(x_n + [0,0,\delta]^T) - F(x_n - [0,0,\delta]^T)\right]/2\delta \end{bmatrix} \tag{3.117}$$

where δ is a constant that is chosen to be much smaller than the granularity of the cost function, but not so small that it challenges the floating point accuracy of the computer performing the calculations. A value of $\delta = 0.005$ was found to be a good compromise. This vector is generated from six Spice simulations, and could therefore be computationally expensive. It is fortunate therefore that a Spice simulation of a circuit with just three active components is extremely quick. Furthermore, an actual Spice simulation is unnecessary since the full analytical solution is known, and can therefore be coded in software.

The descent algorithm is defined as:

$$x_{n+1} = x_n - \gamma \nabla F(x_n) \tag{3.118}$$

where γ is a suitably chosen step size, which changes from step to step according to the Barzilai-Borwein method [158]:

$$\gamma_n = \frac{|(x_n - x_{n-1})^T [\nabla F(x_n) - \nabla F(x_{n-1})]|}{\|\nabla F(x_n) - \nabla F(x_{n-1})\|^2} \tag{3.119}$$

Localised Minima In the course of analysing the 5-second window of measured current waveform delineated by the vertical dashed lines in Figure 3.28 on Page 99, it was discovered that the end-point of the gradient descent varied depending on the starting point. This is a sign that the solution space contained multiple localised minima, which can render gradient descent methods time-consuming, unreliable and ineffective.

The minima can be difficult to visualise in three dimensions, but the task becomes easier in z space since it is clear from inspection of Figure 3.29 on page 99 that the value of E should be approximately 9 µA s^{-1}. Therefore a plot of F and T at constant E should reveal the location of the cost-function minimum, and whether there are any local minima surrounding it. When this was performed using cost-function F_3 as defined in Equation 3.116, the results were as shown in Figure 3.35a, and they confirmed the existence of several minima, and helped to explain why gradient descent methods struggled with this dataset.

Experimental signal processing of the dataset confirmed that the best method to reduce or eliminate the localised minima was to employ a combination of linear and Gaussian interpolation, as shown in Figure 3.35b. The explanation for this is that each of the localised minima occurs when the cost-function for the waveform corresponding to a point in $[E, F, T]$

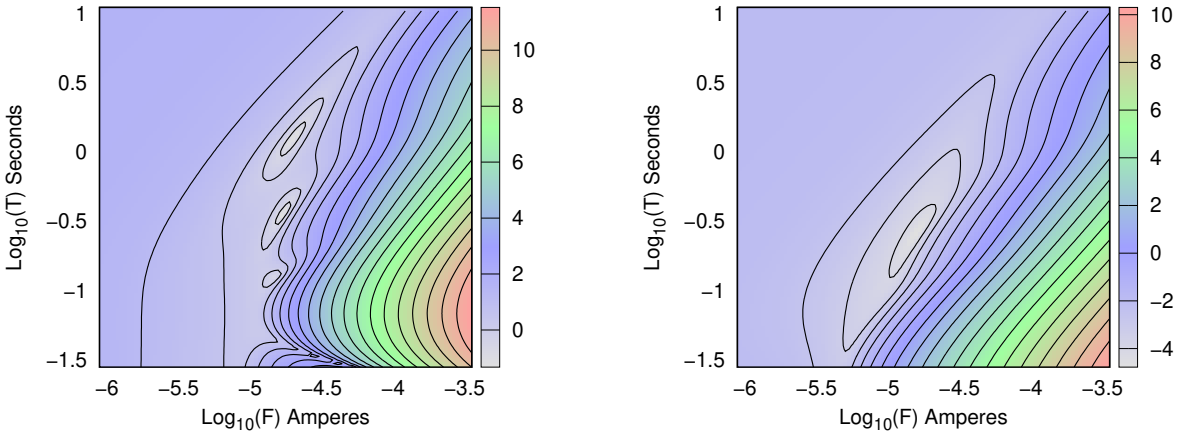

(a) Raw data

(b) After linear and Gaussian interpolation

Figure 3.35: Cross-section showing the cost function in the $[E, F, T]$ solution space at $E = 9\,\mu\mathrm{A\,s}^{-1}$. The small number of samples in the raw data results in many localised minima, thereby preventing gradient descent methods finding the correct global minimum. The incorporation of a small amount of linear and Gaussian interpolation reduces the number of minima to one.

solution space experiences an excessive amount of attraction to one or more measurement datapoints, and is thus incorrectly shaped to permit traversal to a more optimal solution. For example, the waveforms corresponding to two of the localised minima in Figure 3.35a are as shown in Figure 3.36.

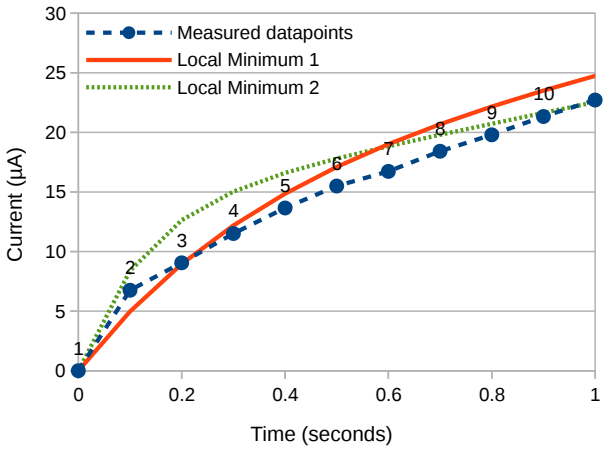

Figure 3.36: Waveforms corresponding to two of the localised minima in Figure 3.35a. The descent algorithm is unable to traverse between them because the waveforms are excessively attracted to individual measurement datapoints. Therefore, gradient descent can be facilitated by the artificial creation of addition datapoints.

The waveform corresponding to Local Minimum 1 (solid orange line) passed close to

datapoint number 3, whereas that for Local Minimum 2 (dotted green line) passed close to datapoint number 2. The creation of additional datapoints using interpolation permitted the descent algorithm to escape from Local Minimum 2 and traverse to the optimal solution. The remarkably small degree of interpolation that was required to achieve this can be assessed in Figure 3.37.

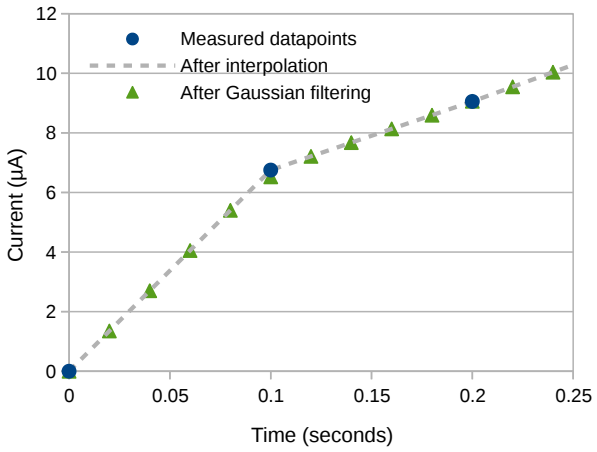

Figure 3.37: Signal processing of the original measured current datapoints using 5× interpolation and then convolution with a 3-point Gaussian filter.

By experimentation it was discovered that it was sufficient to increase the number of datapoints by a factor of five using linear interpolation, and then to convolve with a Gaussian filter consisting of just 3 points. Such a filter reduced the sudden change in slope that was associated with purely linear interpolation, and permitted the rounded analytical waveform to more easily traverse the solution space without encountering barriers due to excessive waveform angularity.

Signal-processing therefore provided a useful set of techniques for assisting gradient descent when it would otherwise not occur. Nevertheless, it is likely that it is in nearly all cases advisable to produce better measurement datasets in the first place.

The final best-fit parameter values generated by gradient descent were as presented in Table 3.15, and a Spice simulation of the resulting RCR-network is as presented in Figure 3.38.

Element	C_{dl}	R_S	R_T
Units	µF	Ω	Ω
Values from Analytical Fitting Method	3766	343.8	743.1
Values from Gradient Descent Method	2301	207.2	798.9

Table 3.15: Values of C_{dl}, R_S and R_T generated by Spice simulation gradient descent.

In comparison with the values generated by analytical fitting, the gradient descent method has produced a lower value for the double-layer capacitance. This has resulted in

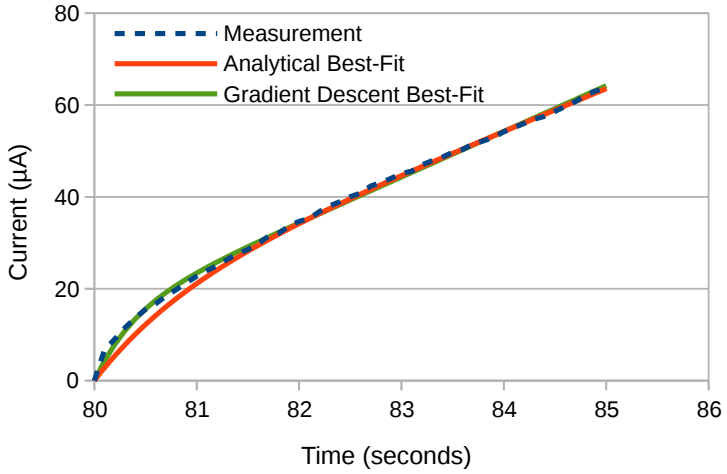

Figure 3.38: Comparison of measurement data and Spice simulations of the best-fit component values from Table 3.13 generated by Analytical Best-Fit and Table 3.15 generated by Gradient Descent.

a simulation which is much closer to the measured data. It therefore appears that gradient descent is a more accurate technique, particularly within the first second. The value of the double-layer capacitance C_{dl} generated by gradient descent (2301 µF) is also a close match to that produced by EIS (2157 µF). However, the value of the series resistance (207.2 Ω) is not a close match to that produce by EIS (0.98 Ω). This reason for this disparity will be investigated in the next section.

3.4 Combined ECSA/EIS

(The work on which the remainder of this chapter is based was accepted for publication in the International Journal of Hydrogen Energy in June 2020 [159])

The CV results for a smooth, TiN-coated 316-grade stainless-steel electrode were as presented in Figure 3.39. Upon each change of direction, the current waveform was observed to consist of a curved RC-type response which decayed to a ramp after several seconds. For this waveform, the RCR network equivalent circuit shown in Figure 3.32a on page 104 was fitted using the gradient-descent method within a 5-second window, as highlighted by the dashed grey rectangles. This ensured that approximately half the window contained a curved response, and half a linear response, a situation which was found to give the best trade-off between competing best-fit parameters. For other waveforms the window was chosen as appropriate.

The simulation of the best-fit RCR network was as presented as the dashed orange line in Figure 3.39b. Note that the current has been normalised to begin at 0 A, and that the cathodic waveform has been inverted so that it can be overlaid. The corresponding parametric values

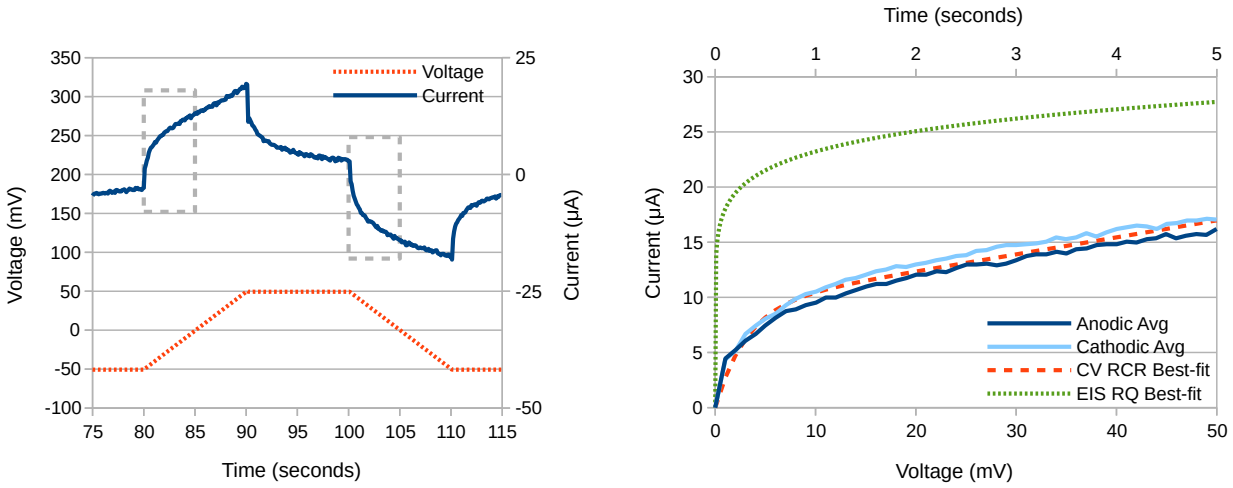

(a) Measured waveforms

(b) Overlaid view of dashed rectangles

Figure 3.39: Cyclic Voltammetry results for a smooth, TiN-coated 316-grade stainless-steel electrode at $10\,\mathrm{mV\,s^{-1}}$ showing (a) the unprocessed measurements and (b) the detail overlaid view of the dashed rectangles, where the current has been normalised to begin at 0 A, together with the responses of the best-fit RCR and RQR networks.

for each sweep are as presented in Table 3.16. The match between the observed response and that of an RCR network was quite close, which suggests that it was an appropriate equivalent circuit. However, the inferred series resistance (R_S) of 320 Ω is misleading, since no such resistance exists.

Parameter	β	**E**	**F**	**T**	$\mathbf{R_S}$	$\mathbf{R_T}$	$\mathbf{C_{DL}}$
Units	$\mathrm{mV\,s^{-1}}$	$\mathrm{\mu A\,s^{-1}}$	µA	ms	Ω	Ω	µF
Anodic 1	10.0	1.57	8.76	275	299	6070	964
Cathodic 1	10.0	1.57	9.95	325	311	6060	1100
Anodic 2	10.0	1.54	8.48	295	330	6160	941
Cathodic 2	10.0	1.50	9.84	352	340	6330	1090
Average		**1.55**	**9.26**	**312**	**320**	**6150**	**1020**

Table 3.16: Best-fit values of an RCR network to the observed waveforms for the TiN-coated electrode in Figure 3.39. β is the voltage ramp rate. E, F and T are as defined in Equation 3.91 on page 97, and correspond to the ramp-rate, step-size and exponential decay time-constant.

The EIS measurements for the same electrode were as presented in Figure 3.40. The RQR network equivalent circuit shown in Figure 3.32b on page 104 was fitted to these results using IviumSoft, with the best-fit parameters as presented in Table 3.17. Since the measurements were conducted around OCP, the resulting value of the transfer resistance R_T was very high at 13 kΩ. This is so high that it can be ignored, with the equivalent circuit thereby reducing to just an RQ network. Significantly, the R_S value obtained from EIS was just 0.83 Ω, which is more than 350 times smaller than that obtained from CV curve-fitting.

Parameter	R_S	Q_{DL}	α	R_T
Units	Ω	$S\,s^{\alpha}$		kΩ
Value	0.83	0.0022	0.89	13

Table 3.17: Best-fit values of an RQR network to the observed waveforms for the TiN-coated electrode in Figure 3.40.

The solid line on the Nyquist plot (Figure 3.40a) shows 'constant-phase element' (CPE) behaviour, where at progressively lower frequencies the trace maintains a constant phase angle relative to the origin. At other values of bias voltage (away from OCP) this produces the classic 'flattened-semicircle' that is characteristic of many electrochemical systems [122, 149–154]. The response of the RQ network is shown as the dotted green lines in Figure 3.40, and produces a very close match to the observed data.

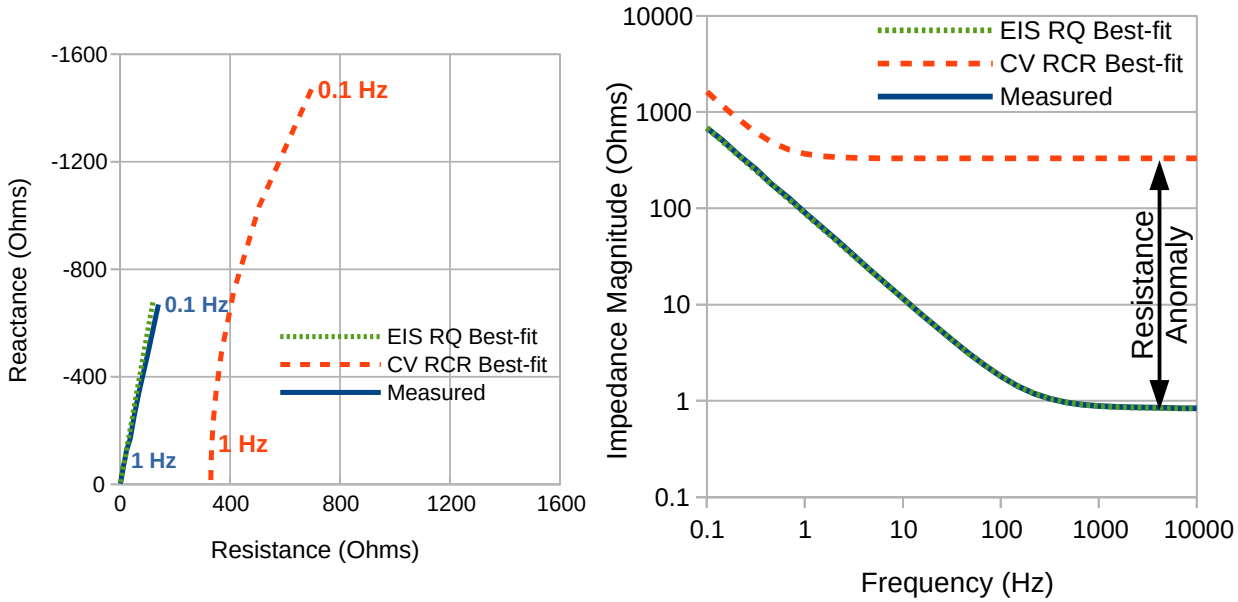

(a) Nyquist plot

(b) Bode Magnitude plot

Figure 3.40: EIS measurements for the TiN-coated electrode presented in Figure 3.39, together with the responses of the best-fit RCR and RQR models.

It is also possible to simulate the RQ network in the time domain to produce its transient response using the method presented in Section 3.4.5 on page 126. When this was done, the result was as shown as the dotted green line in Figure 3.39b. This produced a poor match, particularly within the first few milliseconds, where the response of the RQ network is almost vertical. This is not surprising, since the pseudo-time-constant of the RQ network (R times Q) is just 1.8 ms. However, thereafter the RQ network produced a much slower exponential decay that is similar to the CV measurement.

By performing an *RCR Gradient Descent Best-fit* on the segment of this waveform from 20 ms onwards, so as to exclude the vertical section, a time-constant of 299 ms was measured

by curve-fitting. This is similar to the value of 312 ms presented in Table 3.16. This curve-fitting also produced an apparent series resistance of 369 Ω, which is similar to the value of 320 Ω from Table 3.16. It thus appears that a single RQ network is able to match the EIS and CV results, but it does so by presenting *two different time-constants*.

The size of the apparent resistance mismatch is more clearly illustrated by the frequency response of the CV RCR best-fit, which is presented as the dashed orange lines in Figure 3.40. The Nyquist plot shows that the RCR network is constrained to produce a semicircle, since it is comprised of ideal resistors and capacitors. The resistance mismatch appears at high frequencies on the Bode magnitude plot in Figure 3.40b (hereafter referred to as the 'Resistance Anomaly' or R_A), which amounts to more than two orders of magnitude.

The Resistance Anomaly has been consistently observed across a wide variety of electrodes, whether coated or uncoated, used or unused, smooth or high surface area and porous. Furthermore, its magnitude has been observed to vary in inverse proportion to the roughness factor, as presented in Figure 3.41.

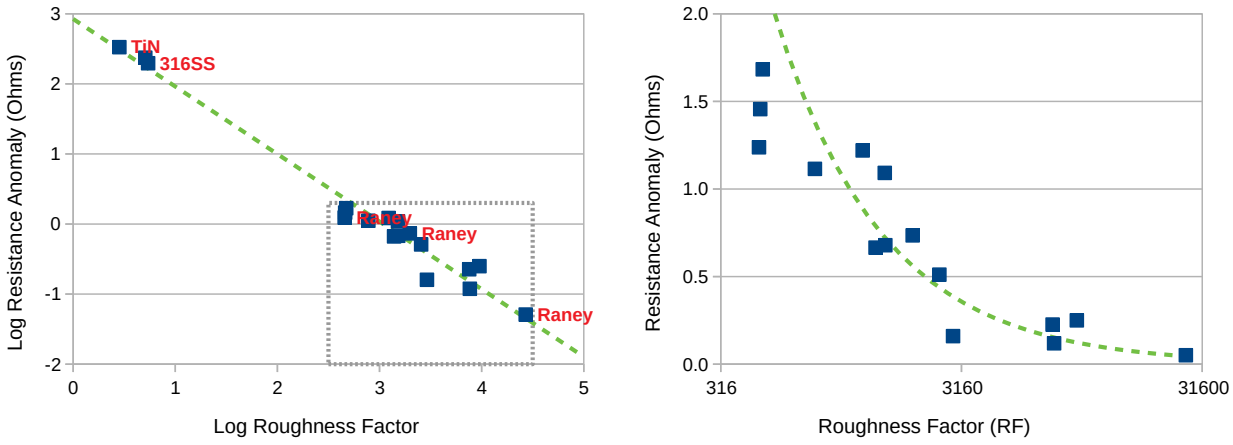

(a) Best-fit on log-log plot

(b) Detail view of dotted rectangle on lin-log plot

Figure 3.41: Plot of Resistance Anomaly (R_A) *versus* roughness factor (RF) for various coated and uncoated electrodes.

The results show a direct relationship between R_A and RF on a log-log plot that extends over 4 orders of magnitude. Figure 3.41b presents a detail view of the dotted box with one linear axis, to highlight how R_A tends to zero as RF increases. The slope of the line in Figure 3.41a is -0.964, which is close to -1. This implies an inverse relationship, specifically:

$$R_A = \frac{759\,\text{m}\Omega\,\text{m}^2}{A \cdot RF} \tag{3.120}$$

where 759 mΩ m^2 is an average figure generated across the complete set of electrodes. This figure will be independent of electrode area and the distance between working and reference electrodes.

Although the RQ network is able to match some of the electrode behaviour observed using CV in Figure 3.39b, it is hereby proposed that a better match could be achieved using a 5-component model.

3.4.1 RCRCR Network: Derivation of response to a voltage ramp.

The addition of an extra RC-network to the Randles equivalent circuit produces the circuit shown in Figure 3.42a, and for the s-domain as shown in Figure 3.42b.

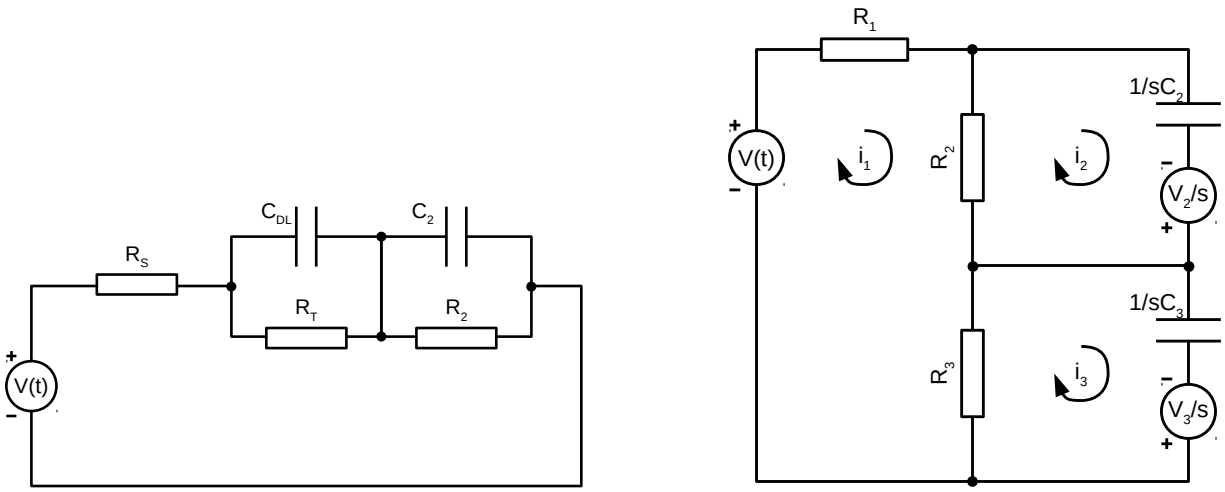

(a) Extended Randles electrical equivalent circuit

(b) As redrawn in s-domain

Figure 3.42: Equivalent circuit for the electrode/electrolyte interface extended to include an additional RC network.

The results of performing mesh-current analysis on the rearranged circuit are the following three equations:

$$R_1 i_1 + R_2(i_1 - i_2) + R_3(i_1 - i_3) = V(t) \tag{3.121}$$

$$\frac{i_2}{sC_2} + R_2(i_2 - i_1) = \frac{V_2}{s} \tag{3.122}$$

$$\frac{i_3}{sC_3} + R_3(i_3 - i_1) = \frac{V_3}{s} \tag{3.123}$$

Assuming that the charge on the capacitors at time $t = 0$ is 0 V, which means that $V_2 = V_3 = 0$, equations 3.122 and 3.123 can be rewritten as:

$$i_2 = \left(\frac{s}{s + \omega_2}\right) i_1 \tag{3.124}$$

$$i_3 = \left(\frac{s}{s + \omega_3}\right) i_1 \tag{3.125}$$

where $\omega_2 = \frac{1}{R_2C_2}$ and $\omega_3 = \frac{1}{R_3C_3}$. Substituting equations 3.124 and 3.125 into equation 3.121 produces:

$$(R_1 + R_2 + R_3)i_1 - R_2\left(\frac{s}{s+\omega_2}\right)i_1 - R_3\left(\frac{s}{s+\omega_3}\right)i_1 = \frac{\beta}{s^2}$$

$$\left[\frac{(R_1 + R_2 + R_3)\,(s+\omega_2)\,(s+\omega_3) - R_2 s\,(s+\omega_3) - R_3 s\,(s+\omega_2)}{(s+\omega_2)\,(s+\omega_3)}\right] i_1 = \frac{\beta}{s^2}$$

$$\left[R_1 s^2 + [(R_1 + R_2)\omega_2 + (R_1 + R_3)\omega_3]\,s + (R_1 + R_2 + R_3)\omega_2\omega_3\right] i_1 = \beta\frac{(s+\omega_2)(s+\omega_3)}{s^2}$$

where β/s^2 is the Laplace transform of the driving voltage waveform, which is defined as a ramp starting at time $t = 0$ with slope β measured in $\mathrm{V\,s^{-1}}$. If it is assumed that the left side can be factored, this can be rewritten as:

$$i_1 = \beta\frac{(s+\omega_2)(s+\omega_3)}{s^2(s+\alpha_1)(s+\alpha_2)} \tag{3.126}$$

where $-\alpha_1$ and $-\alpha_2$ are the roots of the quadratic equation $as^2 + bs + c$, such that:

$$\alpha_1 = \frac{b - \sqrt{b^2 - 4ac}}{2a} \tag{3.127}$$

$$\alpha_2 = \frac{b + \sqrt{b^2 - 4ac}}{2a} \tag{3.128}$$

$$\text{where} \quad a = R_1 \tag{3.129}$$

$$b = (R_1 + R_2)\omega_2 + (R_1 + R_3)\omega_3 \tag{3.130}$$

$$\text{and} \quad c = (R_1 + R_2 + R_3)\omega_2\omega_3 \tag{3.131}$$

The condition for the existence of (real) solutions to the quadratic ($b^2 >= 4ac$) has been investigated numerically and found to be generally true, but efforts to demonstrate this mathematically have not proved successful. It is expected to be true, since any arbitrary network of resistors and capacitors cannot produce oscillatory behaviour. The inverse Laplace transform of Equation 3.126 will produce the analytical time-domain solution $i_1(t)$. To do this, the denominator must be expanded into its individual terms, such that:

$$\beta\frac{(s+\omega_2)(s+\omega_3)}{s^2(s+\alpha_1)(s+\alpha_2)} = \frac{E + Fs}{s^2} + \frac{G}{s+\alpha_1} + \frac{H}{s+\alpha_2}$$

where E, F, G and H are constants. With reference to Table 3.11 on page 97 it is informative to note that the solution is equal to the sum of a ramp, a step, and *two* exponential decays, and will therefore be of the form:

$$i_1(t) = Et + F + G\exp(-\alpha_1 t) + H\exp(-\alpha_2 t) \tag{3.132}$$

The constants E through H must be chosen such that, by the rules of partial fractions, they produce the original numerator, specifically:

$$\begin{aligned}(E+Fs)(s+\alpha_1)(s+\alpha_2)+Gs^2(s+\alpha_2)+Hs^2(s+\alpha_1)&=\beta(s+\omega_2)(s+\omega_3)\\(F+G+H)s^3+(E+F(\alpha_1+\alpha_2)+G\alpha_2+H\alpha_1)s^2+&\\(E(\alpha_1+\alpha_2)+F\alpha_1\alpha_2)s+E\alpha_1\alpha_2&=\beta\left[s^2+(\omega_2+\omega_3)s+\omega_2\omega_3\right]\end{aligned}$$

which produces four simultaneous equations for the matching terms in s^3, s^2, s and units:

$$F+G+H=0 \tag{3.133}$$

$$E+F(\alpha_1+\alpha_2)+G\alpha_2+H\alpha_1=\beta \tag{3.134}$$

$$\begin{aligned}E(\alpha_1+\alpha_2)+F\alpha_1\alpha_2&=\beta(\omega_2+\omega_3)\\E\alpha_1\alpha_2&=\beta\omega_2\omega_3\end{aligned}$$

multiplying equation 3.133 by α_1 and subtracting from equation 3.134 produces:

$$E+F\alpha_2+G(\alpha_2-\alpha_1)=\beta$$

therefore E, F, G and H can be calculated in the sequence:

$$E=\frac{\beta\omega_2\omega_3}{\alpha_1\alpha_2} \tag{3.135}$$

$$F=\frac{\beta(\omega_2+\omega_3)-E(\alpha_1+\alpha_2)}{\alpha_1\alpha_2} \tag{3.136}$$

$$\begin{aligned}G&=\frac{\beta-E-F\alpha_2}{\alpha_2-\alpha_1}\\H&=-(F+G)\end{aligned}$$

Example Let the component values of the equivalent circuit be assigned as follows: $R_1 = 1\,\Omega$, $R_2 = 237\,\Omega$, $C_2 = 1830\,\mu\text{F}$, $R_3 = 4180\,\Omega$, $C_3 = 1830\,\mu\text{F}$. The calculation of the response

will therefore proceed as follows:

$$\omega_2 = 2.306\,\text{Hz} \qquad \omega_3 = 0.1307\,\text{Hz}$$
$$a = 1 \qquad b = 1095$$
$$c = 1332 \qquad b^2 - 4ac = 1194427$$
$$\alpha_1 = 1.217\,\text{Hz} \qquad \alpha_2 = 1094\,\text{Hz}$$
$$E = 2.263\,\mu\text{A}\,\text{s}^{-1} \qquad F = 16.43\,\mu\text{A}$$
$$G = -7.304\,\mu\text{A} \qquad H = -9.130\,\mu\text{A}$$

With reference to Equation 3.132, the analytical response of the 5-component circuit to a voltage ramp of $10\,\text{mV}\,\text{s}^{-1}$ can therefore be plotted, as presented in Figure 3.43a. The figure includes the results of a Spice simulation, which serve to verify that the two methods are in agreement. The detail view of the first 10 ms in Figure 3.43b confirms the presence of an initial rapid exponential decay, which is followed by a slower decay that takes several seconds. The plot is therefore exhibiting the *bi-exponential* behaviour predicted from the analytical solution.

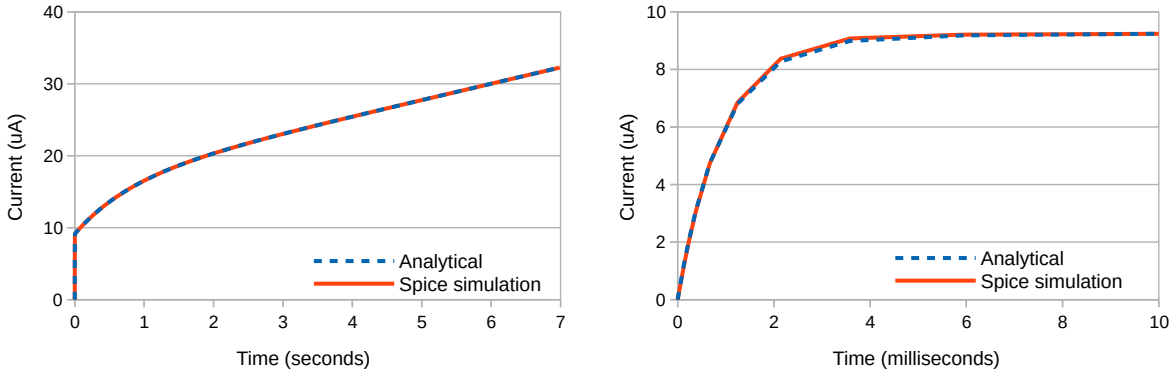

(a) Full view

(b) Detail view of the first 10 ms

Figure 3.43: Transient response of a 5-component extended Randles equivalent circuit to a voltage ramp.

3.4.2 Simplification if solution resistance is small

If R_1 is small compared to both R_2 and R_3, then the definitions of b and c can be simplified to:

$$b \approx R_2\omega_2 + R_3\omega_3 = 1/C_2 + 1/C_3 = 1/C_{23}$$
$$c \approx (R_2 + R_3)\omega_2\omega_3 = \frac{R_2 + R_3}{R_2R_3C_2C_3} = \frac{1}{R_{23}C_2C_3}$$

where $C_{23} = C_2 \parallel C_3$ and $R_{23} = R_2 \parallel R_3$. This means that $b^2 - 4ac$ becomes:

$$b^2 - 4ac = \left(\frac{1}{C_{23}}\right)^2 - \frac{4R_1}{R_{23}C_2C_3} \tag{3.137}$$

which, if R_1 is small, becomes just b^2, which in turn means that Equation 3.127 becomes:

$$\alpha_2 \approx \frac{b + \sqrt{b^2}}{2a} = \frac{b}{a} = \frac{1}{R_1C_{23}} \tag{3.138}$$

This means that the time-constant of the fast exponential decay is $\approx R_1C_{23}$, or the combination of the solution resistance R_S and the two capacitances in series. This is understandable, since initially both capacitors are discharged (or at equilibrium) and their resistance is low. However, they quickly adopt voltages which resist further current conduction, and a slower charging process ensues. To calculate the second time-constant, it is helpful to rewrite the square root as a binomial expansion:

$$(1 + x)^n = 1 + \frac{n}{1!}x + \frac{n(n-1)}{2!}x^2 + \dots$$

therefore Equation 3.128 becomes:

$$\alpha_1 = \frac{b - b\left[1 - \frac{4ac}{b^2}\right]^{1/2}}{2a}$$
$$= \frac{b - b\left[1 - \frac{1}{2}\frac{4ac}{b^2} - \frac{1}{4}\left(\frac{4ac}{b^2}\right)^2 - \dots\right]}{2a}$$

Ignoring all but the first and second terms of the expansion, this simplifies to:

$$\alpha_1 \approx \frac{c}{b} = \frac{1}{R_{23}(C_2 + C_3)} \tag{3.139}$$

This means that the time-constant of the slow exponential decay is $\approx R_{23}(C_2 + C_3)$. This makes sense, since it is a time-constant derived from the two RC-networks combined. The

ratio of the two time-constants is therefore equal to:

$$\frac{\alpha_2}{\alpha_1} = \frac{R_{23}(C_2 + C_3)}{R_1 C_{23}}$$

For any given values of C_3, R_1, R_2 and R_3, this reaches a minimum where $C_2 = C_3$ of:

$$\frac{\alpha_2}{\alpha_1} = \frac{4R_{23}}{R_1}$$

therefore, regardless of the relative values of capacitance, the ratio of the two time-constants will always be large if R_1 is small compared with both R_2 and R_3.

3.4.3 RCRCR Network: Measurable quantities

Given that one of the time-constants for the two exponential decays is so rapid, it is unlikely that it can be accurately measured using CV. Similarly, given that the other time-constant is so slow, it is unlikely that it can be accurately measured using EIS. However, if it is possible to accurately measure the fast time-constant using EIS, and the slow one using CV, information gained from both the time and frequency domains could be combined to obtain a solution.

Accurate measurements can also be obtained for E (the current ramp rate), R_1 (the solution resistance) and the sum of G and H (the magnitude of the two exponential decays added together). From Equation 3.133 it is seen that:

$$G + H = -F$$

therefore the sum of G and H actually provides the value of F. Hence the measurable parameters are:

$$\alpha_1, \alpha_2, E, R_1 \text{ and } F$$

Given that there are five components in the RCRCR network, this means that it should be possible to determine the values of all five. This is assuming that the five measurable parameters are sufficiently independent, and that the solution space is suitably shaped and unambiguous.

From inspection of Equations 3.127 and 3.128, it can be seen that:

$$\alpha_1 \alpha_2 = \frac{c}{a} \qquad \text{and} \qquad \alpha_1 + \alpha_2 = \frac{b}{a}$$

Therefore the definition of E from Equation 3.135 may be rewritten as:

$$E = \beta\omega_2\omega_3\frac{a}{c}$$

$$E = \beta\omega_2\omega_3\left[\frac{R_1}{(R_1+R_2+R_3)\omega_2\omega_3}\right]$$

$$\text{therefore} \quad R_2 + R_3 = k_1 \tag{3.140}$$

$$\text{where} \quad k_1 = \frac{\beta}{E}R_1 - R_1 = R_1\left(\beta/E - 1\right) \tag{3.141}$$

where the definitions of a and c from Equations 3.129 and 3.131 have been used. Since all of the quantities on the right hand side are measurable, this means that if R_2 is known, then R_3 can be calculated, which immediately reduces the size of the solution space by one dimension. Assuming R_1 is small, and given that $C_{23} = C_2 \parallel C_3$, the simplified definition of α_2 from Equation 3.138 can be rewritten as:

$$C_2C_3R_1\alpha_2 = C_2 + C_3$$

$$\text{therefore} \quad C_3 = \frac{C_2}{k_2C_2 - 1}$$

$$\text{where} \quad k_2 = \alpha_2R_1$$

which means that if C_2 is known, then C_3 can be calculated. Given that R_1 is measurable, this means that the potentially five-dimensional solution space has been reduced to just two dimensions. The definition of F from Equation 3.136 describes another of the measurable quantities, and can be rewritten as:

$$\frac{1}{R_2C_2} + \frac{1}{R_3C_3} = \frac{F\alpha_1\alpha_2 + E(\alpha_1+\alpha_2)}{\beta}$$

$$\text{therefore} \quad R_2C_2 + R_3C_3 = k_3R_2C_2R_3C_3$$

$$\text{where} \quad k_3 = [F\alpha_1\alpha_2 + E(\alpha_1+\alpha_2)]/\beta$$

The final measurable quantity, α_1, can be incorporated by rewriting Equation 3.139 as:

$$R_{23}(C_2 + C_3) = 1/\alpha_1$$

$$\text{therefore} \quad R_2R_3(C_2 + C_3) = k_4$$

$$\text{where} \quad k_4 = k_1/\alpha_1$$

This produces four simultaneous equations with four unknowns:

$$R_2 + R_3 = k_1 \tag{3.142}$$
$$C_3 = C_2/(k_2C_2 - 1) \tag{3.143}$$
$$R_2C_2 + R_3C_3 = k_3R_2C_2R_3C_3 \tag{3.144}$$
$$R_2R_3(C_2 + C_3) = k_4 \tag{3.145}$$

$$\text{where} \quad k_1 = R_1\,(\beta/E - 1)$$
$$k_2 = \alpha_2 R_1$$
$$k_3 = [F\alpha_1\alpha_2 + E(\alpha_1 + \alpha_2)]/\beta$$
$$k_4 = k_1/\alpha_1$$

and where two of the pairs of unknowns are directly related. All parameters k_n are defined solely in terms of measurable parameters. It therefore looks feasible to solve the above equations and (in combination with R_1) to determine all of the component values in the electrical equivalent circuit. However, attempts to solve the above equations analytically produced a quartic equation, therefore numerical and graphical methods were employed.

3.4.4 Application

Inspection of the analytical solution of the 5-component RCRCR network, as presented in Equation 3.132 on page 115, predicts that the time-domain response will be the sum of a ramp, a step, and two exponential decays. It may therefore be able to exhibit the same sort of *bi-exponential* behaviour exhibited by the RQ network in Figure 3.39b on page 111, whereby a rapid exponential decay is followed by a slower one.

Whilst the measured data in the figure show some evidence of this, it is much clearer in later waveforms recorded for the same electrode after a small amount of active gas evolution, as presented in Figure 3.44. Note in the detail view that the current jumps quickly from 0 to 15 µA, and thereafter climbs more slowly, thereby indicating the presence of two time-constants. The EIS measurements are as presented in Figure 3.45.

From the EIS results the value of R_1 is determined by measuring the point of closest approach to the origin at high frequency, and the value of α_2 is determined by measuring the position of the main breakpoint. This is defined as the frequency (in radians per second) at which the impedance magnitude reaches $\sqrt{2}R_1$, and is highlighted by the vertical dashed line in Figure 3.45b. The values of E, F and T were determined using RCR-network gradient descent curve fitting, as performed at *https://fitting.gannon.me.uk*. For curves exhibiting a bi-exponential decay, more accurate values of E, F and T were measured by offsetting the measurement window by two sample points (100 ms), with the values measured as presented in Table 3.18. An estimate of the value of H (taken from the second sample point)

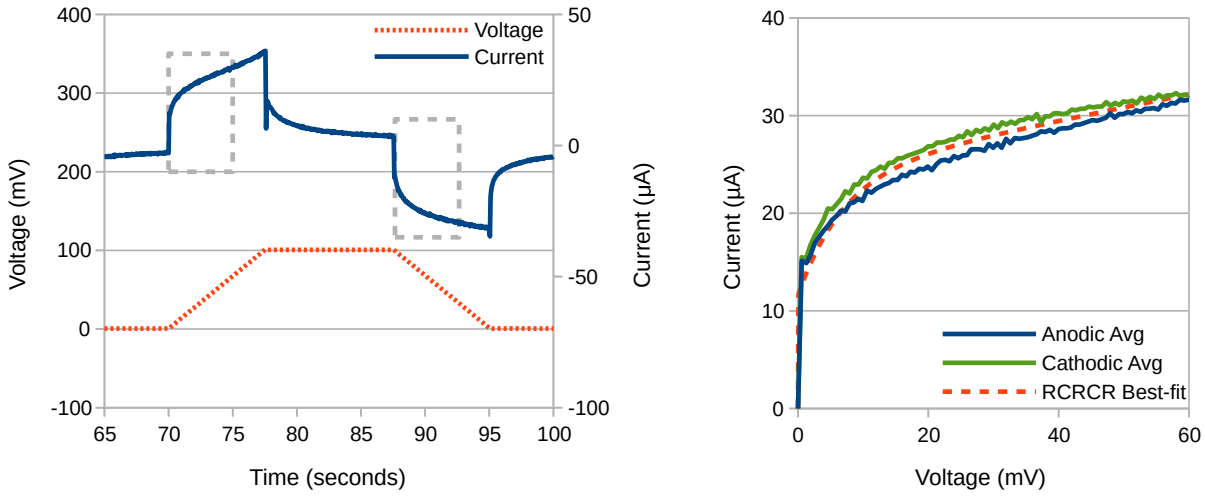

(a) CV

(b) CV Detail View

Figure 3.44: CV measurements obtained for the TiN-coated 316SS electrode in Figure 3.39 after active gas evolution. Figure (a) presents the CV data as recorded, and Figure (b) presents overlaid voltammograms of the dashed grey boxes. EIS bias voltage: 0 V; CV sweep rate: 13.3 mV s^{-1}; Electrolyte: 0.5 M NaOH at laboratory temperature.

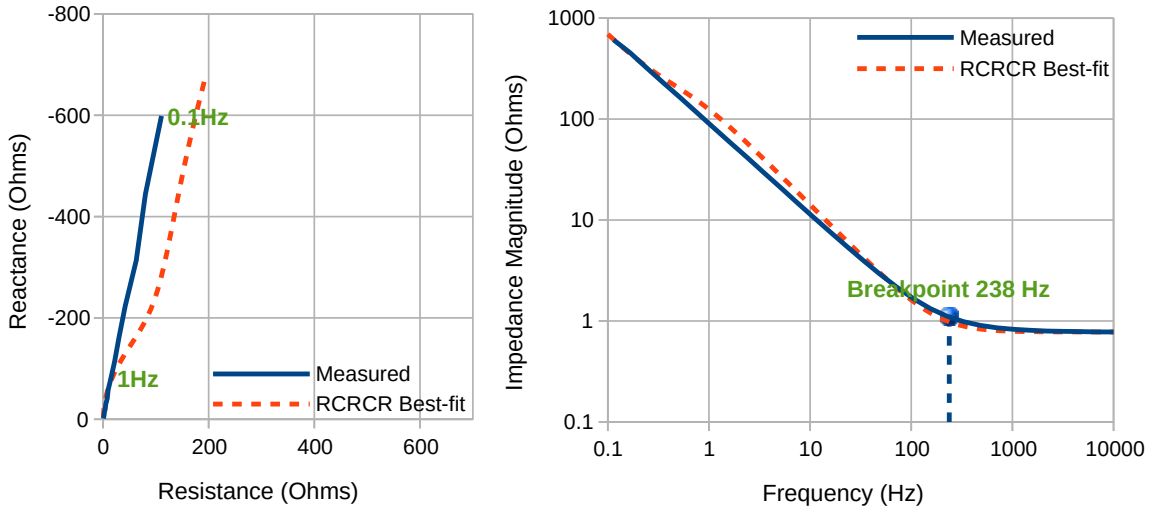

(a) EIS Nyquist Plot

(b) EIS Bode Magnitude

Figure 3.45: EIS measurements obtained for the TiN-coated 316SS electrode in Figure 3.39 as (a) a Nyquist plot and (b) a Bode magnitude plot, from which the breakpoint frequency can be determined. The response of the best-fit RCRCR network to these data is included as a dashed orange line.

was added to the fitted value of F to generate an overall target value of F, as shown in the bottom row of the table.

Using the measured values, and employing the simplification that $R_1 \ll R_2$ and R_3, it is possible to explore the resulting two-dimensional solution space using a suitable cost

Parameter	R_1	α_2	β	E	H	F	T
Units	Ω	rad s^{-1}	mV s^{-1}	µA s^{-1}	µA	µA	ms
Anodic 1			13.3	2.11	-15.0	$7.45 - H$	493
Cathodic 1			13.3	1.52	-15.5	$10.4 - H$	561
Anodic 2			13.3	2.11	-15.2	$7.54 - H$	483
Cathodic 2			13.3	1.49	-15.7	$10.4 - H$	548
Average	**0.778**	**1494**	**13.3**	**1.81**	**-15.3**	**24.3**	**521**

Table 3.18: Measurable parameters determined for the TiN-coated electrode presented in Figures 3.44 and 3.45.

function, as presented in Figure 3.46. In this case the cost-function chosen was:

$$
\begin{aligned}
err_1 &= R_2C_2 + R_3C_3 - k_3R_2C_2R_3C_3 \\
err_2 &= R_2R_3(C_2 + C_3) - k_4 \\
cost &= \log(err_1^2 \times err_2^2)
\end{aligned}
$$

which is derived directly from Equations 3.144 and 3.145. This technique identifies the values of R_2 and C_2 which constitute the best-fit to the EIS and CV data, as highlighted by the black circle. Since R_1 is already known, and (in the simplified solution space) R_3 can be calculated from R_2, and C_3 from C_2, this therefore identifies the full best-fit 5-element RCRCR network, as presented in Table 3.19 in the column headed '2D Values'.

Cross-checking the values of E and F produced by the 2D best-fit 5-element network using Equations 3.135 and 3.136 reveals that this procedure produces a value of F that is too small. Its transient response is therefore a poor match to the measured CV waveform, and this can be attributed to the over-simplification of the solution space to two-dimensions. Nevertheless, the 2D best-fit can be used as a starting point from which to employ conventional gradient descent within the full four-dimensional solution space. It should be noted that because the curvature of the solution space is not conducive to gradient descent, it is observed that the use of a random starting point does not succeed in finding a solution.

Parameter	2D Values	4D Values
R_1	0.778 Ω	0.778 Ω
R_2	237 Ω	118 Ω
C_2	800 µF	2100 µF
R_3	5490 Ω	5610 Ω
C_3	1500 µF	2420 µF

Table 3.19: Best-fit values obtained for the 5-element equivalent circuit model matching the measurement data presented in Figures 3.44 and 3.45. Column 2 presents the values obtained within the simplified two-dimensional solution space, and column 3 those obtained after using column 2 as a starting point for full four-dimensional gradient descent.

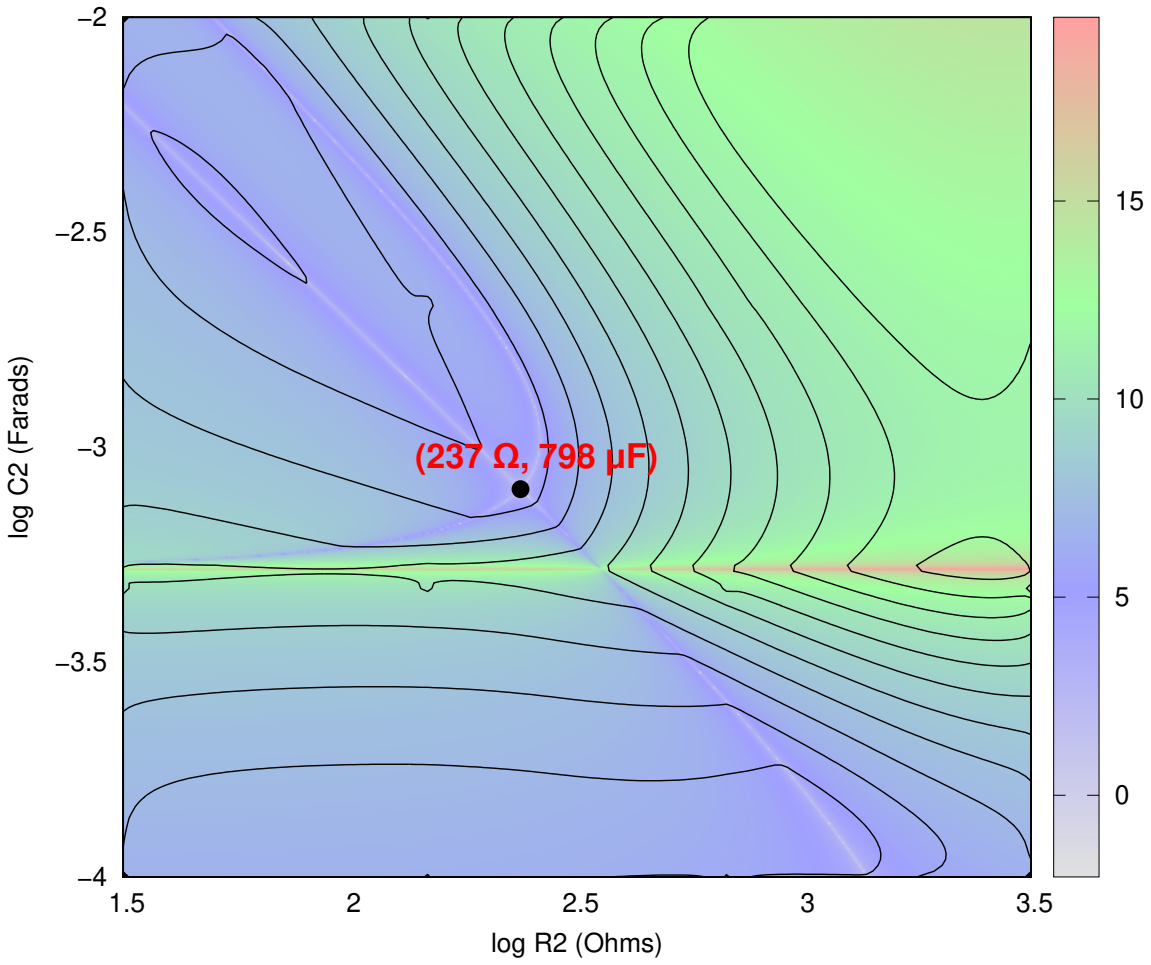

Figure 3.46: Plot of cost function for the simplified two-dimensional solution space, based on the assumption that $R_1 \ll R_2$ and R_3. The above point of best match is then used as the starting point for conventional four-dimensional gradient descent.

The values produced for the 5-element equivalent electrical circuit as a result of four-dimensional gradient descent are as presented in Table 3.19 in column '4D Values'. The descent algorithm used was Barzilai-Borwein, and the cost function was defined as:

$$cost = \log\left([\log(E/E_T)]^2 + [\log(F/F_T)]^2 + [\log(\alpha_1/\alpha_{1T})]^2 + [\log(\alpha_2/\alpha_{2T})]^2\right)$$

where E_T, F_T, α_{1T} (which equals $1/T_T$) and α_{2T} are the target measurable values from Table 3.18. These gradient-descent values constitute the best-known fit to the data.

The '4D Values' from Table 3.19 are also presented as column 'Electrode 1' of Table 3.20. The time-domain response of this network is included as the dashed orange line in Figure 3.44, and the frequency domain response in Figure 3.45. From these it can be seen that the

equivalent circuit is now accurately modelling the measured behaviour of the electrode.

Parameter	Electrode 1	Electrode 2	Electrode 3
RF	2.8	472	7556
R_S	0.778 Ω	0.913 Ω	0.946 Ω
R_T	5610 Ω	101 Ω	4.53 Ω
C_{DL}	2420 µF	185 mF	2.96 F
R_2	118 Ω	0.803 Ω	0.134 Ω
C_2	2100 µF	232 mF	4.56 F

Table 3.20: Best-fit values obtained for the 5-element equivalent circuit model matching the measurement data presented in Figures 3.44 and 3.45 (Electrode 1), as well as two other electrodes with much larger roughness factors.

The table also includes the RCRCR best-fit parameters for two other electrodes with widely varying Roughness Factors. A progression can be seen across the table, which can be more easily visualised in Figure 3.47a. From this figure it can be seen that the values of R_T, C_{DL}, R_2 and C_2 are linearly related, which implies that they are not independent phenomena. To investigate this, a CV experiment was repeated with and without vigorous pumped circulation of the electrolyte, with the results as presented in Figure 3.47b. The results confirm that the measurements are unaffected by pumped circulation, and therefore do not arise as a result of bulk movements of the electrolyte, such as diffusion.

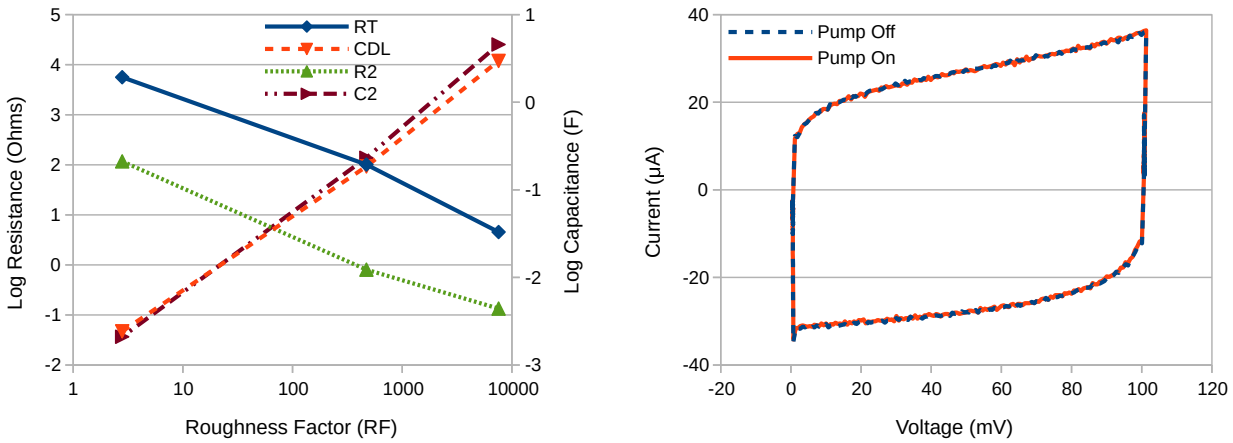

(a) Trends *versus* RF

(b) Effect of pumped circulation

Figure 3.47: a) Trends in the RCRCR best-fit parameters as a function of roughness factor for the three electrodes presented in Table 3.20. b) Cyclic voltammograms of the TiN electrode with and without vigorous pumped circulation of the electrolyte. The pumping has no discernible effect.

3.4.5 Constant Phase Element: Transient Simulation

Although it is possible for the five-component RCRCR network to exhibit bi-exponential behaviour, and therefore match some of the behaviour of an RQ network, it would still be desirable to simulate an RQ network directly. The Q represents a constant phase element (CPE) which has an impedance given by:

$$Z(\omega) = \frac{1}{Q}\left[\frac{1}{(j\omega)^{\alpha}}\right] \tag{3.146}$$

where Q is the magnitude of the CPE, and α is its argument, such that $0 \leq \alpha \leq 1$. A Warburg element is therefore simply a CPE where the argument is equal to 0.5.

$$Z(\omega) = \frac{1}{Q}\left[\frac{1}{\sqrt{j\omega}}\right] \tag{3.147}$$

It is possible to simulate this in the time domain using work published by Athanasiou *et al.*, who reported that as a function of time, the voltage across the CPE is given by a convolution integral:

$$V_{CPE}(t) = \frac{1}{Q\Gamma(\alpha)}\int_0^t (t-u)^{\alpha-1} I(u)du \tag{3.148}$$

where $\Gamma(\alpha)$ is the gamma function [160]. It can thus be seen for an ideal capacitor (for which $\alpha = 1$) that $(t-u)^{\alpha-1} = \Gamma(\alpha) = 1$, and the equation simplifies to:

$$V_C(t) = \frac{1}{C}\int Idt \tag{3.149}$$

which can be recognised as the standard formula for a capacitor. However, Equation 3.148 provides the voltage as a function of the current, which is inconvenient in voltammetry where it is the *voltage* that is controlled and the *current* that is to be measured. Solving this involves expressing the behaviour of the electrical network as a differential equation.

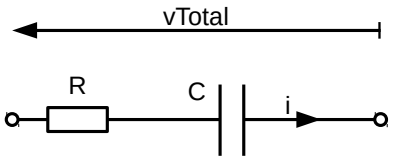

Figure 3.48: Schematic of RC Network

For example, for the basic RC network shown in Figure 3.48 the equation can be expressed as:

$$V_{Total} = \frac{dq}{dt}R + \frac{q}{C} \tag{3.150}$$

where q is electrical charge, such that $i = dq/dt$. Since q/C is equal to the voltage on the capacitor, V_C, this can be expressed more generally as:

$$V_{Total} = \frac{dq}{dt}R + V_C \tag{3.151}$$

The Euler method can be used to approximate a solution to this equation, based on the first-order simplification that:

$$q_{n+1} = q_n + h\frac{dq}{dt} \tag{3.152}$$

where h is the step size in time. Replacing the capacitor by a CPE, and therefore V_C by V_{CPE}, produces:

$$q_{n+1} = q_n + h\left(\frac{V_{Total} - V_{CPE}}{R}\right) \tag{3.153}$$

This iterative scheme can be converted into a computer program, as shown in Listing A.1 on page 262, where the language chosen was PHP. When executed, this produced the simulation results presented in Figure 3.49a.

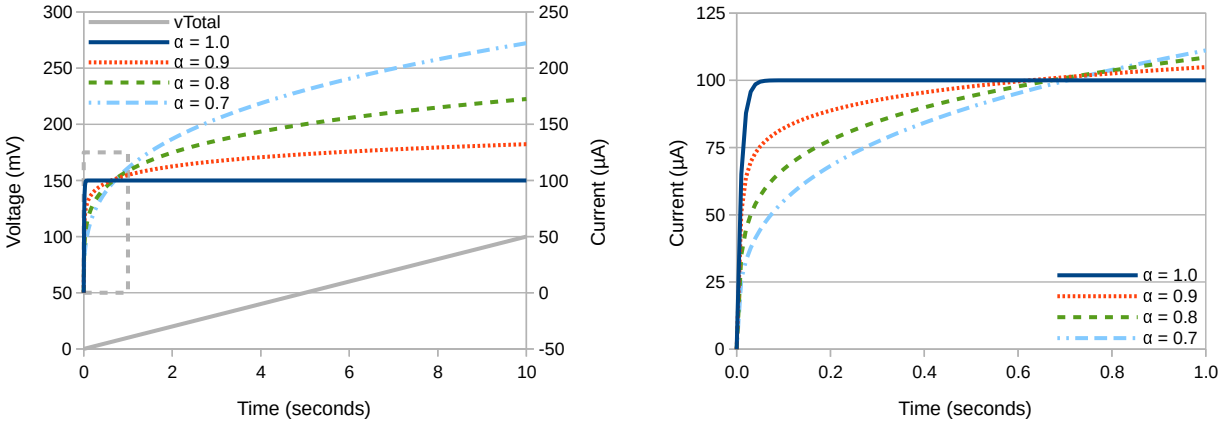

(a) Transient simulation

(b) Detail view of dashed gray box

Figure 3.49: Transient simulation of an RQ network for 4 different values of α. $R = 1\,\Omega$, $Q = 0.01$. Voltage ramp rate: $10\,\mathrm{mV\,s^{-1}}$.

The results show that as the argument α of the CPE decreases, its leakage increases, and therefore so too does the total amount of current. The asymptotic response of the circuit towards a fixed current also changes, and is instead replaced by a more curved response. The RQ network is thus able to emulate the behaviour of a much higher series resistance, even though no such resistance is present.

The detailed view of the dashed gray box in Figure 3.49b shows that when $\alpha = 1$, the current reaches the asymptotic value of 100 µA rapidly in less than 100 ms. For $\alpha = 0.9$, the response appears to be bi-exponential, so the RQ network is therefore exhibiting two separate time-constants. Irrespective of value, all traces converge after about 0.6 s. However,

the current does not asymptote towards a slope, which is the typical behaviour of an RCR network.

For an RQR network (R_1 in series, R_2 in parallel) the iterative scheme can be altered to become:

$$q_{n+1} = q_n + \frac{h}{R_1}\left(V_{Total} - \frac{R_1 + R_2}{R_2} V_{CPE}\right) \tag{3.154}$$

where q is the charge on the CPE. The total current is then:

$$i(t) = \frac{dq}{dt} + \frac{V_{CPE}}{R_2} \tag{3.155}$$

Since the function presented in Equation 3.148 is a convolution integral, it is possible to plot the convolution function, as presented in Figure 3.50. This shows that the function is flat if $\alpha = 1$, which means that none of the charge placed onto the capacitor is lost. For other values of α losses occur, for example if $\alpha = 0.7$ the convolution function states that 50% of the charge placed onto the CPE four seconds ago will have been lost. It would thus appear that the CPE has a characteristic time-constant of its own, and one that is unrelated to its magnitude or any other circuit components.

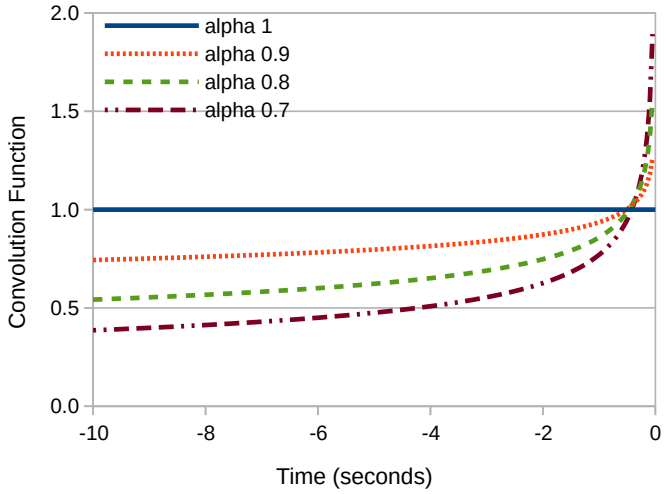

Figure 3.50: Convolution function used in the simulation of a constant phase element.

3.4.6 Computer Simulations

Simulations were conducted to determine how the response of an RQ network to a voltage ramp varies with component values. The value of the apparent time-constant as a function of the resistance R was measured using *RCR Gradient Descent Best-fit*, with the results presented in Figure 3.51a.

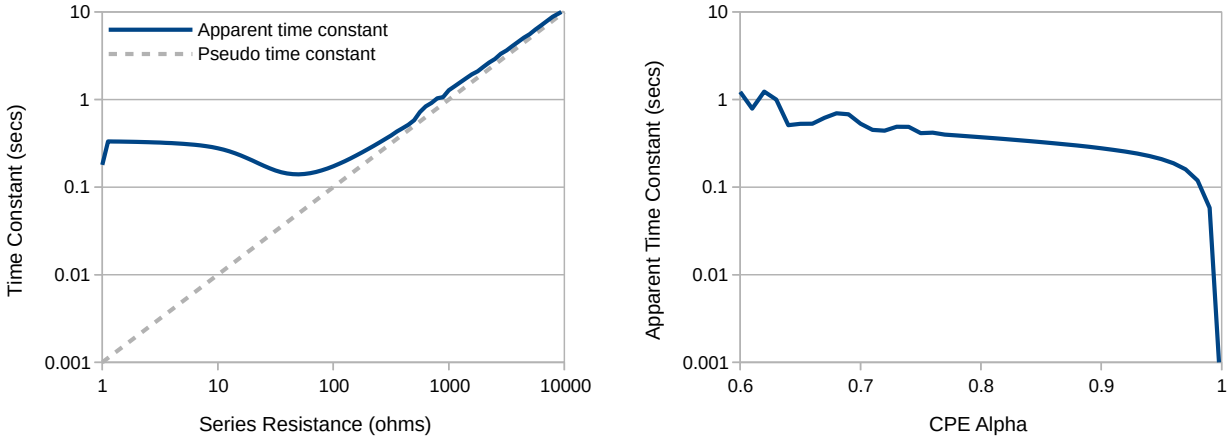

(a) Variation with R

(b) Variation with α

Figure 3.51: Observed time constants of the RQ network *versus* component values. Segment start = 0.03 s, finish = 5 s
a) $Q = 0.001$, $\alpha = 0.9$ b) $R = 1$, $Q = 0.01$

The results show that the apparent time-constant of the RQ network remains invariant until the resistance reaches about 10 Ω, such that the pseudo-time-constant of the RQ network (i.e. R times Q) equals 0.1 s. Between 10 and 100 Ω a brief reduction is observed in the apparent time-constant, which is an artefact of the curve-fitting procedure. Throughout this region the RQ network exhibits *two time-constants*: one pseudo time-constant and one apparent time-constant, for example as shown by the dotted green line in Figure 3.18b on page 86, and by the dotted orange line in Figure 3.49 on page 127. The RCR gradient descent method can only detect one of the time-constants, and consistently measures the slower of the two.

Between 100 and 10 000 Ω the RQ network exhibits just a single time-constant, which is dominated by the conventional product of resistance times (pseudo) capacitance, which is to be expected of an RC network. The cross-over between two time-constant behaviour and one time-constant behaviour occurs when the pseudo time-constant reaches 1 s. Since the shape of the transient response of the RQ network is governed by the pseudo-time-constant, the results for holding R constant and sweeping Q are identical.

The results for sweeping the value of α are as presented in Figure 3.51b. These show that the time-constant is low for a perfect capacitor ($\alpha = 1$), but increases rapidly and is then relatively constant over a wide region. This region covers the typical values of α that occur in many electrochemical experiments, and certainly all of the results published in this thesis. This means that if the first time-constant is short enough that a cyclicvoltammetry experiment fails to reveal it (for example as in Figure 3.39b on page 111), then only the second, longer time-constant will be observed. The shape of this curve is not determined by resistance at all, but solely by the constant phase element.

3.4.7 Conclusions

This section presents an accurate and reliable method for the fitting of a three-component RCR network to the measured response of an electrode during cyclic-voltammetry (CV). This method employs the analytical derivation of the time-domain response of an RCR network to a voltage ramp, calculated using Laplace transforms. Three-dimensional gradient descent was then used to obtain the best-fit solution.

The frequency response of the same electrode, measured using electrochemical impedance spectroscopy (EIS), was fitted to an RQR network using conventional electrochemistry software, where Q represents a constant phase element (CPE). Since all measurements were conducted around OCP, the value of the transfer resistance was large and could be discounted, thereby simplifying to an RQ network.

Comparison of the best-fit RCR and RQ networks revealed an apparent resistance anomaly, which could amount to several hundred ohms (Figure 3.40b on page 112). It was observed across a wide variety of electrodes that the resistance anomaly was inversely proportional to the roughness factor (RF) of the electrode, where the RF was proportional to the double-layer capacitance.

A simplified method was developed to simulate the transient-response of an RQ network to a voltage ramp, with example code presented in the PHP programming language. Inspection of this response reveals that a single RQ network is able to exhibit *bi-exponential* behaviour, with two separate time-constants (Figures 3.39b on page 111 and 3.44b on page 122). Such behaviour was also observed experimentally (Figure 3.44a), although not consistently.

This observation is therefore able to explain the apparent existence of the resistance anomaly, which arises because in practice the RCR gradient descent method measures the second time-constant of the RQ network. As shown by computer simulation (Figure 3.51a on page 129) this second time-constant is *invariant* for low values of the pseudo-time-constant (those below 1 s), which is typical in electrochemical cells containing normal high-conductivity electrolyte. Since C is known to vary, but the time-constant (R times C) is fixed, the illusion is thus created that R is inversely proportional to C (Figure 3.41b on page 113).

A five-component RCRCR model was then proposed, with a fitting procedure based on measurable quantities derived from both the time-domain and frequency-domain measurements. This method employs the analytical derivation of the time-domain response of an RCRCR network to a voltage ramp, calculated using Laplace transforms. The method then makes uses of four-dimensional gradient descent to obtain the best-fit solution, with a mathematical simplification and a two-dimensional plot providing the starting point.

This five-component network produces the most accurate fit to the observed results, even though it does not contain a constant-phase element. One of the component values is fixed and equal to the solution resistance, and the values of the other four are observed to vary

linearly with electrode roughness factor (Figure 3.47a on page 125). This suggests that the fitting procedure is not revealing any new information about the electrode/electrolyte interface. This is because any constant-phase element (such as the double-layer capacitance) can be expanded into an infinite series of parallel RC networks, where the component values of each RC network are a fixed percentage of the previous [161]. The RCRCR network can thus be regarded as the first expansion of an RQ network into an infinite R(CR) network.

The most surprising and unexpected finding is that a single RQ network is able to exhibit bi-exponential behaviour, based on two time-constants. One of these is proportional to the product of R and Q (the pseudo time-constant), but the other is fixed at approximately 0.3 s. Within limits, this time-constant is not a function of any of the three component values of the network i.e. R, Q or α, but emerges directly from the mathematical derivation (Figure 3.50 on page 128). It therefore appears to be an invariant property of the constant phase element itself, and one that has been consistently verified by experimental observation.

Chapter 4

Titanium Nitride

> Since satellite measurements began
> 40 years ago, the Arctic has lost
> 10,000 tonnes of sea ice —
> every second.
>
> *Professor Tore Furevik*
> *University of Bergen*

(The work on which this chapter is based was published by the author in the journal *MDPI Processes* in February 2019 [162])

4.1 Introduction

Titanium Nitride has many properties that make it a good candidate to consider as a coating for electrodes for water-splitting electrolysis [163], including that it:

- is extremely hard ($\sim 20\,\mathrm{GPa}$),
- has a high melting point (2950 °C),
- has unusually high electrical conductivity for a ceramic ($4\,\mathrm{MS\,m^{-1}}$),
- has high thermal conductivity ($\sim 2\,\mathrm{W\,m^{-1}\,K^{-1}}$),
- is chemically stable,
- has good erosion and corrosion resistance.

In addition to its properties, it lends itself conveniently to application as a smooth, homogeneous coating using Physical Vapour Deposition (PVD) onto a wide variety of materials, such as metals, ceramics and some plastics. In combination with its golden appearance, this has led to its widespread use as a decorative coating on innumerable objects, from scissors

and shock-absorbers to light-fittings. Anywhere in fact where it is desired to make something look as though it is made of gold. However, TiN has many less frivolous uses, for example by extending the lifetime of expensive cutting tools and injection moulds, or for use in refractories, cermets and crucibles [164].

Its use as a protective and/or decorative coating means that many commercial services are available, whereby objects can be coated with TiN by return of post. From an academic point of view, this means that research can be conducted quickly using off-the-shelf components. This can in turn be of great benefit to the wider scientific community, since any findings can be quickly verified and improved upon by competing groups. On the other hand, it could also be argued that the precise details of the coating procedure remain locked behind commercial secrecy, which limits the ability to optimise the coating.

Nevertheless, should the properties of TiN combine with a low overpotential for either the hydrogen or oxygen gas evolution reactions, then it could constitute an important scientific breakthrough, and is therefore extremely worthy of research.

The literature reports that in 1987, Milosev1997 *et al.* published a study of the electrochemical and thermal oxidation of titanium, zirconium and chromium nitride coatings at pH 5. The detailed XPS analysis revealed a two-step oxidation reaction for both TiN_x and ZrN_x, first to a mixture of oxynitride/oxide, then at higher potentials to just oxide. In 1988, Azuma *et al.* reported on the differences between niobium, zirconium, titanium and vanadium nitrides for OER under both acidic and alkaline conditions. It was found that NbN_x and ZrN_x produced surface oxidised layers that remained thin (a few nm or less) even after prolonged OER. By contrast, TiN_x produced an oxidised layer which continued to grow extensively, whereas VN_x dissolved. This was attributed to the lower activation energy for the oxidation of Ti and V nitrides [165]. In 2016 Gebauer *et al.* published a study of titanium oxynitrides for OER in acidic conditions, and similarly concluded that the electrode current "results from oxidation of the electrode surface rather than from O_2 evolution", and that "increasing nitride contents were found to increase the electrochemical electrode oxidation reaction" [166].

In 2012, Wirth et al. published a study of 18 different transition metal carbides, nitrides, sulphides, silicides and borides for HER in 0.1 M H_2SO_4. For TiN at 20 mA cm^{-2} they observed an overpotential of 825 mV, compared with just 201 mV for platinum [167]. Similarly, in 2012 Su et al. reported that the overpotential [*sic*] of TiN 'nanocubes' in 0.5 M H_2SO_4 was 0.54 V *vs* SCE at an extrapolated current density of 1 A cm^{-2}, compared to approximately 10 mV for platinum. However, to the knowledge of the author the literature says little about the performance of TiN for HER in *alkaline* conditions, and nothing at all about its performance after long-term *intermittent* ageing.

Accelerated Ageing: Electrode lifetime is often studied and reported within the scientific literature by employing constant currents, which are arguably of limited applicability in the field of renewable energy capture. The inherent intermittency of such sources is recognised to play a significant role in the breakdown of electrocatalysts, particularly ones involving nickel [138]. Therefore, to achieve rapid ageing, it was desired not only to subject the electrodes to large total quantities of current, but also to the destructive on-off cycling caused by the episodic nature of renewable energy. A regime was devised that consisted of 2 minutes on, followed by 2 minutes under open-circuit conditions, permitting the electrodes enough time to both fully charge and discharge within each cycle, applying the corrosive stress on each change of phase. Room-temperature electrolysis is chosen because it is more applicable to renewable energy applications, where the demands of intermittency mean that permanent heating of the electrolyte is unsustainable.

4.2 Experimental set-up

In order to assess whether TiN coated electrodes constitute an improvement over uncoated 316-grade stainless-steel electrodes, it was first necessary to create a reliable experimental set-up in which they could be tested. A protocol was decided early on that consisted of 2000 cycles of 2 minutes on 2 minutes off, which amounted to 6 days. This required a set-up which was able to operate reliably for days, which created various challenges.

4.2.1 Displacement tube

A displacement tube was constructed using acrylic tubes as shown in Figure 4.1, the design of which had been developed by previous researchers. The device was able to store up to 1.5l of H_2 without generating a pressure differential across the gas-separation membrane. However, given the long-term nature of these experiments, no gas was collected.

4.2.2 Pumps

Initially peristaltic pumps were used to gently circulate the electrolyte (as pictured). However, it was discovered that these would often stop rotating after several days, resulting in a ruined experiment. The two pumps were thus replaced by a single, low-cost d.c. brushless pump. This arrangement circulated the electrolyte more quickly, even after the voltage was reduced by more than a factor of two, but had the benefit of being much more reliable.

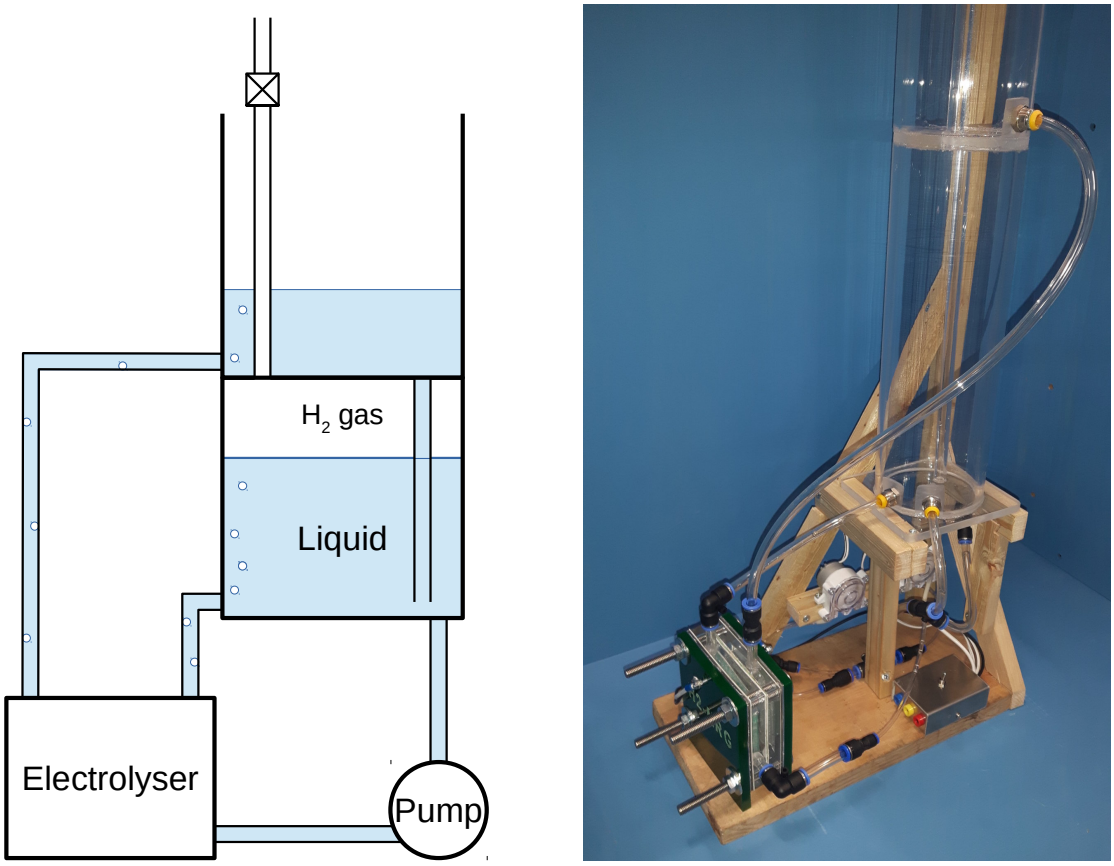

(a) Schematic diagram (b) As constructed

Figure 4.1: The long-term experimental set-up based around a vertical displacement tube

4.2.3 Leaks

A slow drip that is quite acceptable over an experiment lasting a few hours is a different matter over six days, and several experiments were lost. In addition, although electrolyte can be topped up daily, such disruptions inevitably result in unsatisfactory discontinuities in the recorded datasets, therefore a fully leak-proof set-up was paramount to the quest of obtaining publishable results.

Leaks from the gas-separation membrane were a particular issue. A domestic cleaning cloth (Jeyes) was initially used, sandwiched between two gaskets of silicone rubber, however it was quickly found that this arrangement was quite prone to leakage. Therefore, the cloth membrane was replaced with Zirfon, which was an improvement, but it too is prone to lateral leakage. This is because it is constructed of a relatively soft, spongey material (a mixture of polymer and zirconium oxide) surrounding a hard woven mesh (made of polyphenylene sulphide). This means that even when firmly clamped, internal cavities remain between the soft and hard materials along which leakage can occur.

Even if the Zirfon could be clamped firmly enough to prevent leakage all the way to the edge of the electrolyser (a distance of 2 cm), there remained an internal exit route via the

bolt-holes, which only required a few millimetres of lateral leakage. This was not helped by the low tolerance of the laminated acrylic sheets, one of which was found to vary in thickness by 3 mm. In addition, being made of metal, the bolts could in theory short-circuit the electrolyser. This risk would be much higher in a bipolar stack containing many cells in series, where there could be many tens of volts across the length of the bolts.

Laser-cutting operations on acrylic tend to leave a 'lip' on all edges, due to melting of the material, which can be removed by careful filing. However, drilling operations cause 'dips' in the material which can't, along which leakage can occur. In general, the low melting point of acrylic, which is what makes it suitable for laser-cutting in the first place, was found to cause problems for many other operations (particularly sawing).

It was also discovered that the repeated high clamping forces required to reduce Zirfon leakage disturbed the bonding of the solid connecting tubes, with the result that previously reliable connections would then leak. These joints were produced by first applying Tensol 12 glue to the solid tube, and then inserting it into the hole. Inevitably, much of the glue was left behind. In addition, much like any other glue, the unused Tensol 12 in the container became much thicker with age. As a result, any method of joining acrylic that relied on 'flowing' the glue became impossible.

An alternative to solid tubes are threaded push-fit connectors. These appear to be a better solution, but have their own problems, most significant of which is that the force required to turn the tap into the acrylic is quite likely to split it. Certainly, a tap cannot be driven into the edge of a sheet, therefore only end-on connections to the electrolyser are possible, which introduces clamping issues, since they are competing to occupy the same space.

As a rule, pipe threads (such as British Standard Pipe or BSP) are tapered (BSPT), so that leaks can be eliminated by tightening the joint. However, this is not possible with acrylic, since the material will split. As a result, parallel threads (BSPP) must be used, but in practice these are limited for use with through holes, since blind holes would require several tapping operations (taper-tap and plug-tap) otherwise the acrylic will split. Given these design restrictions, and the extra time, effort and care that tapping operations into acrylic require, it was decided to stay with glued solid tube connections. The biggest downside of solid tube connections is that they are easily broken off by careless handling, however should this happen it is quite possible to drill them out and replace them.

4.2.4 Solutions

The lateral leakage of the Zirfon was solved by using 3 silicon gaskets instead of two, as shown in Figure 4.2. The reduced extent of the Zirfon sheet means that it no longer reaches all the way to the edge of the electrolyser, or to the bolt holes. The edges of the Zirfon are thus surrounded on all sides by silicone rubber, and all routes for leakage are fully contained.

This solution was found to be leak-proof, required lower clamping forces, and is suitable for any similar cell. In addition, it was discovered that the burning of the Zirfon and silicone rubber sheets could be minimised by reducing the laser-cutter power by a factor of ten, before completing the cuts with a scalpel.

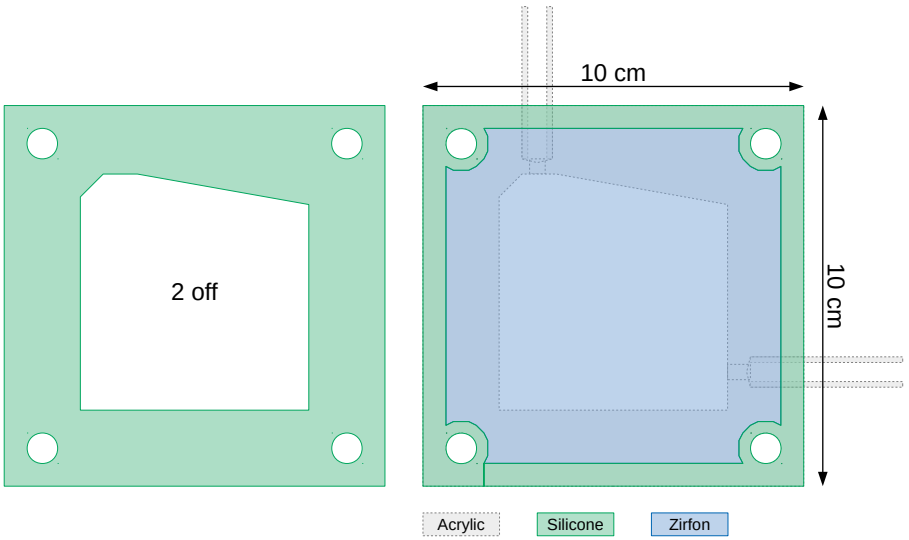

Figure 4.2: Redesigned Zirfon gas-separation membrane with surrounding silicone rubber gaskets to prevent leaks

The issue of leakage and/or short-circuit along the bolt-holes was first solved by using heat-shrink tubing. This is a common item in electronic engineering, and designed to produce reliable electrical isolation. However, it was easily torn, and did not last. A better solution was found by reducing the size of the bolts to 6 mm. This produced a snug fit inside 8 mm polyethylene tubing, which in turn produced a snug-fit inside the bolt-holes if these were drilled to 8.5 mm. Since 6 mm bolts of such length are not a standard item, threaded bar was used instead.

The issue of leakage from the solid connecting tubes was solved by glue injection. By drilling one or more 4 mm holes at right angles to the connecting socket, glue could be injected into the joint with the solid tube in place, using a standard laboratory syringe. This technique could be used to expel the air and thus fill the joint with glue, in a way that was much less affected by its viscosity. In this way, 8 mm solid tubes were successfully installed into the edge of acrylic sheets only 10 mm thick.

Injected glue within the joint could sometimes block the tube, but since the bottom surface of the socket was produced by drilling, this could be reduced by first mounting the solid tube in a pedestal drill and filing a chamfer onto the end of roughly the same angle. In any case, the blockage could be drilled out using a 5.5 mm drill.

4.2.5 Unsolved problems

The pneumatic fittings that were used to make all of the connections were prone to eventual failure, after several months. This would occur by splitting along the injection moulding ridge. The same sort of failure was observed to occur with the brushless d.c. pumps, where the inlet or outlet hose-tail would become weak and eventually perforate. It is therefore concluded that many common plastics are not able to withstand more than a few weeks of continuous exposure to room temperature NaOH at concentrations of 1 M or more. It is believe that careful component selection could solve this problem, given sufficient time.

4.2.6 Dual-test station

Later experiments were conducted on a dual long-term test station, as shown in Figure 4.3. This station was able to perform two ageing experiments simultaneously, freeing up the potentiostat and attendant PC, which on occasions were receiving a lot of use.

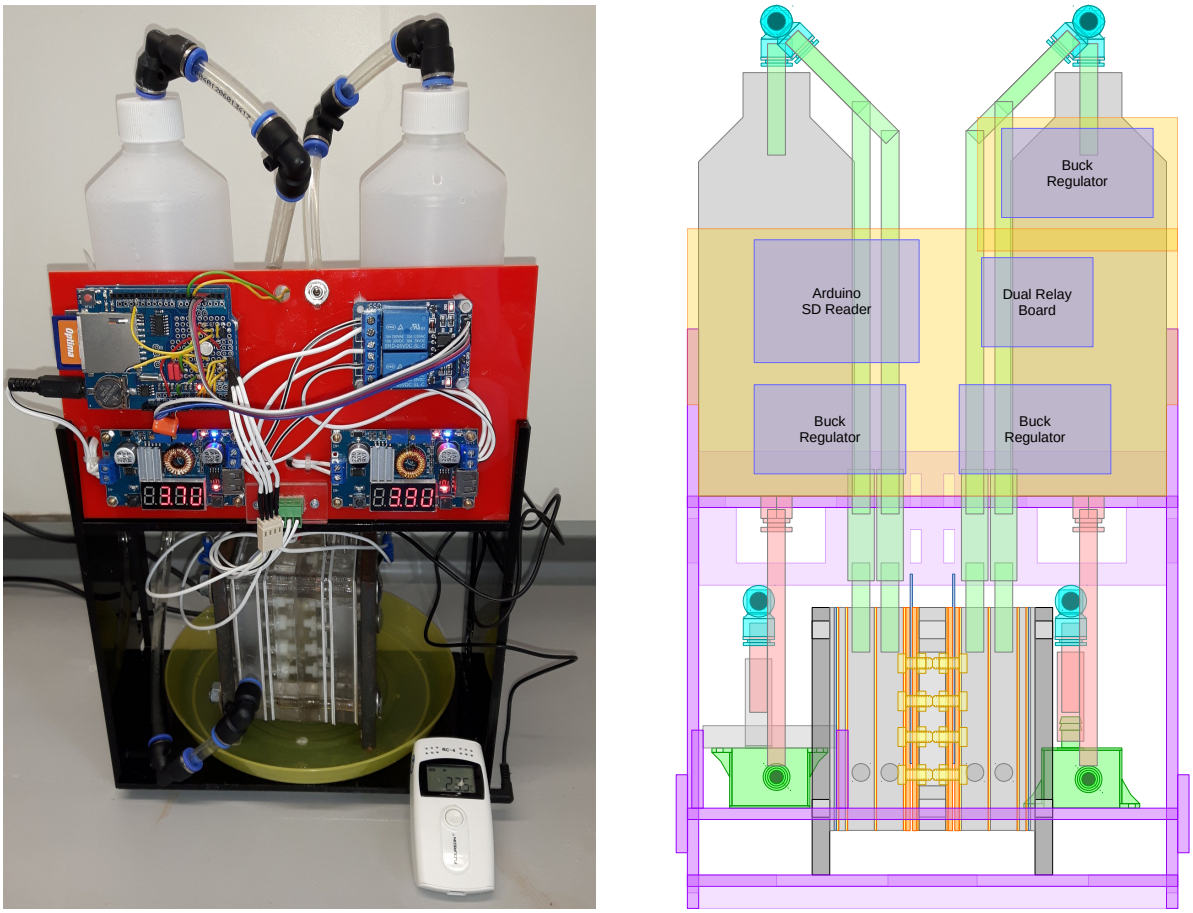

(a) Initial version, as constructed

(b) Final version, with pumps

Figure 4.3: The dual long-term experimental test set-up based around Arduino modules

The station maintained two separate bodies of electrolyte, to prevent cross contamination, which were stored in 500 ml polyethylene bottles. Power was supplied by voltage/current (Buck) regulators set to supply a constant current (typically 1.8 A), with intermittency supplied by the Dual Relay Board, which in turn was controlled by the Arduino microcontroller. This would measure the cell voltages using its A/D converters and write the results to the SD card, together with a time-stamp generated by the real-time clock. The station was designed such that all the electronics (i.e. the red board) could be quickly disconnected and removed, whilst the rest of the station was subsequently dismantled and made safe.

To begin with, a single 5.5 mm (internal diameter) riser-tube was used for each cell, but this led to bad air-locks which would eventually fill each cell with gas. These were solved by inserting a small section of 8 mm ID tube, which was just large enough to permit gas and liquid to gravitate. Also, due to limited bolt length, no gas-separation membranes were used, with the benefit that only a single riser tube was needed.

However, it was feared that the lack of membranes and pumps may affect the results, therefore the final version included both, so as to better emulate the conditions in the displacement tube experiments. It is certainly an interesting possibility that the absence of a membrane and circulation permits evolved and dissolved oxygen from the anode to accelerate corrosion of the cathode.

4.2.7 Electrodes

The initial design of electrode was based on a 10 cm $\times$ 10 cm sheet of metal, onto which a sheet of acrylic was glued, so as to expose a 3 cm $\times$ 3 cm window, as shown in Figure 4.4a.

The decision to expose 9 cm^2 of electrode limited the maximum current density available from the potentiostat to 270 mA cm^{-2}, which is quite low compared to many published results. However, it was felt that a larger surface area would achieve more scalable results, and in any case much higher capacity power supplies are readily available.

Since all electrode activity is calculated per unit area, it was desired to create an accurately defined window, and it was believed that gluing would be the most reliable way to achieve this. However, evidence quickly emerged that the glue was being undercut, albeit slowly. In any case, such a design meant that testing could only be performed destructively, which greatly limited avenues for research.

Therefore the electrode was redesigned around a 'paddle-shaped' piece of metal, together with a laser-cut acrylic mounting which could be dismantled, as shown in Figure 4.4b, and previously described in Section 2.1 on page 41. The asymmetrical shape also meant that four electrodes could be cut from a single 10 cm $\times$ 10 cm piece of metal. The glue was

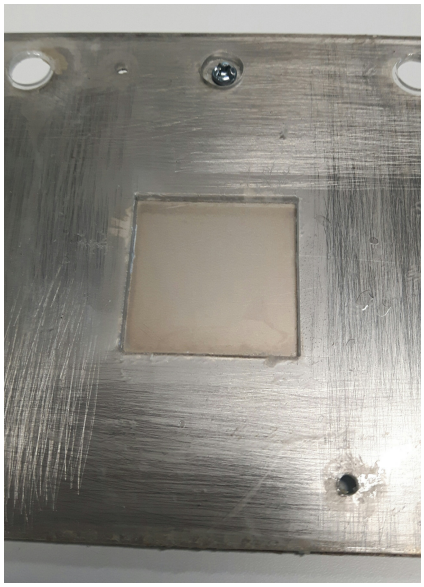

(a) 10x10 electrode with glued window

(b) 'Paddle' shaped electrode, plus mounting

Figure 4.4: The two designs of electrode. The paddle-shaped electrode has the advantage that it can be dismantled.

replaced with silicone rubber, which was immune to undercutting, and which sat in laser-engraved channels. The nylon screws were prone to leaking, therefore a leak-proof chamber was constructed behind each electrode to prevent the leak progressing.

4.2.8 Stainless-steel

This work examines the electrode stability and lifetime potential for stainless-steel and a commercially coated titanium nitride electrode set-up. The composition of stainless-steels is governed by international standards and they are widely available, making them a cost-effective source of a reliable substrate material. Certainly, they are more widely available and cost-effective than a pure nickel substrate. The most common grades investigated for electrolysis are 304 (304SS) and 316 (316SS) [168–170], both of which are composed primarily of Fe, Ni and Cr, but with 316SS featuring a higher percentage of Ni, in addition to about 2.5 wt% Mo. This affords 316SS greater resistance to corrosion, making it the first choice for marine and medical applications, but also making it more expensive, and potentially more difficult to obtain coating adherence. From the results reported by Carta *et al.* an overpotential for a 316SS cathode of $-0.34\,\mathrm{V}$ at $10\,\mathrm{mA\,cm^{-2}}$ was observed [168], but it has been clear to the author over extended use that even 316SS will experience significant cathodic corrosion (*cf.* Figure 4.22b on page 156).

Titanium nitride is known for its high thermal and electrical conductivity, in addition to its mechanical hardness [171], and is known to enhance electrode lifetime for the oxygen and hydrogen reduction reactions in a proton exchange membrane fuel cell [172]. However,

to our knowledge it has not been investigated for use with intermittent alkaline electrolysis, so this work is the first study of its kind. In addition, it is widely available as a bespoke coating service for the lifetime enhancement of machine tools, alongside alternative coatings such as CrN, TiAlN and WS_2 [173]. In this context, the coatings are selected for their extreme hardness, and their ability to resist oxidation at the high temperatures generated during machining (which can exceed 800 °C). These properties are of secondary concern for room-temperature alkaline electrolysis, but the wide availability and accessibility of the coatings makes them potentially cost-effective. However, it remains to be seen which (if any) of these coatings constitutes the optimal trade-off between performance and cost. This study will focus on titanium nitride.

4.3 Materials and Methods

4.3.1 Electrodes

The electrodes used were all 316-grade stainless-steel 0.9 mm thickness cut to size and shape, either as supplied or coated in TiN using a standard commercial preparation delivering a 1 to 4 µm thick TiN coating. The commercial titanium nitride coatings were applied by Wallwork Cambridge Ltd, UK, and their internal specification for the coating was "TIN COAT SPEC 300 1 – 4 MICRONS". In order to respect the intellectual property of the company, no attempts were made to reverse-engineer the coatings, so it is not possible to report in this study how the coating thickness might affect performance. It is not expected that differences in coating thickness above 1 µm will cause significant changes. This is because the material is electrically conductive, and because such a thickness constitutes many thousands of atoms, it is unlikely to affect the surface chemistry.

4.3.2 Ageing

All ageing experiments were conducted using a constant current power supply, connected to a two-electrode laminated electrolytic cell, which was primarily comprised of laser-cut acrylic plastic (see Figure 4.5) [16]. A Zirfon^{TM} membrane was used to keep the evolved gases separate, and the distance between electrodes was approximately 30 mm [17]. It was observed that at the higher current density a stronger electrolyte was needed to keep the total voltage drop across the electrolytic cell, and with it the associated ohmic heating, within reasonable limits. The choice to use NaOH instead of the more usual KOH was made because it is cheaper, and therefore more practical for commercial applications. Also, even though the safety data sheet states that it must never be disposed of down the drain, it is

widely recognized and used as a drain cleaner, and therefore accidental spillage or leakage into the sewer is a manageable environmental hazard.

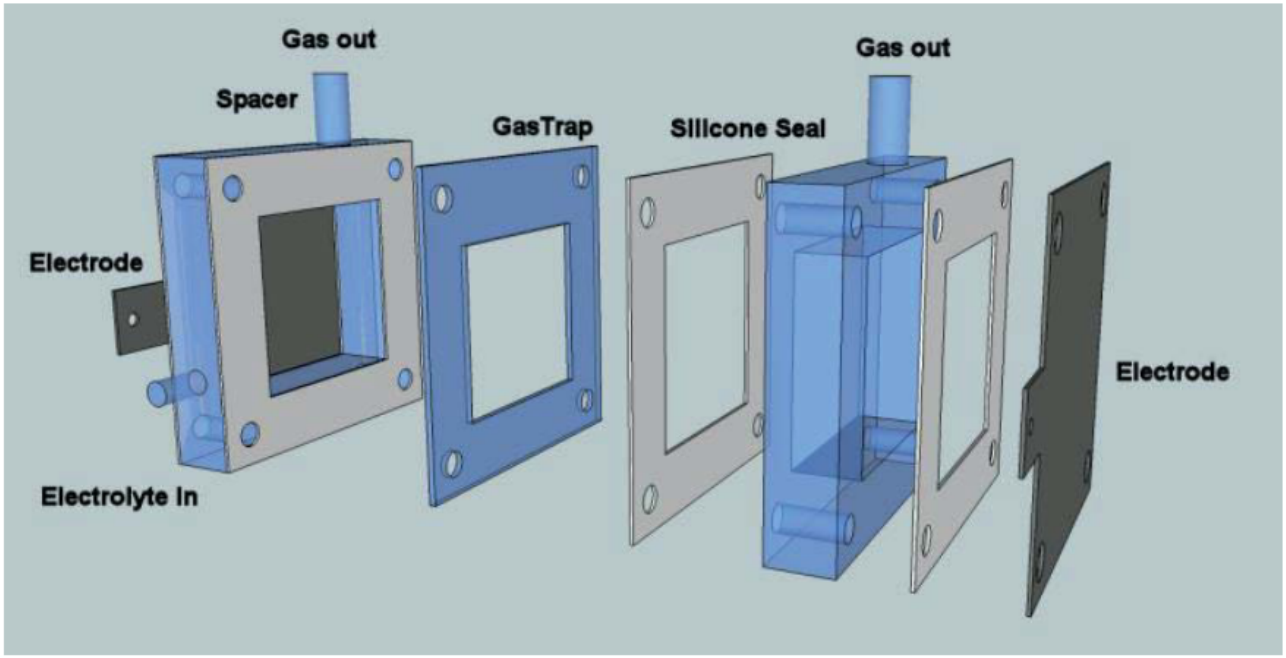

Figure 4.5: Typical design of experimental electrolytic cell, based on laser-cut components.

Each experiment lasted between 5.5 and seven days, made up of 4-minute cycles. In some experiments the electrolyte was circulated through a single external chamber using a small brushless pump.

4.3.3 Three-electrode experiments

All three-electrode experiments were conducted on an Ivium (Eindhoven, Netherlands) n-Stat potentiostat, connected to a similar design of electrolytic cell. The working electrode (WE) surface area was reduced to 9 cm^2 by gluing or bolting the electrode to a laser cut sheet of 3 mm clear acrylic containing a 3 cm $\times$ 3 cm window. The counter electrode was a 316-grade stainless-steel plate (of which 6 cm $\times$ 6 cm was exposed), and the reference electrode (RE) was a commercial design involving a Ag/AgCl wire suspended in 3 M KCl. The distance between working and counter electrodes was approximately 15 mm. The electrolyte was 0.5 M NaOH (standard reagent grade) and deionised water was used throughout. Before each experiment the RE was checked against a standard calomel electrode (SCE), and the electrolyte was bubbled with nitrogen for 10 minutes to reduce dissolved oxygen. All experiments were conducted at laboratory ambient temperature, which was 20 ± 1 °C.

The procedure outlined by Stevens *et al.* was followed to obtain measurements of the Tafel slope [125]. This involved chronopotentiometry steps at varying current densities and durations as specified in Table 4.1.

Steps	Current Density ($A\,cm^{-2}$)	Duration (secs)
1, 13	1×10^{-5}	480
2, 12	3.2×10^{-5}	480
3, 11	1×10^{-4}	240
4, 10	3.2×10^{-4}	120
5, 9	1×10^{-3}	120
6, 8	3.2×10^{-3}	120
7	1×10^{-2}	120

Table 4.1: Current densities and durations for Tafel analysis.

Each experimental run consisted of both ascending and descending Tafel slopes, with the whole procedure repeated twice. The published results are taken from the descending slope of the second run.

4.3.4 iR Correction

In order to correct for voltage losses in the electrolyte between the reference and working electrodes, electrochemical impedance spectroscopy (EIS) was performed between 100 Hz and 1 MHz. The series resistance of the electrolyte was then defined as the magnitude of the point of closest approach to the origin of the resulting Nyquist plot. The voltage drop across the electrolyte could then be cancelled out simply by multiplying this resistance by the total cell current. No use was made of real-time iR-compensation on the potentiostat.

4.3.5 Electron Microscope.

Scanning electron microscope (SEM) imaging and energy-dispersive spectroscopy (EDX) were performed on an Oxford Instruments (Oxford, UK) AZtecOne spectrometer attached to a Hitachi (Japan) TM3030 table top microscope.

4.4 Results

Experiment 4.1: The CV and EIS measurements for an unused TiN-coated 316SS cathode were as presented in Figure 4.6.

The cathodic sweep of cycle 1 shows a peak at -0.85 V *vs* Ag/AgCl, for which there is no corresponding peak on the anodic sweep. On cycle 2 the peak is much reduced in size, but

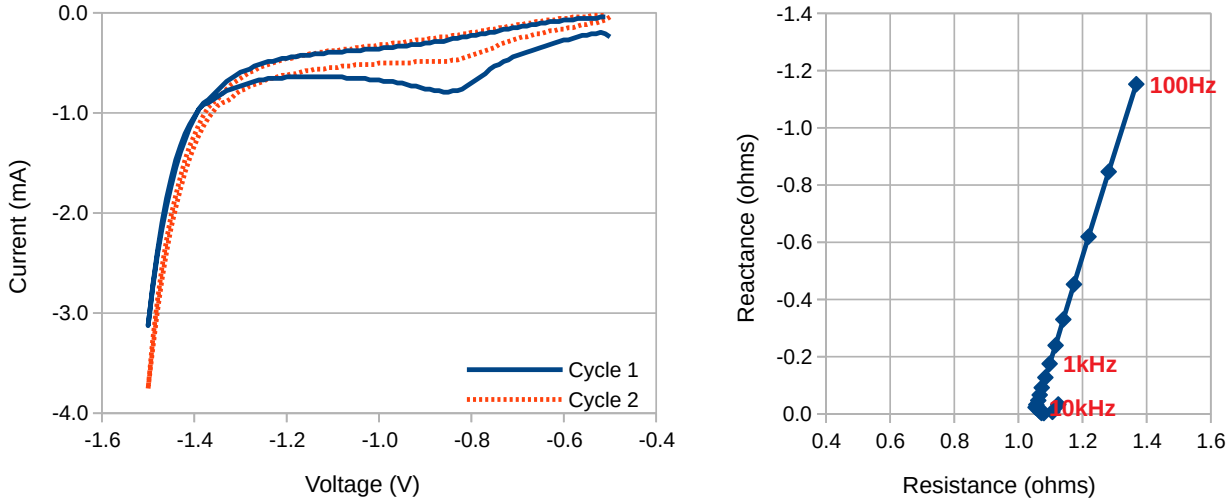

(a) Cyclic Voltammetry

(b) EIS

Figure 4.6: CV and EIS measurements of TiN cathode in 0.5 M NaOH.
CV scan rate: 10 mV s^{-1}. EIS bias voltage: −1.2 V *vs* Ag/AgCl.

at the same voltage. The maximum current under hydrogen evolution is slightly increased. In combination, these observations indicate that the coating is undergoing a progressive, irreversible change that is associated with a slight increase in activity.

The EIS measurements exhibit the classic response of a constant phase element (CPE) in series with a solution resistance of just over 1 Ω. Below a breakpoint frequency of approximately 10 kHz, the magnitude of the impedance increases, but maintains a constant phase angle, which is a response that is typical of many electrochemical systems.

Experiment 4.2: The electrical performance of a 316SS cathode, as measured in a 3-electrode cell, was as presented in Figure 4.7.

The chronopotentiometry plot shows how the measured voltage (grey dashed line) has been corrected for iR losses to produce the net voltage (blue solid line). In this case the series resistance of the electrolyte was measured using EIS as 1.12 Ω. The current measured by the potentiostat was not always the same as that instructed by its program, especially for the lowest two settings. This is a limitation of what can be achieved within a single 'current range' setting on the machine. In any case, even after two minutes at the lowest setting, the voltage was still moving the 'wrong' way. This could be due to capacitive discharge, battery-like behaviour, or inaccurate current reporting. Therefore, it would be wiser to regard the measurements of overpotential for the lowest two values of current density with suspicion. As such, this establishes 10^{-4} A cm^{-2} as a practical lower limit of what can be achieved during a chronopotentiometry experiment of ten minute duration. Although longer experiments were attempted, this situation remained materially unaffected.

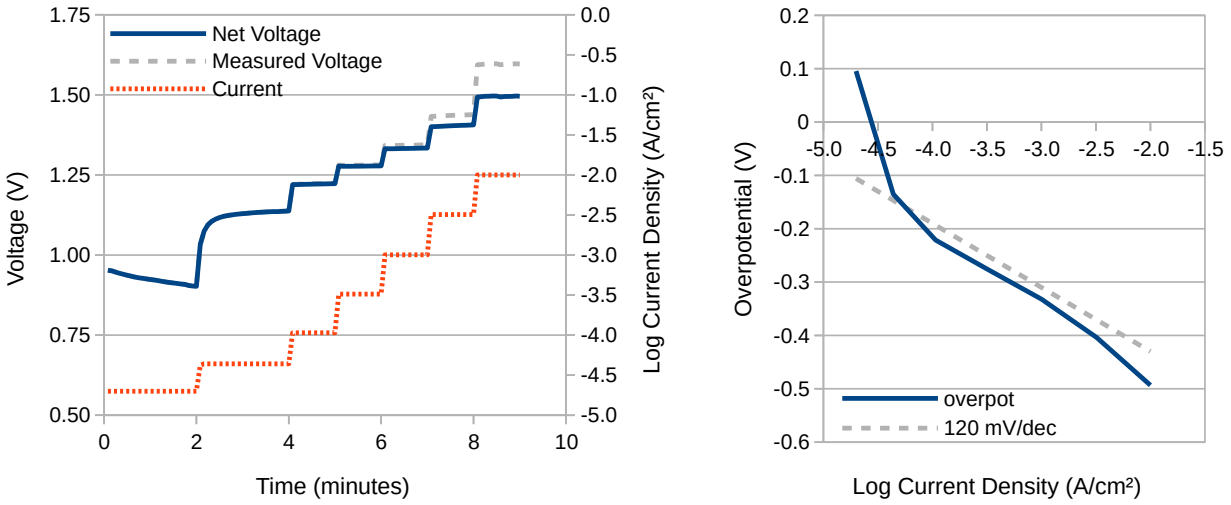

(a) Chronopotentiometry

(b) Tafel plot

Figure 4.7: Electrical performance of 316SS cathode in 0.5 M NaOH.

The Tafel plot in Figure 4.7b presents the same information with different axes. The overpotential was calculated thus:[1]

$$
\begin{aligned}
T &= 26\,^{\circ}\mathrm{C} && \text{(measured)}\\
V_{ref} &= -0.049\,\mathrm{V}\ \textit{vs}\ \mathrm{SCE} && \text{(measured)}\\
E_{SCE} &= 0.2412 - (T - 25) * 0.000661 = 0.2405\,\mathrm{V}\ \textit{vs}\ \mathrm{NHE} && \text{(theory)}\\
E^{0}_{cath} &= -pH * 0.0591 = -0.8097\,\mathrm{V}\ \textit{vs}\ \mathrm{NHE} && \text{(theory)}
\end{aligned}
$$

where V_{ref} was the calibration measurement between the Ag/AgCl electrode and a Standard Calomel Electrode (SCE), E_{SCE} is the theoretical SCE potential, and E^{0}_{cath} is the standard-potential of the hydrogen evolution reaction at pH 13.7. Therefore at the highest current density of 10 mA cm^{-2}, where the average net voltage (*vs* Ag/AgCl) was measured as -1.495 V, the overpotential was:

$$
\begin{aligned}
\eta_{cath} &= V_{net} + V_{ref} + E_{SCE} - E^{0}_{cath}\\
&= -1.495 - 0.049 + 0.2405 + 0.8097\\
&= -0.4934\,\mathrm{V}
\end{aligned}
$$

The Tafel plot includes a dashed grey line with a slope of 120 mV dec^{-1}, which is the value

[1] The equation for the value V_{SCE} is taken from http://www.consultrsr.net/resources/ref/calomeleqns.htm (viewed April 2020), which in turn cites the "Handbook of Analytical Chemistry", L Meites, ed., McGraw-Hill, NY, 1963. The full equation is a cubic Taylor series expansion accurate between 0 °C and 70 °C, but since such a wide temperature range is not needed, it has here been simplified to just one term.

expected from theory [42]. The plot of overpotential is parallel to this line within the range $10^{-4}\,\mathrm{A\,cm^{-2}}$ to $10^{-3}\,\mathrm{A\,cm^{-2}}$, which confirms that the observation is in line with theory. However, at higher current densities, the overpotential exceeds the theoretical value, which could be due to bubble coverage of the cathode. In any case, this experiment suggests that truly reliable values of Tafel slope are available only within a limited range.

Experiment 4.3: The electrical performance of a TiN-coated cathode, as measured in a 3-electrode cell, was as presented in Figure 4.8.

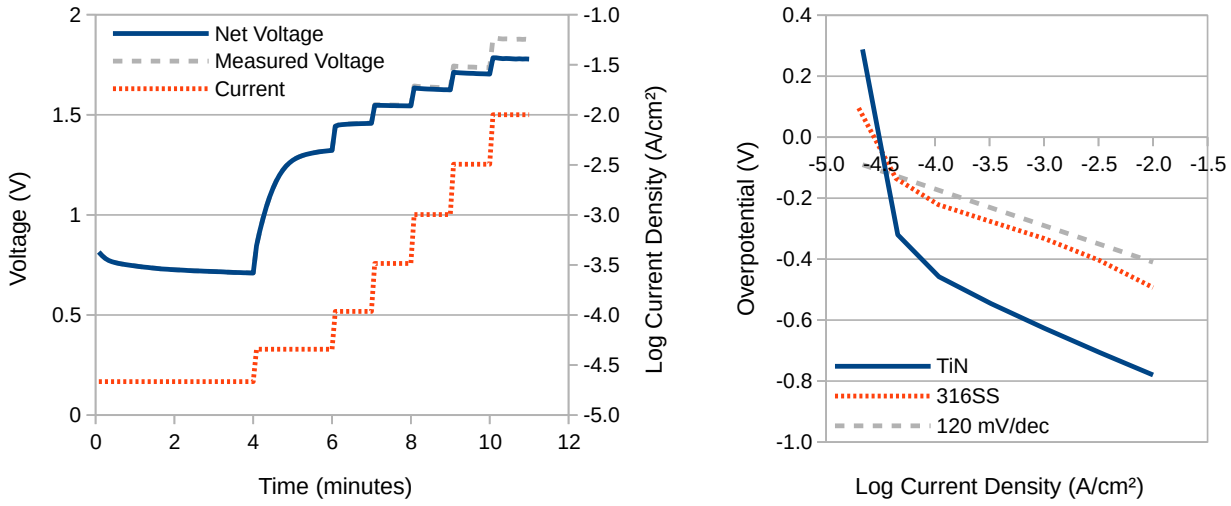

(a) Chronopotentiometry

(b) Tafel plot

Figure 4.8: Electrical performance of TiN cathode in 0.5 M NaOH.

The chronopoteniometry data shows that despite doubling the observation time at the lowest current density to four minutes, the voltage continued to fall. Figure 4.8b shows an overlay of the Tafel plot for TiN over that for 316SS. This confirms that above $10^{-4}\,\mathrm{A\,cm^{-2}}$ the Tafel slopes of the two materials are extremely similar. However, the TiN-coated electrode requires approximately 300 mV extra overpotential to achieve the same current density as the uncoated material.

Experiment 4.4: The electrical performance of a Pt sputter-coated 316SS cathode, as measured in a 3-electrode cell, was as presented in Figure 4.9.

The performance of the Pt electrode was far greater than that of the 316SS electrode, requiring about 300 mV less voltage to achieve the same current density. This experiment therefore demonstrates what can be achieved with the right catalytic material. It is possible that the Tafel plot is exhibiting a transition between $40\,\mathrm{mV\,dec^{-1}}$ and $120\,\mathrm{mV\,dec^{-1}}$, as indicated by the dashed gray line. If so, then this agrees with theory, which predicts such a transition will occur when the surface coverage of adsorbed hydrogen exceeds 50% [42].

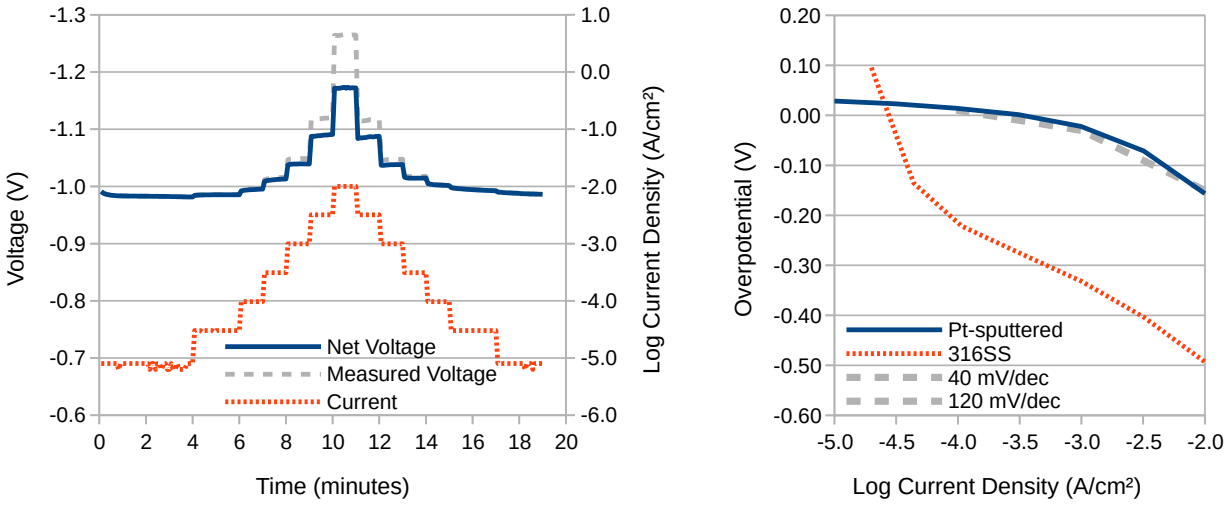

(a) Chronopotentiometry

(b) Tafel plot

Figure 4.9: Electrical performance of a Pt sputter-coated 316SS cathode in 0.5 M NaOH.

At this point, the rate of increase of the hydrogen evolution reaction with voltage will slow down as the Volmer reaction runs out of available electrode surface area. On this electrode, this transition appears to occur at approximately 10^{-3} A cm^{-2}.

Experiment 4.5: The appearance of TiN-coated 316SS after use as an anode, for three linear sweeps from 0 V to 5 V at 10 mV s^{-1}, is as shown in Figure 4.10a. The change in appearance was associated with a dramatic loss of electrical performance, such that the maximum current during the first sweep was just 80 mA. This observation is in agreement with previous findings [166, 174].

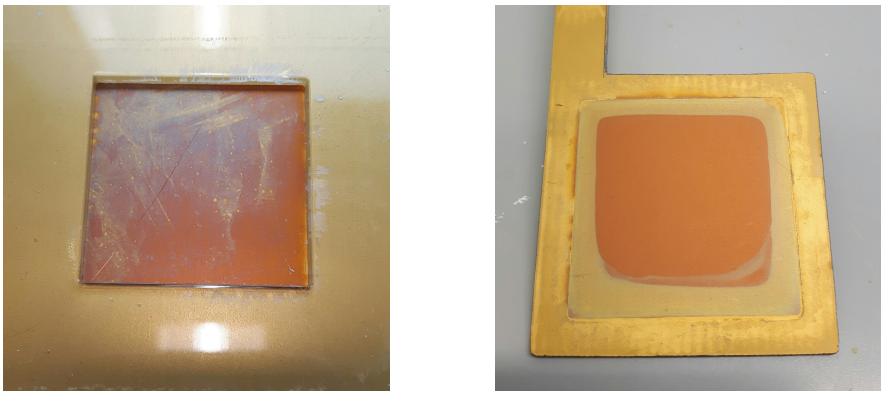

(a) After use as anode

(b) After gentle heating

Figure 4.10: a) appearance of TiN-coated 316SS after brief use as an anode, and b) appearance of TiN-coated 316SS after 24 hours in a drying cupboard.

Experiment 4.6: The appearance of TiN-coated 316SS after 24 hours in a drying cupboard at 60 °C, was as shown in Figure 4.10b. The 4 cm × 4 cm electrode was mounted such that only 3 cm × 3 cm was exposed. The similarity between this colour and that of Figure 4.10a suggests that both electrodes are undergoing a similar chemical transformation. This transformation will be investigated further using XPS, in Section 4.5.2 on page 160.

Experiment 4.7: This experiment tested a 316SS cathode and anode over 2000 cycles at 100 mA cm^{-2}, as presented in Figure 4.11. Both the temperature and voltage showed fluctuations with a discernible 24-hour period, which were due to diurnal temperature variations in the laboratory. An attempt has been made to correct for them by taking a segment of the chart, as highlighted by the dashed green rectangle, and calculating its line of best fit, as shown in Figure 4.11b. This shows that for every 1 °C increase in electrolyte temperature the cell voltage was reduced by 45 mV. Together with some smoothing, this permits the corrected voltage to be calculated, as shown in Figure 4.11a. The correction is quite convincing, and has almost completely removed the diurnal component, thereby demonstrating that most of the voltage variation is temperature related. It also reveals that after an initial fall of 250 mV, the voltage remained constant for the last four days of the experiment.

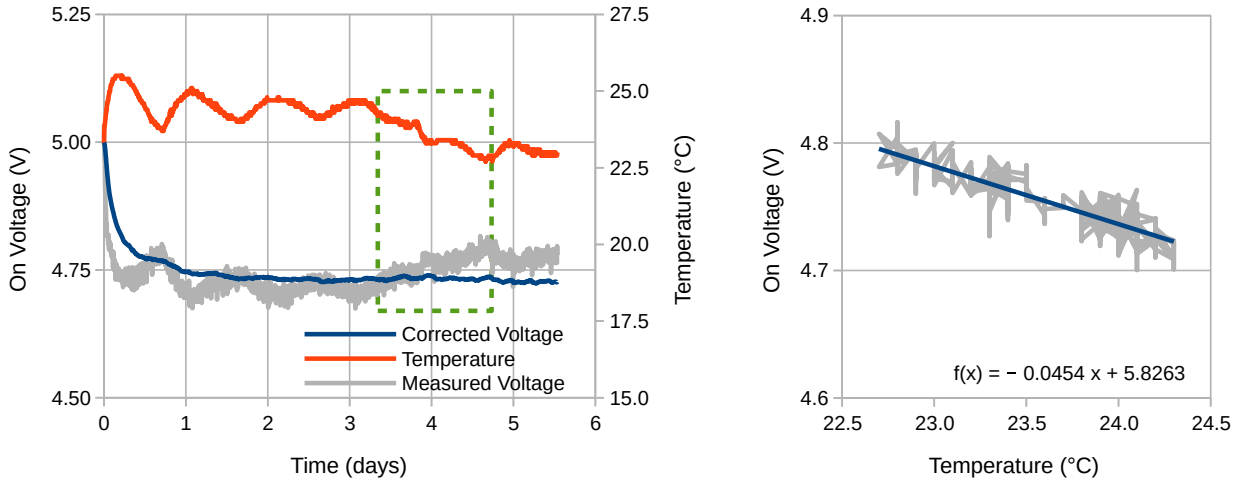

(a) Temperature and On Voltage

(b) Temperature Correlation

Figure 4.11: Results of 2000 cycles at 100 mA cm^{-2} with 316SS cathode and anode. a) Measured temperature and on voltage, and b) voltage *versus* temperature for the green dashed rectangle. The line of best fit was used to generate the corrected voltage in a).

The appearances of the anode and cathode at the end of the experiment were as shown in Figure 4.12. The anode showed almost no change in appearance, compared to the unused material which can be seen through the plastic. The cathode has darkened slightly overall, which supports the view that a 316SS electrode is more likely to experience corrosion when used as a cathode than as an anode. It also shows specific areas where greater corrosion

has occurred, mostly localised around the top and bottom edges. It is possible these were caused by the reduced ability of the electrolyte to reach these relatively inaccessible regions.

(a) Anode (b) Cathode

Figure 4.12: Appearance of the 316SS anode and cathode after 2000 cycles at 100 mA cm^{-2}.

Experiment 4.8: This experiment was the same as Experiment 4.7, except that the cathode was changed from 316SS to TiN, and produced the results presented in Figure 4.13a. As in the previous experiment, the corrected voltage has been constructed using smoothing plus temperature compensation based on the measurements within the dashed green rectangle. This again shows that after correction for temperature variations the voltage remains constant, except in this case for a small unexplained peak towards the end.

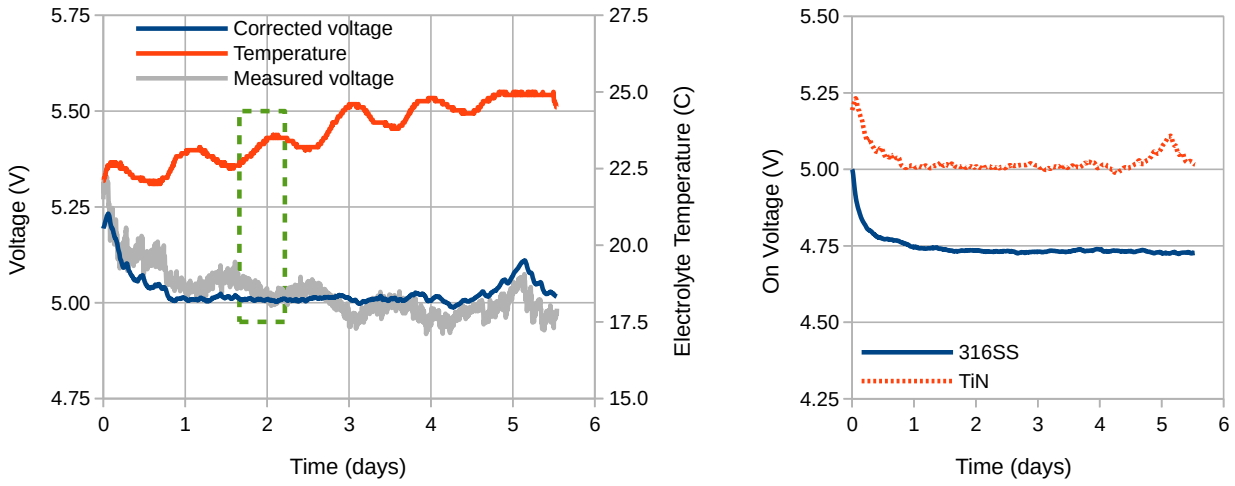

(a) Temperature and On Voltage (b) Comparison between TiN and 316SS

Figure 4.13: Results of 2000 cycles at 100 mA cm^{-2} with TiN cathode and 316SS anode. a) Measured temperature, on voltage and corrected voltage, and b) direct comparison between cells containing the TiN and 316SS cathodes.

A direct comparison between the results of Experiments 4.7 and 4.8 is presented in Figure 4.13b. This indicates that the cell containing the TiN cathode required an extra 250 mV to achieve the same current density, but otherwise performed very similarly. This finding is in agreement with that observed in Figure 4.8b on page 147.

(a) After ageing (b) Original appearance

Figure 4.14: a) shows appearance of the TiN cathode after ageing over 2000 cycles at 100 mA cm^{-2}. b) shows the typical appearance of the TiN coating before ageing.

The appearance of the TiN cathode at the end of the experiment was as shown in Figure 4.14a. Compared to the typical appearance of the TiN coating before ageing (as shown in Figure 4.14b) the cathode appears to have lost much of its golden colour. However, this colour change was not associated with a decrease in electrical performance.

Experiment 4.9: This experiment simultaneously tested both a TiN-coated 316SS cathode and an uncoated 316SS cathode at 200 mA cm^{-2}, both in conjunction with a 316SS anode. This was performed using the Dual Test Station, as described in Section 4.2.6 on page 139.

The on voltages and electrolyte temperature were as shown in Figure 4.15. They show that, after an initial adjustment period, the TiN-coated cathode slightly outperformed the uncoated cathode. Neither the temperature nor voltage measurements showed much diurnal variation, therefore these results have not been temperature corrected.

The chronopotentiometry results for the TiN-coated cathode before and after ageing were as shown in Figure 4.16a. This experiment was extended to over 50 minutes in an effort to obtain stable voltage readings. On the ascending staircase, the voltage does not stabilise at a realistic (non-positive) overpotential until $10^{-3.5}$ A cm^{-2}. On the descending staircase the voltage showed reversals, which indicates that a species existed which was temporarily lowering the voltage. This could be due to an electrochemical reaction other than hydrogen evolution. At $10^{-4.5}$ A cm^{-2} the current density was too low to complete the reversal, and the voltage thereafter remained unrealistic. The solid grey line shows the situation before

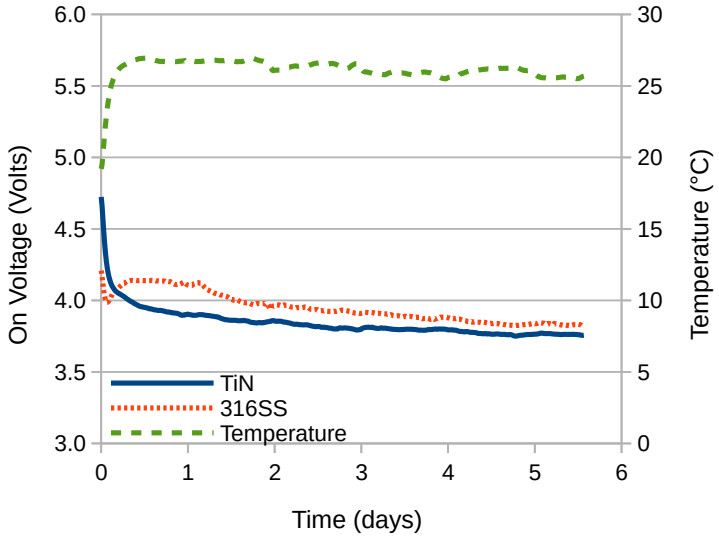

Figure 4.15: 2on-2off results for TiN-coated and uncoated 316SS cathodes in 1 M NaOH for 2000 cycles at 200 mA cm^{-2}. Gas-separation membrane: Zirfon. Electrolyte circulation: none.

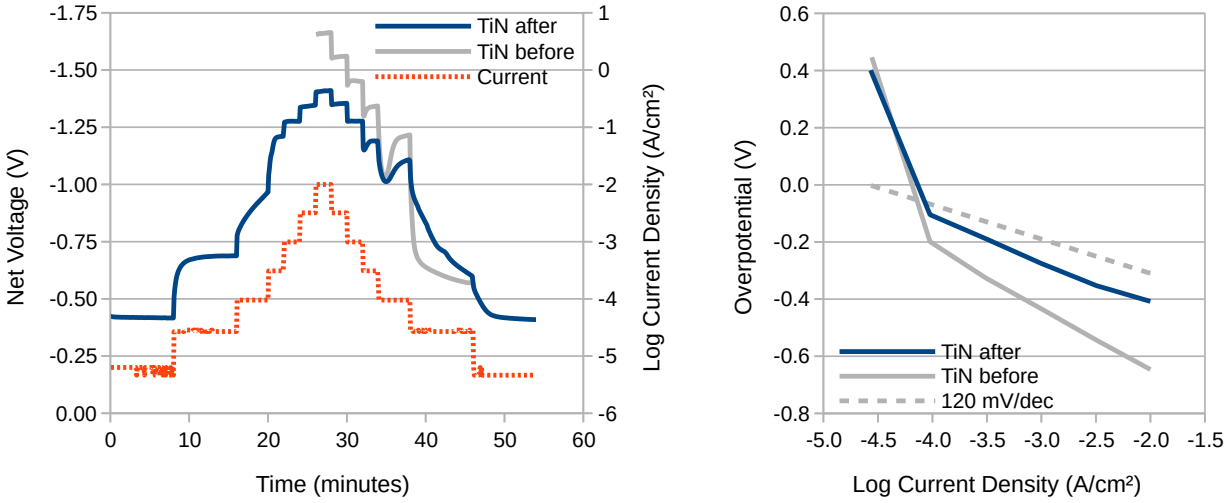

(a) Chronopotentiometry

(b) Tafel plot

Figure 4.16: Electrical performance of a TiN-coated 316SS cathode in 0.5 M NaOH after 2000 cycles at 200 mA cm^{-2}.

ageing, and shows that the voltage reversals were even more pronounced, which indicates that this is an intrinsic property of the TiN coating.

A Tafel plot of the performance of the TiN-coated cathode before and after ageing is as shown in Figure 4.16b. This shows that the activity of the cathode has improved by about 200 mV after ageing.

The appearances of the two cathodes after ageing were as shown in Figure 4.17. Both electrodes are showing signs of contamination with a copper-coloured deposit.

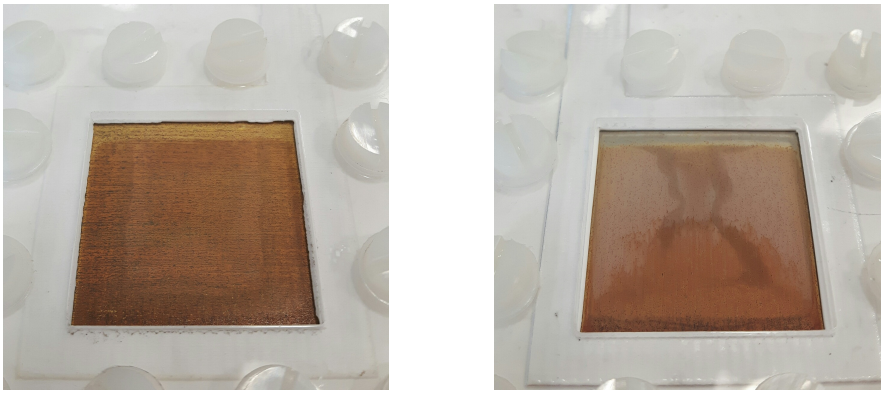

(a) TiN-coated cathode (b) 316SS cathode

Figure 4.17: a) Appearance of a TiN-coated 316SS cathode after ageing run1 over 2000 cycles at 200 mA cm^{-2}, and b) appearance of a 316SS cathode after the same treatment. Both cathodes are showing signs of contamination with a copper-coloured deposit

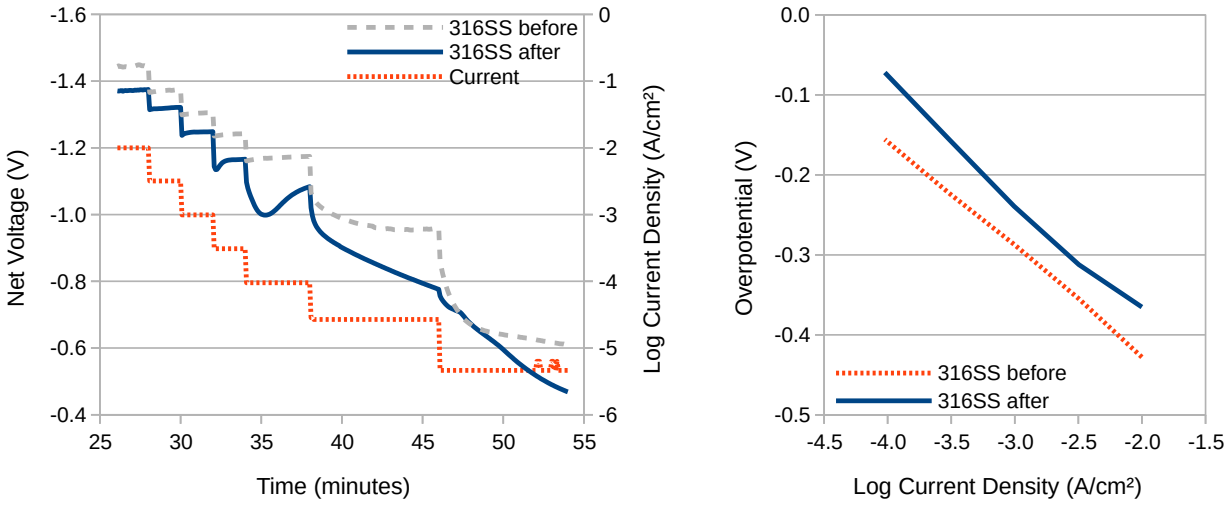

(a) Chronopotentiometry (b) Tafel plot

Figure 4.18: Electrical performance of an uncoated 316SS cathode in 0.5 M NaOH before and after 2000 cycles at 200 mA cm^{-2}. a) shows voltage on descending current staircase. The presence of voltage reversals after ageing confirms the presence of some form of electrochemically active species. b) shows that the activity of the electrode has slightly improved.

The presence of a contaminant is confirmed by the chronopotentiometry plot of the descending current staircase for the uncoated 316SS cathode before and after ageing, as presented in Figure 4.18a. Before ageing, there are no voltage reversals, whereas after ageing they are visible on three of the current steps. The Tafel plot in Figure 4.18b indicates that despite (or perhaps because of) the presence of the contaminant, the electrical activity of the uncoated 316SS cathode after ageing has improved by approximately 60 mV.

Experiment 4.10: This experiment was a repeat of Experiment 4.9, to determine if the contamination would recur. Hereafter, Expt 4.9 shall be referred to as 'run1', and Expt 4.10 as 'run2'.

(a) TiN-coated cathode (b) 316SS cathode

Figure 4.19: a) Appearance of a TiN-coated 316SS cathode after ageing run2 over 2000 cycles at 200 mA cm^{-2}, and b) appearance of a 316SS cathode after the same treatment.

The appearances of the two cathodes after ageing were as shown in Figure 4.19. This indicates that the amount of copper-coloured contamination appears to have been reduced, but not eliminated. The TiN-coated electrode has a striated appearance, which is similar to that after run1.

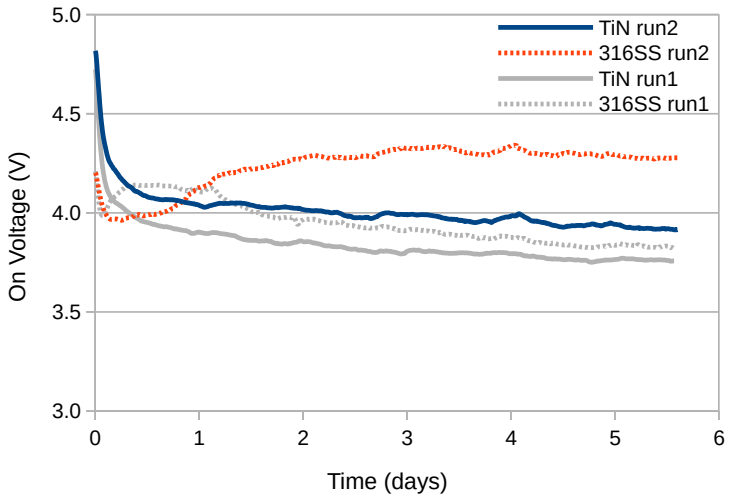

Figure 4.20: 2on-2off results for TiN-coated and uncoated 316SS cathodes in 1 M NaOH for 2000 cycles at 200 mA cm^{-2}. Gas-separation membrane: Zirfon. Electrolyte circulation: none.

The voltages recorded were as reported in Figure 4.20. These were in general higher than in run1, but followed similar trajectories. For example, the on voltage for the TiN coated electrode fell monotonically, whereas that for the uncoated electrode fell, then climbed, then fell

again. In particular, the voltage for the uncoated electrode was nearly 0.5 V higher at the end of the experiment than in run1. This suggests that its degree of performance improvement may be related to the level of contamination.

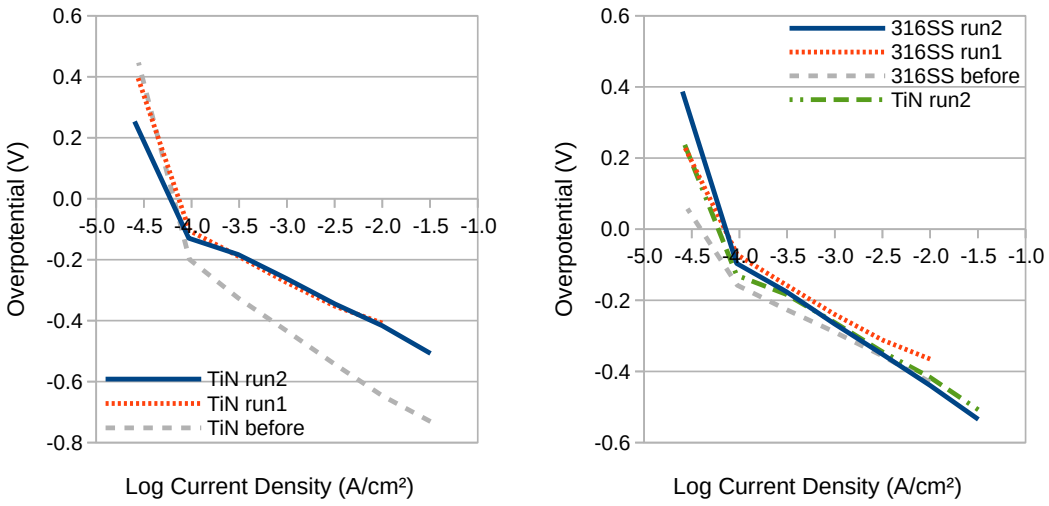

(a) TiN cathode

(b) 316SS cathode

Figure 4.21: Tafel plots for TiN-coated and uncoated 316SS cathodes in 0.5 M NaOH after 2000 cycles at 200 mA cm^{-2}.

The Tafel plot for the TiN-coated cathode was as reported in Figure 4.21a, and shows that the activity of the electrode at the end of run2 was almost identical to that at the end of run1. The observed improvement of 200 mV therefore appears to be repeatable. The Tafel plot for the uncoated electrode in Figure 4.21b has shown hardly any improvement at all, especially at higher current densities. Of perhaps greater significance is that after ageing, the performance of TiN-coated and uncoated electrodes has converged. However, from Figure 4.20, it is clear that there is more to overall system performance than just that of the cathode.

Experiment 4.11: This experiment was a third and final repeat of Expt 4.9, hereafter referred to as 'run3'.

The appearances of the two cathodes after ageing were as shown in Figure 4.22. On this occasion the electrodes had turned almost completely black.

The voltages recorded were as reported in Figure 4.23. Their level and trajectory are similar to the previous two runs.

The Tafel plot for the TiN-coated cathode was as presented in Figure 4.24a. It shows that after ageing, the performance of all three TiN cathodes was extremely similar, regardless of appearance. The Tafel plot for the uncoated anode in Figure 4.24b shows a little more variation, but is also very similar. This indicates that it is wrong to assume that the electrical performance of an electrode will be in proportion to the degree of corrosion which it appears to have undergone.

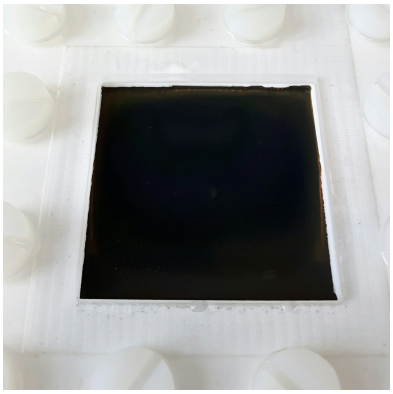

(a) TiN-coated cathode

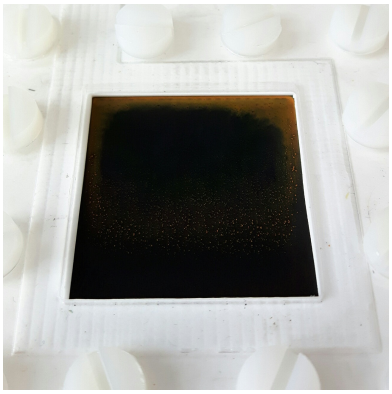

(b) 316SS cathode

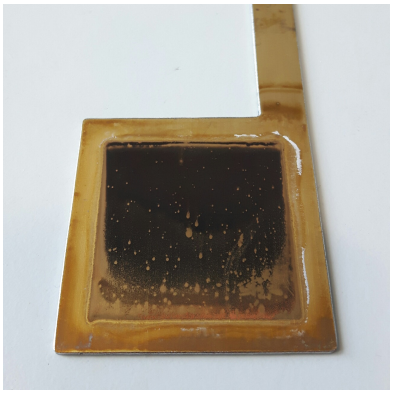

(c) TiN after immersion

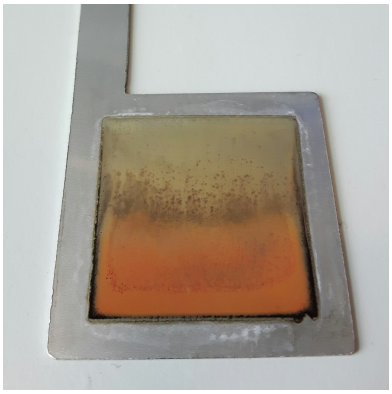

(d) 316SS after immersion

Figure 4.22: a) shows appearance of a TiN-coated 316SS cathode after ageing run3 over 2500 cycles at 200 mA cm^{-2}. b) shows the appearance of a 316SS cathode after the same treatment. Photographs c) and d) show the same two electrodes after 3 days immersed in 0.5 M NaOH.

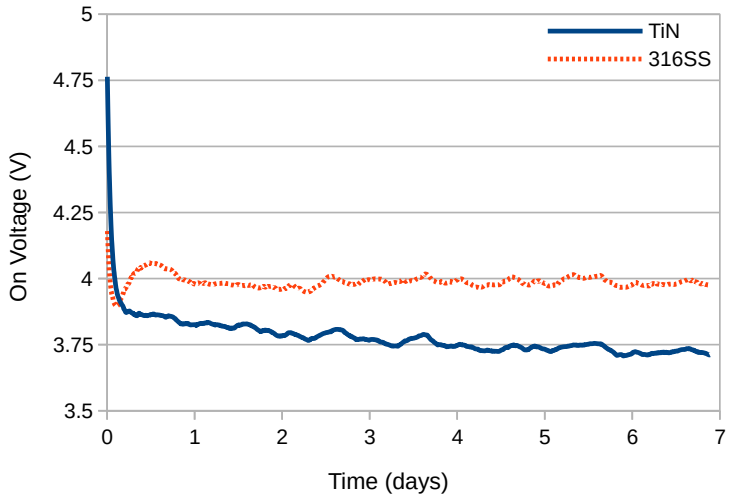

Figure 4.23: 2on-2off results for TiN-coated and uncoated 316SS cathodes in 1 M NaOH for 2500 cycles at 200 mA cm^{-2}. Gas-separation membrane: Zirfon. Electrolyte circulation: none.

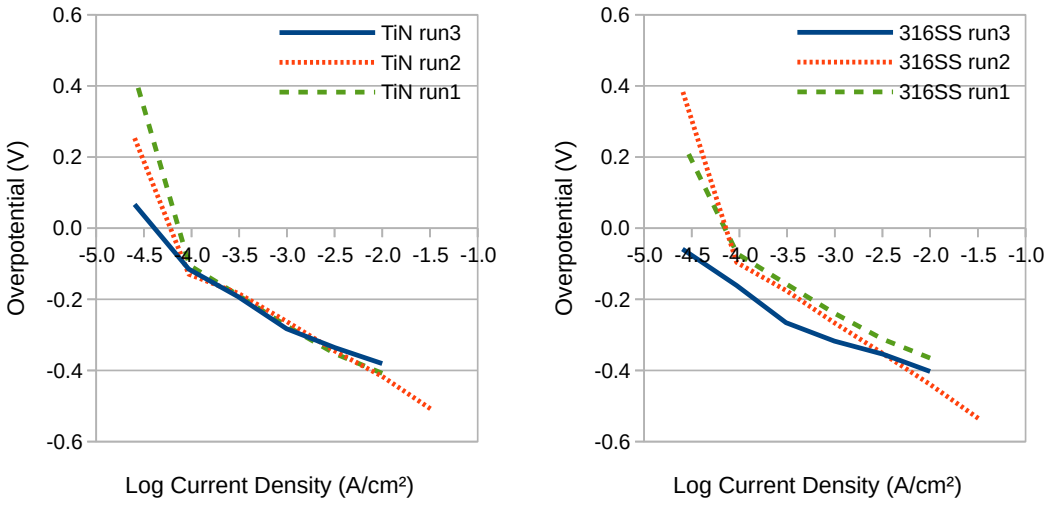

(a) TiN cathode

(b) 316SS cathode

Figure 4.24: Tafel plots for TiN-coated and uncoated 316SS cathodes in 0.5 M NaOH after 2500 cycles at 200 mA cm^{-2}.

4.5 Discussion

The electrical performance comparison of both the stainless-steel and TiN-coated cathodes is as shown in Figure 4.8b on page 147. These results show that the Tafel slopes for both materials are very nearly the same. Both are largely parallel to the 120 mV dec^{-1} value (shown as a dashed line), which is the value anticipated from theoretical calculations within the literature [42]. However, the coated electrode requires approximately an extra 300 mV of overpotential to achieve the same current density as the uncoated material.

During these experiments, neither combination exhibited much variation in two-electrode electrical performance, as shown in Figure 4.13b on page 150. This indicates that both materials are electrically stable long term, at least at this current density. Note also that the TiN cell consistently required approximately an extra 250 mV, which agrees well with the three-electrode results. We may therefore conclude that most of this additional voltage is a result of the TiN coating on the cathode.

Further long-term tests were conducted in 1 M NaOH at 200 mA cm^{-2} to test whether the electrical performance of the uncoated stainless-steel cathode would degenerate if subjected to greater accelerated ageing, as shown in Figures 4.15, 4.20 and 4.23 on pages 152, 154 and 156 respectively.

Although the results varied, it was observed that the voltages were lower in general, due to the higher concentration of the electrolyte. Also, any initial voltage difference was quickly overturned, and thereafter the gap gradually extended until the TiN cell outperformed the stainless-steel cell by up to about 250 mV. This performance improvement was not necessarily attributable to the cathode, since it was a two-electrode cell, and therefore did not permit

an individual assessment to be made of either electrode. To assess this, three-electrode experiments were again performed to measure the electrical performance of the cathodes in isolation, as shown in Figure 4.21 on page 155.

The TiN cathodes were thus able to match the stainless cathodes. The improvement seen in the ageing experiments was therefore likely due to factors other than the cathode alone, such as the electrolyte, membrane or anode. Perhaps of greatest significance was the observation that the anode used in conjunction with the TiN cathode had taken on a coppery appearance, and it is possible that this led to an unexpected and unexplained increase in performance. Also significant was that both cathodes improved over the course of the experiment, with the TiN cathode overpotential decreasing by a remarkable 400 mV.

Despite this improvement in electrical performance, both electrodes could exhibit significant deterioration in their visual appearance, as shown in the top two images of Figure 4.22 on 156. Nevertheless, it is perhaps indicative of their potential for real-world longevity that their appearance improved after immersion for three days in fresh 0.5 M NaOH (as shown in the bottom two images) despite being almost completely black immediately after accelerated ageing.

4.5.1 SEM and EDX

The cathodes from Figure 4.22 on page 156 were analysed using SEM and EDX, since their smaller design permitted them to be mounted inside the electron microscope, with the results for the TiN-coated cathode as presented in Figure 4.25 and Table 4.2. The SEM micrograph showed the presence of crystals, and it was apparent from the EDX spectrum obtained that they were comprised primarily of copper. This could be attributed to the copper that it is believed is applied as the first layer during the commercial TiN deposition.

Element	Line Type	Weight %	Sigma	Atomic %
Cu	L series	61.00	0.58	31.84
O	K series	24.07	0.38	49.90
Ti	K series	6.86	0.15	4.75
Fe	K series	3.30	0.16	1.96
C	K series	3.28	0.36	9.05
N	K series	0.90	0.64	2.13
Cr	K series	0.60	0.09	0.38
Total				**100.1**

Table 4.2: Quantitative analysis of the EDX spectrum for the crystalline deposit presented in Figure 4.25b

For the uncoated 316SS cathode, the appearance was as shown in Figure 4.26. There was a marked difference between the top half of the electrode (location 'a'), which appeared

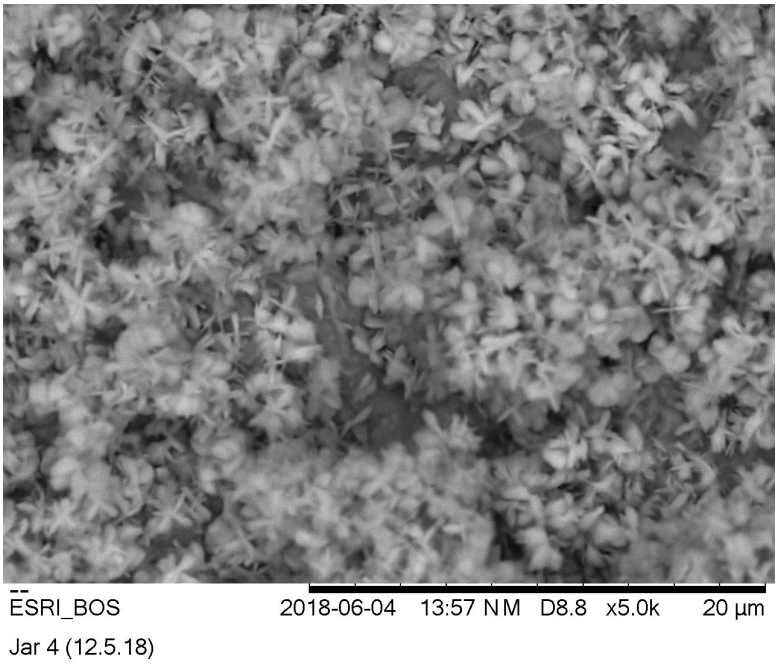

(a) SEM

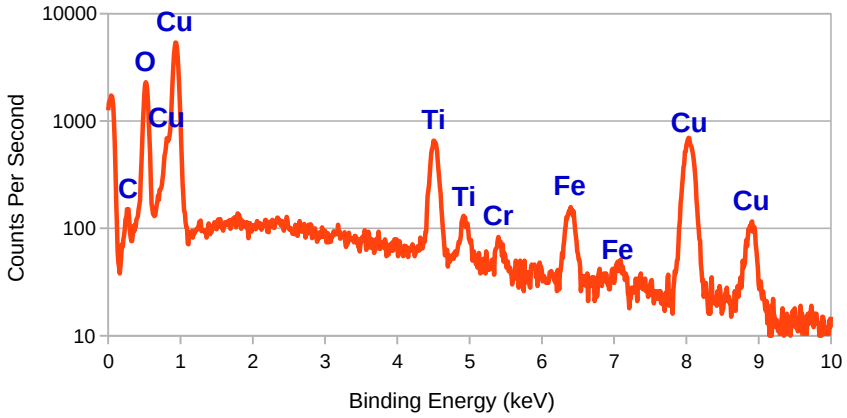

(b) EDX

Figure 4.25: a) Electron micrograph at 5000× magnification and b) EDX spectrum of the crystalline deposit for the TiN cathode after ageing at 200 mA cm^{-2}.

unaffected, and the bottom half (location 'b'), which was covered in small particles approximately 500 nm across. EDX analysis of the particles confirmed that they were 70% copper by weight.

This is in agreement with the coppery colour exhibited by the electrode, but is nevertheless a surprising result, as no explicit source of copper exists in the experiment. It is therefore speculated that trace levels of copper must have been present in the electrolyte, the membrane or the stainless-steel. This is supported by EDX results obtained by Kao *et al.* [175], and by experiments on samples of 316-grade stainless-steel from two separate steel suppliers, where percentages of copper between 1 and 1.6 wt % were observed, even though

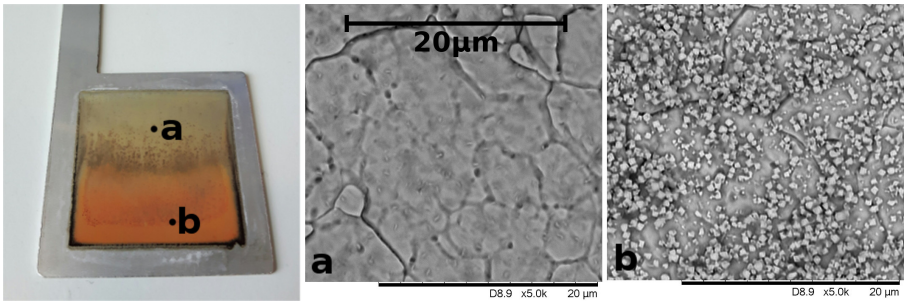

Figure 4.26: Electron micrographs at 5000x magnification of the uncoated 316SS cathode after ageing at 200 mA cm^{-2}.

according to official standards, 316-grade stainless-steel does not contain copper. Regardless of the source of the contamination, this result highlights the extent to which copper can become highly concentrated on the cathode during intermittent use. There is, however, a negligible effect on the long-term performance of the electrode.

4.5.2 XPS (X-ray photoelectron spectroscopy)

The TiN coating undergoes rapid deterioration if used even briefly as an anode, as discussed in Experiment 4.5 on page 148. After sweeping from 0 to 5 V at 10 mV s^{-1}, the coating changed to a deep orange-brown colour, and the electrical performance was drastically reduced. Examination of the original coating using XPS before and after this alteration produced results as shown in Figure 4.27. It is clear there are more components present in the XPS signal of the original TiN coating.

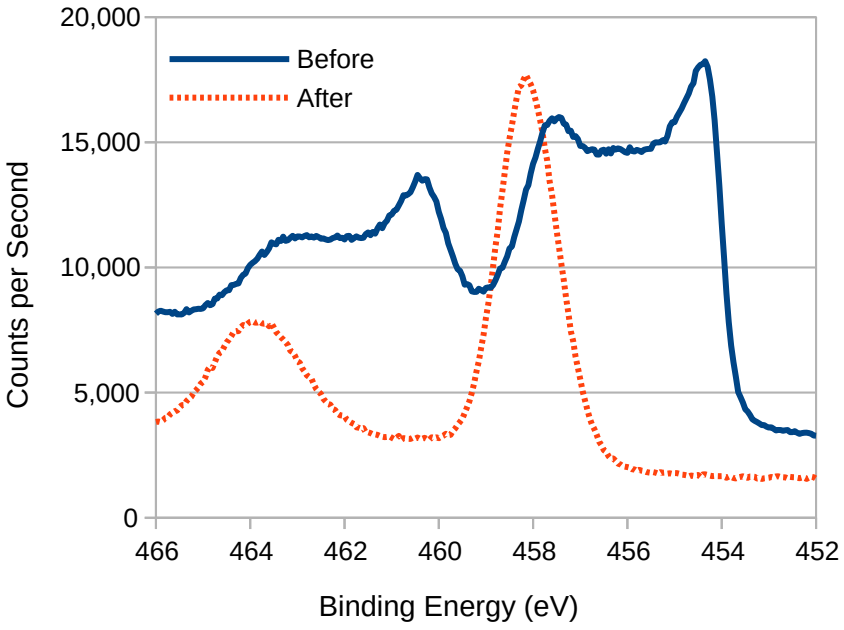

Figure 4.27: XPS results for the Ti 2p region before and after use as an anode

In order to identify these components, the results were analysed using CasaXPS software, which is able to perform peak fitting. Typically, all 2p electron orbitals produce an XPS signal consisting of doublets, whereby the lower binding energy peak ($2p_{1/2}$) has double the area of the higher peak ($2p_{3/2}$), but the same full-width half-maximum (FWHM). However, it is known that the FWHM constraint is not entirely applicable to titanium, due to the Coster–Kronig effect, which causes a broadening of the $2p_{1/2}$ peak [176]. Nevertheless, it is still possible to perform outline peak deconvolution, the results of which are as presented in Figure 4.28.

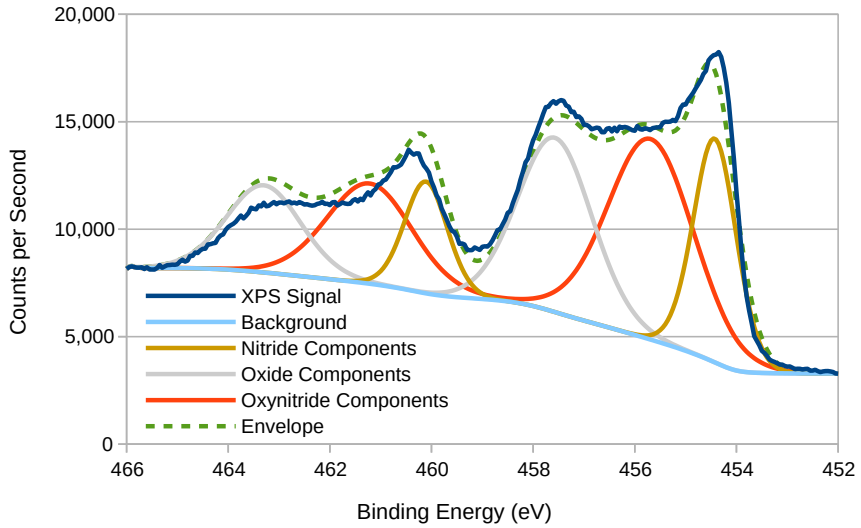

Figure 4.28: XPS results component fitting for the Ti 2p region of titanium nitride

The fitting indicates the presence of three separate components within the overall XPS signal, which are accepted to correspond to the presence of titanium nitride and oxide [171, 177], as well as oxynitride [166, 176], as indicated. Given the positioning of the remaining component in Figure 4.27 (at $\sim$ 458 eV), it is clear that after even brief use as an anode, the surface layers of the coating lost all traces of nitrogen and became oxidised titanium. This is understandable, since anodes are prone to oxidation in general, and titanium is prone to oxidation in particular [176]. A similar finding has been made by Wang *et al.*, who observed that the higher the concentration of nitride in their oxynitride coating, the higher its tendency to be irreversibly oxidised under anodic conditions [178].

Since XPS is an extremely surface-sensitive analytical technique, examining exclusively the top $\sim$ 10 nm, it is possible to use an ion beam to mill into the surface, and thereby obtain depth profiling information, the results of which are as shown in Figure 4.29. Here the numbers 1 to 9 refer to successively deeper XPS measurements, and show that the nitrogen peak becomes progressively stronger with increasing depth.

The nitrogen peak reappearance indicates that the stainless-steel remained protected and coated with TiN at depth, but overall the electrode incurred a loss of electrical performance

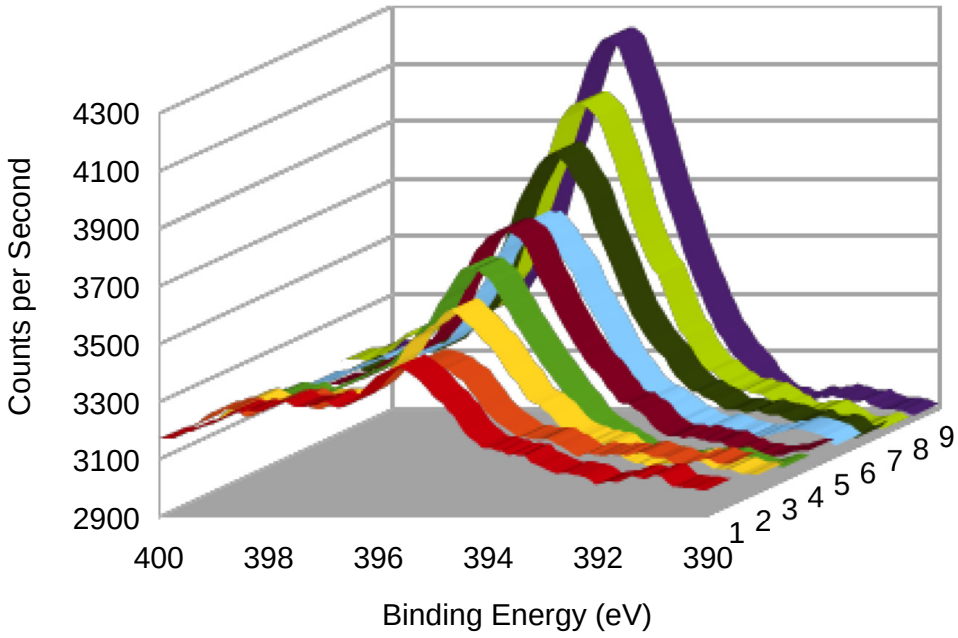

Figure 4.29: XPS depth profile (with smoothing) of the Ti N1s region of anodically altered titanium nitride

caused by the oxide on the surface, which is insulating at these voltages [178]. It is therefore concluded that the phase composition of the anodically altered coating changes from TiO_x at the surface, to TiN at depth, via a mixture including titanium oxynitride, as is confirmed by the change to an orange-brown colour [179] and the changing XPS [180–182]. The practical significance of this is that incorrect wiring or fluctuations in the polarity of the electrical input would fast render the electrolysis equipment ineffective. Therefore, in practice some sort of protection would need to be provided against reverse polarity, for example via the use of a diode and fuse, or alternatively a field-effect transistor (FET). Both solutions, however, would incur some liability, either in terms of cost or reliability.

4.6 Conclusions

The improvement to the electrical performance and reliability of 316-grade stainless-steel as a cathode for water splitting by the application of a commercially available titanium nitride coating has been investigated. Initially this appears to incur a 300 mV increase in overpotential. However, over long-term intermittent experiments at 200 mA cm^{-2}, a two-electrode cell incorporating the coating was observed to outperform the uncoated material by 250 mV. At this current density, both stainless-steel and TiN cathodes experienced significant discolouration (*cf.* Figure 4.22). The discolouration appears to be partially reversible, since the deposit is observed to dissolve into the electrolyte over several days.

More importantly, the TiN-coated material demonstrated a significant increase in electrical performance after such intermittent usage, improving by 400 mV, which was enough to surpass the uncoated material. Figure 4.21 shows that the coated material has matched the uncoated material in a three-electrode system, but Figure 4.20 shows that it has outperformed the coated material when employed as a complete system, an observation that was repeated in three separate long-term tests. The SEM results in Figures 4.25 and 4.26 show that the 'black appearance' of both cathodes after the third long-term test (Experiment 4.11 on page 155) actually has different underlying causes.

Characterisation using SEM (scanning electron microscopy) confirmed that the migration and deposition of copper might be responsible for some of this increase. Electron micrographs of the coated material after ageing reveal a large number of sharply pointed copper crystals. It is theorised that these grew from a layer of copper that was deposited by the coating supplier before the titanium nitride coating was applied. For the uncoated material, many copper particles approximately 500 nm in diameter were observed to have been deposited. Whilst the source of this copper contamination remains unknown, their appearance is not associated with a decrease in performance.

It was also confirmed that TiN cannot be used as an anode at all, therefore any TiN-coated electrodes present in a commercial electrolyser would be at significant risk of destruction should the incorrect polarity mistakenly be applied. Characterisation using XPS (X-ray photoelectron spectroscopy) revealed that the coating experiences a rapid conversion to TiO_x, with the loss of all nitrogen from the surface layers. Ion beam milling revealed that the transition from TiO_x at the surface to TiN at depth is progressive, and therefore will necessarily encompass intermediary compositions of titanium oxynitride. It is possible that a ternary compound of TiAlN or CrAlN might demonstrate greater resistance to electro-oxidation, as confirmed for thermal oxidation by Chim *et al.* [183]. Nevertheless, this does little to detract from the applicability of TiN as a cathode for electrolytic water-splitting under intermittent room-temperature alkaline conditions.

Chapter 5

Electrodeposited Raney nickel

> It seems to me clear that hydrogen is the obvious replacement [for petrol and diesel]
>
> *Jeremy Clarkson, The Sunday Times*

(The work on which this chapter is based was published by the author in the journal Electrochimica Acta in August 2019 [82])

5.1 Introduction

Raney nickel has been studied extensively since its invention in 1926, and is made by dissolving nickel in molten aluminium, followed by the addition of zinc or chromium whilst quenching. It was invented by American engineer Murray Raney for the hydrogenation of vegetable oils, which it achieves both through its catalytic properties and through its large surface area. The catalytic properties are based on the ability of nickel to adsorb hydrogen, and on *Sabatier's Principle*, which states that:

> the best catalysts should bind atoms and molecules with an intermediate strength: not too weakly in order to be able to activate the reactants, and not too strongly to be able to desorb the products [184]

This principle predicts that the optimum energy of hydrogen adsorption for hydrogen evolution should occur close to the thermoneutral state, i.e. where $\Delta G = 0$ [185]. This means that the change in enthalpy of adsorption ΔH is balanced by the change in entropy to and from hydrogen gas $T\Delta S$, which clearly produces the situation whereby hydrogen can adsorb and desorb at the fastest possible rate.

The material that comes closest to this optimal situation is platinum, which is why Pt is so often seen right at the top of a volcano plot for hydrogen evolution activity [186]. It is also the reason why the exchange current density on Pt in a normal hydrogen electrode is

the second highest known, and that is before the surface area is increased by a coating of platinum black. The ability of such an electrode to resist changes in potential is precisely what makes it the ultimate reference. However, there are many other materials, alloys and compounds that achieve a far better trade-off between activity and abundance, and one of these is nickel.

The process of 'activating' the Raney-nickel coating refers specifically to its reaction with sodium hydroxide:

$$M_xAl\,(s) + OH^- + 2\,H_2O \longrightarrow M_x(s) + Al(OH)_3{}^- + H_2(g) \tag{5.1}$$

Aluminium hydroxide is almost completely insoluble in water, but it is amphoteric. As a result, it is able to dissolve in sodium hydroxide via the formation of sodium aluminate, so long as the sodium hydroxide is strong enough:

$$Al(OH)_3 + NaOH \longrightarrow Na^+[Al(OH)_4]^- \tag{5.2}$$

An alternative employed by Schiller *et al.* with Raney nickel deposited by vacuum plasma spraying was 30 wt% KOH at 80 °C. However, the precipitation of aluminium hydroxide still had to be avoided by the inclusion of 10 wt% K-Na-tartrate-tetrahydrate [187]. The temperature of the solute during the activation process can have a large influence on the properties of the catalyst, with lower temperatures tending to promote a larger surface area [188]. Via the activation process, the bulk of the aluminium is removed, leaving behind a highly porous metallic sponge that is ideal for catalysis.

Alloying is not the only method by which Raney nickel can be produced, and electrodeposition methods have been investigated commercially since the 1950's [189], and in academia since the 1980's [189–192], in addition to other methods such as pressed powders and plasma spraying [193, 194]. Although typically investigated for hydrogen evolution [127, 150, 195–200], as well as in combination with non-abundant compounds [83, 153, 201], the coating is also known to perform well for oxygen evolution [129, 202].

The mechanism by which nickel and zinc can be successfully codeposited is not fully understood. According to Tozar *et al.* various explanations have been suggested, but none is conclusive. Regardless of the explanation, the codeposition not just of zinc with nickel, but zinc with many ferrous group metals is regarded as an instance of Anomalous Co-deposition (ACD) [151].

As the deposition current density is reduced, the mass fraction of zinc will increase. In fact at 10 mA cm^{-2} a deposition that was 93 wt% zinc was recorded [151]. Since for electrolysis, it is expected that deposits which are 50 wt% zinc to be the most effective [196], it is expected that higher electrodeposition current density would be required.

Pure, polished nickel cathodes show a marked increase in overpotential after active hydrogen evolution in alkaline electrolytes of up to 400 mV, which is ascribed to the formation of hydrides [130]. This effect is even more pronounced at the high current densities and strong alkaline electrolytes typically found in commercial electrolysers [203]. Nickel is also more prone to the formation of hydrides in NaOH than in KOH [169].

In this study a comparison will be made between two different types of electrodeposited Raney nickel, as listed in Table 5.1. Coating Raney1 is based on that refined by I. Herraiz-Cardona *et al*. [127], itself based on earlier work [191], and ultimately based on processes which are widely used in the nickel plating industry, and were first formulated by Professor Oliver P. Watts in 1916 [204]. Coating Raney2 is new, and differs only in the choice of counter electrode. It is our aim to present evidence for the profound and beneficial effects this produces for the performance and longevity of the coating.

Coating	Substrate	Coating	Electrodeposition Counter-electrode
Raney1	316SS	Ni/Zn	Graphite rod
Raney2	316SS	Ni/Zn	316SS

Table 5.1: The two electrolcatalytic coatings compared in this study, which differ only in the choice of counter-electrode used during electrodeposition. 316SS = 316-grade stainless steel.

5.1.1 Intermittency and Corrosion

In the field of alkaline water-splitting electrolysis, it is recognised that insufficient attention has been paid to long-term system performance when driven from variable and discontinuous renewable energy sources. To quote from Chapter 8 of *Hydrogen Production by Electrolysis* (edited by Agata Godula-Jopek):

> it seems fair to say that the detrimental effects of intermittent operation, frequent start, fluctuating input power and stop and low duty operation have not received enough attention from the water electrolysis community [205]

The aim of this study is to add to this highly practical area of research by focussing on the performance of electrocatalytic coatings when subjected to a simulated intermittent environment, whereby ageing may be achieved over reduced time-scales [162].

In very long-term studies completed between 1989 and 1994, some running to more than 10 000 hours, it was reported by Divisek *et al*. that a Ni/Al Raney nickel cathode experienced 'complete destruction' when subjected to electrolyser shutdown [131], forcing the authors to conclude that "the only catalytic coating resistant to depolarization consists of the metals of the Pt group". A Raney coating based on zinc fared little better, and in bi-polar operation

"to avoid major deterioration, the cells were polarized with a protective current" [206], i.e. a permanent back-up power supply was required to permit the electrolyser to cope with intermittent usage. Although some protective effect was discovered via the incorporation of Mo into the coating, this protection was only temporary.

When the power input to a water-splitting electrolyser is interrupted, the electrodes will have stored charge within them in the form of capacitances, adsorbed species, ionisation changes and as chemically altered compounds. As the electrodes subsequently discharge this can lead to corrosion currents that will selectively leach out vital components of the catalytic coating. If this process continues far enough, it can lead to the sort of 'complete destruction' reported by Divisek *et al.* [131]. The possibilities for discharge currents are greater in bipolar electrode stacks, because the presence of electrolyte side-channels running through the stack mean that there are many possible electrolyte pathways by which currents can flow. Some of these will be connecting electrodes at greatly differing voltages, which could permit the corrosion of components which would otherwise be stable. Despite this, the current study focuses on a monopolar design, due to its simplicity.

Corrosion will also be considerably different at the anode and cathode. Since metals form positively charged ions in solution, their dissolution is associated with loss of electrons i.e. anodic oxidation. During continuous operation, such as in a commercial electrolyser, the water-splitting reactions dominate, and the corrosion rate of a well-designed electrode can be minimal. During discharge, reverse currents can flow, and it is therefore the cathode that can experience the greatest rate of corrosion, especially of components that have the most negative electropotential such as zinc, which are therefore the most stable in solution [203, 207]. Charting what changes occur, how these affect the performance of the electrocatalytic coating, and how they may potentially be avoided is of great interest to the goal of harnessing intermittent renewable energy to power the hydrogen economy.

5.2 Materials and Method

All procedures were conducted in standard laboratory 100 ml beakers. Such beakers are large enough to accommodate up to two 4 cm × 4 cm paddle-shaped stainless-steel electrodes, as shown in Figure 5.1. For Raney2 the graphite rod counter electrode is exchanged for one made from 316-grade stainless-steel, which is partially consumed during the deposition, thereby progressively altering the composition of the coating.

Pretreatment The 4 cm × 4 cm stainless-steel electrode was degreased in hot 25 wt% NaOH for 1 minute, then submerged in 18 wt% HCl for 1 minute at room temperature, before being placed in 70 wt% H_2SO_4 for 3 minutes at an anodic current of 108 mA m^{-2}. Lastly the electrode was placed in a Nickel Strike solution consisting of 240 g l^{-1} $NiCl_2 \cdot 6\,H_2O$ and

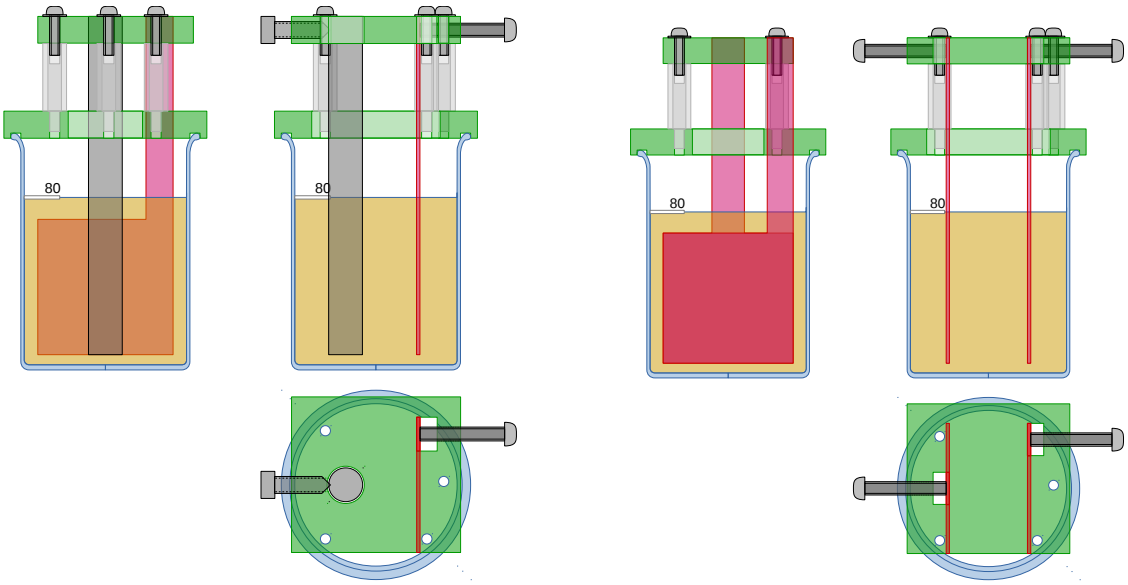

(a) Raney1 deposition (b) Raney2 deposition

Figure 5.1: Mechanical drawings of the electrodeposition chambers for a) Raney1, which employs a graphite rod counter-electrode and b) Raney2, which employs a 316-grade stainless steel counter-electrode. Both chambers were primarily constructed using laser cut acrylic components, plus a standard 100 ml laboratory beaker

120 ml l^{-1} HCl for 5 minutes at a cathodic current of $-26.8\,mA\,cm^{-2}$. Between each step the electrode was rinsed with deionised water, and the air-exposure time between each step kept to a minimum. At this point the electrode was covered in a thin, adherent coating of nickel that is able to act as a base for any subsequent functional coatings [197].

Functional Coating The electrode was immersed in a modified Watt's Bath consisting of 330 g l^{-1} $NiSO_4 \cdot 6\,H_2O$, 45 g l^{-1} $NiCl_2 \cdot 6\,H_2O$, 37 g l^{-1} H_3BO_3 and 20 g l^{-1} $ZnCl_2$ at 50 °C for 60 minutes at a cathodic current of $-50\,mA\,cm^{-2}$. During this procedure, for Raney1 the graphite rod experienced no corrosion, whereas for Raney2 the 316SS counter electrode experienced high levels of pitting and corrosion, and a black sediment accumulated. The sediment appeared at times to influence the quality of the coating. The typical appearance of the Raney2 coating was shown in Figure 5.2 (left).

5.2.1 Three electrode experiments

All 3-electrode experiments were conducted on an Ivium n-Stat potentiostat, connected to a laminated electrolytic cell, chiefly comprised of laser-cut acrylic plastic, as shown in Figure 5.2 (right), which is similar to previous test cells [16].

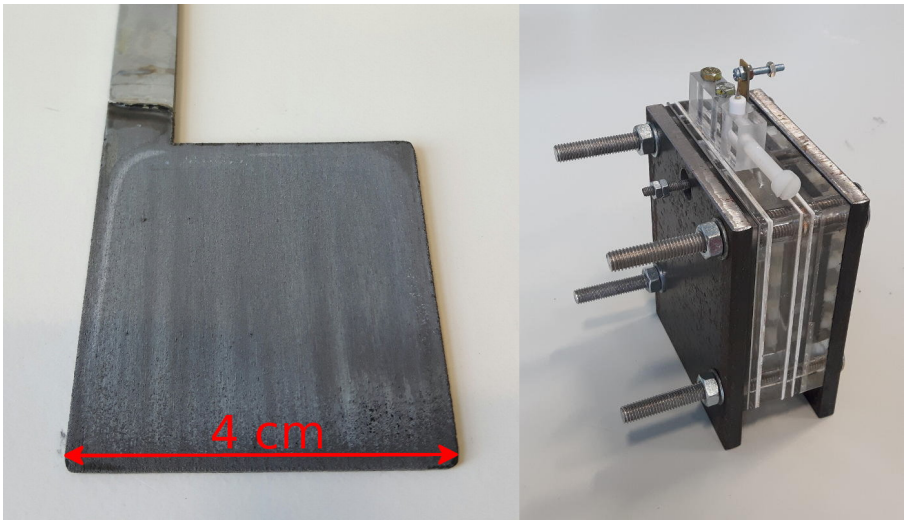

Figure 5.2: Raney2 electrode (left) and as assembled into the three-electrode cell (right)

The exposed area of the working electrode (WE) was 3 cm × 3 cm, the counter electrode was a 316 stainless-steel plate (of which 6 cm × 6 cm was exposed), and the reference electrode (RE) was a commercial design involving a Ag/AgCl wire suspended in 3 M KCl. The distance between working and counter electrodes was approximately 15 mm. The electrolyte was 0.5 M NaOH (standard reagent grade) and deionised water was used throughout. Before each experiment the RE was checked against a standard calomel electrode (SCE), and the electrolyte was bubbled with nitrogen for 10 minutes to reduce dissolved oxygen. All experiments were conducted at laboratory ambient temperature, which was 20 ±1 °C. The overpotentials were calculated according to the method in Experiment 4.2 on page 145.

5.3 Results

Experiment 5.1: The electrical performance of an old sample of 316SS used as an anode was as shown in Figure 5.3.

Initially the performance of the electrode was quite poor, but after 3 days immersed in the electrolyte the sample showed an improvement for OER overpotential of about 100 mV. The precise cause of this improvement is not known, but this result serves to highlight how the electrical performance of an electrode is not simply a function of the material from which it is made, but also of its history.

Experiment 5.2: A coating of $Ni_{0.8}Fe_{0.2}O_xH_y$ is simple to deposit in a one-step electrodeposition procedure, as well as being one of the best reported catalysts for OER [125]. The deposition bath consisted of a mixture of 0.095 M $Ni(NO_3)_2$ and 0.005 M $FeCl_2$, with the

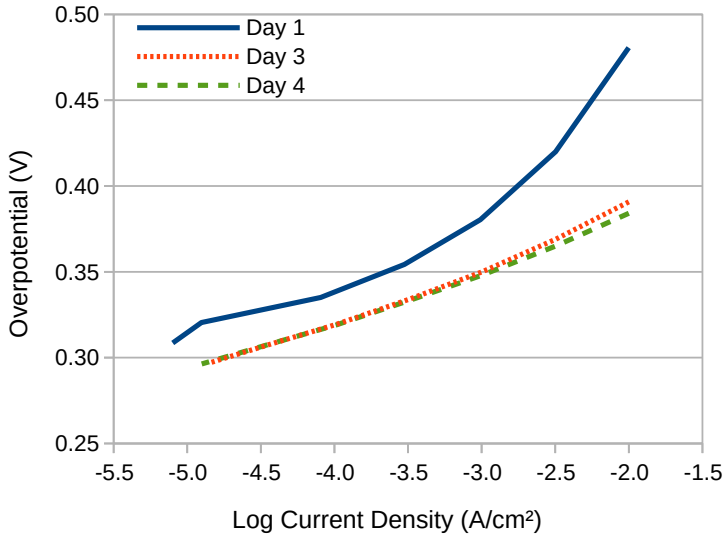

Figure 5.3: Electrical performance of old sample of uncoated 316SS used as an anode in 0.5 M NaOH. A marked improvement is observed over 3 days.

electrodeposition consisting of 30 s at $-0.1\,\mathrm{mA\,cm^{-2}}$. The measured activity for OER was as reported in Figure 5.4.

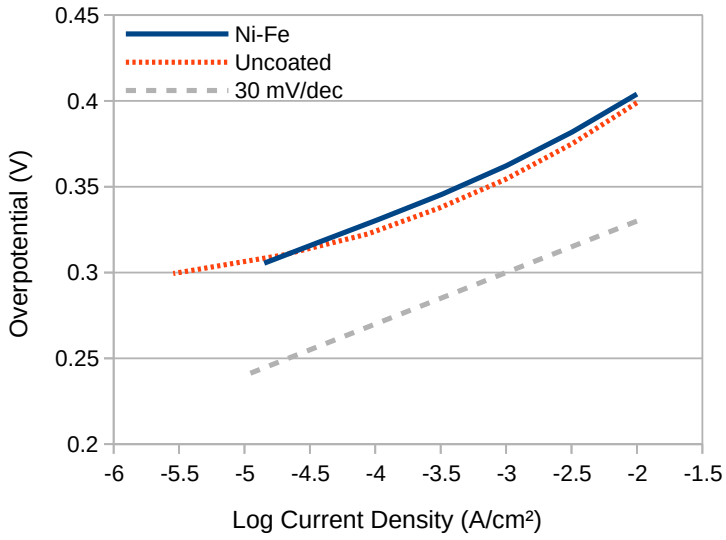

Figure 5.4: OER activity of 316-grade stainless-steel before and after Ni-Fe deposition.

The performance of the stainless-steel anode was therefore certainly no better after coating with nickel iron hydroxide than it was before. It is possible this is because the coating did not adhere to the stainless-steel. After even a brief exposure to air, stainless-steel develops a thin layer of oxide, and as such is a difficult material on which to deposit coatings of any variety. Removal of the oxide was therefore ultimately key to obtaining adherence, and specific procedures were sought to achieve this.

Experiment 5.3: The choice of counter electrode material can have a profound influence on the resultant electrodeposited coating. The variation of the electrodeposition voltage, at a constant current of $-50\,\mathrm{mA\,cm^{-2}}$, was as shown in Figure 5.5.

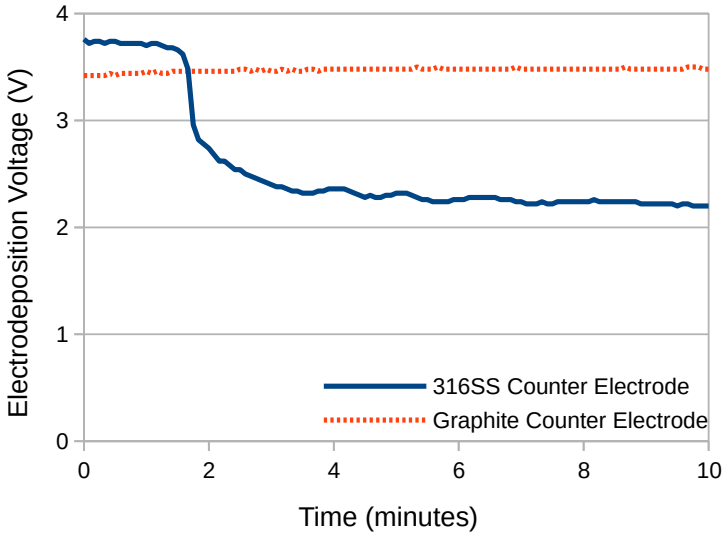

Figure 5.5: Variation of deposition voltage during first 10 minutes for two different counter electrode materials

Because the graphite electrode did not corrode, the voltage remained constant at about 3.5 V, and thereafter remained so throughout the 60 minute deposition. By contrast, the stainless-steel counter electrode corroded extensively, with a sudden drop in voltage of 1.5 V occurring after 2 minutes. It was clear that the stainless-steel counter electrode was being corroded, and it was these corrosion products which lowered the resistance of the electrodeposition bath, which resulted in the drop in voltage.

Experiment 5.4: A typical result for linear sweep voltammetry on a Raney nickel cathode was as shown in Figure 5.6, and an anode in Figure 5.7.

Both plots show that the slope of the iR-corrected voltage becomes almost vertical above $20\,\mathrm{mA\,cm^{-2}}$, which is to be expected since a typical Tafel slope is just a few tens of millivolts per decade. To achieve the most consistent results the sweep rate was set to $1\,\mathrm{mV\,s^{-1}}$, which was the lowest setting possible on the Ivium potentiostat, but which took more than 15 minutes per volt.

When redrawn as Tafel plots, both results tend towards a straight line, as indicated by the dashed grey lines, which is Tafel-like behaviour. For the cathode the slope is low at $60\,\mathrm{mV\,dec^{-1}}$ and very close to zero overpotential (at most $-20\,\mathrm{mV}$). For the anode the slope is also low at $68\,\mathrm{mV\,dec^{-1}}$, but the linear region begins at a much higher overpotential of 0.3 V.

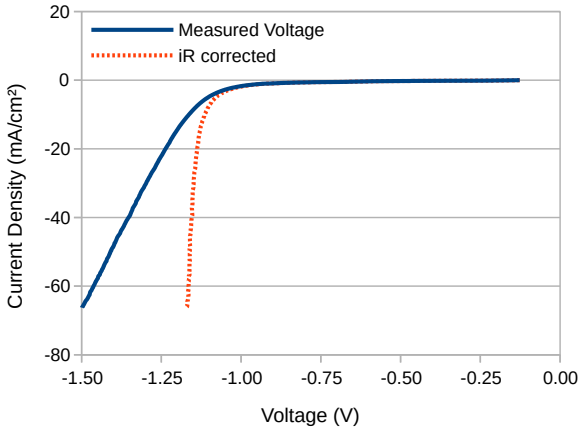

(a) LSV

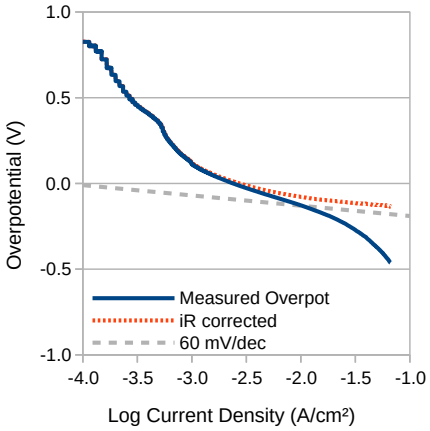

(b) Redrawn as a Tafel plot

Figure 5.6: Linear sweep voltammetry of Raney nickel cathode in 1 M KOH at $1\,\mathrm{mV\,s^{-1}}$.

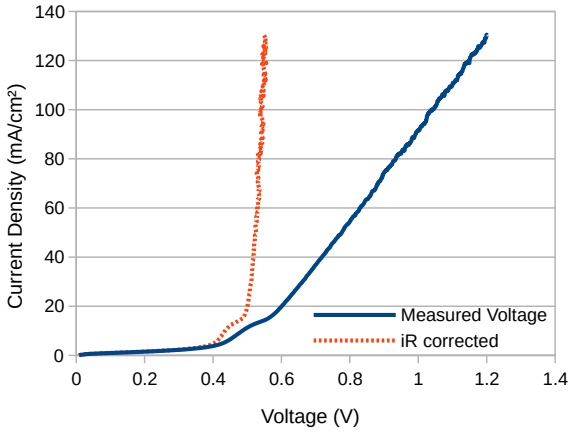

(a) LSV

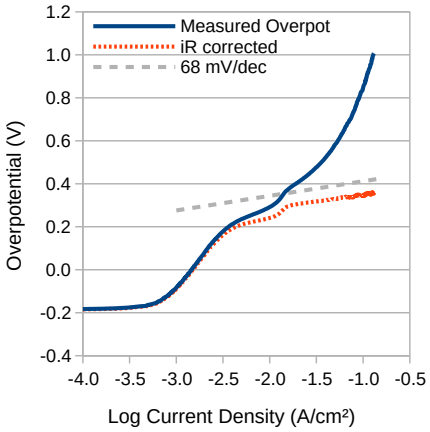

(b) Redrawn as a Tafel plot

Figure 5.7: Linear sweep voltammetry of Raney nickel anode in 1 M KOH at $1\,\mathrm{mV\,s^{-1}}$.

Although the Tafel slopes are low, they are not consistent with results from chronopotentiometry (see Experiments 5.9 and 5.8 on page 177), which are slightly lower and more consistent with theory [42]. This is because chronopotentiometry spends one or more minutes at each current setting before taking a voltage measurement, and is therefore a more reliable technique.

Experiment 5.5: A typical result for cyclic voltammetry on a Raney nickel anode is as shown in Figure 5.8.

On the anodic sweep of cycle 1, the current remained close to zero until the voltage reached 0.5 V, at which point a distended peak was observed. The peak became clearer on cycle 2, which implies that irreversible changes were occurring. The voltage gap between

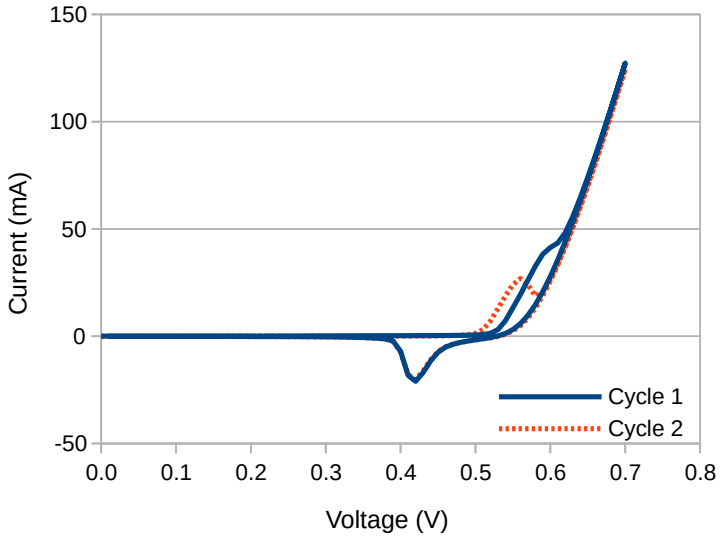

Figure 5.8: Cyclic voltammetry of Raney2 anode. Sweep rate: 10 mV s^{-1}

the two ionisation peaks on cycle 2 was 140 mV. This supports this view, since if the change were fully reversible, the gap between the peaks would be 59 mV/n, where n is the number of electrons involved in the redox reaction. Above 0.6 V the electrode evolved oxygen. On the cathodic sweep a de-ionisation peak was observed at 0.42 V, which was consistent for both cycles.

The ionisation peaks are associated with the $Ni(OH)_2/NiOOH$ redox couple, and therefore a change in the ionisation state of nickel from $+2$ to $+3$, with the separation of 140 mV being in broad agreement with published data [208]. Repeated potential cycling, and the associated deprotonation and reprotonation, is known to lead to an increase in the thickness of both the $Ni(OH)_2$ layer, and the NiO layer that sits beneath it [44]. This further supports the view that irreversible changes were occurring, not just at the surface of the electrode, but also below.

Experiment 5.6: A typical result for cyclic voltammetry on a Raney nickel cathode is as shown in Figure 5.9a.

On the cathodic sweep of cycle 1 the current remained negative, and below -1.1 V the electrode was evolving hydrogen. However, on the anodic sweep the current went positive at -1 V, which means that the electrode was supplying electrical power. This continued until the voltage reached -0.75 V on cycle 2.

Since power is equal to current times voltage, it is possible to integrate the total electrical power supplied by the electrode between these two points. However, the voltage must be corrected for iR losses, as shown in Figure 5.9b, for which it is helpful to refer to the schematic diagram shown in Figure 5.10a.

The potentiostat is represented by an amplifier, which continually alters the voltage of

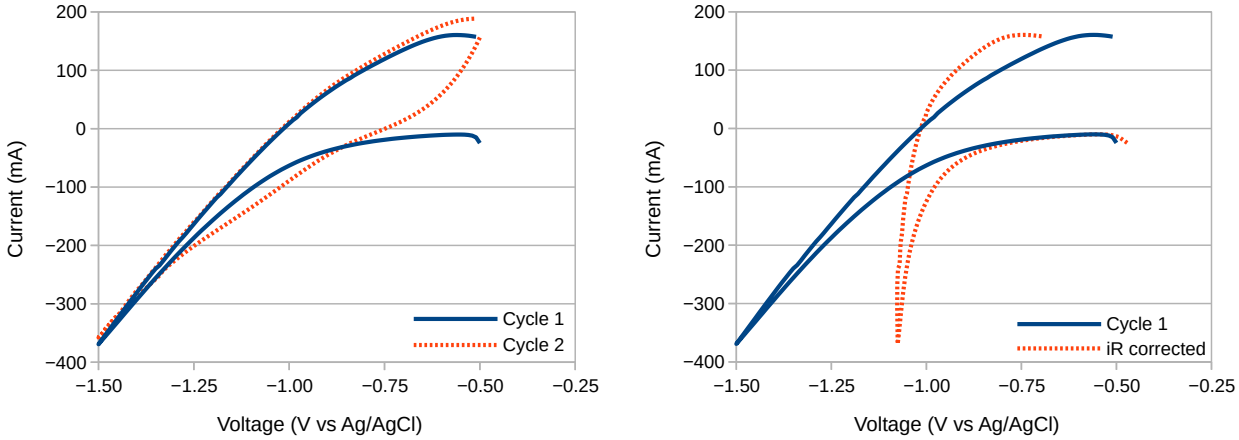

(a) Cyclic voltammetry

(b) First cycle with iR-correction

Figure 5.9: Cyclic voltammetry of a Raney2 cathode, starting at $-0.5\,\mathrm{V}$. All sections with negative voltage and positive current are due to capacitance and hydride formation. Sweep rate: $10\,\mathrm{mV\,s^{-1}}$

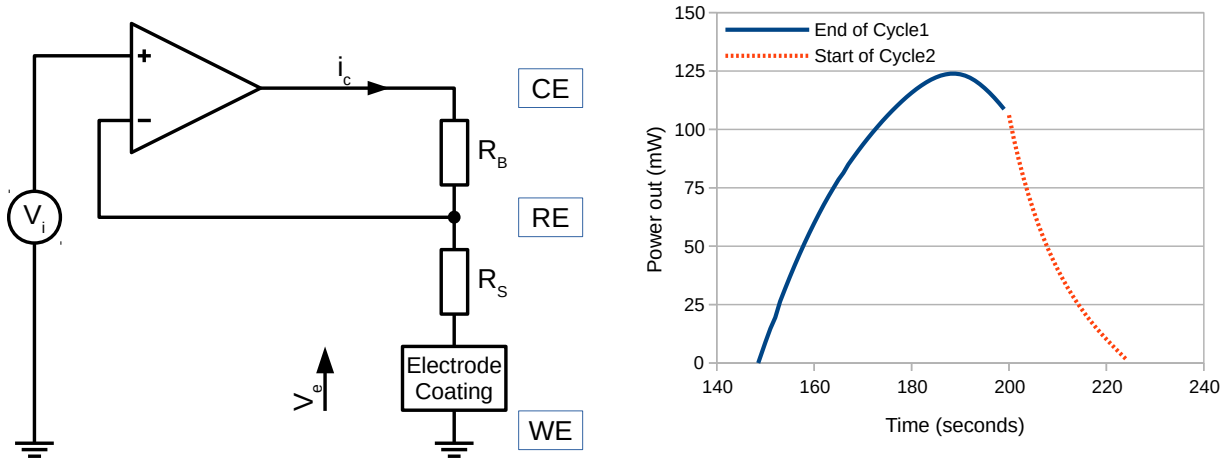

(a) Schematic diagram of potentiostat

(b) Power out from electrode coating

Figure 5.10: Schematic diagram of potentiostat.

CE until the difference between RE and WE is equal to the desired input voltage V_i. No current passes into the negative input of the amplifier since it is high impedance, and in fact on the Ivium potentiostat it is maintained as an 'active' high impedance of at least $1\,\mathrm{T\Omega}$

The solution resistance R_S of the electrolyte between RE and WE is known from EIS, based on the valid assumption that the electrode coating is a short-circuit at high-frequency. Regardless of the sign of i_c, this permits V_e to be calculated as:

$$V_e = V_i - i_c R_S \tag{5.3}$$

which is the equation for standard iR correction. Note that if i_c is of opposite polarity to V_i, then V_e will be *larger* than V_i. If at any time V_e and i_c are of opposite polarity, this means

that the electrode coating is generating electrical power, and the total energy out can be calculated by integrating the product of the two:

$$E_{e,out} = -\int V_e(t) i_c(t) dt \tag{5.4}$$

which is equivalent to measuring the area under the curve in Figure 5.10b. When this is done, a figure of 5.5 J is produced, which is the same as a 560 g weight lifted to a height of 1 m.

By contrast, when the same coating was used as an anode (in Experiment 5.5) the current and voltage were only in opposition during the brief de-ionisation peak, with the result that the total electrical power generated by the coating during discharge was just 50 mJ. This is less than 1% of the energy stored when the coating is used as a cathode.

It is therefore possible to state that at least 99% of the energy stored by the Raney nickel coating when used as a cathode is not due to any intrinsic electrical properties (such as capacitance), since the same storage would occur when used as an anode. Instead the energy storage must be due to ionic or chemical alteration, such as the formation of nickel hydride, which is known to occur with nickel cathodes [209].

Experiment 5.7: Chronoamperometry results for a Raney2 cathode at −2.5 V over the course of 24 hours were as presented in Figure 5.11a.

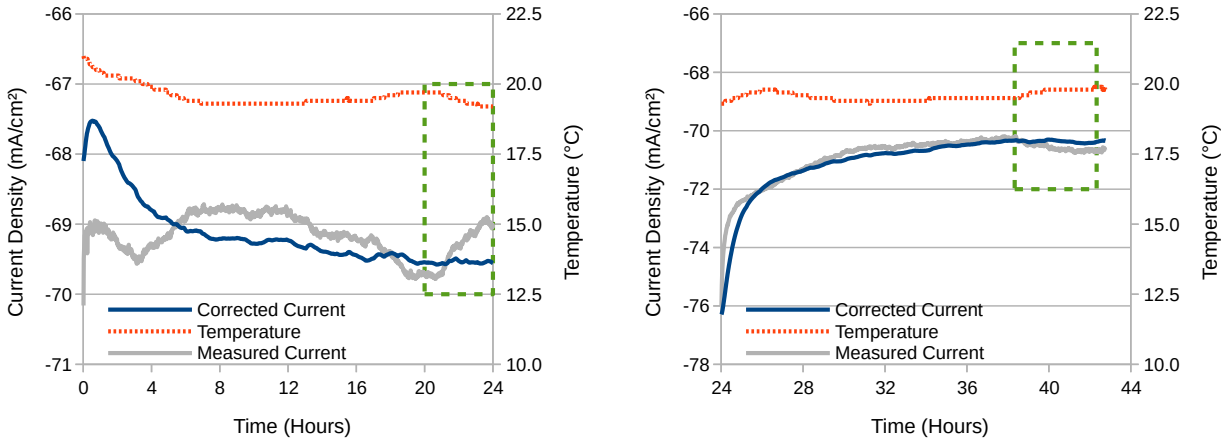

(a) 0 to 24 hours

(b) 24 to 42 hours

Figure 5.11: Chronoamperometry results for a Raney2 cathode over a total of 42 hours at −2.5 V. Electrolyte: 1 M NaOH; Circulation: pumped. The temperature correction is based on the data within the dashed green rectangles.

The results show that the measured current is a strong function of temperature, therefore temperature correction and some smoothing has been performed to assist interpretation. The corrected current fell for about the first hour, but then gradually climbed for the next 23

hours, but was in general constant to within a few percent. The coating was therefore stable within this limited time frame.

The experiment was extended for a further 18 hours with no significant alteration of outcome, as shown in Figure 5.11b. This result is not unexpected, since similar coatings have survived for thousands of hours [195, 206, 210].

Experiment 5.8: The electrical performance of a Raney2 nickel cathode was as presented in Figure 5.12.

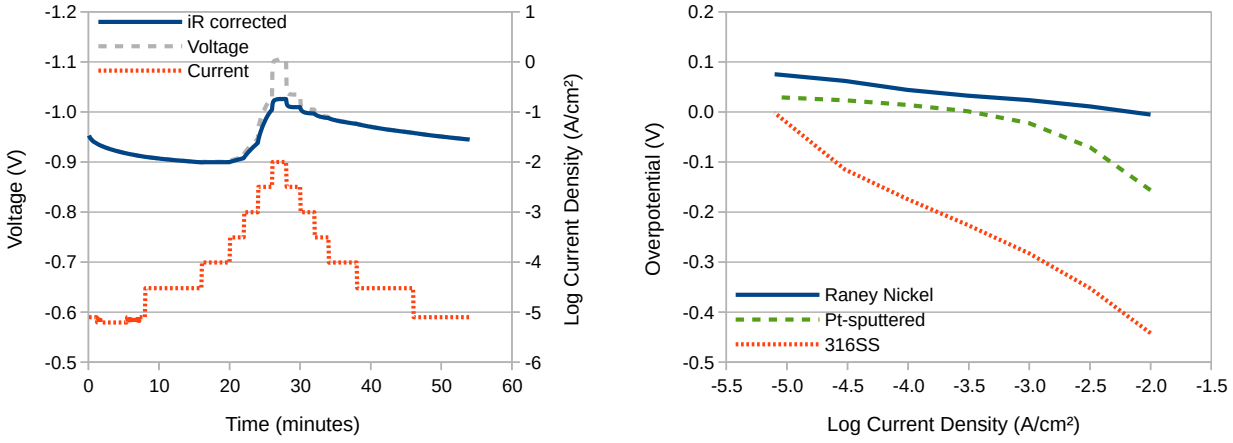

(a) Chronopotentiometry

(b) Tafel plot

Figure 5.12: Electrical performance of Raney nickel cathode

.

In the chronopotentiometry the voltage did not have enough time to stabilise at currents below $10^{-3.5}$ A cm^{-2}, despite the acquisition lasting nearly an hour. This is due to the large amounts of nickel hydride formed during hydrogen evolution. As a result, the Tafel plot appears to exhibit *non-negative overpotentials*. These are not due to the evolution of hydrogen, but instead to the breakdown of nickel hydride, and should be interpreted accordingly.

The Tafel plot includes curves for uncoated and Pt-sputtered 316SS taken from Experiment 4.4 on page 147, and it is noteworthy that the Raney nickel coating was able to comfortably outperform both. Since Ni is certainly not more catalytically active than Pt for HER, this indicates that Raney nickel must have far more surface area.

Experiment 5.9: The electrical performance of a Raney2 nickel anode was as presented in Figure 5.13.

Due to the absence of nickel hydride, the chronopotentiometry measurement only needed to run for 15 minutes to obtain stable voltage readings. The Tafel plot shows that the catalytic performance is better than for the uncoated 316SS, but only by about 50 mV.

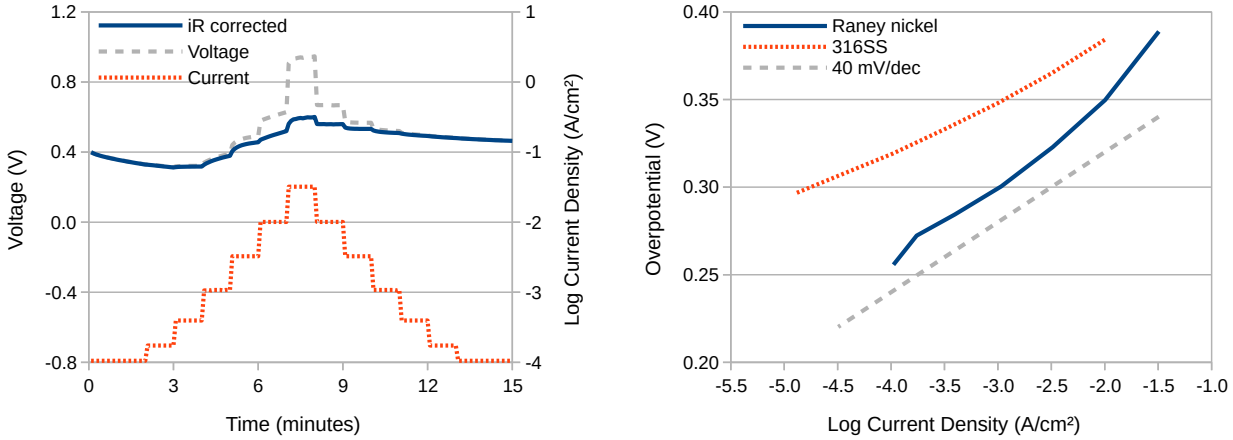

(a) Chronopotentiometry

(b) Tafel plot

Figure 5.13: Electrical performance of Raney nickel anode

.

Considering that the surface area of the nickel is so much larger, this is a surprising result, and shows how good uncoated 316SS is by itself as an electrode for oxygen evolution.

Experiment 5.10: The progressive formation of a layer of nickel hydride can be deduced by observing the behaviour of a Raney nickel cathode undergoing '2on2off' accelerated ageing, as shown in Figure 5.14.

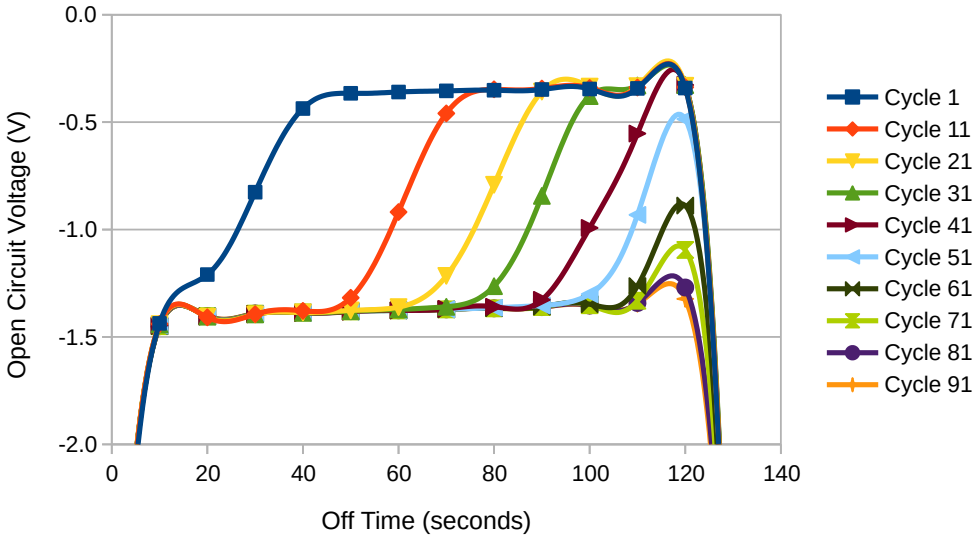

Figure 5.14: Open-Circuit voltage plotted against time during successive 'off' periods for a Raney nickel cathode undergoing '2on2off' accelerated ageing.

The figure plots the open-circuit voltage during the 'off' periods against time, and shows that the voltage initially rises to $-0.4\,\mathrm{V}$, where it remains until the next 'on' period begins. However, as the number of cycles increases, the voltage spends an increasing amount of

time at $-1.4\,\mathrm{V}$ before rising to $-0.4\,\mathrm{V}$, before finally, after about 90 cycles, spending the whole 'off' period at $-1.4\,\mathrm{V}$. Thereafter there is no further change in behaviour.

The explanation is the build-up of a layer of nickel hydride, which increases in thickness with each passing cycle of '2on2off' accelerated ageing.

5.3.1 Accelerated Ageing Experiments

The two coatings Raney1 and Raney2 underwent accelerated ageing experiments for HER and OER, thereby resulting in four sets of experiments. Note that since the experiments on Raney2 were conducted *before* those on Raney1, and therefore to better assist in interpreting the logical train of thought, that is the order in which the results are presented.

Experiment 5.11: The performance of two electrolytic cells each containing a Raney2 anode over 2000 cycles of '2on2off' accelerated ageing at $200\,\mathrm{mA\,cm^{-2}}$ was as shown in Figure 5.15.

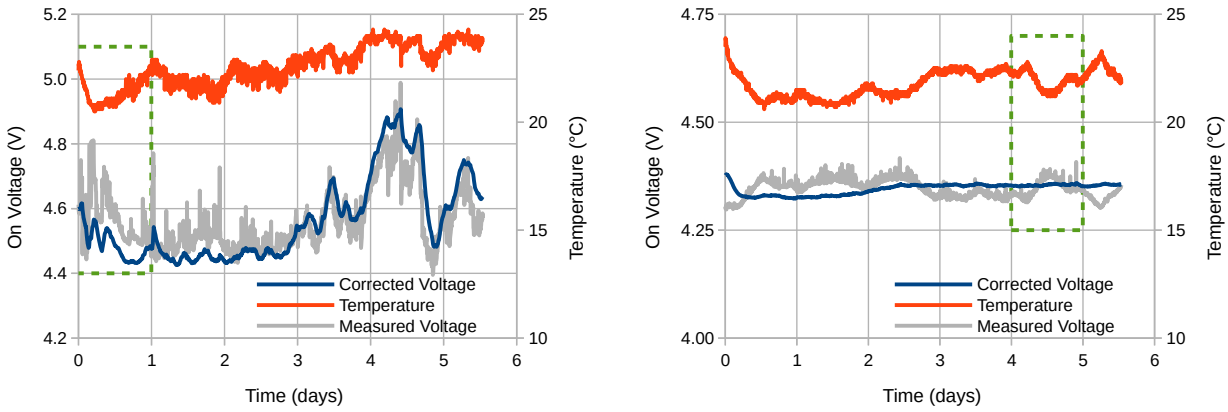

(a) Raney2 Anode #1

(b) Raney2 Anode #2

Figure 5.15: 2on2off accelerated ageing results for two electrolytic cells, each containing a Raney2 anode. Electrolyte: 0.5 M NaOH; Membrane: Zirfon; Circulation: none; Apparatus: displacement tube. The temperature correction is based on the data within the dashed green rectangles.

Both experiments were conducted using the displacement tube (as described in section 4.2.1 on page 135) and under the same conditions. However, for the cell containing Raney2 Anode #1 the voltage was much more variable, particularly for the last three days. The reasons for this are not known, but nevertheless the results for the cell containing Raney2 Anode #2 demonstrate that the temperature correction principle is sound. In any case, both sets of results indicate that the voltage of the electrolytic cell remained stable.

On retrospect, a more direct relationship between temperature and voltage would have been maintained had pumped electrolyte circulation been employed. However, there is no reason to believe that its absence was significant in any other respect, since vigorous gas evolution produces its own circulation.

The Tafel plots before and after accelerated ageing were as shown in Figure 5.16.

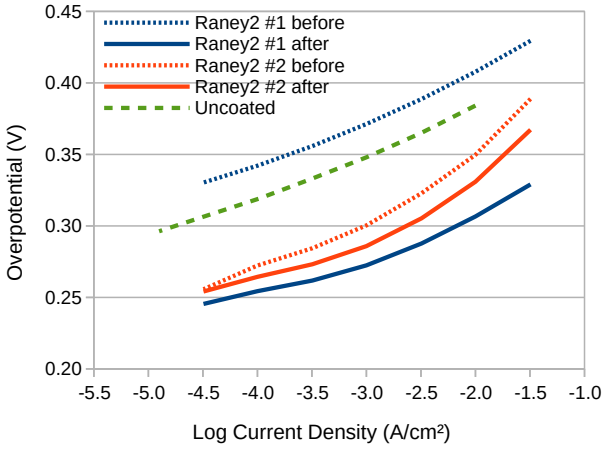

Figure 5.16: Tafel plots for two Raney2 anodes before and after 2on2off accelerated ageing.

Both anodes showed an improvement after ageing, which may have been due to an increase in surface area. To investigate this, a measurement of the double-layer capacitance was performed using cyclic-voltammetry, with the results as presented in Table 5.2.

	Before		After		
	C_{DL}	RF	C_{DL}	RF	Ratio
Electrode #1	546 mF	1,517	2.76 F	7,667	5.1
Electrode #2	3.43 F	9,528	9.73 F	27,028	2.8

Table 5.2: Double-layer capacitance and roughness factor for two Raney2 anodes before and after accelerated ageing.

The Tafel plots show that Electrode #1 improved by a lot more than electrode #2, but that is because it started from a lot further back. This is confirmed by the measurements of roughness factor (RF), which show that the surface area of electrode #2 increase by a factor or 2.8, whereas that of electrode #1 increased by more than a factor of 5.

Inspection of the experimental records reveals this was due to a six week delay between deposition and initial characterisation. By contrast, the corresponding delay for electrode #2 was just 1 day. This result is in agreement with that observed for uncoated 316SS in Experiment 5.1 on page 170, and highlights how electrodes can quickly recover from periods of non-use.

The total improvement over the uncoated material was approximately 50 mV, which is nonetheless significant since it equates to an increase of more than a factor of ten in current density. The roughness factor of electrode #2 after ageing was more than 27,000, which is the largest figure produced during the course of these experiments. It shows that Raney nickel can be used to produce a surface area which is within the range expected of a supercapacitor, which can be up to 100,000 [211].

Experiment 5.12: The performance of an electrolytic cell containing a Raney2 cathode over 2000 cycles of '2on2off' accelerated ageing at $-200\,\mathrm{mA\,cm^{-2}}$ was as shown in Figure 5.17a.

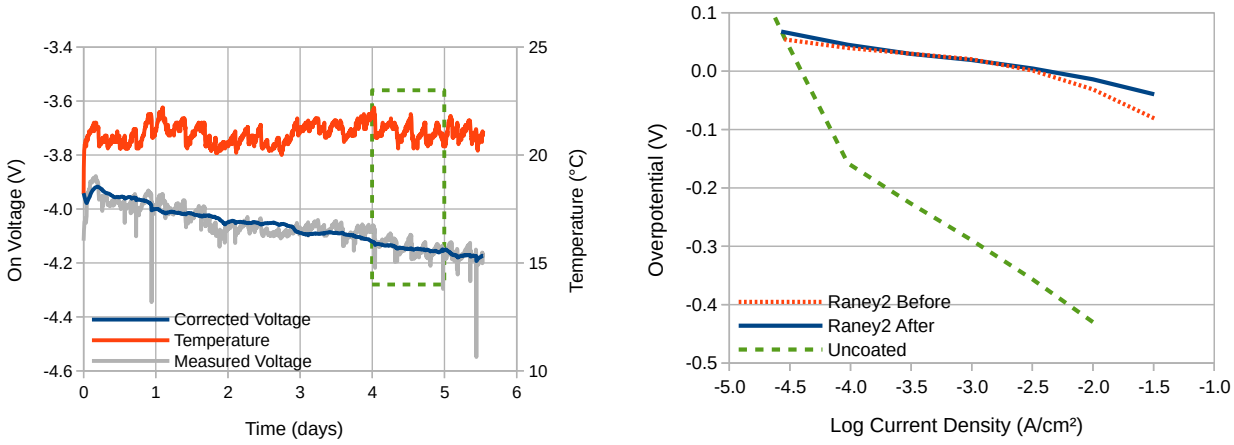

(a) On voltage and temperature

(b) Tafel plots

Figure 5.17: 2on2off accelerated ageing results and Tafel plots for an electrolytic cell containing a Raney2 cathode. Electrolyte: 0.5 M NaOH; Membrane: Zirfon; Circulation: none; Apparatus: displacement tube. The temperature correction is based on the data within the dashed green rectangle.

The cell showed a general decrease in performance over the six day experiment of about $-200\,\mathrm{mV}$. However, since these results are for a two-electrode experiment, it is not possible to state whether this decrease in performance was due to the cathode, or to some other part of the apparatus.

To assess this, 3-electrode measurements were conducted on the Raney2 cathode before and after ageing, as presented in the form of Tafel plots in Figure 5.17b. The appearance of a Raney2 cathode before and after ageing was as shown in Figure 5.18, and the measurements of double-layer capacitance and roughness factor were as reported in Table 5.3.

	Before		After		
	C_{DL}	RF	C_{DL}	RF	Ratio
Electrode #1	442 mF	1,228	1.06 F	2,944	2.4

Table 5.3: Double-layer capacitance and roughness factor for a Raney2 cathode before and after accelerated ageing.

The results show that there was a slight improvement in 3-electrode performance after accelerated ageing, which is in agreement with all similar results. It is also in agreement with measurement of the roughness factor, which increased by a factor of 2.4. It is concerning that despite the *increase* in performance of the cathode, the electrolytic cell exhibited a *decrease* in performance, the explanation for which is not known. However, it can be stated

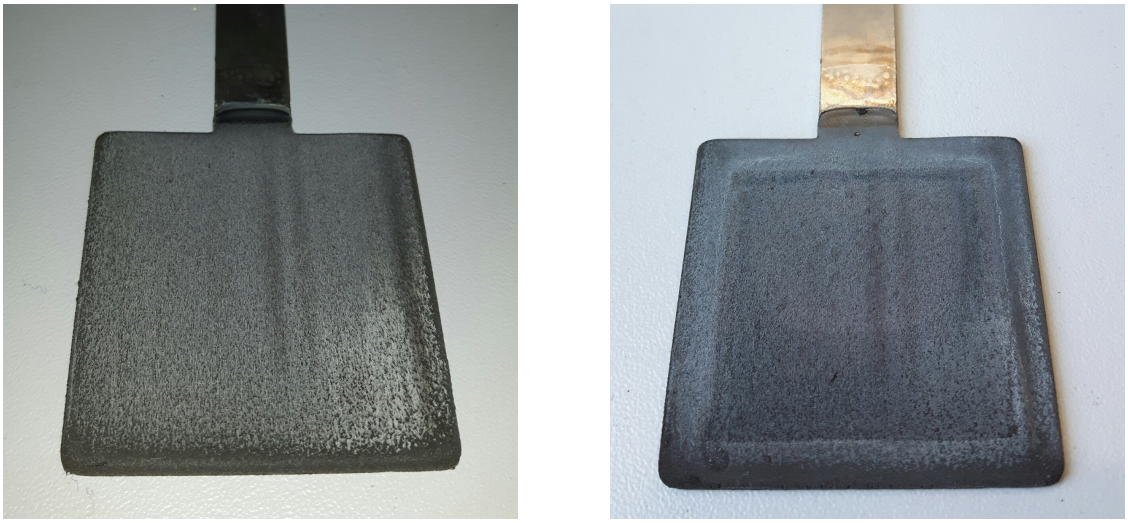

(a) Before (b) After

Figure 5.18: Appearance of a Raney2 cathode before and after accelerated ageing.

that after ageing the Raney2 cathode was able to sustain a current density of $10^{-1.5}$ A cm^{-2} (-32 mA cm^{-2}) at a hydrogen evolution overpotential of just -40 mV.

At lower current densities the overpotential became *non-negative* due to the breakdown of nickel hydride. Therefore, the only reliable overpotential figure is that taken at the highest current density, where the rate of hydrogen evolution far exceeded the rate of nickel hydride breakdown. Analysis of the chronopotentiometry data reveals that the voltage was still changing when this Tafel measurement was taken, but only at a rate of -2 mV min^{-1}. Therefore, despite the confounding presence of nickel hydride, the headline overpotential figure is considered sufficiently reliable for publication.

Experiment 5.13: The performance of an electrolytic cell containing a Raney1 anode was as shown in Figure 5.19a, with the corresponding 3-electrode performance of two anodes as presented in Figure 5.19b. The measurements of the double-layer capacitance and roughness factor of two Raney1 anodes were as presented in Table 5.4.

	Before		After		
	C_{DL}	RF	C_{DL}	RF	Ratio
Electrode #1	–	–	3.99 F	11,083	–
Electrode #2	361 mF	1,003	713 mF	1,981	2.0

Table 5.4: Double-layer capacitance and roughness factor for two Raney1 anodes before and after accelerated ageing. The measurement for electrode #1 before ageing is missing.

In contrast to the cells containing the Raney2 anodes subjected to accelerated ageing in Experiment 5.11, the on voltage of the cell containing a Raney1 anode increased by 200 mV over the course of 2000 cycles. The reason for this is not known, since according to the Tafel

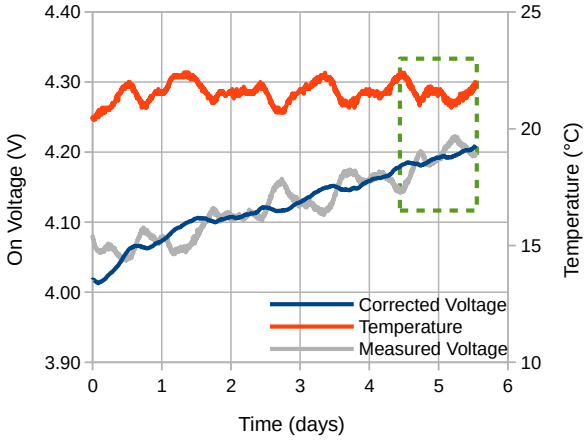

(a) On voltage of electrode #1

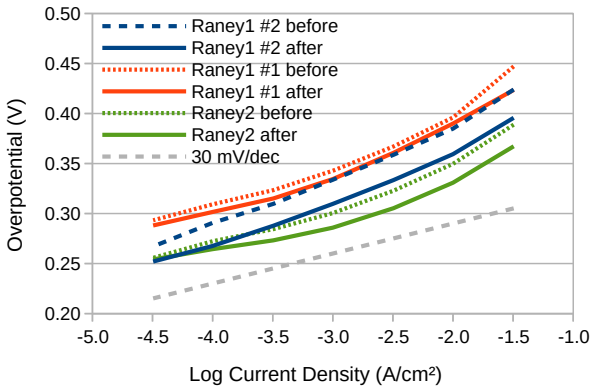

(b) Tafel plots

Figure 5.19: 2on2off accelerated ageing results and Tafel plots for electrolytic cells containing a Raney1 anode. Electrolyte: 0.5 M NaOH; Membrane: Zirfon; Circulation: none; Apparatus: displacement tube. The temperature correction is based on the data within the dashed green rectangle. The 2on2off results for electrode #2 were affected by a leak.

plots, the electrical performance of the anode improved slightly, a result which is consistent with that observed for the Raney2 cathode. The decrease in performance could be due to a deterioration of any part of the electrolytic cell, such as the cathode, but one that is prevented by the Raney2 anode. However, such theorising is pure conjecture.

The roughness factor of electrode #2 increased by a factor of two during the experiment, which is consistent with the observed improvement in performance. The value of capacitance is generally lower than for the Raney2 anode, but there is a large spread of values, which implies either that the deposition procedure could be more tightly controlled, or that the coating is sensitive to small variations in conditions.

Experiment 5.14: The performance of two electrolytic cells each containing a Raney1 cathode over 2000 cycles of '2on2off' accelerated ageing at $-200\,\mathrm{mA\,cm^{-2}}$ was as shown in Figure 5.20, with the corresponding 3-electrode performance of the cathodes as presented in Figure 5.21. The measurements of the double-layer capacitance and roughness factor of the cathodes were as presented in Table 5.5.

	Before		After		
	C_{DL}	RF	C_{DL}	RF	Ratio
Electrode #1	181 mF	503	164 mF	456	0.9
Electrode #2	189 mF	525	508 mF	1,411	2.7

Table 5.5: Double-layer capacitance and roughness factor for two Raney1 cathodes before and after accelerated ageing.

The discontinuity at the end of the third day for the cell with electrode #1 was due to

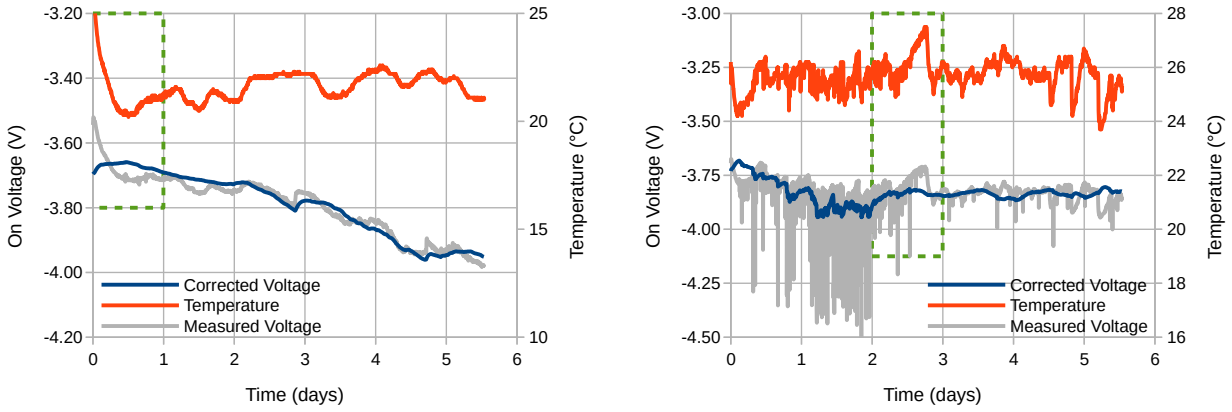

(a) Cell with electrode #1

(b) Cell with electrode #2

Figure 5.20: 2on2off accelerated ageing results for two electrolytic cells each containing a Raney1 cathode. Electrolyte: 0.5 M NaOH; Membrane: Zirfon; Circulation: none; Apparatus: displacement tube. The temperature correction is based on the data within the dashed green rectangles.

a leak from the Zirfon membrane, which required the electrolyte to be topped up. Both cells showed a slight increase in (temperature corrected) voltage of between −100 mV and −300 mV by the end of the experiment. This was consistent with the voltage increase shown by the cell containing the Raney2 cathode.

Electrode #1 was the only one not to show an increase in surface area. It is possible this result was atypical, since electrode #2 showed an increase by a factor of 2.7, which was consistent with other results.

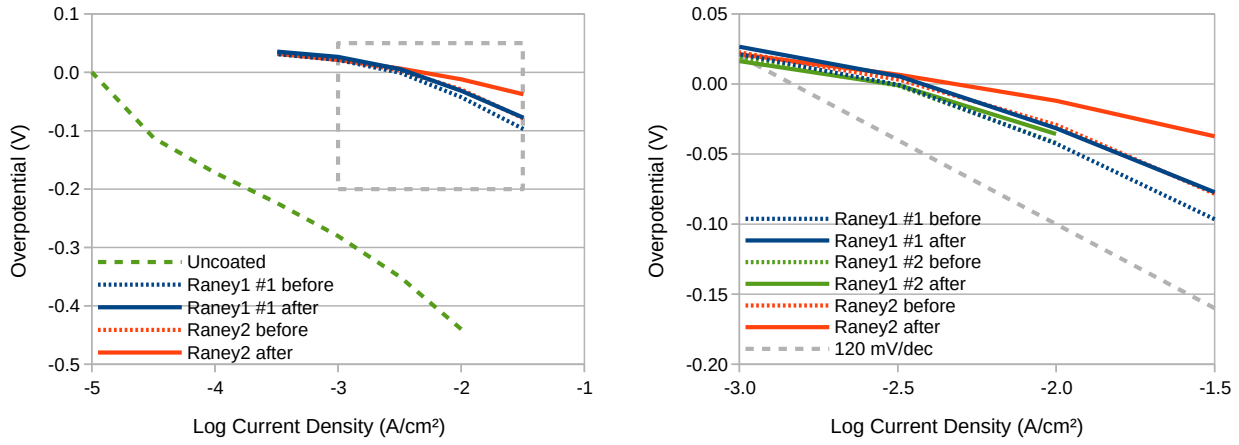

(a) Tafel plots

(b) Detail view of dashed grey box

Figure 5.21: Tafel plots for Raney1 cathode before and after accelerated ageing. Electrolyte: 0.5 M NaOH.

The 3-electrode measurements of the Raney1 cathodes show that their performance increased slightly after ageing, which is consistent with other results. There was also a very

high level of consistency, with different electrodes producing results which agreed to a few millivolts. The performance of the Raney1 cathodes was therefore good, but not as good as the Raney2 cathode.

In conclusion: Across all the ageing experiments, a consistent picture emerged that both the electrical performance and the surface area of Raney1 and Raney2 improved after ageing, for both OER and HER. However, Raney2 was initially more active than Raney1, *and* improved by more than Raney1, and had more surface area. The factor by which the surface area increased appeared to be consistent, and to be between 2 and 3.

(a) Before ageing (b) After ageing

Figure 5.22: Appearance of the Raney1 cathode before and after ageing.

The appearance of the Raney1 cathode before and after ageing was as shown in Figure 5.22. The electrode coating had developed a crack in the top right corner, and although it is not clear in the photograph, was bulging in three other locations. The coating was therefore detaching from the 316SS substrate.

This was symptomatic of a generally observed problem in obtaining adherence of the Raney1 coating to 316SS, especially when used for HER. For Raney2, close inspection of Figure 5.18b on page 182 in fact reveals the presence of a number of small bumps in the upper middle area of the electrode. This was the only occasion when the Raney2 coating showed signs of detachment (during normal use), and it is perhaps significant that this too was for HER.

5.3.2 Improved Coating Adherence

The ageing experiments highlighted the issue of poor coating adherence to 316SS, particularly for Raney1 and for HER. To assess whether adherence could be improved, stainless-steel that had been treated by wetblasting was investigated.

Wetblasting is an industrial process whereby abrasive particles mixed with a liquid are fired by compressed gas at a target in order to produce an improved surface finish. As a development from sandblasting, the inclusion of liquid was found to produce a more even finish across the workpiece. The use of glass beads typically leaves a polished finish, whereas alumina (as used here) is far more abrasive and leaves a matt finish.

Experiment 5.15: The appearance of 316-grade stainless-steel under SEM before and after wetblasting was as shown in Figure 5.23.

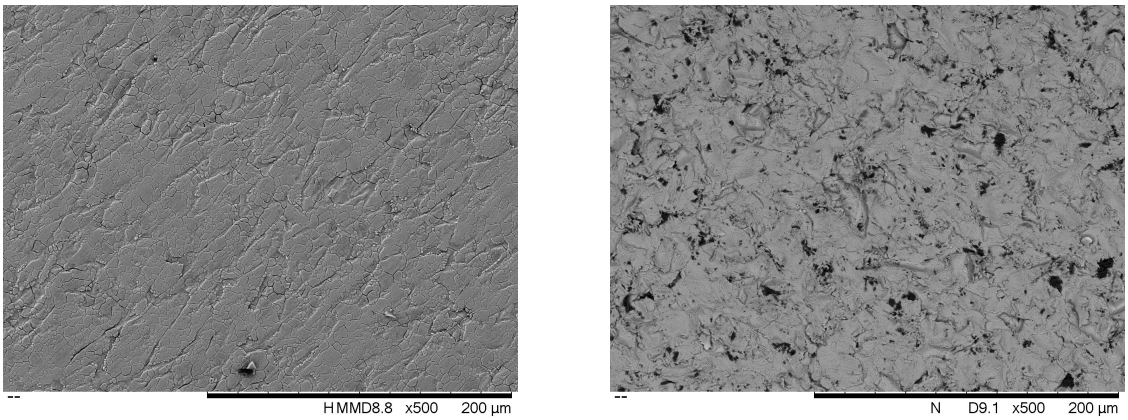

(a) Standard 316SS

(b) After wetblasting

Figure 5.23: Appearance at 500× magnification of 316-grade stainless-steel before and after wetblasting.

Before entering the SEM, the wetblasted steel had been sonicated in water for 10 minutes. Despite this, many small lumps remained of a material that produced few secondary electrons (therefore black). EDX analysis of one of the lumps produced the data presented in Table 5.6.

Element	Line Type	Weight %	Sigma	Atomic %
O	K series	46.26	0.24	56.23
Al	K series	43.62	0.22	31.44
Fe	K series	2.14	0.09	0.75
Cr	K series	0.58	0.05	0.22

Table 5.6: EDX analysis of one of the 'black lumps' in Figure 5.23b.

The analysis shows that the lumps consisted almost entirely of aluminium and oxygen, and were therefore confirmed as alumina, which was the abrasive material used by the

wetblaster. Many of the lumps were deeply embedded, which is understandable since they would have hit the surface of the steel with some velocity.

The double-layer capacitance and roughness factor measurements for the wetblasted stainless-steel were as presented in Table 5.7.

	Wetblasted		After 24 hours	
	C_{DL}	RF	C_{DL}	RF
Electrode #1	462 µF	1.3	959 µF	2.6

Table 5.7: Double-layer capacitance and roughness factor for a 316SS electrode after wetblasting.

The CV results show a very low RF of just 1.3 after wetblasting. However, this figure should be treated with some caution, since after a further 24 hours immersed in 0.5 M NaOH it had increased to 2.6. It is therefore likely that the double-layer capacitance was being artificially reduced by the presence of an insulating surface impurity, such as grease.

Despite the presence of the lumps of alumina, the finished appearance of the Raney1 coating after deposition and leaching appeared unaffected, as shown in Figure 5.24.

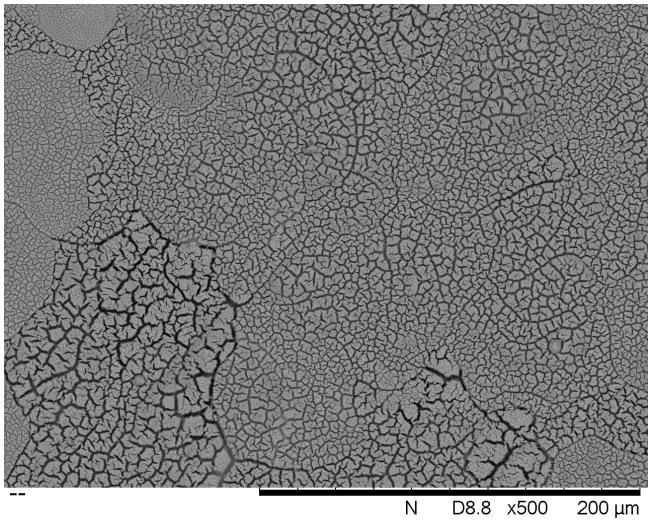

Figure 5.24: SEM micrograph of a Raney1/wetblasted-316SS cathode after deposition and leaching.

The visual appearance of a Raney1/wetblasted-316SS cathode before and after 2000 cycles of '2on2off' accelerated ageing at $-200\,\mathrm{mA\,cm^{-2}}$ was as shown in Figure 5.25.

The electrode did not show any indications that the Raney1 coating was detaching from the substrate. This was in contrast to the results obtained with non-wetblasted steel, as shown in Figure 5.22b. It may therefore be concluded that the wetblasting process has had a beneficial effect as regards coating adherence.

The pronounced colour change of the cathode was due to contamination with copper, as confirmed by EDX analysis, as presented in Table 5.8.

(a) Before ageing (b) After ageing

Figure 5.25: Appearance of the Raney1/wetblasted-316SS cathode before and after ageing.

Element	Line Type	Weight %	Sigma	Atomic %
Cu	L series	40.54	0.4	30.65
Ni	K series	31.18	0.3	25.52
O	K series	6.68	0.12	20.05
Zn	L series	17.4	0.36	12.78
C	K series	2.38	0.26	9.51

Table 5.8: EDX analysis of the Raney1/wetblasted-316SS cathode shown in Figure 5.25b.

This form of contamination occurred in many of the ageing experiments, both with Raney nickel and with TiN (see pages 153 and 158). The original source of the contamination is believed to be the 316-grade stainless-steel counter electrodes, although after many long-term ageing experiments, it may have become endemic in the apparatus, which was largely constructed of plastic. Its presence, although undesirable, appeared to have no negative impact on the electrical performance observed in any of the experiments.

Experiment 5.16: To determine the response of the Raney nickel coating to long periods of non-use, electrode #1 from Experiment 5.13 (on page 182) was reassessed after an interval of 15 months. During this time the electrode had been stored in a zip-lock plastic bag, and therefore its exposure to atmospheric oxygen was limited, but not zero. The double-layer capacitance and roughness factor measurements were as presented in Table 5.9, with the corresponding Tafel plot as presented in Figure 5.26.

The results show that after 15 months, the electrochemical surface area of the electrode had fallen by more than factor of four. It is likely this was caused by a chemical change of the electrode that reduced the access of the electrolyte to the porous interior of the Raney

	Before		After 15 months		After OER	
	C_{DL}	RF	C_{DL}	RF	C_{DL}	RF
Electrode #1	3.99 F	11,083	921 mF	2,558	2.72 F	7,556

Table 5.9: Double-layer capacitance and roughness factor for a Raney1 anode before and after a long period of non-use.

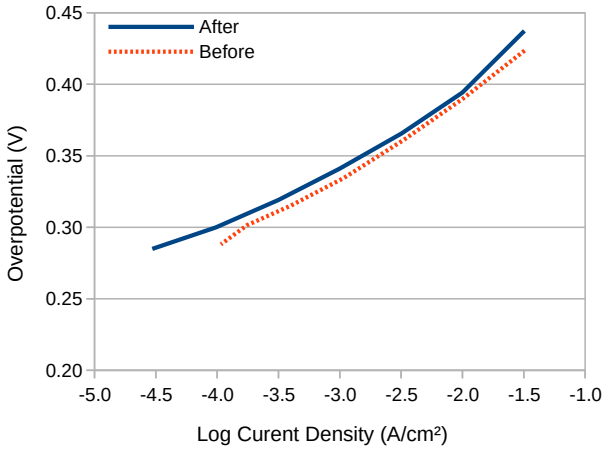

Figure 5.26: Tafel plot for a Raney1 anode before and after a 15 month period of non-use.

nickel coating, such as oxidation. However, after a brief period (15 minutes) of active oxygen evolution, the coating had regained much of the lost surface area, and the electrical performance was within 10 mV of the previous values. This was in agreement with the results of Experiment 5.11 (on page 179) and demonstrates that Raney nickel quickly recovers lost performance upon active use.

Experiment 5.17: To assess whether the Raney2 coating is suitable for use at large scale, an experiment was conducted with the aim of producing a deposit over a 8 cm × 5 cm area. Whilst not of industrial scale, it is expected such an electrode would nevertheless be sufficient to pass a current of at least 20 A. The apparatus for the deposition, and the appearance of the finished electrode, was as shown in Figure 5.27.

This was the first deposition to employ pumped circulation of the electrolyte. This was to assist with the dispersal of the black precipitate which accumulated in the deposition chamber, due to the rapid corrosion of the counter electrode. It was also to assist with the heating of the electrolyte on an adjacent hotplate. As a result the Raney2 deposit acquired a distinctive pattern which reflected the flow of electrolyte across its surface.

The deposition procedure (as specified in Section 5.2 on page 168) had to be modified, since the acrylic plastic of the deposition chamber was not able to withstand contact with 70 wt% H_2SO_4. The concentration was therefore reduced to 20 wt%, and the time from 3 minutes to 1 minute. Also, even though the Watt's Bath had been preheated to 60 °C, it was

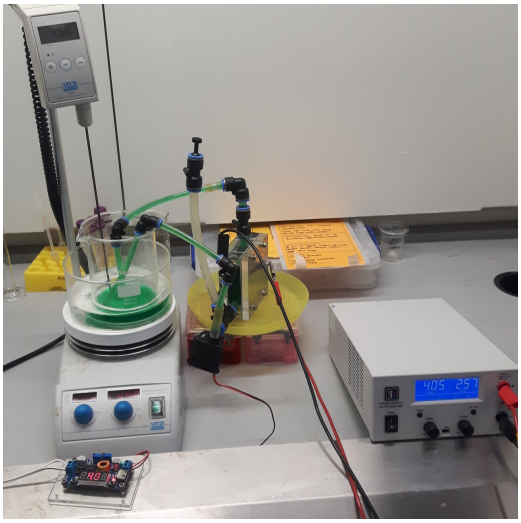

(a) Apparatus

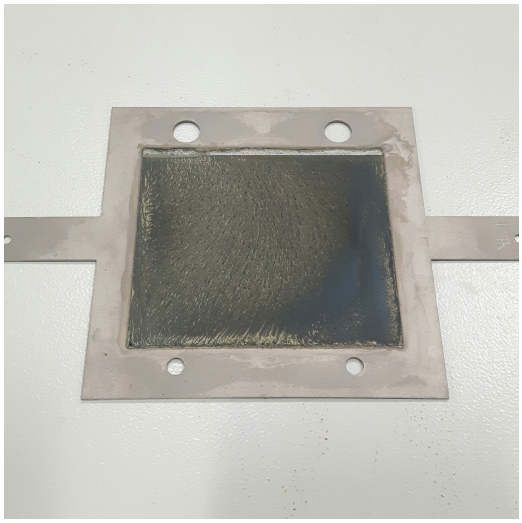

(b) Appearance

Figure 5.27: Large-area Raney2 deposition onto wetblasted 316-grade stainless-steel.

noted that the time taken for emptying and filling the chamber, and particularly for heating the new electrolyte to 50 °C took significantly longer than it had with the 100 ml beaker. Therefore, since delays can lead to oxidation, and thereby significantly affect the success of the finished coating, this is an aspect of scaling-up that should receive further attention.

5.3.3 SEM and EDX

The Raney nickel electrodes were characterised using SEM and EDX, for both HER and OER, and before and after accelerated ageing. Typical SEM images at 500× magnification for Raney1 and 2 as deposited are shown in Figure 5.28.

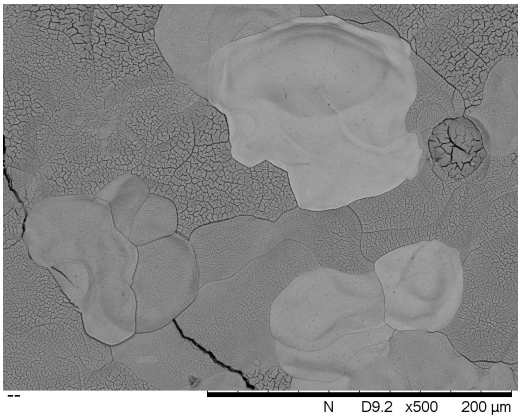

(a) Raney1

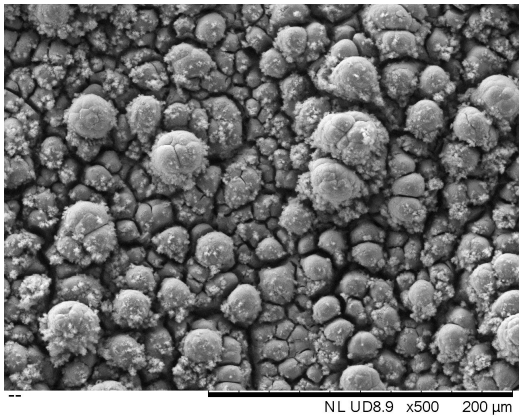

(b) Raney2

Figure 5.28: SEM images of the two Raney nickel coatings as deposited at 500× magnification

The images reveal that the morphology of the Raney nickel coating has been greatly affected by the change of counter electrode. The Raney1 coating has a relatively flat, cracked paving appearance, with many areas appearing to be almost solid. By contrast the Raney2 coating has a much more three-dimensional appearance that suggests it will have a larger surface area, and be better able to engage with the electrolyte. This is borne out by the better electrical performance of the coating prior to the ageing tests. A comparative view of the Raney2 coating before and after accelerated ageing as cathode is shown in Figure 5.29 at 500× magnification. The micrographs confirm that no deterioration of the coating is visible.

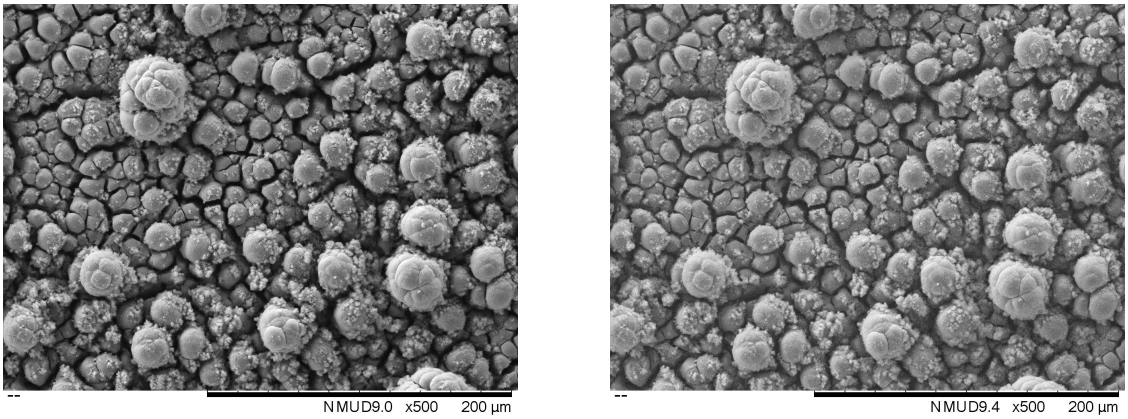

(a) As deposited (b) After ageing

Figure 5.29: SEM images of Raney2 at 500× magnification before and after accelerated ageing as anode

The EDX results for the Raney nickel anodes are shown in Figure 5.30a. For both anodes oxygen levels increase during use, which is perhaps not surprising for an electrode that is evolving oxygen. This increase makes it appear as if nickel was being lost, however once the figures are adjusted to exclude oxygen (as shown in Figure 5.30b), it becomes clear that the percentages of Ni, Zn, Cu and Fe were remaining constant, with just a small increase for carbon. This was in contradiction of comparable results obtained by Divisek *et al.* where a large loss of zinc from the anode was observed, although it was stated that this had little effect on its performance [206]. It has been confirmed that nickel electrodes gradually dissolve when used for oxygen evolution, as the $Ni(OH)_2/NiOOH$ film produces soluble Ni(II) species [212], and these results produce nothing in contradiction with this finding.

The EDX results for the Raney nickel cathodes are shown in Figure 5.31. At the cathode the opposite effect is observed, with a decrease in the level of oxygen after ageing. If oxygen and copper are numerically excluded from the analysis, nickel abundance is observed to increase, largely due to the loss of zinc. Nevertheless, the marked increase in the level of copper is quite noticeable. In fact, places on the cathodes were discovered at which the surface was more than 60 at% copper. For Raney2 the source of this copper before ageing is speculated to be the sacrificial stainless-steel counter electrode used during deposition,

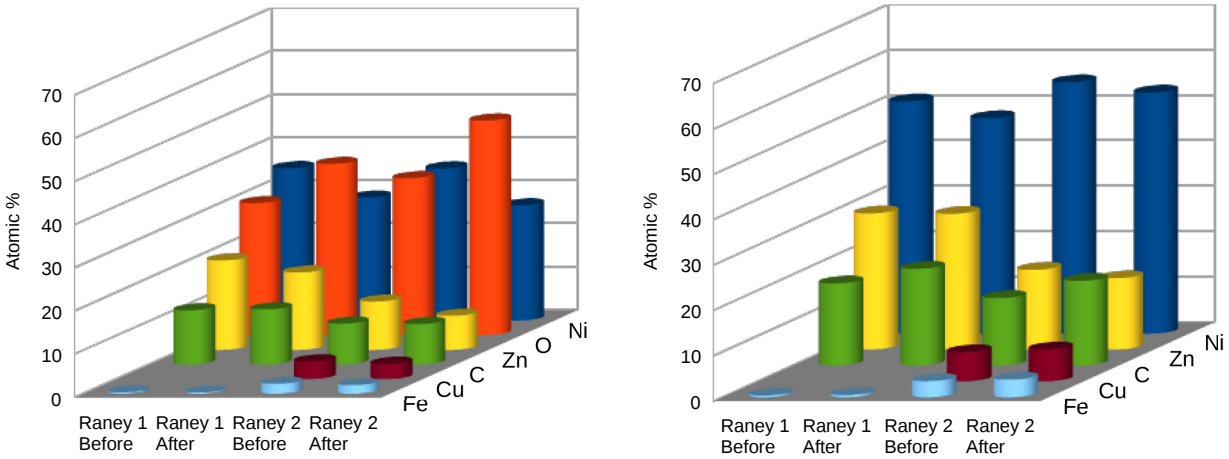

(a) including oxygen

(b) excluding oxygen

Figure 5.30: EDX results before and after accelerated ageing of Raney nickel anodes

which undergoes marked pitting and corrosion. This is confirmed by observing that for Raney1, which is deposited using a graphite rod counter electrode, no copper is present after deposition. After ageing copper levels have increased for both cathodes, and the source of this copper is speculated to be the stainless-steel anode used during the accelerated ageing experiments. This will have released small amounts of copper into the electrolyte, which are then preferentially deposited and concentrated onto the surface of the cathode.

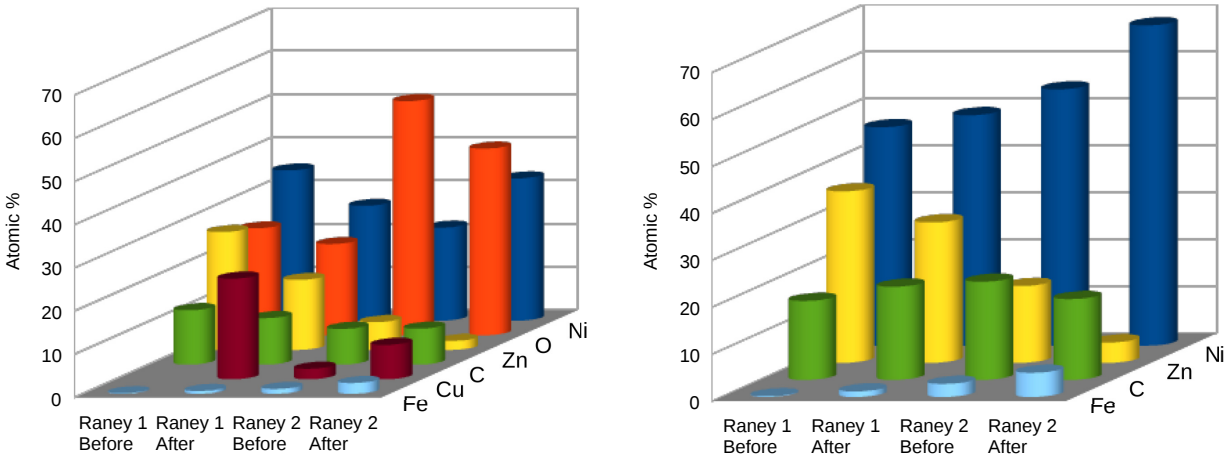

(a) including oxygen

(b) excluding oxygen and copper

Figure 5.31: EDX results before and after accelerated ageing of Raney nickel cathodes

According to published official standards, 316-grade stainless-steel does not contain any copper. To investigate this, EDX experiments were conducted on samples from two separate suppliers, and small amounts of copper between 1 and 1.6 wt% were observed in both. This

result is interesting because it appears to highlight the extent to which sources of copper contamination can become highly concentrated on the surface of the cathode during use.

Experiment 5.18: Although the electrical performance of Raney2 is an improvement over Raney1, the deposition method is not, since it involves the deliberate corrosion of the counter electrode. Also, the relatively large amount of precipitate produced inevitably increases the quantity of potentially hazardous material for disposal, not to mention the additional expense of electrode replacement.

From EDX measurements on Raney2 nickel prior to ageing, it was known that the coating was approximately 1 wt% Cr, as shown in Table 5.10.

Element	Line Type	Weight %	Sigma	Atomic %
Ni	K series	50.68	0.91	21.05
O	K series	20.84	0.45	46.86
Zn	L series	18.18	0.65	10.00
Fe	K series	3.78	0.18	2.43
Cu	L series	2.85	1.38	1.61
C	K series	2.31	0.39	6.92
Cr	K series	0.96	0.11	0.67

Table 5.10: EDX analysis of a Raney2 electrode subsequent to deposition and leaching.

It was also clear from its list of ingredients that the Modified Watt's Bath (MWB) already contained Ni and Zn. In addition, it was also very likely to contain Fe, since it is present as a contaminant in many standard grade chemicals [133, 213, 214]. In nature, deposits of nickel ore are invariably associated with Fe, and therefore so too are the salts produced from them. However, the same cannot be said of Cr, and its presence as a prominent component of 316SS made it a prime candidate.

Therefore, in an effort to assess whether simple additions to the deposition bath could bring about a similar beneficial change in coating morphology, several experiments to that end were conducted, as listed in Table 5.11. The list shows the number of grams of additive per 75 ml beaker of Modified Watt's Bath. It also shows the calculated number of grams per litre of water, based on the density of the MWB solution, which was measured at 1.16 g ml^{-1}.

	$CrCl_3$		$FeCl_2 \cdot 4\,H_2O$	
Experiment	**g/beaker**	**g l^{-1}**	**g/beaker**	**g l^{-1}**
1	0.36	5.8		
2	0.36	5.8	0.76	12.2
3	0.36	5.8	0.25	4.1

Table 5.11: Deposition experiments to duplicate the Raney2 coating without the use of a sacrificial electrode. The base electrolyte was a Modified Watt's Bath, as described in section 5.2 on page 168. The size of a beaker-full was 75 ml.

The appearance of the electrode resulting from Deposition Experiment 1 was as shown in Figure 5.32.

(a) Experiment 1

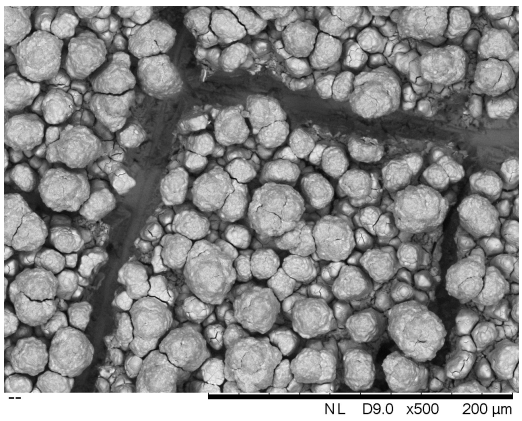

(b) SEM of Expt 1

Figure 5.32: Appearance of Raney nickel coating after addition of $CrCl_3$, i.e. experiment 1 listed in Table 5.11, together with an SEM of the surface at 500× magnification.

The addition of $CrCl_3$ has made the appearance of the coating much worse than standard Raney1 (see Figure 5.22a on page 185). Despite this, the SEM micrograph confirms that the morphology has in fact successfully been modified from the typical cracked appearance of Raney1 to the more cauliflower-like appearance of Raney2 (see Figure 5.28 on page 190). It may therefore be concluded that the constituent of the electrodeposition bath that helps to bring about this dramatic change is chromium.

EDX analysis confirmed the presence of Cr in the coating, but only at the level of 0.3 wt%. The amount of Fe was also low, at only 0.25 wt%, therefore it was determined to add a suitable iron salt for experiments 2 and 3, the results of which were as presented in Figure 5.33.

Sadly, the quality of the coating deteriorated further still. It may prove possible to improve this situation by alteration of the anions from chloride to sulphate or nitrate, or of the oxidation states from Cr^{3+} and Fe^{2+} to one of the other combinations, or by delaying the addition of one or more of the constituents, but it was not felt that this was a productive avenue of research in the time available, and no further experiments were conducted.

In any case, the deposition process by sacrificial counter electrode is *progressive*, and gradually alters the composition of the electrodeposition bath in a way that is difficult to duplicate. It is quite possibly an unreasonable expection that there exists a single deposition bath that can duplicate the Raney2 coating.

(a) Expt 2 (b) Expt 3

Figure 5.33: Appearance of Raney nickel coated electrodes produced as a result of experiments 2 and 3 listed in Table 5.11.

5.4 Performance Comparisons

In order to assess how the Raney2 electrodeposited coating compares with other bi-functional catalysts, a small survey was conducted to find other recently-published bi-functional catalysts for water-splitting in alkaline conditions, as shown in Table 5.12.

Name	Electrolyte	Temp	Lead Author	Ref
FeP/Ni_2P	1 M KOH	n/s	Yu Fang	[215]
Co-P	1 M KOH	n/s	Jiang Nan	[216]
NiFeOx/CFP	1 M KOH	25 °C	Wang Haotian	[217]
CoP/rGO-400	1 M KOH	n/s	Jiao Long	[218]
NiCoP	1 M KOH	n/s	Li Yingjie	[219]
NiSe-NF	1 M KOH	n/s	Tang Chun	[220]
NiS/Ni	1 M KOH	n/s	Zhu Wenxin	[98]
CoP-MNA	1 M KOH	n/s	Zhu Yun Pei	[112]

Table 5.12: Recently published bi-functional electrocatalysts for water-splitting in alkaline conditions. n/s = not specified, but presumed to be room temperature.

The results of these comparisons are shown in Figure 5.34, where the results chosen for Raney2 are those produced in 1 M KOH. The Tafel slope and overpotential figures for Raney2 are as presented in Table 5.13.

They show that for hydrogen evolution the Raney2 coating compared extremely favourably with recently published bi-functional catalysts. For hydrogen evolution it was the front-runner, and for oxygen evolution it was near the middle. When both were combined the coating was second only to the world-leading FeP/Ni_2P, which is a coating that features a more complicated deposition method involving chemical vapour deposition

Coating	Reaction	Current Density $mA\,cm^{-2}$	Tafel Slope $mV\,dec^{-1}$	Over-potential mV
Raney2	HER	10	50	28
Raney2	OER	10	38	291
Raney2	Both	10	88	319

Table 5.13: Tafel slopes and overpotentials for coating Raney2 in 1 M KOH at laboratory temperature, as presented in Figure 5.34.

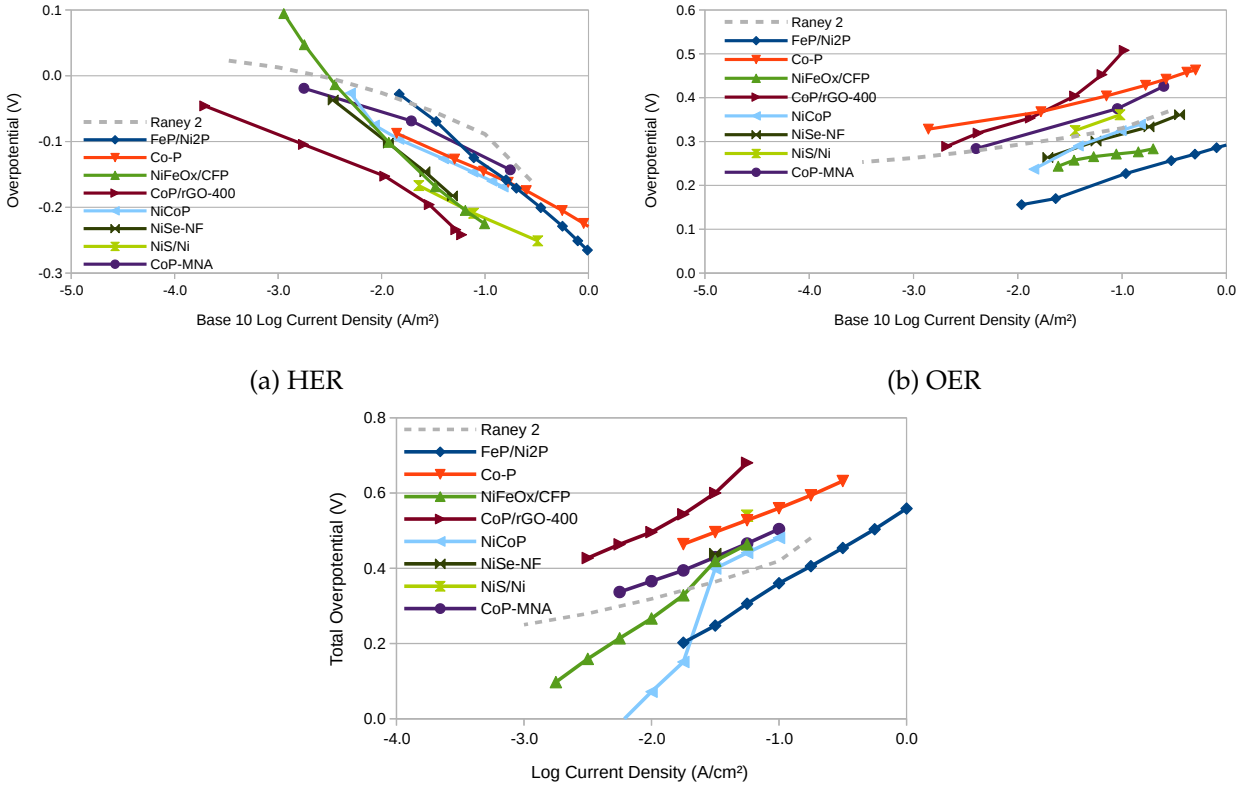

(a) HER

(b) OER

(c) Overall

Figure 5.34: Raney2 bifunctional comparisons.

within a tube furnace. It may therefore justifiably be claimed that Raney2 is the most active, simple bifunctional electrocatalyst known.

The performance of the coating was also compared with various results reported by Herraiz-Cardona *et al.* and Solmaz *et al.* There are a selection of materials with which to compare, as listed in Tables 5.14 and 5.15, with the results as shown in Figures 5.35a and 5.35b.

These results show a high degree of agreement, especially when it is considered that the Herraiz-Cardona *et al.* measurements were all performed in stronger electrolyte, and at higher temperature. Solmaz *et al.* aged their Cu/NiCuZn coating to 120 hours at a constant $100\,mA\,cm^{-2}$, and observed a similar increase in activation over this period, which was

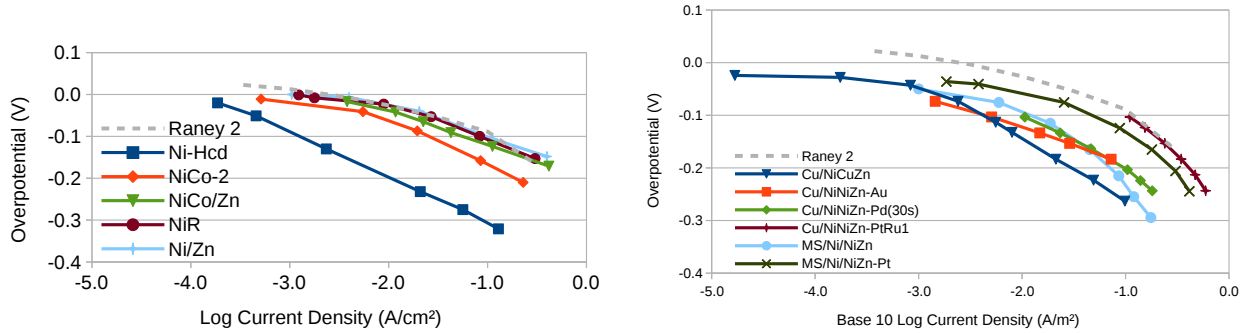

(a) Herraiz-Cardona *et al.* (b) Solmaz *et al.*

Figure 5.35: Comparisons with the coatings listed in Tables 5.14 and 5.15

Name	Electrolyte	Temp	Ref
Ni/Zn	30 wt% KOH	50 °C	[127]
NiCo-2	30 wt% KOH	30 °C	[150]
Ni-Hcd	30 wt% KOH	50 °C	[221]
NiR	30 wt% KOH	30 °C	[198]
NiCo/Zn	30 wt% KOH	30 °C	[197]

Table 5.14: Nickel catalysts reported by Herraiz-Cardona *et al.*

Name	Electrolyte	Temp	Ref
Cu/NiCuZn	1 M KOH	RT	[199]
MS/Ni/NiZn-Pt	1 M NaOH	298 K	[200]
Cu/NiNiZn-PtRu1	1 M KOH	298 K	[201]
Cu/NiNiZn-Pd(30s)	1 M KOH	298 K	[153]
Cu/NiNiZn-Au	1 M KOH	298 K	[83]

Table 5.15: Nickel catalysts reported by Solmaz *et al.*

attributed to a probable removal of material from the pores. It is not possible to perform comparisons for OER, as to our knowledge these experiments were not reported.

5.5 Conclusions

This paper presents for the first time a simple modification to the procedure for the electrodeposition of Raney nickel that enhances not just its electrical performance for alkaline water-splitting, but also its lifetime. The performance of the Raney2 coating for both the hydrogen and oxygen evolution reactions is such that it easily matches or outperforms many more complicated and expensive bifunctional electrocatalysts. The combination of a high-performance, industry-standard Raney nickel coating, together with the progressive incorporation of 316-grade stainless steel (316SS), has transformed the coating and permitted it to break new ground in this area of research. It is possible that the new coating is thus a hybrid,

able to combine the advantageous properties of both materials, creating a new coating that is effectively 'Stainless Raney nickel'.

The choice of a 316SS counter-electrode that corrodes during deposition will inevitably have affected the constituents of the finished coating, since 316SS contains a variety of elements, most notably Fe, Cr, Mo and (according to our analysis) Cu. Interestingly no Mo at all was detected in the EDX results, which implies that it remained in solution, but Fe was co-deposited, and is well-known for enhancing the catalytic activity of Nickel, especially towards OER [44]. In fact, even the levels at which Fe is present as a contaminant in many laboratory-grade chemicals has been known to bring about a 10-fold increase in activity [213].

Most significantly the choice of counter-electrode appears to have dramatically altered the morphology of the coating from a cracked appearance [127, 198], to a more cauliflower-like appearance (as shown in Figure 5.28). This morphology change is confirmed to be associated with a marked increase in electrochemical surface area (ECSA).

Similarly, although the standard Raney1 coating is observed to improve its performance with normal usage, either as anode or cathode, the new Raney2 coating is observed to improve its performance by an even greater amount. This performance increase is also associated with large increases in the ECSA, a surface area that the coating is able to utilise even up to large current densities where mass-transport issues would be expected. This appears to occur whether zinc continues to be leached out (at the cathode) or not (at the anode).

For OER on nickel-based electrodes it has been suggested by several authors that potential cycling across the $Ni(OH)_2/NiOOH$ redox couple is associated with several chemical and physical changes which are conducive to enhanced electrical performance [44, 222, 223]. First is that the more amorphous α-phase of $Ni(OH)_2$ is transformed into the more crystalline β-phase as water molecules are progressively driven out. Second is that during each anodic sweep, the β-phase is itself oxidised to the β-phase of NiOOH which, perhaps as a result of its more optimal average oxidation state, has a lower overpotential for OER. Lastly, the repeated disruption of the crystalline hydroxide leads to an increase in surface roughness. None of the results here obtained serve to contradict these suggestions.

At the cathode, the increase in surface area is certainly not related to a hydroxide redox couple, but instead is more likely to be due to the continued leaching of zinc, a suggestion which is supported by the results of EDX. However, it is expected from work by Divisek *et al.* that once the level of zinc falls below 10 wt% the cathodic overpotential should begin to increase by up to approximately 200 mV [206]. This effect has not been observed in this study, even though cathodic levels of zinc were observed to fall to approximately 2 at%. This disparity could possibly be explained by the difference in the method of assessing the level of zinc, which in the work by Divisek *et al.* was assessed by complexometry (a bulk analytical technique), whereas in this work was assessed by EDX (a non-invasive surface

technique). It is quite possible that the low bulk concentrations of zinc reported by Divisek *et al.* were associated with an almost complete absence of zinc at the surface.

A further explanation may rest with the issue of copper contamination, which cannot be ruled out as a contributory factor. Although it is not a common topic of research in the literature in combination with nickel electrodes, in work by Ngamlerdpokin *et al.* all Ni-Cu alloys were observed to have higher electrocatalytic activity for HER than pure nickel alone [224]. It appears that contamination of the cathode with copper need not be regarded as destructive. This could be of great importance, since stack degradation in service due to the contamination and poisoning of electrodes is of great concern from a commercial perspective. Finally, it is the hope of the authors that the accelerated ageing tests here outlined will constitute a new and useful benchmark for future comparisons between new electrode materials, thereby condensing the work of months or years into just one week.

Chapter 6

Zero-gap Electrolysis

> There's a thin line
> between heating a planet up,
> and frying it.
>
> *Prof. Brian Cox*

All of the measurements presented thus far in this thesis have been *iR-corrected*. Therefore, the resistance effects of the electrolyte, diaphragm and electrodes have been subtracted, so as to isolate the behaviour of the working electrode. In this chapter, such additional effects will now be considered, so as to build up a more complete picture of the behaviour of an electrolyser. In particular, the behaviour of a *zero-gap* electrolyser (ZGE) will be considered, since this configuration offers attractive levels of performance.

A ZGE is based on the concept that the electrodes, and more specifically the catalyst, are in contact with the gas-separation diaphragm or membrane. As such, the electrolyte sits behind the electrodes, and the electrodes must therefore be porous. In theory, this reduces the electrolyte losses to zero, but in practice the membrane is itself saturated with electrolyte, so membrane thickness becomes an issue, with thicknesses reported down to just a few tens of microns. This has a knock-on effect on gas purity, with the result that high efficiency can come at the cost of high standby power.

Equally, the requirement for the electrode to be porous can force a trade-off between the ability of the electrode to transport electrons (its electrical resistance) and its ability to transport reactants in and products out (its mass-transport resistance). The first requirement demands a closed structure that is mostly conductive material; the second an open structure that is mostly electrolyte. This combination, in tandem with the membrane, is referred to as a Membrane Electrode Assembly (MEA) and is an extremely active area of research, particularly for fuel-cells. In this chapter these design trade-offs will be examined in detail, and models developed which will permit not only simulation but understanding of the zero-gap design concept, a configuration that to date represents the highest performance that can be achieved without recourse to rare metals or high temperatures.

6.1 Bubbles

There are significant differences between the behaviour of hydrogen and oxygen bubbles as they are evolved from the electrode surfaces. Hydrogen bubbles are considerably smaller in alkaline solutions, and do not coalesce as easily [225]. These two factors combine to mean there is considerably less fluctuation in the performance of the cathode during electrolysis. Another observation (for vertical electrodes) is the formation of two distinct layers of hydrogen bubbles, with a rising layer of free bubbles gliding continuously over a layer of bubbles still attached, and with no discernible interaction between the two [225]. This phenomenon is not observed for oxygen bubbles, where the bubbles are much larger, and there is considerably more coalescence between bubbles, with the result that they are continually breaking free, colliding, coalescing, and then breaking free again.

Hydrogen bubbles are smaller because the electrolyte nearest the cathode becomes supersaturated with dissolved hydrogen during electrolysis, with the result that nucleation takes place at many more sites [126, 226]. Bubble detachment occurs when the balance of forces between the buoyancy, liquid drag (in the case of electrolyte convection/circulation) and surface tension combine to bring the bubble into motion [142, 226, 227]. Since oxygen bubbles are larger, the forces of liquid drag upon them, and therefore of pumped circulation, are more significant. As evidence of this, oxygen bubble detachment size was observed by Janssen *et al.* to reduce by more than a factor of 8 between zero flow and $1\,\mathrm{m\,s^{-1}}$ at $200\,\mathrm{mA\,m^{-2}}$ in KOH [225].

As regards electrolyte resistance, and thereby the additional iR-penalty, this is observed to depend on a mixture of the surface screening (i.e. the fraction of the electrode surface covered by attached bubbles) and the void fraction (i.e. the fraction of the electrolyte volume filled with detached bubbles) [126]. Here it is necessary to be specific about which volume of the electrolyte is to be considered, since clearly for a vertical electrode and a large electrode gap, the gas will be highly concentrated close to the electrode surface.

Consider a round electrode of radius r placed inside a hemi-spherical counter electrode of infinite size, the space between being filled with an electrolyte of bulk resistivity ρ. It can be shown that the resistance between the two electrodes is equal to $\rho/4r$ [228]. It can be also be shown that this is equal to the resistance between two circular electrodes just $\pi r/4$ apart. This situation is shown diagrammatically in Figure 6.1, where the diagram on the right is drawn to scale.

What this means is that even an *infinite* volume of electrolyte at some distance from the electrode contributes little to the overall resistance, whereas the electrolyte immediately above the electrode has greater influence. This stands to reason, since this is where the path taken by the electric current is most constrained. Signficantly, this is also the region of the electrolyte most likely to contain bubbles of gas.

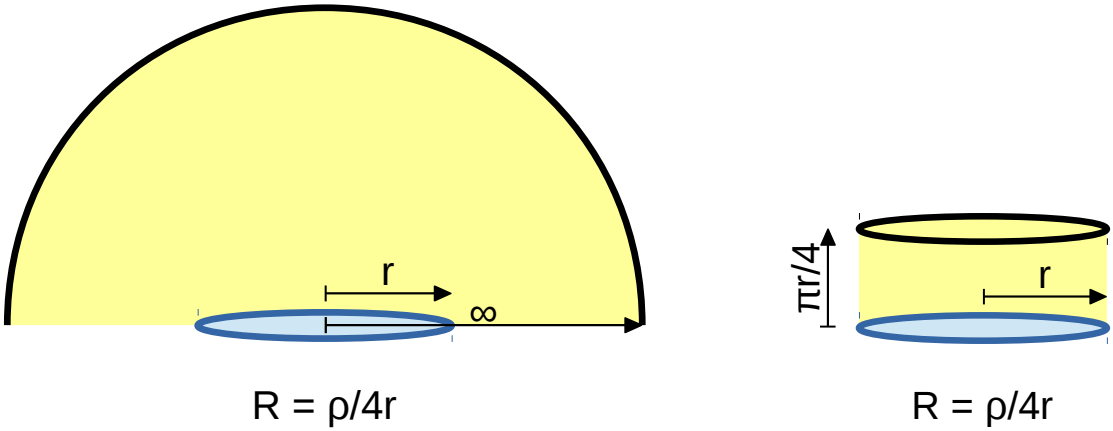

(a) Hemisphere of infinite radius

(b) Finite cylinder

Figure 6.1: Two bodies of electrolyte with *equal* electrical resistance. The blue eillipse represents a circular electrode of radius r, the yellow area electrolyte with bulk resistivity ρ, and the black line the counter electrode.

The bulk resistivity of any volume of conductive liquid has been shown to be dependent on the void fraction contained within it, in accordance with the Bruggeman equation: [126, 229, 230]

$$\rho = \rho_0 \left(1 - f\right)^{-3/2} \tag{6.1}$$

where ρ_0 is the bulk resistivity of the bubble-free electrolyte, f is the void fraction, and ρ is the resultant increased resistivity. Visually, this relationship appears as shown in Figure 6.2.

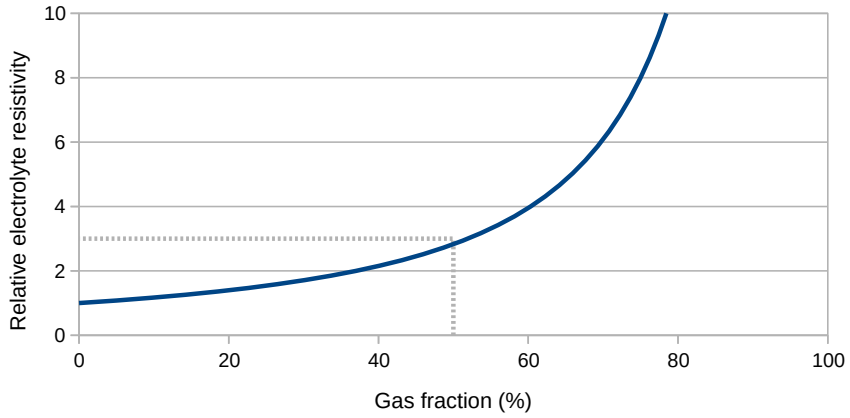

Figure 6.2: Relative electrolyte resistivity as a function of the void fraction of bubbles within, according to the Bruggeman equation. Note that at a void fraction of 50% the resistivity has tripled, as indicated by the dotted line.

Regarding the connection between electrode bubble coverage and void fraction, it was reported by Z. Abdin *et al.* that:

> subject to usual assumptions, in the steady state the surface bubble fraction at the electrode and the volume fraction in the bubble zone are in fact the same [231]

The author went on to report that the effect of temperature on electrode bubble coverage, and therefore by extension on volume fraction, is dramatic. At a current density of $350\,\mathrm{mA\,cm^{-2}}$, a temperature increase from 50 °C to 80 °C resulted in a reduction in bubble coverage by a factor of 3 from 0.87 to 0.3, and a decrease in the associated activation potential by a factor of 5 from 175 mV to 35 mV. From a system point of view, this is a significant voltage saving per pair of electrodes, and adds further weight to the argument that one of the simplest and most effective routes towards improved system efficiency is to warm the electrolyte, or to ensure that it can warm itself.

As a result of experiments that filmed the formation of both hydrogen and oxygen bubbles on the surface of a transparent nickel electrode in KOH, and that then made a detailed analysis of the bubble populations over multiple frames, it was possible to make quantitative predictions of bubble behaviour. Most notably a combined parameter was proposed by Janssen *et al.*, subsequently called J, which produced a linear log-log relationship when plotted against current density, where J was defined as [225]:

$$J = \frac{V_a d}{\theta} \tag{6.2}$$

where V_a is the average volume of attached bubbles per unit surface area, d the average number of bubbles per unit surface area, and θ the average fraction of the electrode screened by bubbles. However, despite the elegance of this observation, this parameter remains defined purely in terms of coefficients that cannot be directly measured, except with the benefit of transparent electrodes.

A more practical and very simple hydrodynamic model was developed by Vogt *et al.*, which demonstrated a close match to published empirical measurements [232]. The model applies to a conventional electrolyser with vertical electrodes, separated by a distance s. It assumes the presence of a stagnant layer of gas/electrolyte attached to each electrode, of total thickness Υs, and with an electrical resistance K times that of the bubble-free electrolyte. In between lies a mobile layer of gas/electrolyte, of thickness $(1-\Upsilon)s$, which is circulated by pumping at a volume flow rate of V_L'. The electrolyte velocity therefore depends on the electrode width and separation. It was calculated that for all but the slowest velocities, the gas bubbles and electrolyte travel at the same speed.

As the electrolyte passes between the electrodes, the volume of gas within it increases as a function of height. Therefore, the current density *falls* with height, as the resistance of the electrolyte between the electrodes increases. Despite this, the authors state that the same overall solution is obtained whether this variation is considered or not, that solution being:

$$\rho_r = \frac{(1-\Upsilon)}{2.5}\frac{V_L'}{V_G'}\left[\left(1+\frac{V_G'}{V_L'}\right)^{2.5} - 1\right] - \Upsilon K \tag{6.3}$$

where ρ_r is the relative increase in resistance of the electrolyte, and V'_G is the total volume flow rate of gas produced. The solution results from a limit integral of the Bruggeman equation (see Equation 6.1), which explains how an exponent of 2.5 has arisen. Taking $Y = 0.01$ and $K = 5$, this produces the relationship shown in Figure 6.3 (adapted from Vogt *et al.*). This graph can be used to obtain a design criterion for the current density. For example, if it

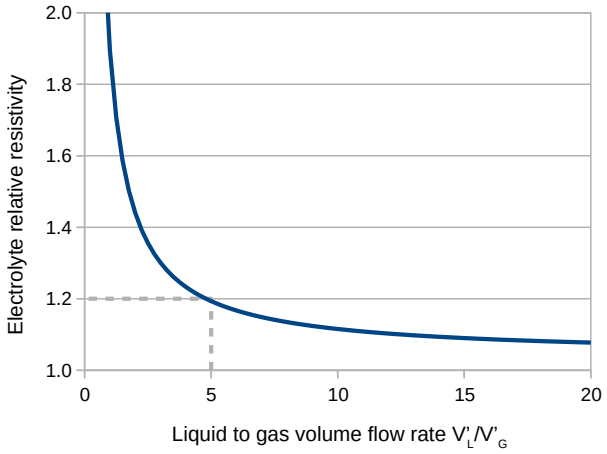

Figure 6.3: Relative electrolyte resistance ρ_r *versus* liquid to gas volume flow rate in a conventional electrolyser with vertical electrodes [232].

is assumed that the relative resistivity should not be allowed to increase by more than 20%, this creates a limit to the gas production rate:

$$V'_G \leq 0.2V'_L \tag{6.4}$$

as shown by the dashed grey line. Evidently, this also limits the maximum void fraction exiting the electrolyser to 0.2. The gas production rate can then be related to the current density using a combination of Faraday's law and the ideal gas law:

$$V'_{G,max} = j_{max} A \frac{RT}{pF} \left(\frac{1}{2} + \frac{1}{4} \right) \tag{6.5}$$

where R, T, p and F have their usual meanings, j is the current density, A the electrolyser area, and 2 and 4 are the number of electrons per hydrogen and oxygen molecule respectively. Combining Equations 6.4 and 6.5 produces:

$$j_{max} = \frac{4}{15} \frac{pF}{RT} \frac{V'_L}{A} \tag{6.6}$$

Given that V'_L / A can be regarded as the amount of pumping per unit area, this means that the maximum current density is directly controlled by the electrolyser pressure p, and inversely proportional to temperature T. However, given that the electrolyte resistance goes

down with increasing temperature, but is invariant with pressure, this means that increasing the pressure directly reduces losses. This is the reason why commercial electrolyers operate at elevated pressure.

To continue the design example, if an electrolyser has an area of $0.25\,\mathrm{m}^2$, and the pumping rate is $0.25\,\mathrm{l\,s}^{-1}$, such that the area-specific pumping rate is $1\,\mathrm{l\,s}^{-1}\,\mathrm{m}^{-2}$, the maximum permissible current density at 1 bar equates to just $106\,\mathrm{mA\,cm}^{-2}$. Above this current density, losses due to gas bubbles in the electrolyte increase sharply, and these losses will be *independent* of electrode width, height and electrode spacing. Therefore, although it would appear that making the electrolyser wider and shorter might increase efficiency, it does not, because the flow velocity is reduced. Note also that even though the *overall* efficiency increases as the electrode spacing is reduced,the *relative* electrolyte losses are unaffected. However, should the pressure be increased to 10 bar, the maximum permissible current density increases to $1063\,\mathrm{mA\,cm}^{-2}$, which is a level at which other inefficiencies in the electrolyser will dominate.

The minimum practicable electrode spacing is also given by Vogt *et al.* to be about 2 mm per chamber. Thus, an electrolyser with a gas-separation diaphragm, which therefore has two chambers, requires at least 4 mm between electrodes. Below this separation, additional losses occur in a rapidly increasing fashion, as confirmed by other researchers [142, 233]. It is surmised that these losses occur as the size of the non-stagnant channel is reduced to a point where plug flow can no longer occur. Despite the fact that this hydrodynamic model applies to a conventional electrolyser, there is little doubt that the same processes are at work in a zero-gap electrolyser (ZGE). However, a ZGE has the advantage that the size of the electrolyte channels can be increased *without* increasing the gap between electrodes.

6.1.1 Bubble Inflation Losses

The total surface energy of a bubble of radius r is given by the product of the surface tension γ and its surface area:

$$E_S = \gamma \cdot 4\pi r^2 \tag{6.7}$$

where r is the bubble radius. The relative pressure inside the bubble (the Laplace pressure) is:

$$p_L = 2\gamma / r \tag{6.8}$$

Note that when the bubble is first created radius r will be close to zero, and the pressure inside will potentially be very high, and it could therefore take a lot of energy to inflate it. For any volume of gas, the product of its pressure and volume gives the volume energy:

$$E_V = \text{pressure} \times \text{volume} = p_L \cdot \frac{4}{3}\pi r^3 = \frac{8}{3}\pi\gamma r^2 \tag{6.9}$$

Combining Equations 6.7 and 6.9 produces an equation for the total bubble creation energy:

$$E_b = E_S - E_V = 4\pi\gamma r^2 - \frac{8}{3}\pi\gamma r^2 = \frac{4}{3}\pi\gamma r^2 \tag{6.10}$$

Note that because the pressure inside the bubble is *higher* than that of the surrounding liquid, E_V is *subtracted* from E_S. This is because the gas is performing work *on* its environment as it expands. The total moles of H_2 gas produced is:

$$\text{Moles}_{H_2} = \frac{Q}{2F} \tag{6.11}$$

where Q is electrical charge in Coulombs, and F is the Faraday constant. The total volume of H_2 gas produced (from $pV = nRT$) is:

$$V_H = \frac{\text{Moles}_{H_2} RT}{p_L} = \frac{Q}{2F} \cdot RT \cdot \frac{r}{2\gamma} = \frac{QRTr}{4F\gamma} \tag{6.12}$$

where R is the gas constant, and T the temperature in Kelvin. If it is declared that the average bubble size is b, the average bubble volume is:

$$V_B = \frac{4}{3}\pi b^3 \tag{6.13}$$

and the number of bubbles is:

$$N_b = V_H / V_B = \frac{QRTb}{4F\gamma} \cdot \frac{3}{4\pi b^3} = \frac{3QRT}{16\pi F\gamma b^2} \tag{6.14}$$

The total work to inflate all bubbles is:

$$E_B = E_b \cdot N_b = \frac{4\pi\gamma b^2}{3} \cdot \frac{3QRT}{16F\pi\gamma b^2} = \frac{QRT}{4F} \tag{6.15}$$

The total electrical energy is:

$$E_E = UQ \tag{6.16}$$

where U is the voltage in Volts. Therefore the percentage bubble loss is:

$$E_B / E_E = \frac{RT}{4UF} \times 100\% \tag{6.17}$$

The expression RT/F is a common term in electrolysis, occurring as it does in the Nernst equation (see Section 1.3.2 on page 17), and is equal to approximately 26 mV at room temperature. Thus, if a typical value is taken for U of about 2.5 V, we obtain:

$$E_B / E_E = 0.26\% \tag{6.18}$$

Thus the rest of the electrolysis process is at liberty to achieve 99.74% efficiency.

This surprising result implies that the energy lost to bubble inflation is in fact independent of average bubble radius or electrolyser pressure. However, certain simplifications have been made during this analysis, perhaps most notably that the inflation process is adiabatic. Whilst the bubble radius is small the Laplace pressure inside means that bubble inflation will generate heat, in the same way that inflating a tyre generates heat. Should this heat be transferred to the surroundings, the process becomes non-adiabatic.

It is questionable whether this simplification has any appreciable impact on the result. The inflation process is potentially so rapid that heat-losses do not have sufficient time to occur, in which case the process can be approximated as adiabatic. Also, taking the surface tension $\gamma = 72.8\,\mathrm{mN\,m^{-1}}$ for pure water, at a bubble radius of 1 µm the Laplace pressure is just 1.4 bar, and the bubble volume is $4.2 \times 10^{-18}\,\mathrm{m^3}$. It is therefore likely that the volumes and pressures involved are simply too small to be significant.

6.2 Gas-Separation

In a ZGE the hydrogen and oxygen product gases are evolved within 1 mm of each other, and quite possibly a lot less. Not only that, but a continuous region of highly mobile fluid of necessity must exist between them. Despite this, as a minimum the gases must be kept separate to a sufficient degree to maintain safety, and as an end goal to ensure downstream usability. These requirements have been discussed in Section 1.2.3 on page 11. Further, the various choices of gas-separation material will be discussed in Section 6.6 on page 240. Therefore, the discussion at this point will be restricted to more theoretical concerns.

6.2.1 Gas Stratification

On Friday 11th March 2011 an undersea earthquake occurred off the coast of Japan. The earthquake was detected by sensors at the nearby Fukushima Daiichi nuclear power plant, which automatically shut down all active reactors. Because of this shutdown and other problems, electrical power failed, and the plant switched over to backup diesel generators, which were needed to maintain the supply of cooling water to the reactors. However, the subsequent tsunami, which inundated dozens of coastal settlements, also over-topped the sea wall of the power plant, and flooded the basements that contained the generators. The unprotected reactors, thus deprived of cooling, overheated and as a result generated large quantities of hydrogen gas. This gas mixed with air inside the containment buildings, and over the next four days a number of explosions occurred, causing extensive damage and hampering efforts to bring the plant back under control.

The behaviour of a hydrogen release is of great pertinence to hydrogen production, since a similar situation could easily reoccur. Such rapid releases are therefore of interest to the research community, and have been modelled in detail [34]. The buoyancy of hydrogen in air is such that it collects against ceilings, and the inevitable stratification that results means that the ideal explosive mixture is guaranteed to occur somewhere. However, for electrolysis, the question is whether stratification can still occur with much slower releases of hydrogen, such as would result from the gradual mixing of gases inside an electrolyser.

The normal form of the ideal gas law is:

$$pV = nRT$$

but since the density of the gas ρ can be expressed as:

$$\rho = \frac{\text{mass of gas}}{\text{volume of gas}} = \frac{nM}{V}$$

where M is the relative molecular mass, the gas law can be rewritten as:

$$p\frac{nM}{\rho} = nRT$$
$$\text{therefore } \rho = \frac{pM}{RT}$$

In a vertical column of gas, the rate of change of pressure with height z will be:

$$\frac{dp}{dz} = -\rho g$$
$$= -\frac{Mg}{RT}p$$

where g is the force of gravity. This is a first-order differential equation in p, therefore its solution will be an exponential function:

$$p = p_0 \exp\left[-\frac{Mg}{RT}z\right] = p_0 \exp\left[-\frac{z}{L}\right]$$
$$\text{where } L = \frac{RT}{Mg}$$

The coefficient L describes a 'Scale Length', which is the distance over which the pressure will reduce by a factor e, and depends on the molecular mass of the gas, as shown in Table 6.1 [234].

Gas	Molecular Mass (M)	Scale Length (L)
Hydrogen	$2 \times 10^{-3}\,\mathrm{kg\,mol^{-1}}$	124 km
Oxygen	$32 \times 10^{-3}\,\mathrm{kg\,mol^{-1}}$	7.76 km

Table 6.1: Molecular Masses and Scale Lengths for Hydrogen and Oxygen

Finally, by invoking Dalton's law of partial pressures, which states that the partial pressure of each gas can be considered in isolation, we obtain:

$$\frac{p_{H_2}}{p_{O_2}} = \frac{p_{0H_2}\exp\left(-z/L_{H_2}\right)}{p_{0O_2}\exp\left(-z/L_{O_2}\right)} = R_0\exp(z/L_{O_2} - z/L_{H_2}) \tag{6.19}$$

$$= R_0\exp\left[\left(\frac{L_{H_2} - L_{O_2}}{L_{O_2}L_{H_2}}\right)z\right] = R_0\exp\left[\frac{z}{8277\,\mathrm{m}}\right] \tag{6.20}$$

where R_0 is the ratio between the partial pressures of hydrogen and oxygen at the bottom of the column. It's clear therefore that the column of gas would need to be many kilometres in height to appreciably increase the hydrogen concentration based on buoyancy alone. As a result, in the field of electrolysis, where the rate of cross-contamination is low, it is safe to say that stratification may be discounted.

As regards the release of radioactive material from the Fukushima Daiichi nuclear power plant disaster, the role of the hydrogen explosions in breaching the containment buildings is over-stated. The spectacular nature of the explosions fixated public attention, however most contamination was released in cooling water, and pumped directly into the ocean. Of the remainder, the majority was released deliberately to reduce gas pressure, and thus a result of the loss of coolant flow, not the explosions.

Nevertheless, the explosions could have been avoided with the installation of Passive Autocatalytic Recombiners (PARs). These operate by the use of Pt or Pd coated pellets that catalytically recombine hydrogen with oxygen to generate water, and given sufficient surface area are able to maintain the concentration of hydrogen in air to completely safe levels, even at temperatures down to 10 °C [235]. In fact, the devices are so effective they can easily overheat [236]. As a result of the accident, nuclear operators all across the world installed PARs. On a smaller scale, such an item could form a very useful component part of an electrolyser.

6.2.2 Gas-mixing model

If it is assumed that the rate of diffusion of unwanted gas across the membrane is *not* a function of current density, but *is* a linear function of temperature, then it is possible to construct a simple mathematical model and ascertain how well it fits the measurement dataset. In this respect, results by Hug *et al.* are available in which measurements of the concentration of H_2 in O_2 were performed for a 25-plate bipolar electrolyser operating with 28 wt% KOH [237].

The proposed model states:

$$D_{H_2} = D_0(T - T_0) \tag{6.21}$$

where D_{H_2} is the rate of diffusion of H_2 across the membrane, D_0 is a constant, T is the temperature, and T_0 is a notional temperature at which the rate of diffusion falls to zero. The rate of production of O_2 due to normal electrolysis is given by:

$$P_{O_2} = j/4F \tag{6.22}$$

where j is the current density, F is the Faraday constant, and the number 4 corresponds to the four electrons that are passed for each molecule of O_2 produced. Thus the fractional contamination of the O_2 outlet is:

$$C_{O_2} = \frac{D_{H_2}}{P_{O_2}} = \frac{4FD_0(T - T_0)}{j} + C_0 \tag{6.23}$$

where C_0 has been included to permit the removal of any remaining offset. Differentiating Equation 6.23 with respect to $(1/j)$ yields:

$$\frac{dC_{O_2}}{d(1/j)} = 4FD_0(T - T_0) \equiv C_j \tag{6.24}$$

where as a shorthand this quantity has been labelled C_j. Plotting the measurements from Hug *et al.* against $(1/j)$ produces the results shown in Figure 6.4. Since a lot of data-points are compressed close to the origin, Figure 6.4b has been included to show this region in more detail.

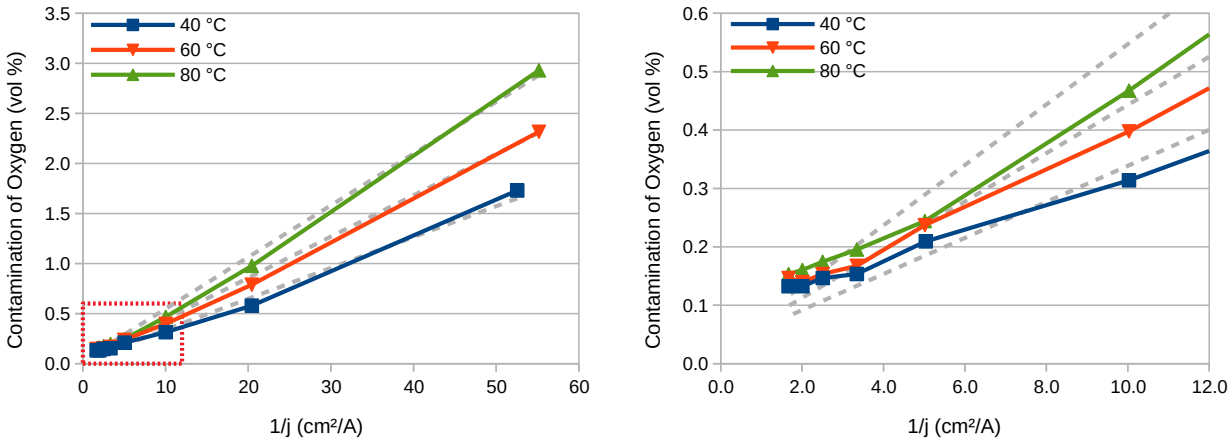

(a) Full view

(b) Detail view of dotted red box

Figure 6.4: Gas impurity measurements in 28 wt% KOH, adapted from Hug *et al.* [237] *versus* inverse of current density.

It is clear that the empirical data is more curved than the model, which is constrained

to produce straight lines. In particular, there is more contamination in the oxygen outlet at high current densities (i.e. low values of $1/j$) than would be expected, which indicates that the rate of hydrogen diffusion across the membrane is not invariant, but has increased, possibly as a result of the rapid rate of gas evolution on both sides of the membrane. Since the rate of gas evolution is proportional to the current density, a term proportional to j can be added to Equation 6.21 to account for it, producing:

$$D_{H_2} = (D_0 + D_1 j)(T - T_0) \tag{6.25}$$

where D_1 is the constant of proportionality for the new term. As a result, Equation 6.23 becomes:

$$C_{O_2} = \frac{4F(D_0 + D_1 j)(T - T_0)}{j} + C_0 \tag{6.26}$$

$$= \frac{4FD_0(T - T_0)}{j} + 4FD_1(T - T_0) + C_0 \tag{6.27}$$

From inspection it is clear that the terms $4FD_1(T - T_0)$ and C_0 are analogous, and the new term is just another method of representing C_0. As such, the lines of the model in Figure 6.4 will remain straight, and whatever function of j that has to be added to Equation 6.21 to produce a better fit would have to be at least 2nd-order. Since it is hard to think of any physical justification for such a parameter, it has been discounted.

Differentiating C_j (i.e. the slopes of the lines of best-fit, which are shown as dashed lines in Figure 6.4) with respect to T produces:

$$\frac{dC_j}{dT} = 4FD_0 \tag{6.28}$$

therefore:

$$D_0 = \frac{1}{4F} \cdot \text{slope}\left[\text{slope}(C_{O_2}, 1/j), T\right] \tag{6.29}$$

where $\text{slope}(y, x)$ is a common spreadsheet function that returns the slope of the line of best-fit through the set of points $[x, y]$. Similarly:

$$T_0 = \text{intercept}\left[T, \text{slope}(C_{O_2}, 1/j)\right] \tag{6.30}$$

where $\text{intercept}(y, x)$ is a companion function to $\text{slope}(y, x)$ that returns the y-value where the line of best-fit intercepts the y-axis. The remaining parameter C_0 is obtained from:

$$C_0 = \text{average}\left[C_{O_2} - \frac{4FD_0(T - T_0)}{j}\right] \tag{6.31}$$

Performing this procedure for the set of measurements reported by Hug *et al.* produces the fitting parameters shown in Table 6.2.

Parameter	$\mathbf{D_0}$	$\mathbf{T_0}$	$\mathbf{C_0}$
Units	$\mathrm{mol\,s^{-1}\,m^{-2}\,K^{-1}}$	K	vol%
Value	1.35×10^{-7}	254	0.03

Table 6.2: Best-fit parameters of the model to the results published by Hug *et al.*

When plotted against the log of current density the results appear as shown in Figure 6.5, where the symbols represent the published measurements, and the grey dashed lines represent the model.

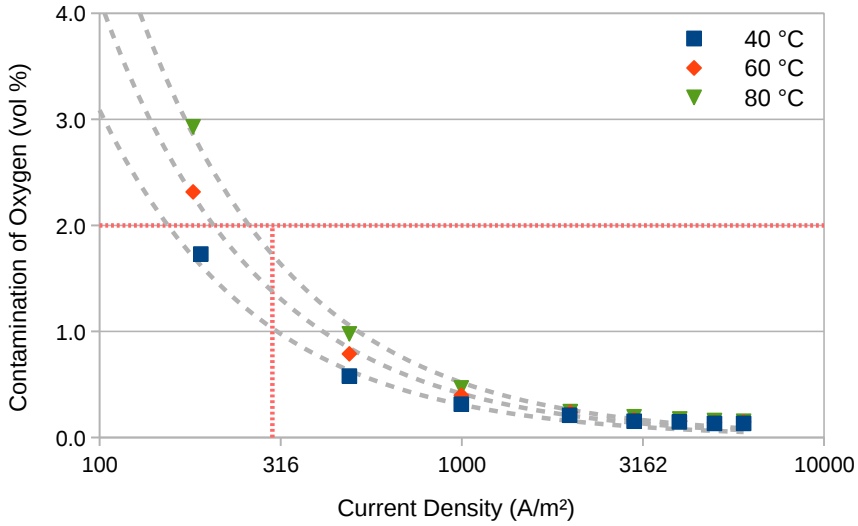

Figure 6.5: Comparison of the model results and the measurements in 28 wt% KOH published by Hug *et al.*

On this scale, the consistent mismatch between predicted and measured gas contamination at high current densities looks much less significant, and in any case is non-hazardous. At low current densities, it is clear that there is an inverse relationship between temperature and minimum standby current for any given maximum permitted level of contamination. For example, at 80 °C and a safety limit of 2 vol% H_2 in O_2, the minimum standby current is $\sim$300 $\mathrm{A\,m^{-2}}$ (30 $\mathrm{mA\,cm^{-2}}$), which is represented by the red dotted lines. Reducing the electrolyte temperature could reduce this figure to $\sim$200 $\mathrm{A\,m^{-2}}$, but in terms of increased safety this is not particularly significant.

For this electrolyser, this means that if the available current falls below 5% of the maximum design current, it should be shut down. Should the electrolyser use less concentrated electrolyte, gas-mixing will increase, and this figure will be a lot higher. This was confirmed by R. Phillips, who found that increasing the concentration of the electrolyte greatly reduced

gas-mixing, even at low current densities. This appeared to be simply because both hydrogen and oxygen were less soluble in strong alkaline solutions [143]. However, there are two relatively simple schemes that could permit an electrolyser to continue operating at low-current without excessive gas-mixing:

Reduced Stack: If at low input voltages the current density falls to a level that is too low for gas-safety, the current density could be increased by reducing the size of the stack. A simple way to achieve this would be to short-circuit one or more of the bipolar-electrodes within the stack, such that the total number of cells is reduced. Ideally, this would be performed in such a fashion that the duty-cycle on each side of every electrode were equalised in the long-term, such that the lifetime of the stack could be maximised.

Reduced Duty-Cycle: Another method of artificially increasing the current density would be to store incoming energy in a super-capacitor, and then periodically discharge this through the electrolyser stack. In this fashion the stack would operate in a similar way to some desktop toys that store energy from a small solar panel, and then release it rapidly into a motor.

In any case, if for no other reason than to reduce gas-mixing and thereby extend the safe operating range of the electrolyser, the strongest possible electrolyte should be used. An attendant benefit is of course also increased electrolyser efficiency. This is subject to the corrosion limits of the electrodes and other electrolyser components, but this is where it is notable that stainless-steel has a remarkably low rate of corrosion in KOH at concentrations up to 30 wt% and temperatures up to 100 °C [238].

6.3 Electrolyser Model

The voltage seen at the terminals of an electrolyser is comprised of several components:

$$V_{elect} = V_{therm} + V_{act} + V_{ohmic} \tag{6.32}$$

where V_{elect} is the total electrolyser voltage, V_{therm} is the minimum voltage required to thermodynamically split water (1.23 V), V_{act} is the activation voltage required to overcome the reaction overpotentials, and V_{ohmic} are the losses due to electrical resistance in the electrodes and electrolyte.

Various electrolyser models have been proposed in the literature, including that by Ulleberg *et al.*, which expressed the voltage as a function of the current, and used 6 electrochemical parameters [238]. The authors then proceeded to extend their own model to include

Faradaic efficiency, thermal modelling, and even transient effects such as electrolyte heating. This model was further extended to 31 coefficients by Sanchez *et al.*, including 18 coefficients to model the gas-purity [239]. An alternative model based on the Butler-Volmer equation was developed for a unitised regenerative fuel-cell by Doddathimmaiah *et al.* [15], however the method did not feature any fitting for temperature variation.

A detailed model specifically for ZGE designs with porous electrodes was published by Z. Abdin *et al.* [231]. Maximal use of constants with a physical basis were employed, so that the relative contributions to total system efficiency of each system component could be judged. So too fault diagnosis in use could be improved by tracing performance degradation back to individual system components.

The ohmic losses in conductors such as the electrodes will increase with temperature, whereas the losses in electrolytes such as NaOH will decrease with temperature, as the electrolyte becomes more conductive. Using potassium hydroxide as a guide, for which good results are published, a relationship for the conductivity of NaOH would be expected to be similar to that shown in Figure 6.6 [240].

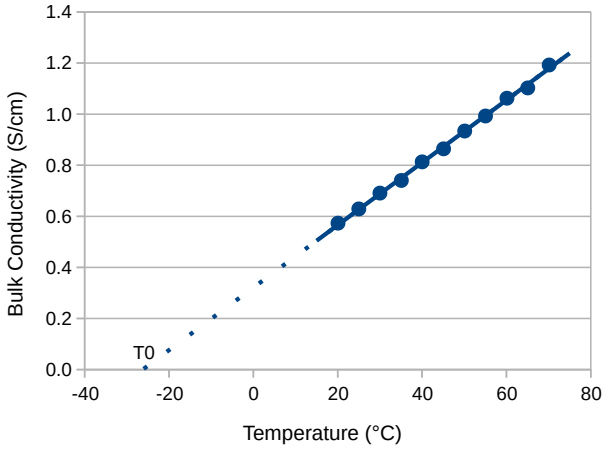

Figure 6.6: Published empirical results for the bulk conductivity of 27 wt% KOH, adapted from Gilliam *et al.* [240]. The conductivity increases linearly with temperature, and by extrapolation appears to intercept the x-axis at temperature $T_0 = -26\,^{\circ}\mathrm{C} (247\,\mathrm{K})$

It should therefore be possible to represent the conductivity of NaOH as the expression:

$$\kappa = (T - T_0)\kappa_0 \tag{6.33}$$

where T_0 is the temperature at which the conductivity intercepts the x-axis, and κ_0 is the slope of the line of best fit. Note that the conductivity reported in Figure 6.6 has units of $\mathrm{S\,cm^{-1}}$ because it is a *bulk* conductivity, whereas an electrolyser will have an *area* conductivity with units of $\mathrm{S\,m^{-2}}$.

To verify this relationship, an experiment was conducted using EIS to measure how the resistance of 1 M NaOH varied with temperature. The experiment was conducted in a 2-electrode cell similar to that shown in Figure 2.2 on page 41, except that no reference electrode was present, the gap between electrodes d was 3.6 cm, and both electrodes had an exposed area A of 36 cm^2. The cell was heated using an external beaker placed on a hot-plate, and the electrolyte was circulated using a small d.c. pump. The results were as presented in Figure 6.7a. They confirm the linear nature of the relationship, and produce an extrapolated value of T_0 of -34 °C (239 K). If the measured conductivity is converted to a bulk conductivity, by multiplying by d/A, and then compared with Figure 6.6, the results are as shown in Figure 6.7b. The figure shows that the conductivity of 1 M NaOH is about 7 times less than that of 27 wt% KOH, irrespective of temperature.

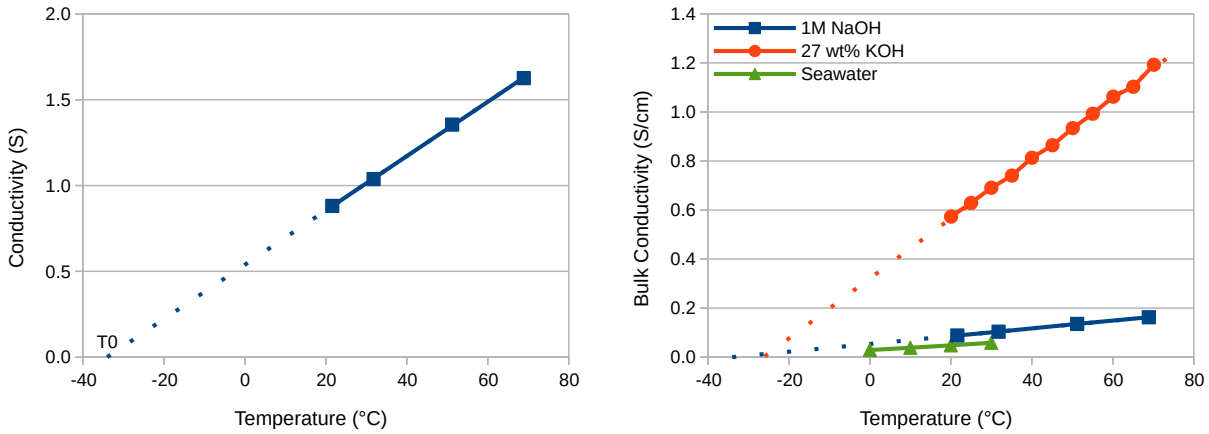

(a) Measured conductivity

(b) Comparison with KOH

Figure 6.7: a) Experimental results for the conductivity of 1 M NaOH. EIS frequency range: 100 Hz to 100 kHz, and b) comparison of bulk conductivity to that of 24 wt% KOH from Figure 6.6.

The conductivity of seawater, being approximately 0.5 M NaCl, is about half as much again, as shown by the green triangles.[1] This implies that even if all the other problems of seawater electrolysis could be solved, such as ionic build-up, poisoning and the evolution of chlorine gas, there still appears to be an upper performance limit based on its relatively low bulk conductivity.

If the assumption is made that the overall ohmic conductivity of the *electrolyser*, and not just the electrolyte, is a linear function of temperature, for example because the electrolyte losses dominate, then Equation 6.32 can be rewritten as:

$$V_{elect} = V_{therm} + V_{act} + \frac{j}{(T - T_0)\kappa_0} \tag{6.34}$$

[1] source: https://www.engineeringtoolbox.com/sea-water-properties-d_840.html

where j is the current density, and V_{ohmic} has been replaced by j/κ.

The thermodynamic splitting voltage for liquid water V_{therm} is known to vary with temperature and pressure according to the formula [241]:

$$V_{therm} = 1.23\,\mathrm{V} - 0.00067(T - 298\,\mathrm{K}) + \frac{3RT}{4F}\ln\left(\frac{p}{1\,\mathrm{bar}}\right) \tag{6.35}$$

When plotted, this produces results such as those shown in Figure 6.8. The figure shows that the water-splitting voltage falls with temperature, but rises with pressure, which is because at higher pressures more work must be performed to generate gaseous products. However, for any given pressure, the water-splitting voltage is unlikely to vary by more than 100 mV.

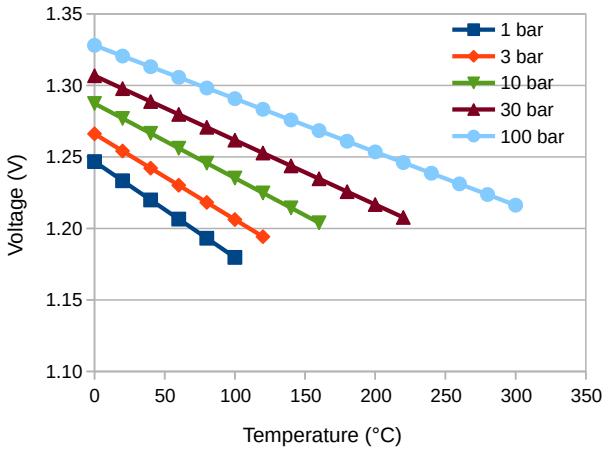

Figure 6.8: Thermodynamic water-splitting voltage as a function of temperature and pressure, in accordance with Equation 6.35.

Similarly, the activation voltage V_{act} is known to vary with temperature in accordance with Equation 1.28 on page 26, here reproduced:

$$U = \frac{T}{k_2}\ln(j) - \frac{k_1}{k_2} - \frac{k_3}{k_2}T \tag{6.36}$$

Substituting in the values for k_n from Table 3.9 on page 84, this can be rewritten as:

$$V_{act} = \frac{T}{23081}\ln(j) + 1.018 - 0.0024T \tag{6.37}$$

When plotted, this produces results such as those presented in Figure 3.16 on page 84. The figure shows that the variation of the Tafel slope with temperature is slight. It also shows that even if the variation of the Tafel offset with temperature is ignored, the error will not exceed about 60 mV.

In any case, at least to a first-order of approximation, any linear variation with temperature of V_{therm} and V_{act} will be incorporated into V_{ohmic}, even though V_{ohmic} is scaled relative to

T_0, not 0 K. This means that the model will be slightly inaccurate, especially at the extremes of the temperature range, but the correct question is whether the increase in accuracy would be worth adding an extra parameter to the model. If the losses due to V_{ohmic} are more than about 100 mV, then this will not be the case. Incorporating these simplifications produces the equation:

$$V_{elect} = V_0 + b\log(j) + \frac{j}{(T - T_0)\kappa_0} \tag{6.38}$$

Here V_{therm} has been replaced by V_0 (a constant), and V_{act} has been replaced by the Tafel equation $b\log(j)$. This mathematical model states that the electrolyser voltage can be simplified such that it is the summation of:

1. a component that is invariant (V_0)
2. a Tafel component that is proportional to $log(j)$ but invariant of temperature
3. a component that is proportional to j and inversely proportional to $(T - T_0)$ i.e. such that it behaves like an ideal electrolyte

It is interesting to note that the value of 247 K produced for T_0 in Figure 6.6 on page 215 is extremely close to the value of 254 K produced from the analysis of gas-mixing in Section 6.2.2 on page 210. It therefore seems possible that the conductivity of the electrolyte and the ability of gas to diffuse through it are linearly related, which is understandable since both properties are dependent on mobility. If so, then Equations 6.21 and 6.33 can be combined to produce:

$$\kappa = k_\kappa \cdot D_{H_2} \tag{6.39}$$

where k_κ is a new constant of proportionality, and one that may well be a fundamental property of the electrolyte.

6.3.1 Model Fitting

In order for the mathematical model represented by Equation 6.38 to be fitted to empirical data, four parameters must be selected and optimised, namely V_0, b, κ_0 and T_0. This could be performed using numerical methods and a descent algorithm to find the optimal point of a suitably defined cost-function in the four-dimensional solution space. However, it is possible to reduce the number of solution space dimensions first by differentiating with respect to $1/(T - T_0)$:

$$\frac{dV_{elect}}{d\left(\frac{1}{T-T_0}\right)} = \frac{j}{\kappa_0} \tag{6.40}$$

If the model is correct, this tells us that T_0 will be chosen optimally when a plot of V_{elect} against $1/(T - T_0)$ produces lines which are *most linear* with respect to the current density

j, with the constant of linearity equal to $1/\kappa_0$. In a similar fashion to that which was used previously in Section 3.3.4 on page 91, a suitable and widely-available measure of linearity is the square of the Pearson coefficient, which is present in all common spreadsheet programs as the function RSQ(). Given any dataset, this produces a value that ranges from 0 (uncorrelated) through to 1 (linear). Thus, a suitable first cost function would be:

$$Cost_1(T_0) = RSQ(V_{elect}, 1/(T - T_0)) \tag{6.41}$$

If both the values of T_0 and κ_0 are chosen correctly, such that they optimally model the contribution from V_{ohmic}, then the remaining part of the voltage, V_{rem}, will reduce to:

$$\begin{aligned} V_{rem} &= V_{meas} - \frac{j}{(T - T_0)\kappa_0} \\ &= V_0 + b\log(j) \end{aligned}$$

where V_{meas} is the measured voltage. Differentiating this with respect to $\log(j)$ yields:

$$\frac{dV_{rem}}{d\log(j)} = b \tag{6.42}$$

Therefore, the values of T_0 and κ_0 will be chosen optimally when a plot of V_{rem} against $\log(j)$ produces lines which are *most linear* with respect to $\log(j)$, with the constant of linearity equal to the Tafel slope b. This gives us a suitable second cost function, specifically:

$$Cost_2(T_0, \kappa_0) = RSQ(V_{rem}, \log(j)) \tag{6.43}$$

Since $Cost_1$ and $Cost_2$ will not be maximised at the same point, an overall cost function is required to trade-off the two potentially conflicting requirements, for example by multiplying them together:

$$Cost_{total}(T_0, \kappa_0) = Cost_1 \times Cost_2 \tag{6.44}$$

The resulting electrolyser dataset fitting procedure is therefore:

1. Plot the two-dimensional solution space (T_0, κ_0) to find the lowest value of $Cost_{total}$
2. Obtain the Tafel slope b from the average value of $dV_{rem}/d\log(j)$
3. Obtain the value of V_0 as that which minimises the offset between V_{meas} and V_{elect}

To assist in visualising the fitting of the model, a slightly abbreviated version of a typical dataset is as shown in Table 6.3, and graphically in Figure 6.9.

It can be seen that the voltage increases with current density, and decreases with temperature, but it is difficult to see much more than that, and it is certainly difficult to quantitatively assess the contribution of the various components. Therefore, it can be seen that the

		Current Density ($A\,m^{-2}$)					
		250	**500**	**1250**	**2500**	**3750**	**5000**
Target Temperature	**30 °C**	1.78 V	1.88 V	2.11 V	2.44 V	2.75 V	3.04 V
	50 °C	1.68 V	1.77 V	1.95 V	2.20 V	2.45 V	2.77 V
	70 °C	1.59 V	1.67 V	1.83 V	2.05 V	2.26 V	2.47 V

Table 6.3: Typical dataset of electrolyser voltages at various values of temperature and current density. Electrolyser: ZGE-A; Pump voltage: 8 V. The full dataset is as listed in Table A.1 on page 258. All temperatures were within ±1 °C of the target.

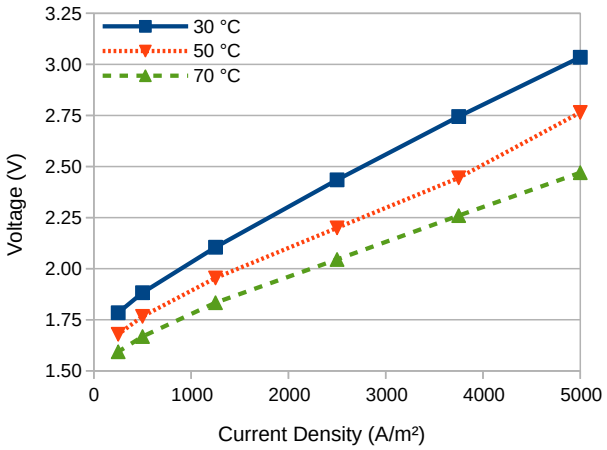

Figure 6.9: The same measurements as in Table 6.3, but in graphical form

development of a mathematical model, and a procedure to fit it to any given dataset, is in fact a method of accurately assessing the impact of any design changes.

Step 1 The solution space that is produced as a result of applying step 1 of the above procedure to the dataset presented in Table 6.3 on page 220 is as shown in Figure 6.10.

6.3.2 Improved Fitting

The most obvious feature of the solution space shown in Figure 6.10 is that it is highly directional. This indicates that there is a wide range over which T_0 can be chosen, so long as a corresponding value of κ_0 is chosen. This is unsatisfactory, but can be comprehended if two additional pairs of values from the 'ridgeline' of the solution space are selected, as shown by the blue numbers in Figure 6.10, and then compared as shown in Figure 6.11 as the lines 'Point 1', 'Point 2' and 'Point 3'.

These 3 pairs of values differ in terms of T_0 by 20 K, but the corresponding values of κ_0 vary in such a fashion that the conductivities all converge within the 30 to 70 °C region, which is where the dashed lines have been positioned. This is the range of temperatures

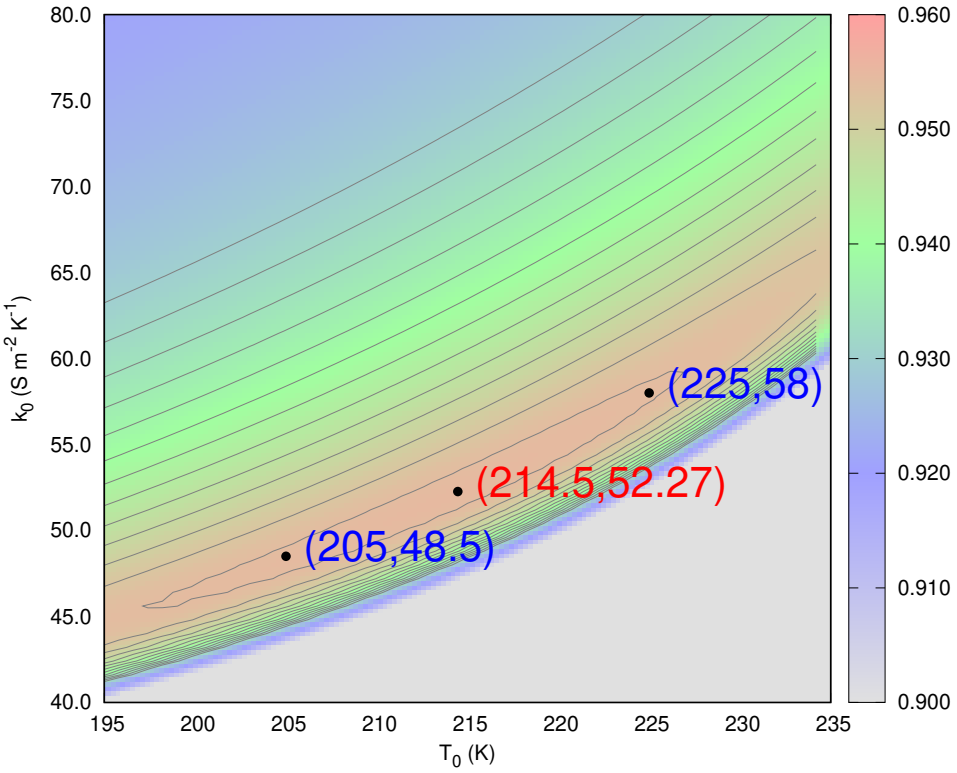

Figure 6.10: Two-dimensional best-fit cost function for the variables T_0 and κ_0 for electrolyser ZGE-A with pump voltage = 8 V. For this set of measurements, the best-fit is shown by the red numbers i.e. $T_0 = 214.5\,\mathrm{K}$ and $\kappa_0 = 52.27\,\mathrm{S\,m^{-2}\,K^{-1}}$.

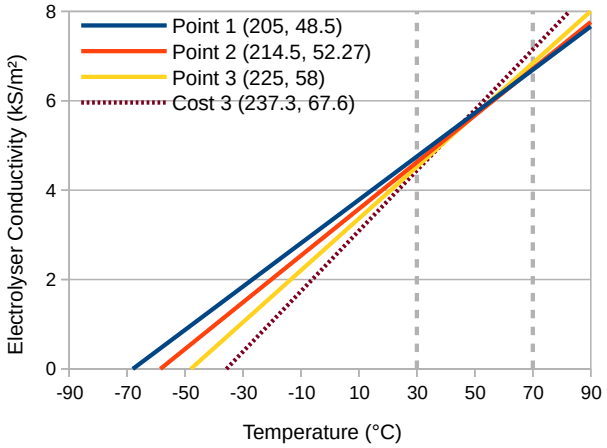

Figure 6.11: Three different models for the conductivity of the electrolyte chosen from different regions along the ridgeline of Figure 6.10. The dashed line indicates the temperature region in which the models converge.

over which the dataset was taken, and is indicating that an insufficiently wide range of temperatures has been covered to properly pin down precise values for T_0 and κ_0.

For some of the other datasets (specifically for ZGE-C) the procedure fails to pin down

any value for T_0 at all. This is because the curve of the voltage *versus* temperature bends slightly the wrong way, as far as the model is concerned, which causes the lines of V_{elect} against $1/(T - T_0)$ to be *most linear* when $T_0 = -\infty$.

What this is indicating is that the dataset is incapable of providing reliable values for *both* T_0 and κ_0. However, a figure for T_0 of $-34\,°C$ has *already* been generated using EIS for 1 M NaOH in Figure 6.7a on page 216. This figure was generated for a *large body* of electrolyte, which will therefore produce a figure for T_0 that is dominated by the temperature dependence of the electrolyte. The value of T_0 for the ZGE could be different, since it contains a much smaller body of electrolyte, and therefore much larger contributions from non-electrolytic components, such as the electrodes. It can therefore be argued that the cost function should be altered such that T_0 is constrained to be much closer to $-34\,°C$ (239 K), for example by including a third cost-function:

$$Cost_3(T_0) = \exp\left[-w(T_0 - 239)^2\right] \tag{6.45}$$

where w is a weighting value that determines how rapidly the cost function varies around the target, as shown in Figure 6.12.

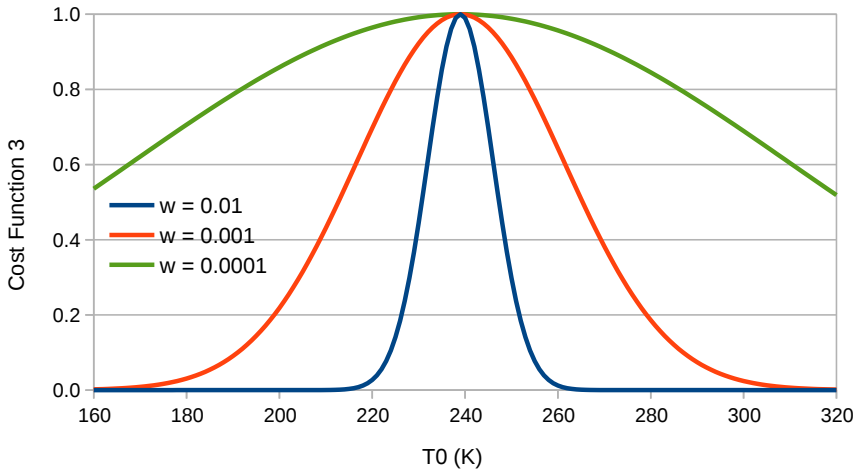

Figure 6.12: Additional cost function to assist in constraining the value of T_0 to approximately 239 K. The value w determines how tightly T_0 is constrained.

The total cost-function previously shown in Equation 6.44 is therefore replaced by:

$$Cost_{total}(T_0, \kappa_0) = Cost_1 \times Cost_2 \times Cost_3 \tag{6.46}$$

Taking $w = 0.0001$, such that T_0 can vary relatively freely, the result of applying the third cost-function to the solution space previously shown in Figure 6.10 is shown in Figure 6.13.

The solution space still has a directional component, but it is much reduced, and the value of T_0 is closer to 239 K. The new best-fit values $T_0 = 237.3\,K$ and $\kappa_0 = 67.6\,S\,m^{-2}\,K^{-1}$

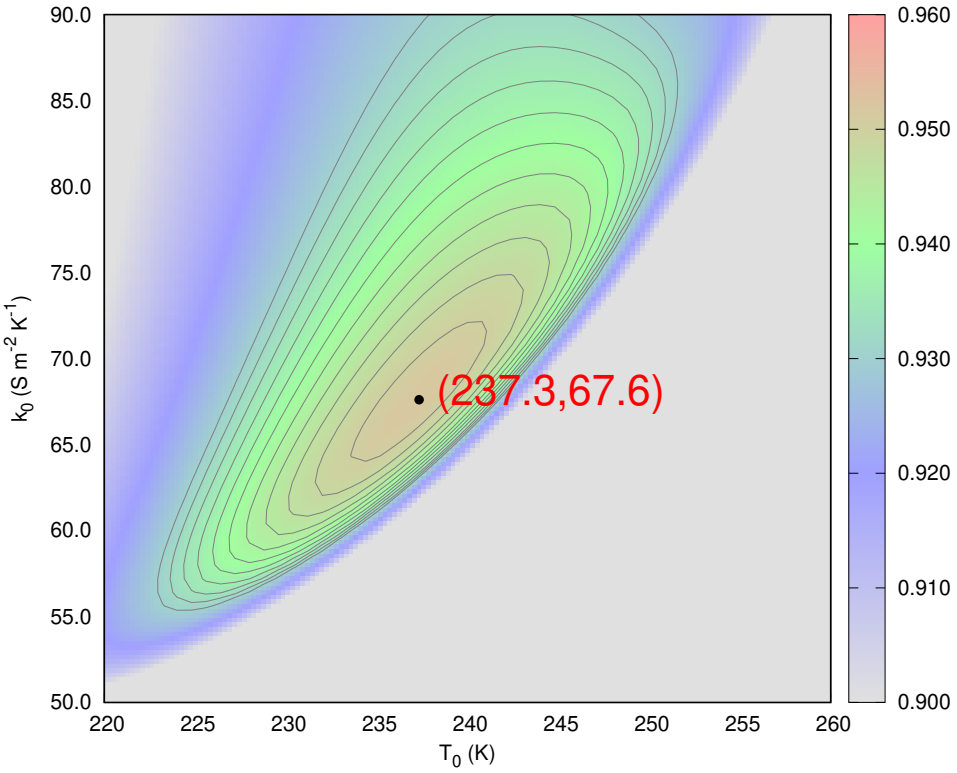

Figure 6.13: Repeat of Figure 6.10, but with the addition of the third cost-function to restrict the amount by which T_0 can vary. The best-fit is now at $T_0 = 237.3\,\mathrm{K}$ and $\kappa_0 = 67.6\,\mathrm{S\,m^{-2}\,K^{-1}}$

combine to produce the line 'Cost 3' on Figure 6.11 which, although steeper, is also observed to converge with the other three lines within the 30 to 70 °C region. The addition of the third cost function, although distinctly artificial, has relatively little effect on the fitting of the final two parameters, since they have zero temperature dependence. In fact, it can seen as forcing the model to interpret the measurements more realistically, based on how we already know the conductivity of the electrolyte *should* vary with temperature.

Step 2 The results of applying Step 2 of the procedure on page 219, based on the values of T_0 and κ_0 extracted from Step 1, are as shown in Figure 6.14. The figure also shows that the average slope of all three plots, which is the best-fit value for the Tafel slope, is 158 mV dec^{-1}. This is remarkably close to the value of 150 mV dec^{-1} which would be expected from theory, that being equal to the sum of 120 mV dec^{-1} for HER at the cathode and 30 mV dec^{-1} for OER at the anode. It is also surprising considering how little of the curved, activation part of the current-voltage transfer characteristic has been collected in the dataset.

The figure also shows that the relationship between V_{rem} and $\log(j)$ becomes less linear at the highest current densities. This can be interpreted as the onset of mass-transfer resistance.

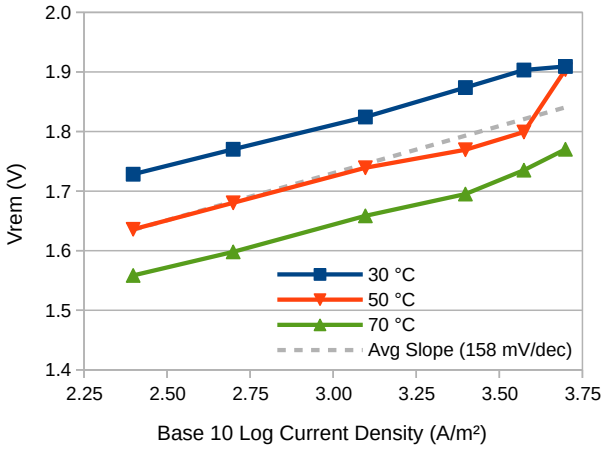

Figure 6.14: Plots of how the remainder voltage V_{rem} varies against $\log(j)$ for the three different target temperatures in the dataset from Table 6.3. The average slope of all three plots is the best-fit value for the Tafel slope.

Although not observed with this dataset, this can have the greatest impact at the lowest temperature. Sodium hydroxide can be surprisingly viscous, with a 50 wt% solution at 20 °C having a viscosity that is close to that of SAE20 engine oil.[2] This viscosity falls rapidly at lower concentrations and with increasing temperature, which will significantly increase the ability of the electrolyser to keep the gas evolution reaction surfaces supplied with sufficient reactant molecules.

Step 3 of the procedure is to determine the optimal value of V_0, as shown in Equation 6.47. The value generated (1.255 V) is quite close to the reversible voltage of the water-splitting reaction (1.23 V). This further supports the hypothesis that the data-fitting procedure is extracting meaningful information from the dataset in a way that is both reliable and tolerant to random measurement errors.

$$\begin{aligned} V_0 &= \text{Average}\left(V_{meas} - V_{act} - V_{ohmic}\right) \\ &= 1.255\,\text{V} \end{aligned} \tag{6.47}$$

The full set of model-fitting parameters for the dataset are as shown in Table 6.4, and the resulting voltage contributions of the three components to the overall electrolyser voltage are as shown in Figure 6.15. Note that the model now permits the predicted data to be extended into regions that are outside of the range of the original dataset. Also note that at a current density of 5000 A m^{-2} the ohmic losses are making up more than 30% of the total electrolyser voltage. This means the electrolyser will be consuming nearly 50% more

[2]Sources: http://www.liquiflo.com/v2/files/pdf/applicationnotes/AN0101-1-SodiumHydroxide-Jan2016.pdf viewed May 2020; https://hydramotion.com/uploads/view/20160224144736_Hydramotion_Viscosity_Units.pdf viewed May 2020

energy for the same quantity of hydrogen produced than it would if the ohmic losses could be eliminated.

Parameter	$\mathbf{T_0}$	$\boldsymbol{\kappa_0}$	**b**	$\mathbf{V_0}$
Units	K	$\mathrm{S\,m^{-2}\,K^{-1}}$	$\mathrm{mV\,dec^{-1}}$	V
Value	237.3	67.6	158	1.255

Table 6.4: Optimal set of parameters resulting from the fitting of the mathematical model shown in Equation 6.38 to the dataset shown in Table 6.3.

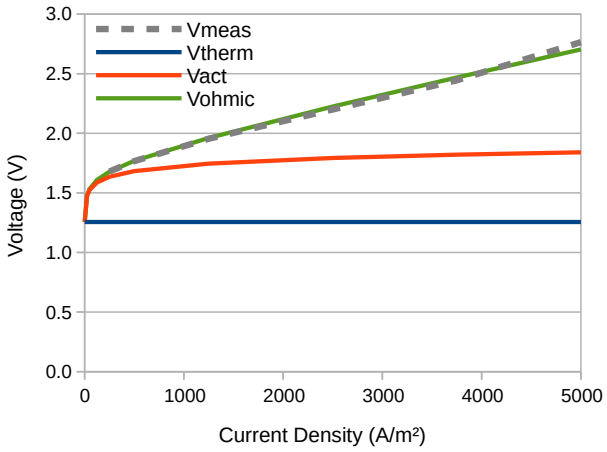

Figure 6.15: Plot showing the sum of the three components of the mathematical model, V_{therm}, V_{act} and V_{ohmic} at 50 °C and how they compare with the measured voltages from the dataset in Table 6.3.

According to the model, the value of the total electrolyser conductivity is given by the expression in Equation 6.33 on page 215, which at 50 °C is equal to:

$$\begin{aligned}\kappa &= (T - T_0)\kappa_0 \\ &= (323 - 237.3) \times 67.6 \\ &= 5793\,\mathrm{S\,m^{-2}}\end{aligned}$$

This means that were the electrolyser expanded up to $1\,\mathrm{m^2}$, it would have an ohmic resistance of just $1/5793\,\mathrm{S} = 0.17\,\mathrm{m\Omega}$. Nevertheless, as an aid to visualising how much of the power supplied to the electrolyser is lost to such conductivity, it is possible to define an 'ohmic efficiency' as the proportion of the electrical energy supplied that is *not* dissipated as ohmic losses, i.e. according to the expression:

$$\begin{aligned}\eta_{ohmic} &= \frac{\text{energy not dissipated as ohmic losses}}{\text{total electrical energy supplied}} \\ &= \frac{j \times (V_0 + b\log(j))}{j \times (V_0 + b\log(j) + j/\kappa)} \times 100\%\end{aligned}$$

which produces the results shown in Figure 6.16a. The dashed line has been positioned at 5793 S m^{-2}, and reveals that in order for the electrolyser to maintain an ohmic efficiency of at least 80%, the current density must be kept below 2500 A m^{-2}, which is just 250 mA cm^{-2}. This is a factor of four short of the 1 A cm^{-2} that is typical of commercial alkaline electrolysers, which are able to achieve this because they operate at higher temperatures and with stronger electrolyte.

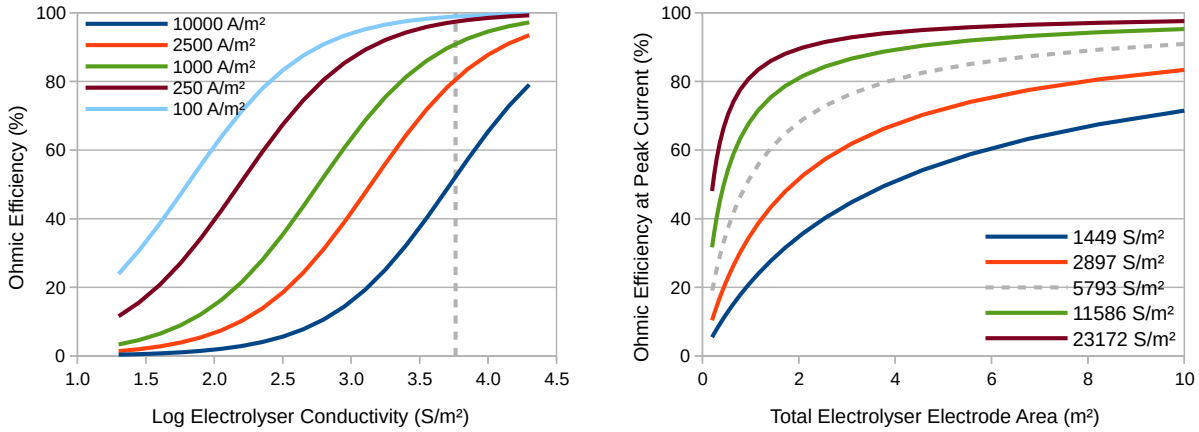

(a) Ohmic efficiency

(b) Electrolyser Area

Figure 6.16: Effect on the ohmic efficiency of a) electrolyser conductivity and b) total electrolyser area. The dashed line represents the conductivity of electrolyser ZGE-A. Peak design current: 10 000 A.

The capital expenditure on any given electrolyser is, at least to a first order of approximation, inversely proportional to its maximum current density, since this governs its overall size. Therefore the cost is governed by the conductivity, and any factor that can increase this is worthy of pursuit. Another way to visualise this is as shown in Figure 6.16b, which shows the trade-off between total electrolyser area and minimum ohmic efficiency for various values of specific electrolyser conductivity. As a design exercise, the electrolyser is designed for a maximum current of 10 000 A, and the dashed line represents an electrolyser with the same specific conductivity as ZGE-A. The figure shows how if the electrolyser conductivity were to be improved by a factor of two, then the electrolyser area needed to achieve 80% ohmic efficiency would be reduced by a factor of two. Therefore conductivity and cost are inversely related for the same target efficiency.

The model also permits an assessment of the cooling requirements that would be required for an electrolyser stack of different sizes and under different conditions. The heat dissipation per cell is equal to:

$$P_{heat} = I_{cell} \times (V_{cell} - 1.48\,\mathrm{V}) \tag{6.48}$$

where 1.48 V is the thermoneutral voltage. This takes account of the electrical power in that comes out in the form of chemical energy (i.e. hydrogen and oxygen gas), rather than thermal energy. For example, assuming that a ZGE stack were constructed of 24 cells, each of size 50 cm × 50 cm, the heat dissipated at three different temperatures would be as presented in Figure 6.17.

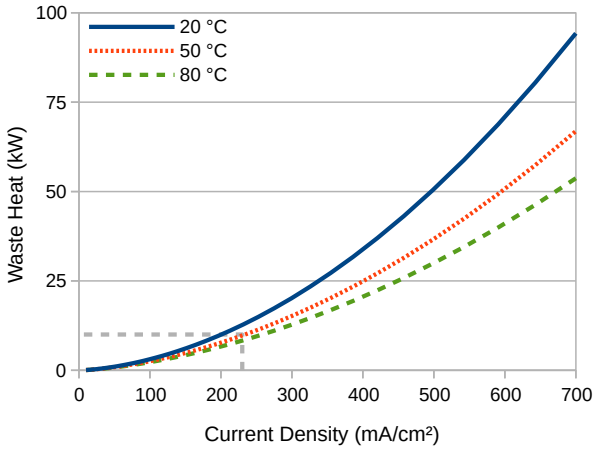

Figure 6.17: Cooling requirements of a 50 cm × 50 cm 24-cell ZGE based on the performance of ZGE-A.

This figure shows that if the cooling system is limited to 10 kW and the electrolyte to 50 °C, then the current will be limited to 230 mA cm^{-2} (as shown by the dashed grey box). However, it is known that an automotive radiator from the car industry is able to dissipate 50 kW at a wind speed of 6 m s^{-1} [242]. In combination with an electrolyte temperature of 80 °C this would permit the same electrolyser to safely accept nearly 700 mA cm^{-2}.

6.4 Performance Assessments

In order to assess the performance of the zero-gap design concept, a basic device was constructed using laser-cut and laser-engraved acrylic components. In general, its appearance was as shown in Figure 6.18. A more detailed description of its individual components and assembly is listed in Section 2.3 on page 58.

Several versions of the device were constructed in order to assess the impact of changing various components, as shown in Table 6.5, with the objectives as shown in Table 6.6.

Two of the electrolyser model parameters are primarily related to the electrolyte (i.e. T_0 and κ_0), and the other two (V_0 and b) to the thermodynamics and kinetics. Therefore, the effect of changing the electrolyte to 0.5 M NaOH for ZGE-B should only affect the first two. In this way, the model helps to isolate the three different aspects of electrolyser performance.

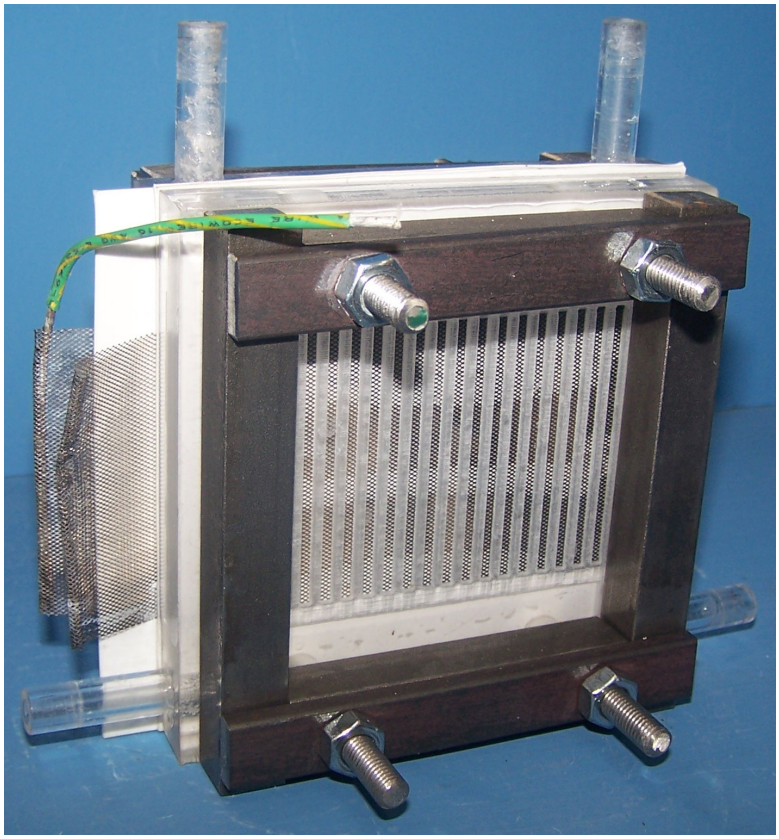

Figure 6.18: Physical appearance of Electrolyser ZGE-A

Electrolyser	Electrodes	Catalyst	Flowplates	Membrane	Electrolyte
ZGE-A	Perforated	Raney 2	Acrylic	Zirfon	1 M NaOH
ZGE-B	Woven	Raney 2	Acrylic	Zirfon	0.5 M NaOH
ZGE-C	Perforated	Raney 2	Conductive Plastic	Zirfon	1 M NaOH
ZGE-D	Woven	Raney 2	316SS	Zirfon	1 M NaOH
FGE-E	316SS	None	N/A	Woven	1 M NaOH

Table 6.5: Zero-gap (ZGE) and Finite-gap (FGE) designs and their component construction.

Electrolyser	Objective
ZGE-A	To act as baseline.
ZGE-B	To determine if the performance could be improved by the addition of a high surface-area woven stainless-steel mesh electrode, to increase the kinetics.
ZGE-C	To measure the performance using flow-plates made of conductive plastic, to reduce the ohmic resistance.
ZGE-D	To determine the performance using flow-plates made of solid stainless-steel.
FGE-E	To determine if the Zirfon membrane could potentially be replaced by woven stainless-steel.

Table 6.6: Experimental objectives of the different electrolyser models.

6.4.1 Electrolyser Components

Perforated Nickel Mesh Supplied by Dexmet, Connecticut USA, the mesh is manufactured from nickel metal sheet that has been perforated to produce diamond-shaped holes. The mesh used in this experiment was 0.005" thick, with a 0.005" strand thickness and 0.05" long rhombus-shaped holes. The appearance of the mesh before and after coating with the Raney 2 electrocatalyst (as described in Section 5.2 on page 168) was as shown in Figure 6.19. The sheet resistance of the mesh was measured at 2.2 mΩ/□, which means that the resistance across any square-shaped piece was 2.2 mΩ.

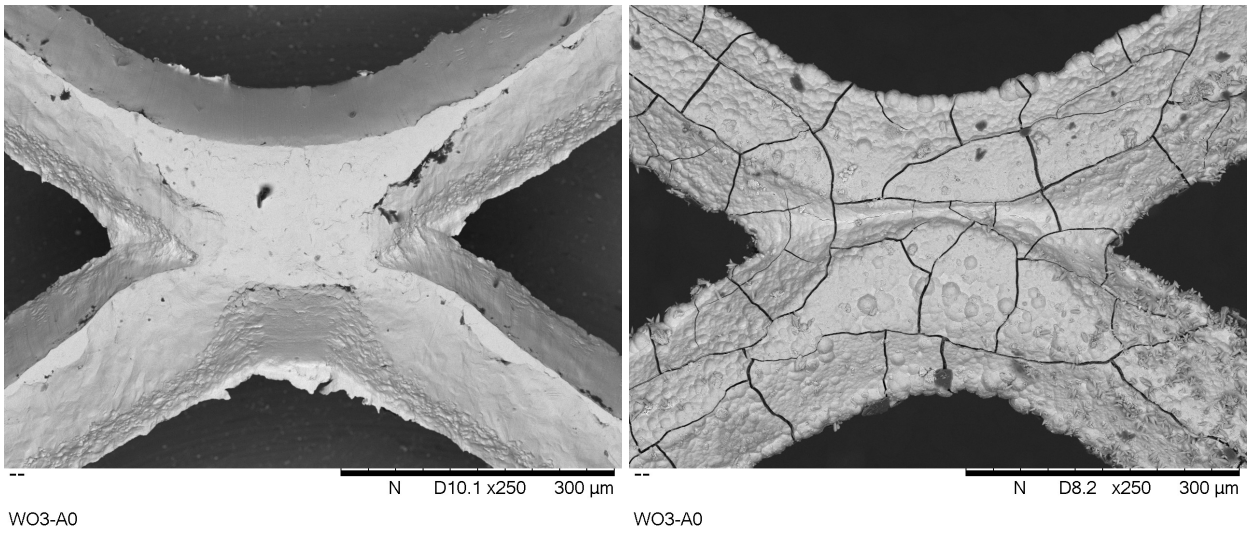

(a) As supplied (b) After Raney 2 deposition

Figure 6.19: Perforated nickel mesh before and after deposition. The length of the black bar at the bottom of each image is 300 µm.

Woven stainless-steel Supplied by Inoxia Ltd, UK, the mesh is manufactured from woven strands of stainless-steel. The mesh used in this experiment had 200 tpi (threads per inch), and each strand had a diameter of about 50 µm. The appearance of the mesh before and after coating with the Raney 2 electrocatalyst was as shown in Figure 6.20. The sheet resistance of the woven mesh was measured (before electrodeposition) at 49 mΩ/□, which is more than 20 times higher than that of the perforated mesh. Therefore the woven mesh was backed by uncoated perforated mesh to achieve sufficiently low sheet resistance.

Since the Raney 2 coating is highly porous, the intention was to completely fill the gaps in the woven mesh with catalyst. This was based on the hypothesis that product and reactant molecules would be able to diffuse rapidly through the coating. This would therefore present the maximum possible surface area for the water-splitting chemical reaction to the Zirfon membrane. Nevertheless, it is clear that a trade-off must be struck between catalytic

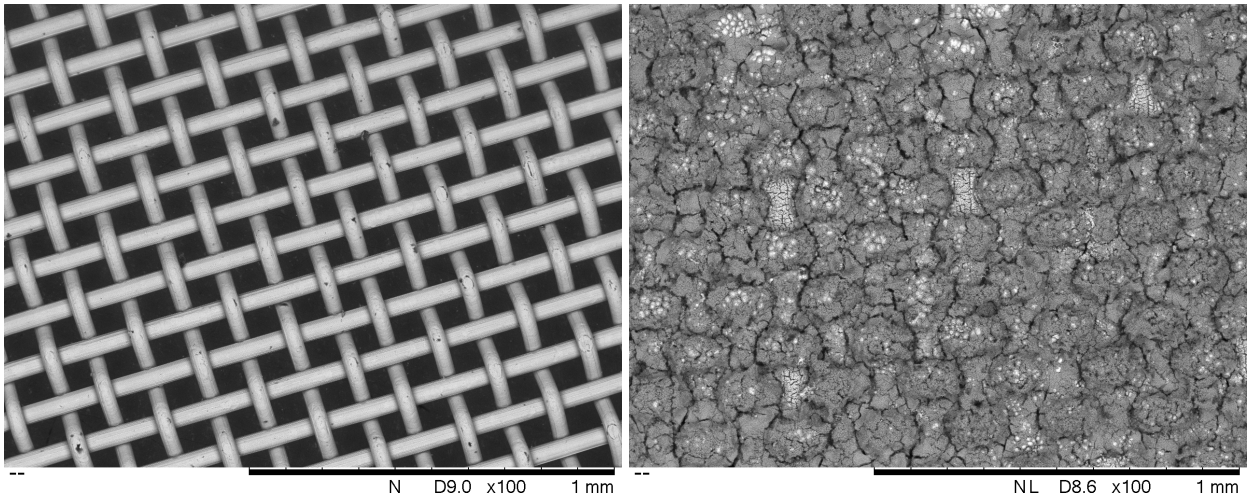

(a) As supplied (b) After Raney 2 deposition

Figure 6.20: Woven 200 tpi 316-grade stainless-steel mesh before and after deposition. The length of the black bar at the bottom of each image is 1 mm.

surface area and the ability of reactant molecules to access that surface area, i.e. the mass transport resistance. Every design of ZGE encounters this issue.

Sheet Resistance If a ZGE such as the one shown in Figure 6.18, with perforated nickel electrodes and an active area of $40\,\mathrm{cm}^2$ passes a current of $1\,\mathrm{A\,cm}^{-2}$, there is an additional voltage drop of:

$$V = 40\,\mathrm{A} \times 2.2\,\mathrm{m\Omega/\square} \times (12\,\mathrm{cm}/5\,\mathrm{cm}) = 0.21\,\mathrm{V\ per\ electrode\ pair} \tag{6.49}$$

due to sheet resistance. This assumes the average distance over which voltage is dropped is about 12 cm from the middle of one electrode to the middle of the next. For a larger design of electrolyser, for example (50×50) cm, the sheet resistance remains the same, therefore the voltage drop does *not* scale with electrolyser size. Although it is possible to supply power to each electrode from more than one side, this complicates the design. Ultimately, this highlights the problem of a design featuring non-conducting flow-plates, and is why potential solutions such as conductive plastic shall be investigated.

It is important to understand that the effect of electrode resistance is greatly magnified in a bipolar stack electrolyser, due to the presence of shunt currents in the feed channels to each cell, and leakage currents in the flow channel connecting all the cells. The leakage current, which is the difference between the current supplied to each end of the stack, and the current passing through each cell, is especially detrimental to overall electrolyser performance because its effect is greatest in the middle two-thirds of the stack [206].

Using a computer simulation of the effect of electrode resistance on such currents, Kuhn and Booth were able to demonstrate that an increase of electrode resistance from zero to just 3 mΩ was sufficient to increase the leakage current by more than a factor of 3 [23]. The effect on the stack of this leakage current is most pronounced at low current densities, and together with its capacity to create explosive gas mixtures is thereby another factor helping to set a minimum safe current density, below which the stack must be shut down. It is in this way that a trade-off must inevitably be made between the manufacturing benefit of using cheap, non-conducting plastic flow-plates with perforated mesh electrodes over solid, machined stainless-steel, and the safety deficit that comes from enhanced leakage currents, and the attendant gas-mixing and explosion hazard that results.

Conductive Plastic Flow-plates This material is subject to a Non-Disclosure Agreement protecting the Intellectual Property, and was supplied by a commercial organisation in the USA. Publicly available information states that it is an injection-moulded material which contains electrically conducting fibres. The supplied plates did not feature any flow channels, therefore these were created by the Swansea University Bay Campus Workshop using a CNC (Computer Numerically Controlled) milling machine. The flow channel depth was 1.5 mm, and the appearance of the finished flow-plate was as shown in Figure 6.21a.

316-grade Stainless-Steel (316SS) Flow-plates The Bay Campus Workshop also produced a set of flow-plates from solid stainless-steel, an example of which is as shown in Figure 6.21b. The machining of each plate took at least 1 day, and as such represents a significant level of expense. The intention was therefore not to measure how much performance could be *gained* by using solid metal, but to measure how much performance was *lost* by using cheaper alternatives.

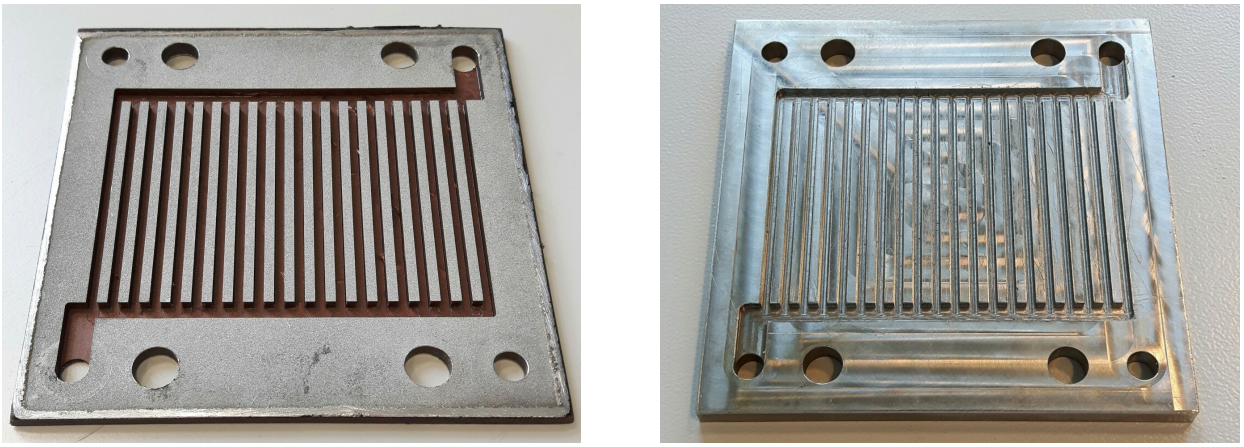

(a) Conductive plastic (b) 316SS

Figure 6.21: Flow-plates in different materials after CNC machining.

6.5 Results

6.5.1 Faradaic Efficiency

A basic test of the capability of an electrolyser to maintain gas separation is to measure whether it produces twice as much gas from the hydrogen outlet as it does from the oxygen outlet. If it does not, then something is awry. Furthermore, the Faradaic Efficiency of the electrolyser can be calculated by measuring the total amount of electric charge that has passed between the terminals. This experimental procedure is described in Section 2.1.5 on page 48, and for electrolyser ZGE-A produced the measurements shown in Table 6.7.

Measurement	Value
Current	2.751 A
Temperature	23.5 °C
Pressure	1000 mbar
Density	1.04 g cm^{-3}
Diameter	90.5 mm
H_2 h1	85 mm
H_2 h2	175 mm
H_2 time	1600 s
O_2 h1	44 mm
O_2 h2	134 mm
O_2 time	1660 s

Table 6.7: Measurements taken during the Faradaic efficiency experiment on electrolyser ZGE-A. Pressure obtained from Meteorological Office weather forecast. Density obtained from https://handymath.com/cgi-bin/naohtble3.cgi?submit=Entry (viewed Dec 2018).

With reference to Figure 2.5 on page 51, the measurement H_2 h_2 can be used to calculate a more accurate value for the pressure in the H_2 collection chamber using:

$$\begin{aligned} P_{H_2} &= P_{atm} + \rho g h_2 \\ &= 1000\,\text{mbar} \times 101.325\,\text{Pa mbar}^{-1} + 1040\,\text{kg m}^{-3} \times 9.81\,\text{m s}^{-2} \times 0.175\,\text{m} \\ &= 103\,110\,\text{Pa} \end{aligned}$$

The volume of H_2 was:

$$V_{H_2} = h_1 \cdot \pi/4 \cdot d^2 = 0.085\,\text{m} \times \pi/4 \times (0.0905\,\text{m})^2 = 0.000\,547\,\text{m}^3$$

Therefore the number of moles of H_2 was:

$$M_{H_2} = \frac{pV}{RT} = \frac{103\,110\,\text{Pa} \times 0.000\,547\,\text{m}^3}{8.314 \times 296.5\,\text{K}} = 0.022\,87\,\text{mol}$$

At 100% efficiency, the amount of charge would be:

$$Q_{H_2} = M_{H_2} \cdot nF = 0.022\,87\,\text{mol} \times 2 \times 96\,485\,\text{C}\,\text{mol}^{-1} = 4413.3\,\text{C} \tag{6.50}$$

The number of seconds this would take is:

$$T_{\text{pred},H_2} = Q_{H_2}/A = 4413.3\,\text{C}/2.751\,\text{A} = 1604.3\,\text{s} \tag{6.51}$$

Therefore the Faradaic Efficiency for H_2 was:

$$\eta_{\text{faradaic}} = \frac{T_{\text{pred},H_2}}{T_{\text{meas},H_2}} = \frac{1604.3\,\text{s}}{1600\,\text{s}} = 100.3\% \tag{6.52}$$

Repeating this calculation for O_2 produces a figure of 99.6%. Both figures are close to 100% efficiency, therefore it may be concluded that the electrolyser is as close to 100% efficient as can be measured by this technique.

It would be tempting to go further, however Equation 6.52 makes it clear that an efficiency difference of 0.3% equates to a time difference of just 4.3 s. Considering that all measurements are taken by eye with a ruler to the nearest millimetre, and the H_2 level falls at only $\sim$20 s mm^{-1}, the accuracy of this method is at best $20/4.3 \times 0.3 = 1.4\%$. In fact, during this period two measurements must be taken, and the time recorded is an approximation. For the O_2 measurement the inaccuracy is double, since the level falls at only half the speed.

In combination with the other sources of inaccuracy identified in Section 2.1.5, it is fairer to conclude that the H_2 efficiency lies between 98% and 100%, and the O_2 efficiency lies between 96% and 100%. Finally, it is important to note that a high Faradaic Efficiency proves only that the electrical charge has been converted into gas. It does not prove that the gases have not been mixed.

6.5.2 Gas Chromatography (GC)

The purity of the hydrogen emitted from electrolyser ZGE-A was measured using the procedure described in section 2.2.4 on page 56. The signal produced was as shown in Figure 6.22.

Once these signal peaks had been integrated by the GC software, and compared with the calibration signals, the compositional analysis was as shown in Table 6.8.

The H_2 figure of 59.00% is not reliable, since the calibration does not work well with high concentrations. However, the O_2 and N_2 figures are reliable, and permit the figures to be corrected for the small amount of atmospheric air that has remained in the system after purging, in accordance with Equation 2.8 on page 58.

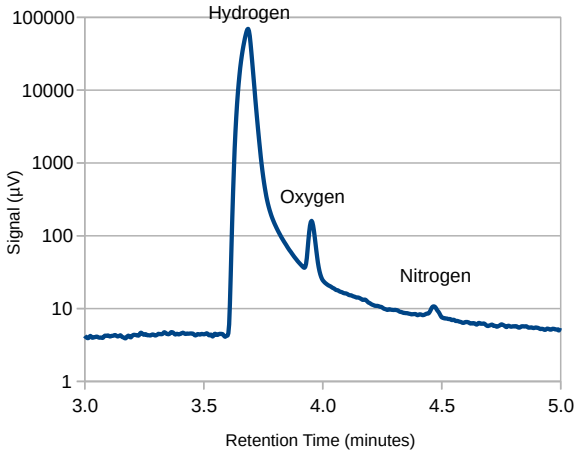

Figure 6.22: Gas Chromatography signal detected for the hydrogen output of ZGE-A operating at 250 mA cm^{-2} with 0.5 M NaOH electrolyte pumped at ~250 ml min^{-1}.

Name	Retention Time (minutes)	Area	Height	RF	Amount (%)	Corrected (%)
H_2	3.683	6922	2658	0.00852	59.00	98.76
O_2	3.954	20.73	5.87	0.06162	1.28	1.24
N_2	4.467	1.73	0.20	0.08184	0.14	

Table 6.8: Gas Chromatography compositional analysis for the hydrogen output of ZGE-A

Once this is done the corrected value of 1.24% is produced, as shown in Table 6.8. From this it may also be concluded that the corrected value for H_2 is 98.76%, since it will be the remainder.

A value of 1.24% O_2 for the gas-mixing of O_2 into H_2 is quite concerning, especially at a current density of 250 mA cm^{-2}. However, from doctorol thesis work conducted by R. Phillips *et al.*, it is known that the rate of gas-mixing decreases markedly as the concentration of the electrolyte increases [143]. This is due to the simple principle that as more hydroxide salt is dissolved into the electrolyte, the less gas it is able to dissolve. Thus, in moving from 1 M NaOH up to the 6.9 M concentration more typical of industrial electrolysers, R. Phillips observed a *20-fold* decrease in the rate of gas-mixing at any given current density. This would also lead to a 20-fold reduction in minimum standby current required to achieve a specific level of gas safety.

Provided that sufficient gas evolution is occurring to maintain the amount of dissolved gases close to saturation point, the rate of diffusion of gas across the membrane will be invariant. As a result, the purity of the hydrogen and oxygen outlets will decrease as the current density decreases. Inevitably a point will be reached at which the current density is so low that the outputs start to become hazardous.

6.5.3 EIS

Electrolyser ZGE-A was analysed using EIS at three different temperatures, with the results as presented in Figure 6.23. The bias voltage was held at 1.1 V, which means that no water-splitting reaction was present.

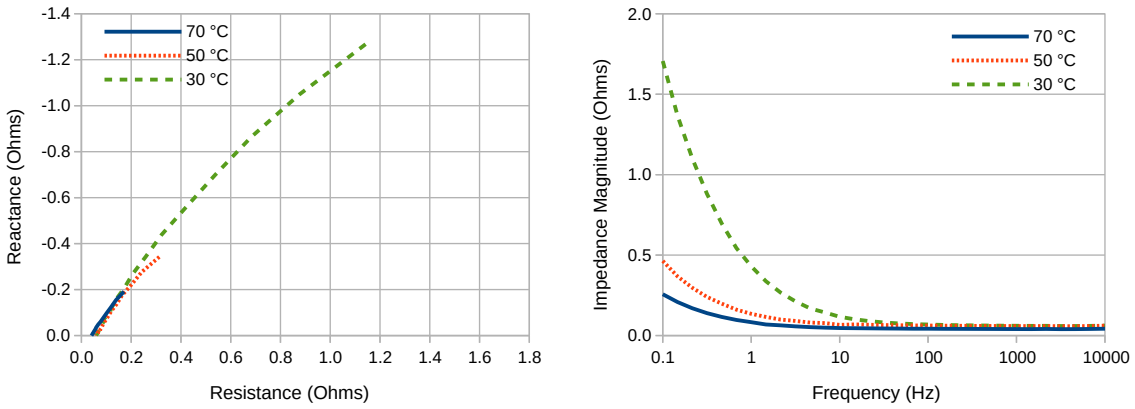

(a) Nyquist Plot

(b) Frequency Plot

Figure 6.23: EIS results for electrolyser ZGE-A between 0.1 and 10 000 Hz at three different temperatures.

The Nyquist plot shows a low-frequency tail at approximately 45°, which is consistent with a Warburg diffusion-related impedance. At high frequencies, the impedance tended towards the ohmic resistance R_Ω, which lay between 40 and 60 mΩ. As such, the equivalent circuit for the electrolyser (in the absence of water-splitting) is as shown in Figure 6.24, where both R_Ω and W_D are temperature dependent.

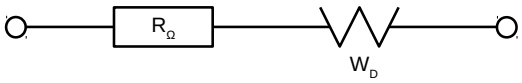

Figure 6.24: Equivalent circuit for the EIS results presented in Figure 6.23

The Warburg impedance is expressed as:

$$W_D = \frac{A_W(1-j)}{\omega^{0.5}} \tag{6.53}$$

where A_W is the Warburg coefficient, and ω the frequency in rad/ sec. The Frequency Plot shows the effect of increasing the temperature was to greatly reduce the impedance due to diffusion, and the ohmic resistance R_Ω was also reduced by ∼20 mΩ, as confirmed by the best-fit values shown in Table 6.9.

Because the electrodes are in contact with the membrane, the only resistance being measured is that of the electrodes plus the solution inside the membrane itself. Assuming, as before in Equation 6.49 on page 230, that the total average conducting path involves ∼12 cm of perforated mesh per electrode pair, then the resistance of the solution at 30 °C was:

Parameter	Units	30 °C	50 °C	70 °C
R_Ω	Ω	0.060	0.059	0.041
A_W	$\Omega \text{rad}^{0.5}$	0.78	0.27	0.17

Table 6.9: Best-fit parameters for the equivalent circuit in Figure 6.24 to the results in Figure 6.23.

$$R_S = R_\Omega - 2.2\,\text{m}\Omega/\square \times (12\,\text{cm}/5\,\text{cm}) = 54\,\text{m}\Omega$$

This is an important point. Even with a zero-gap configuration, the majority of the resistance of the electrolyser (in the absence of water splitting) was *still* due to the membrane and the electrolyte, not the electrodes. This is despite the fact that the zero-gap configuration is conceived in an effort to reduce the electrolytic losses to zero.

6.5.4 Chronopotentiometry

The performance of each ZGE was analysed in the temperature controller test-rig, as shown in Figure 6.25. The figure shows (from left to right): hot-plate with temperature probe to control electrolyte temperature; large beaker containing water-bath; smaller beaker inside (not visible) containing the electrolyte; d.c. pump power supply; multimeter to measure electrolyser voltage; brushless d.c. pump; ZGE under test; electrolyser power supply. As pictured, the set-up therefore shows an electrolyte temperature of 69 °C, a pump voltage of 6 V, an electrolyser voltage of 1.826 V, and an electrolyser current of 4.97 A.

Note that the water-bath serves to increase the surface area of contact between the hot-plate and the smaller beaker containing the electrolyte. Note also that the multimeter clips are attached to the electrolyser, so as to avoid the voltage drops that occur in the power-supply cables. The pump flow-rate was measured by running the outlet tubes into a beaker, and measuring the time required to pump a specific volume. In practice, the electrolyser and tubes would be covered to reduce heat loss, especially in a fumehood with powered extraction. Ideally, the temperature would have been measured inside the electrolyser, but this was not possible given the small size of the channels within the design.

Note that the lowest current density at which measurements were taken was 250 A m^{-2} (i.e. 25 mA cm^{-2}). Experimentally, as the current density reduced it became increasingly difficult to get reliable voltage measurements. This was due to the highly capacitative nature of the electrode coatings, as well as the gradual alteration of the catalytic coatings in terms of chemical and ionisation states, as a result of which voltages were observed to drift for extended periods of time. The decision was therefore taken to operate the power-supply solely between 1 and 20 A, although it is clear that this did not take the electrolyser far out of its linear (ohmic) range and into the curved (activation) region.

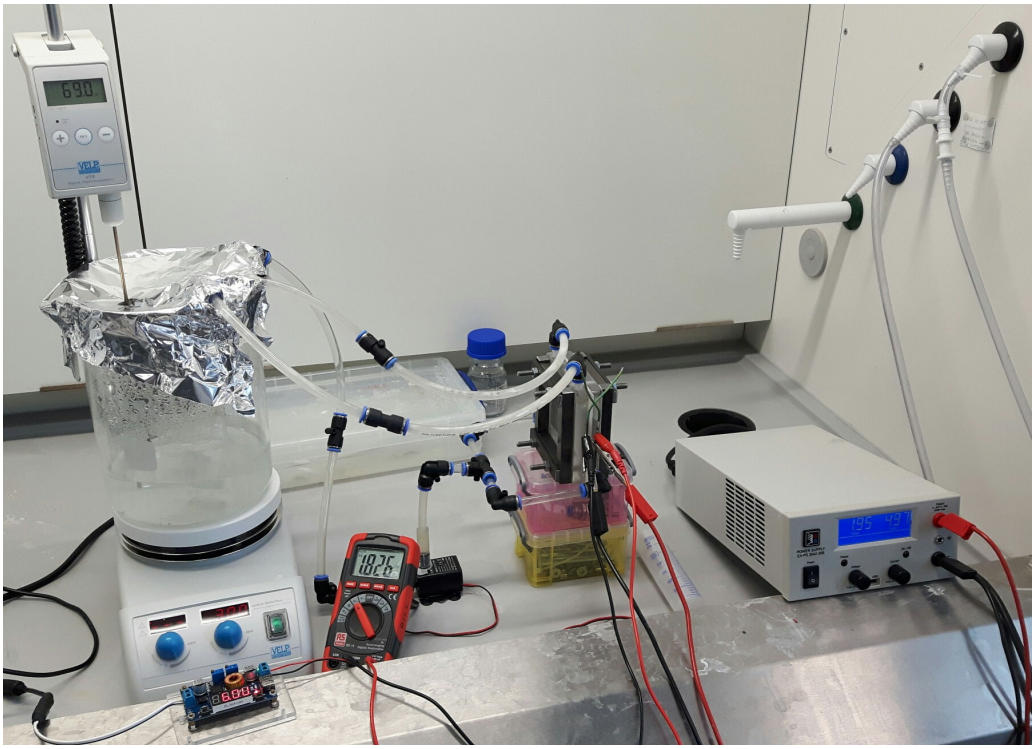

Figure 6.25: Experimental set-up for measuring the performance of a ZGE.

The full measurement datasets are listed in Section A.1.1 on page 257. Once the mathematical model developed in Section 6.3 on page 214 was fitted to the datasets for the four models of ZGE listed in Table 6.5 on page 228, the results were as shown in Table 6.10.

Electrolyser	**Pump** V	**T_0** K	**κ_0** $S\,m^{-2}\,K^{-1}$	**b** $mV\,dec^{-1}$	**V_0** V	**κ at 50 °C** $S\,m^{-2}$	**at 0.5 A cm^{-2}** V
ZGE-A	6	238.9	63.3	126	1.338	5324	2.74
ZGE-A	8	237.3	67.6	158	1.255	5791	2.70
ZGE-A	10	237.3	69.0	140	1.300	5911	2.66
ZGE-B	6	234.3	28.7	129	1.207	2543	3.65
ZGE-B	8	234.4	29.9	142	1.188	2646	3.60
ZGE-B	10	234.7	31.3	179	1.094	2761	3.57
ZGE-C	6	235.3	64.0	261	1.048	5611	2.90
ZGE-C	8	234.7	63.3	260	1.054	5594	2.91
ZGE-C	10	233.7	63.3	249	1.073	5658	2.88
ZGE-D	6	237.5	71.3	211	1.022	6099	2.62
ZGE-D	8	237.4	74.5	191	1.068	6377	2.56
ZGE-D	10	236.2	75.7	164	1.139	6568	2.51

Table 6.10: The full set of best-fit parameters for the various designs of ZGE listed in Table 6.5 on page 228. To aid comparison, column 7 gives the resulting area conductivity at 50 °C, and column 8 gives the resulting voltage at both 50 °C and 0.5 A cm^{-2}.

With reference to the objectives listed in Table 6.6 on page 228, the following conclusions may be drawn. First is that, with the value of T_0 successfully constrained to be close to

234 K, the value of κ_0 is a useful indication of overall conductivity. The two parameters combine to produce a value for the area conductivity κ at 50 °C, as presented in column 7. This conductivity was lowest for ZGE-B, which used 0.5 M NaOH, and for the other three versions varied between 5300 and 6600 S m^{-2}. It is thus clear that the strength of the electrolyte had the greatest impact on the performance of the electrolyser, even though they were all of zero-gap configuration, which is in-line with other results.

The value of κ for ZGE-B is less than half that of any other electrolyser, therefore it may be concluded that the high surface-area woven mesh electrodes (as shown in Figure 6.20b on page 230) did not improve performance. It is likely that too much Raney 2 catalyst was deposited onto the mesh, and as a result the mass transport resistance was increased.

Column 8 of Table 6.10 presents a best-fit value for the electrolyser voltage at 50 °C and 0.5 A cm^{-2}. This is able to distinguish between ZGE-A and ZGE-C, which otherwise appear quite similar. This voltage shows that the use of conductive plastic actually made the performance worse by about 200 mV. This is a confusing result, since even if the conductive plastic did not conduct at all, it should not have been worse than the unconductive acrylic. It therefore suggests that some other aspect of the flowplate, e.g. the depth of the channels or the inlet and outlet ports, was different between the laser-engraved acrylic and the CNC machined conductive plastic. It also raises questions over the repeatability of this kind of experiment.

The high value of the Tafel slope b for ZGE-C highlights the fact that the datasets do not incorporate enough of the curved activation region of the electrolyser I-V curve to produce a reliable measurement. The model has therefore traded off a high value of b against a low value of V_0. Over the bulk of the model domain, where $\log(j)$ varies less than j, this will have little effect. There is therefore an argument to artificially constrain V_0 to approximately 1.23 V, in a similar fashion to T_0, since this is a known figure. However, it is likely this would be purely an aesthetic improvement.

The highest performing electrolyser was ZGE-D, but this is not surprising since it had flow-plates made of solid stainless-steel. Such a design is of little use as regards mass-production, and therefore does not constitute a practical solution. On the contrary, it highlights that the cost even of using completely unconductive flow-plates is only 150 mV at the highest current density. There is no question therefore that ZGE-A remains the most practical design of ZGE investigated, and that none of the efforts to improve it were successful. Despite this, a voltage figure of 2.7 V is not a viable commercial proposition, since it constitutes an efficiency of just 55% (relative to the thermoneutral voltage 1.48 V).

6.5.5 Optimal Pump Control

The effect on the overall electrolyser conductivity of varying the pump voltage shown in Table 6.10 was not significant. ZGE-C showed less than 1% variation, whereas the other three models of electrolyser showed that increasing the pump voltage from 6 V to 10 V increased the conductivity by approximately 7% to 9%. However, this does not answer the question of whether such an increase in conductivity was worthwhile.

To investigate this further, the total power consumption of ZGE-A (electolyser and pump) was measured over a range of current densities and pump voltages. It was found that the electrical pump current was a linear function of voltage, as shown in Figure 6.26a. Whilst the exact rate of flow varied between electrolysers, depending on the drag presented by its channels, the flow-rate was also found to be a linear function of voltage, as shown in Figure 6.26b.

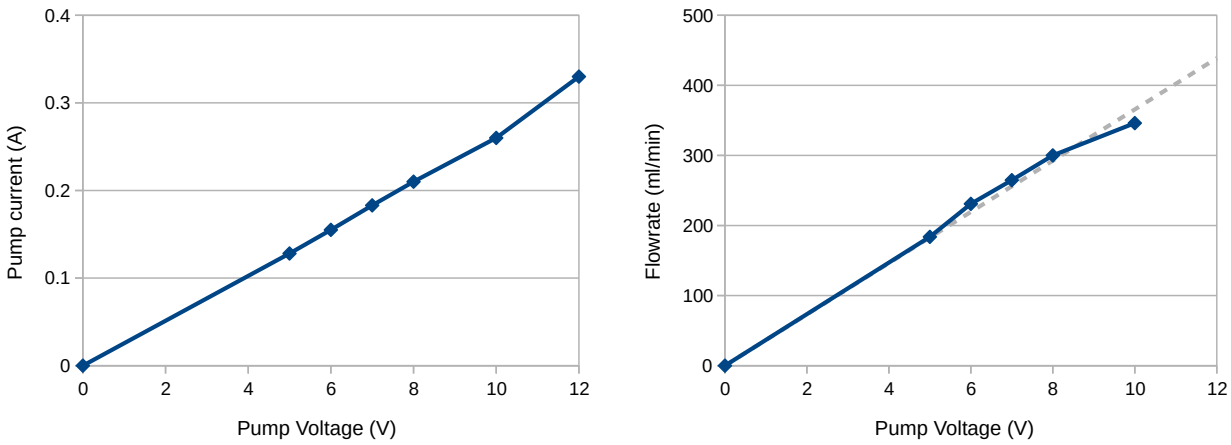

(a) I-V Curve

(b) Flow-rate

Figure 6.26: I-V curve and flow-rate of the circulation pump of ZGE-A.

In combination, the total power consumption of the electrolyser at the highest current density was as shown in Figure 6.27a.

The figure shows that at 500 mA cm^{-2}, the optimal pump voltage for ZGE-A was 8 V. At lower voltages, the electrolyte circulation was too low to cope with the volume of gases produced, whereas at higher voltages the power consumption of the pump was such that total electrolyser power increased. Since the pump had a rated voltage of 12 V, it did not operate at all below 5 V, which explains why there are no results between 0 and 5 V.

At other current densities the optimal pump power and voltage, expressed relative to the electrolyser power and voltage, was as presented in Figure 6.27b. The figure shows that above 250 mA cm^{-2} the optimal pump power was about 2.5% of the electrolyser power, and the optimal pump voltage similarly about 2.3 times the electrolyser voltage. Below this level

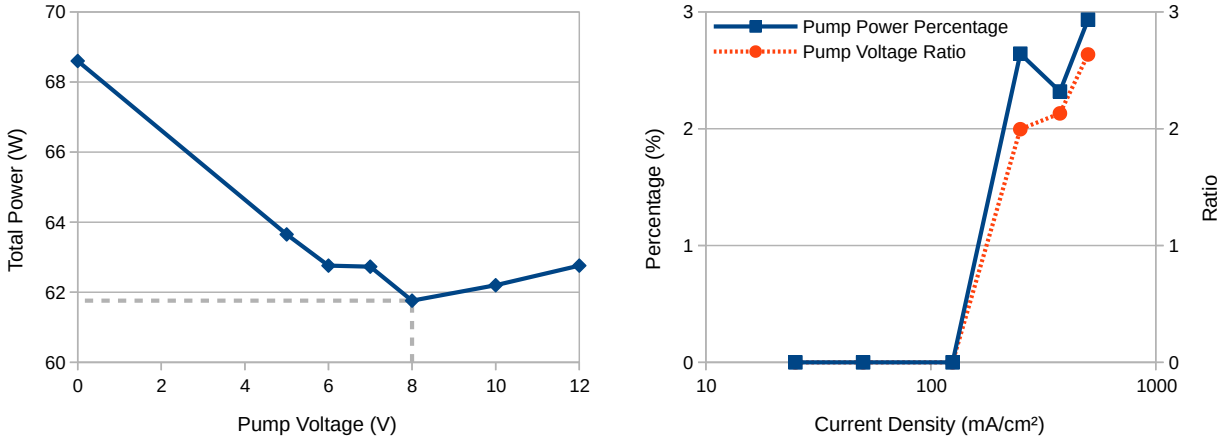

(a) Total electrolyser power

(b) Optimal pump power and voltage

Figure 6.27: a) Total electrolyser power *vs.* pump voltage at 500 mA cm^{-2}, and b) optimal pump power as a percentage of electrolyser power, and the ratio of optimal pump voltage to electrolyser voltage.

the optimal pump power and voltage were both zero, but this may have been due to the large gap in pump voltages between 0 and 5 V.

To implement optimal pumping therefore would require maintaining either the pump power or voltage at a fixed proportion of the electrolyser power or voltage. However, given that it is difficult to think of a simple electronic scheme that could maintain the pump power consumption as a fixed proportion of the electrolyser power consumption, it would be more practical to control the voltage. Given the linear nature of the pump I-V curve shown in Figure 6.26a, this means controlling the square-root of pump power.

In practice, any such scheme might be slightly more difficult, since the I-V curve of a bipolar electrolyser stack is not like a scaled-up version of that of a single pair of electrodes. This is because the cells switch on in sequence, with some cells rising quickly to 2 V whilst others remain on zero. It may therefore prove more optimal to maintain the pump voltage as a fixed proportion of the electrolyser *current*. However, since even a modestly sized electrolyser may pass a current exceeding 1000 A, this could prove difficult in practice. Despite this, it is believe that a relatively optimal pumping scheme could be devised with some more research. In any case, the difference in total power consumption between 6 and 12 V shown in Figure 6.27a was only 1 W, therefore the cost of non-optimal pumping is very low.

6.6 Woven Stainless-Steel Membrane

(The results presented in this section were published by the author in the journal *MDPI Membranes* in May 2020 [243])

During experiments involving electrolyte pumped around a circuit featuring a horizontal woven stainless-steel membrane, it was observed that gas bubbles collecting underneath the mesh would not pass through. This was despite the fact that the holes in the mesh were approximately 100 µm across, and clearly visible. For reference, a scanning electron micrograph of 180 thread-per-inch woven mesh is as shown in Figure 6.28. It was therefore decided to investigate whether such mesh could be employed as a gas-separation membrane in its own right.

From the point of view of cost this could be significant, since it has been found to be considerably cheaper than commercially available alternatives. At the time of publication, the cost of woven stainless-steel mesh (excluding sales tax) was GBP 22 per square metre.[3] As a rule, the prices of alternative membranes are not advertised, but the cost of Zirfon is known to be greater by approximately an order of magnitude. Competitor membranes such as Sustainion are newer and more expensive. Therefore, if conditions can be found under which the electrical and gas-separation capabilities of the woven membrane prove adequate, it would constitute a break-through in price and performance which could bring entry-level alkaline electrolysis within the reach of many hitherto discounted applications. This is of particular relevance to many less economically developed countries (LEDC) which have abundant sources of renewable energy, but high costs of conventional electricity, and thus offer the greatest economic case for surplus renewable energy capture by alkaline electrolysis. Despite this, the costs of commercial electrolysers are still too high.

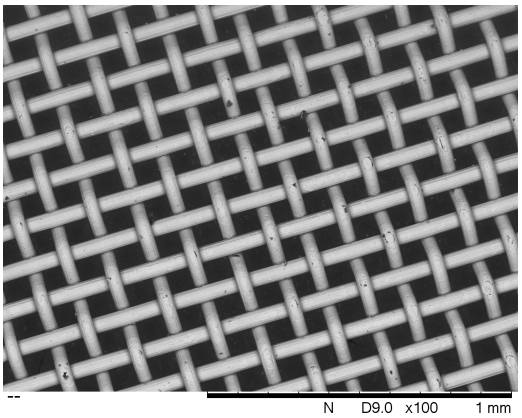

Figure 6.28: Scanning electron micrograph at ×100 magnification of 180 threads-per-inch 316-grade stainless-steel woven mesh.

The aim of this experiment was to measure the resistance of woven stainless-steel mesh *relative to* that of a market-leading commercial alternative, namely Zirfon. As a result, no attempt was made to replicate the conditions inside a commercial electrolyser, which typically involve high temperature (e.g. 90 °C), high pressure (e.g. 10 bar) and high concentration (e.g.

[3]Source: https://www.meshdirect.co.uk/woven-stainless-wire-cloth-200-mesh-0.07-mm-aperture.html viewed May 2020

30 wt% KOH). In any case, room-temperature electrolysis is of greater applicability to intermittent renewable energy, where the additional electrical and system cost of heating cannot be justified. Low-pressure electrolysis is also of greater relevance to LEDC, where operating an electrolyser at atmospheric pressure significantly reduces construction costs and system complexity, and greatly increases safety.

In both conventional and zero-gap alkaline electrolysis, gas-separation is normally achieved by the use of a dedicated membrane. One well-known commercial product is Zirfon^{TM}, which is constructed of a relatively soft, spongey material (a mixture of polymer and zirconium oxide) surrounding a hard woven mesh (made of polyphenylene sulphide) [244]. The membrane works via a combination of its chemical stability and high wettable area. Zirconium oxide is recognised for being chemically unreactive, and is able to withstand extended exposure to concentrated alkali solutions [245]. Its resistance in 30 wt% KOH has been measured as 0.3 $\Omega\,cm^2$ [246].

Fumasep FAS-50 is an anion exchange membrane (AEM) with a thickness of 50 µm. It therefore operates by the direct conduction of OH^- ions along polymer chains, in a similar way that Nafion conducts H^+ ions. It has a list price of USD 783 per square metre[4], and exhibited an impedance of 0.3783 $\Omega\,cm^2$ in 1 M KOH at 60 °C. However, the voltage required to sustain 1 A cm^{-2} was observed to increase by 200 to 400 µV h^{-1}, and the membrane failed completely after 200 h, even though the membrane should have been stable at pH 14 [247].

Sustainion is an AEM with a thickness of 50 µm, comprised of imidazolium functionalized styrene polymer. It has a list price of USD 6304 per square metre[5], and exhibited the lowest reported resistance of just 0.045 $\Omega\,cm^2$ [247]. However, the strength of the electrolyte is limited to 1 M KOH "due to the lack of chemical stability of the materials in a very strongly basic environment" [143]. The commercial use of any samples purchased is also prohibited by an End User Agreement. The membrane exhibited a gas-crossover rate 20 times higher than Zirfon in 30 wt% KOH at all current densities from 100 to 2000 mA cm^{-2} [143]. It has also proved mechanically fragile, and extremely easy to perforate during electrolyser assembly and disassembly.

Other membranes include Neosepta, AMI 7001 and Celazole PBI, but all exhibited higher resistances than the above three materials [247]. It is also possible to maintain gas-separation without a membrane, for example by using a rotating electrolyser [248], or divergent electrolyte flow [249], and these are certainly concepts worthy of consideration. It is also possible to mix the evolved hydrogen and oxygen gases, as a stoichiometric mixture known as 'HHO', thereby avoiding the need for a membrane, so long as the gas is for immediate use with zero storage [250].

[4]Source: https://www.fuelcellstore.com/fumasep-fas-50 viewed May 2020
[5]Source: https://www.fuelcellstore.com/sustainion-x37-50-grade-60-membrane viewed May 2020

6.6.1 Method

All membranes and electrodes were mounted in a 3-electrode cell constructed in a laminar fashion from laser-cut acrylic, as described in Section 2.1 on page 39 [16, 162]. The exposed area of all membranes was 6 cm × 6 cm, and the distance between anode and cathode was 36 mm. The distance between electrodes was large to increase repeatability, both by reducing the effect of cell assembly variation, and by reducing void fraction under gas evolution. An extra silicone gasket was inserted when no membrane was present to maintain inter-electrode spacing. The stainless-steel membrane consisted of woven mesh with 180 threads per inch and was obtained from a commercial supplier. The Zirfon^{TM} membrane was obtained from a commercial supplier, and had a thickness of 0.9 mm. Other membrane materials are available, but were not part of this study [247].

The exposed area was 3 cm × 3 cm for the working electrode (WE, cathode), which had been coated with Raney Nickel version 1 in accordance with the procedure in Section 5.2 on page 168 [82]. The exposed area was 6 cm × 6 cm for the 316-grade stainless-steel counter electrode (CE, anode). The reference electrode (RE) was a commercial Ag/AgCl design, which was routinely corrected against a Standard Calomel Electrode (SCE). The cell evolved hydrogen and oxygen gas bubbles, which were kept apart by the membrane, thereby ensuring gas purity at each gas outlet. For experiments on the potentiostat the electrolyte was 0.5 M NaOH with no pumped circulation, at normal laboratory temperature, which was 21 ±1 °C. For experiments on the GC, the electrolyte was 3 M NaOH with optional pumped circulation, at normal laboratory temperature plus some self-heating.

All electrochemical experiments were performed on an Ivium n-Stat potentiostat. All EIS results were analysed within the IviumSoft software package. **Safety:** The electrolysis of water evolves small amounts of hydrogen and oxygen gas, which constitute a risk of explosion. The experiments were therefore performed with fume extraction, so as to prevent the build-up of gases, and to achieve isolation from possible sources of ignition. Strong electrolyte up to 3 M NaOH was used, which is dangerous to skin and eyes, therefore normal laboratory eye protection and gloves were employed.

Linear Sweep Voltammetry LSV was performed using 2-electrodes (CE and WE) between 1.4 V and 2.5 V at 20 mV s^{-1}. A temperature probe was used to measure the temperature of the electrode inside the electrochemical cell, which was higher than ambient temperature due to self-heating, but within 2 °C.

Electrochemical Impedance Spectroscopy EIS was performed between 0.1 Hz and 10 kHz, starting at low frequency, at a bias voltage of 2 V to ensure water-splitting reactions were present. Method: impedance; technique: constant voltage; signal magnitude: 10 mV. The electrolytic cell was pre-treated for 60 s at 2 V to reduce initial transient currents.

Gas Chromatography GC was performed in accordance with the procedure laid out in Section 2.2.4 on page 56.

6.6.2 Results

The LSV and EIS results for the three different membrane options were as shown in Figure 6.29. At first glance, it appears that the choice of membrane made little difference, but this is misleading. This is because the test cell was designed for experimentation, not for efficiency, and the solution resistance of the electrolyte constitutes a much higher proportion of the total than would normally be the case. The results confirm that performance was highest with no membrane at all, as is to be expected since this configuration did not separate the product gases, and was included solely as a baseline for performance comparison. Between the two membranes, the woven stainless-steel demonstrated performance that was approximately halfway between that of Zirfon and no membrane.

More quantitatively, the series electrical resistance (R_S) between the electrodes can be calculated from the EIS results at high frequency, its value being given by the point of intercept closest to the origin between the semi-circle and the x-axis [247]. Since the semi-circles did not quite intercept the x-axis, this was taken to be the minimum value of the real component of the impedance, as presented in Table 6.11.

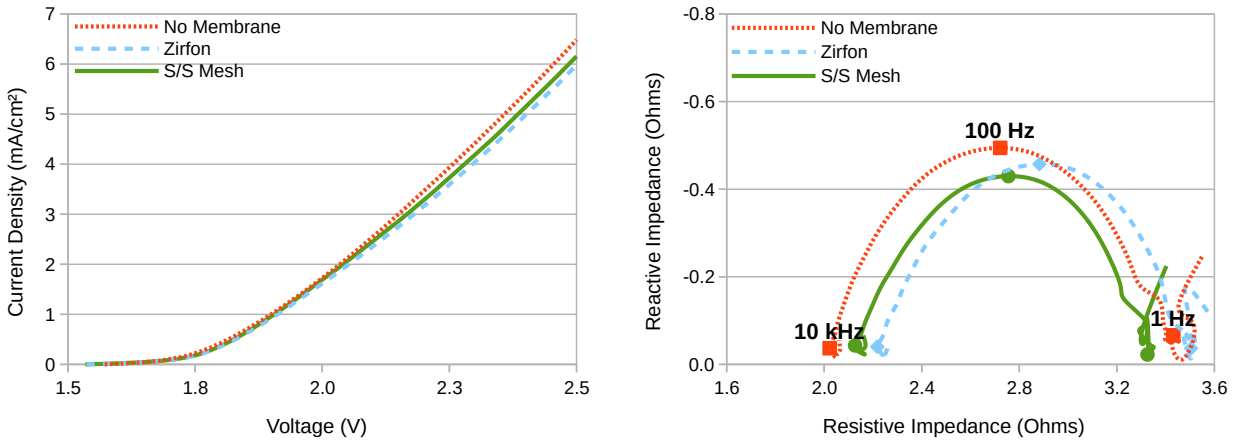

(a) Linear sweep voltammetry

(b) Electrochemical impedance spectroscopy

Figure 6.29: LSV and EIS characteristics obtained with two gas-separation membranes, plus with no membrane for comparison.

The 36 cm^2 stainless-steel mesh therefore exhibited a resistance that was 90 mΩ lower than the same area of Zirfon membrane, which equates to a reduction of 3.2 Ω cm^2 or 44%. The absolute value measured for the area resistance of the Zirfon membrane at 7.2 Ω cm^2 demands further attention, since the published value for this by Vermieren *et al.* is more than 30 times lower at 0.2 Ω cm^2. However, this was measured using pre-production samples in a much stronger electrolyte (30 wt% KOH) and at a slightly higher temperature (30 °C) [244,

Membrane	R_S	ΔR_S	R_M
No Membrane	2.02 Ω	–	–
S/S Mesh	2.13 Ω	+110 mΩ	4.0 Ω cm^2
Zirfon	2.22 Ω	+200 mΩ	7.2 Ω cm^2

Table 6.11: Series electrical resistance between the electrodes derived from the EIS results presented in Figure 6.29b. The membrane area resistance R_M is derived from the value of ΔR_S in column 3. The woven stainless-steel membrane therefore exhibited just over half the electrical resistance of Zirfon.

251]. A slightly higher figure of 0.3 Ω cm^2 was produced by Rodríguez *et al.*, who also used 30 wt% KOH. However, another measurement by R. Phillips placed its area resistance at 1.2 Ω cm^2 in 1M NaOH at 20 °C as part of a zero-gap electrolyser [17, 142, 143].

If it is assumed that 0.5M NaOH has approximately double the electrical resistance of 1M NaOH, this still means that the area resistance measured for Zirfon is three times higher than it should be. However, the measurements by Vermeiren and Rodríguez *et al.* were performed by pressing electrodes into close contact with each side of the membrane, whereas those by R. Phillips were performed in a zero-gap electrolyser with copious electrolytic circulation. It is known from experiments with ion-exchange membranes that significant additional resistances occur due to ionic transport through diffusion boundary layers and electrical double-layers that occur each side of the membrane [252]. Therefore, in relatively low concentration uncirculated electrolytes where the resistance due to diffusion is greater, a figure of 7.2 Ω cm^2 is a possibility.

In any case, the EIS-based measurement of membrane resistance can be cross-checked by analysing voltage differentials at equal currents in Figure 6.29a. Since the kinetic overpotentials at the anode (η_a) and the cathode (η_c) are a function of current, and the thermodynamic water-splitting potential (V_{th}) is only a function of temperature, it is possible to state that:

$$\begin{aligned} V_1 - \eta_a - \eta_c - V_{th} &= I(R_S + R_{M1}) \\ V_2 - \eta_a - \eta_c - V_{th} &= I(R_S + R_{M2}) \\ \implies R_{M2} - R_{M1} &= \frac{V_2 - V_1}{I} \end{aligned} \tag{6.54}$$

where R_s is the non-varying solution resistance of the electrolyte, and V_1 and V_2 are the total voltages measured at current I for the membranes with resistance R_{M1} and R_{M2} respectively. A plot of $V_2 - V_1$ against current derived from Figure 6.29a appears as presented in Figure 6.30a. The figure includes an origin-constrained line of best-fit, the slope of which is therefore equal to $R_{M2} - R_{M1}$. This is measured as 3.7 Ω cm^2, which compares well with the figure of 3.2 Ω cm^2 generated from EIS.

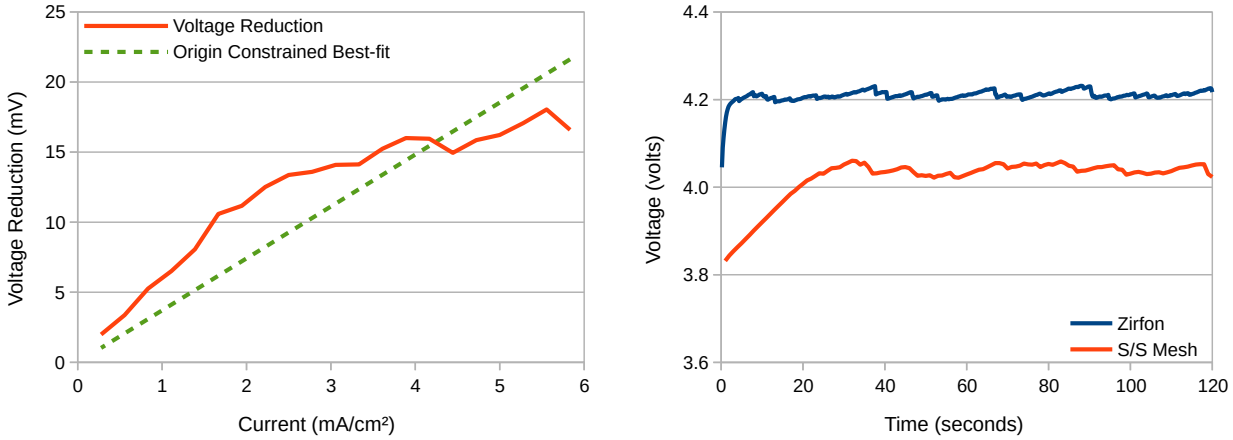

(a) Differential voltage

(b) Chronopotentiometry

Figure 6.30: a) Voltage improvement *versus* current observed for a 2-electrode electrolyser featuring a stainless-steel mesh membrane relative to Zirfon, and b) voltage variation *versus* time for the same two membranes. Current density: 25 mA cm^{-2}

It is possible to state how much of a voltage difference this would make at different current densities. Since a current density of 500 mA cm^{-2} would equate to 18 A, this would result in a voltage reduction of:

$$18\,\text{A} \times 90\,\text{m}\Omega = 1.62\,\text{V} \tag{6.55}$$

This figure serves to highlight how high the resistance of 0.5 M NaOH is. Since not just the resistance of the electrolyte is increased, but also that of the membrane and any diffusion boundary layers, increasing the conductivity of the electrolyte is critical. This is highlighted in the chronopotentiometry waveforms presented in Figure 6.30b, which were conducted at a current density of 25 mA cm^{-2}. The woven mesh membrane produced an average terminal voltage just over 150 mV lower than Zirfon. The waveforms present the characteristic 'saw-tooth' profile that is the result of the build-up and sudden release of bubbles on the electrode surfaces, which is not attributable to the membrane.

6.6.3 Gas Chromatography

The gas chromatography results for the hydrogen outlet of the electrolyser are as presented in Figure 6.31a. The gas-separation membrane consisted of 180 threads-per-inch 316-grade stainless-steel woven mesh. The electrolyser current was 5 A, which equated to 140 mA cm^{-2}. Separate measurements were taken with and without pumped circulation of the electrolyte. Peak-fitting analysis within the GC system software against a recent calibration produced the gas purity figures presented in Table 6.12. The figures have been corrected

for contamination by atmospheric air in-line with the method outlined in Equation 2.8 on page 58.

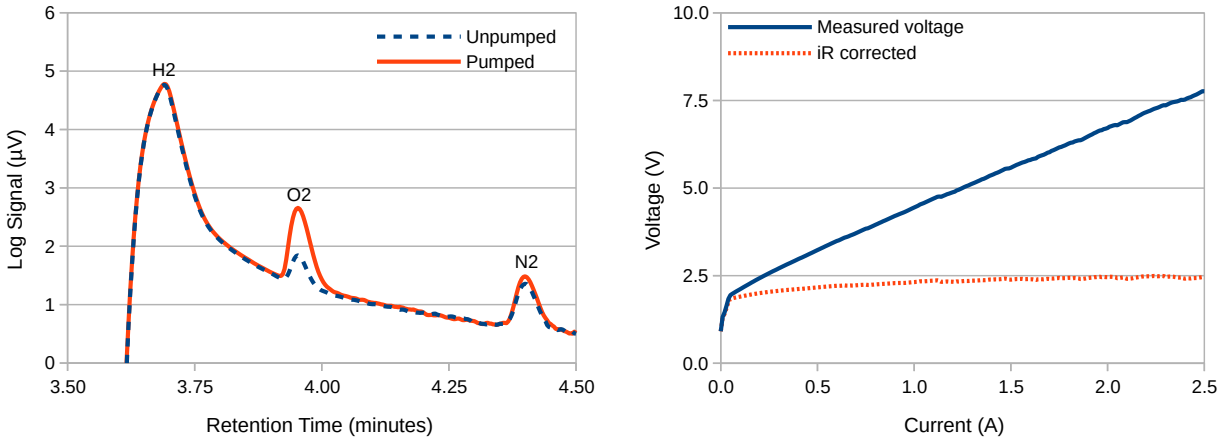

(a) GC signal with peak assignations

(b) Linear Sweep Voltammetry

Figure 6.31: a) Gas chromatography (GC) measurements of gas purity of the hydrogen outlet of the electrolyser with and without pumped circulation of the electrolyte. Gas-separation membrane: 180 threads-per-inch 316-stainless steel woven mesh; electrolyser current: 5 A; electrolyte: 3 M NaOH. b) Linear sweep potentiometry (LSP) between 0 A and 2.5 A to check for evidence of bipolar-electrode behaviour. No such behaviour is observed.

Name	Peak Area	Response Factor	Amount (%)	Corrected (%)
H_2 (not pumped)	5454	0.00852	46.47	99.25
O_2	12.9	0.06162	0.80	0.75
N_2	2.17	0.08184	0.18	0.00
H_2 (pumped)	5734	0.00852	48.85	97.48
O_2	41.9	0.06162	2.58	2.52
N_2	2.89	0.08184	0.24	0.00

Table 6.12: Gas purity calculations based on the data presented in Figure 6.31a.

6.6.4 Bipolar Operation

Since the woven stainless-steel membrane is itself conductive, the possibility exists that instead of behaving like a porous membrane, at some current density it will begin to behave like a bipolar-electrode. In this situation, hydrogen and oxygen gas would be evolved on opposite sides of the separator, and the electrolytic cell would start to behave like a two-cell bipolar electrolyser. As such, the rate of increase of the total voltage with current density would be expected to increase, since extra voltage would be needed to account for the extra water-splitting reactions. In addition, the purity of the gases at the outlets would decrease, since a mixture of both gases would be evolved in each half of the electrolyser.

The point at which 'membrane behaviour' gives way to 'bipolar-electrode behaviour' will depend on the magnitude of the charge transfer resistance of the water-splitting reactions *versus* the electrolyte resistance through the membrane. This in turn will depend on the size of the holes in the mesh. As proof, it is simple to envisage a thought experiment whereby a solid metal sheet (which will by definition behave like a bipolar-electrode) is altered gradually through the inclusion of holes first into a perforated mesh, then into a woven mesh, then into no membrane at all. At some point, as the hole/metal ratio increases, the behaviour will change from bipolar-electrode to porous membrane.

To investigate this, the cell was swept from 0 A to 2.5 A, with the results as presented in Figure 6.31b. This represented the maximum current available from this particular model of potentiostat. Since the series resistance of the cell is known to be 2.13 Ω (see Table 6.11 on page 245) it is possible to calculate the iR-corrected voltage, which is displayed as the dotted orange line. This shows that the proportion of the voltage used for water-splitting does not exceed 2.5 V, which is consistent with a single water-splitting reaction and rules out any bipolar-electrode behaviour. However, given the size of the membrane, this equates to a current density of just 70 mA cm^{-2}, which is well below that typically seen in a commercial electrolyser. To take the current density higher would require either a higher capacity potentiostat, or a redesign of the electrochemical cell, both of which are left for future endeavour.

6.6.5 Conclusions

The gas purity calculations presented in Table 6.12 show that pumping of the electrolyte increases the concentration of O_2 in the H_2 outlet by more than a factor of three. This is to be expected, since the woven membrane is much more porous than Zirfon, and will therefore be much more sensitive to pressure differentials across it. No attempt was made to equalise the pressures of the two pumps, since it was believed this might create an unrealistic expectation of the performance of the membrane. However, it is quite possible to design electrolysers such that pressure differentials across the membrane are kept to an absolute minimum, even with pumped circulation.

The upper flammability limit (UFL) for H_2 mixed with pure O_2 is 94% [29] (i.e., 6% O_2 in H_2) therefore the figure of 2.52% under pumped circulation is still more than a factor of two within the limit. It is, however, more conventional to measure the gas-purity of the oxygen outlet [237, 253], since the lower flammability limit (LFL) for H_2 in O_2 appears a more severe constraint at just 4% [29]. However, this can be misleading, since the gas produced at the oxygen outlet is not normally stored, but instead immediately vented to the atmosphere [122]. Nevertheless, there are some applications where oxygen storage is beneficial, for example to increase the maximum power available from a fuel-cell [123], and for

these some form of outlet gas purification such as a heated platinum wire could be considered [225], or a Passive Autocatalytic Recombiner (PAR) as described on page 210.

In conclusion, it is possible to report that the woven stainless-steel mesh membrane:

- Presents approximately half the electrical resistance of commercial Zirfon^{TM} gas-separation membrane. This could result in a significant efficiency saving in most applications, where the resistance of the electrolyte constitutes a smaller proportional of the total,
- Maintained gas-separation such that at the H_2 outlet of the electrolyser only 0.75% O_2 was observed (with uncirculated electrolyte, at a current density of 140 mA cm^{-2}),
- Produced 2.5% O_2 at the H_2 outlet with pumped circulation, most likely due to an uncompensated pressure differential across the membrane. This is still more than a factor of two below the upper flammability limit (UFL) of hydrogen in oxygen,
- Has been found to be considerably cheaper than commercially available alternative membrane materials

It is therefore possible that woven stainless-steel mesh membrane could prove to be a cost-effective gas-separation membrane in some applications. It is also possible that its properties could be further enhanced using suitable structural modifications or coatings.

Chapter 7

Conclusions

> Anyone who thinks that you can have infinite growth in a finite environment is either a madman, or an economist.
>
> *David Attenborough*

The task of generating hydrogen and oxygen from water and electricity is essentially a simple one. The process has been known since at least the year 1800, and its contemporaneity with the discovery of mechanical and chemical methods of generating electricity shows that it was a fairly conspicuous experiment to perform. It has been optimised as an industrial process since the end of the nineteenth century, and (just like the safety bicycle) many of the basic concepts of what constitutes an alkaline electrolyser have not changed since then. The fact that water electrolysis happens at all is a minor miracle, but this should not blind us to the opportunities it offers to understand matter at the smallest scales.

With increasing computing power and software sophistication comes a growing ability to solve the Schrödinger equation for not just dozens, but hundreds and thousands of atoms. The Density Functional Theory (DFT) method is permitting the ever-expanding capabilities of computational chemistry to be brought to bear on all of the fundamental aspects of the water-splitting process, many of which still remain mysterious. As the DFT process is extended for use on less periodic structures, it increasingly benefits from the use of Finite Element Methods (FEM), which feature a long track-record of innovations which have transformed its accuracy, efficiency and applicability to real-world problems. It is therefore appropriate that not only has the work for this thesis been conducted at the same academic institution at which FEM was originally developed, but the scholarship that made this thesis possible was created in honour of the man who invented it, Professor Olek Zienkiewicz.

Just because the electrolyser is constrained to work at room temperature does not mean that the electrolyte should be. The main lesson to be learnt from Section 3.2 on page 85 is that if a choice has to be made between warming the electrolyte and developing a new and more efficient catalyst, warming the electrolyte is by far the more effective route. Figure 5.34

on page 196 shows that the difference between a 'good' and an 'excellent' catalyst is quite possibly just a few millivolts, whereas Figure 3.14 on page 81 shows that a 50 °C temperature increase is associated with an improvement of over 150 mV, and that is just for one half-reaction, and does not include the losses in the electrolyte.

Likewise, Table 1.5 on page 36 shows that even a bifunctional catalyst such as Raney nickel is only 100 mV behind the world leading OER catalyst. Table 1.4 on page 35 shows that for HER, the same coating is remarkably only 16 mV behind. From a system point of view, conceding just 115 mV per cell in return for greatly increased simplicity and reliability is a perfectly acceptable compromise.

By contrast, for the zero gap electrolyser that was modelled in Section 6.3.1 on page 218, at 500 mA cm^{-2} a 50 °C temperature increase reduces the voltage by 0.63 V, per cell. This single step would reduce the avoidable losses, i.e. those not due to thermodynamics and kinetics from 6.6 kW m^{-2} to 3.5 kW m^{-2}, a decrease of 47%.

The self-heating effect of an inefficient electrolyser serves to accomplish this task regardless of whether it is desired or not. A low-cost, slightly undersized electrolyser connected to an unpredictable source of power, such as a wind-turbine, is far more likely to need a cooling system than a means to keep it warm. Nevertheless, it would be wrong to conclude that there is no need for insulation, since its low-cost means it will undoubtedly pay for itself during the long periods of time at low ambient temperatures and low current densities when the self-heating effect is minimal.

If it is accepted that there is a combined need for *both* insulation and cooling, then an active system is required. At low current, circulation is minimal as the electrolyser is given the maximum chance to self-heat. At medium current, circulation is employed to keep the electrolyte at the optimal temperature, with the electrolyser losing heat through its external storage tanks. At high current, maximum circulation is needed together with an external radiator and electric fan to lose heat as quickly as possible, just like a car engine. Such components are readily available, and the extra energy required to drive the pump and fan conveniently coincides with a potentially dangerous surplus of supply. Such a system is sufficient to permit an electrolyser to handle *three times* as much current, as shown in Figure 6.17 on page 227.

Failure to handle maximum load either requires expensive and wasteful over-sizing of the electrolyser, or the far worse prospect of boiling electrolyte. Fortunately, modern wind turbines are able to feather their blades to safely limit their maximum power output, and to shut down completely above an accepted design limit. Although the failure of wind turbines is often spectacular, it is a rare event and ostensibly of zero relevance to electrolyser design.

Maximum load also coincides with the surprisingly high losses due to bubbles increasing the void fraction within the electrolyte, as graphically illustrated in Figure 6.3 on page 205. As discussed in the text that follows, using these losses as part of a design constraint can

impose a surprisingly low limit to the current density. For this reason, a modest increase in electrolyser pressure would easily permit this constraint to be avoided, and at little mechanical cost. With the addition of pressure regulation valves on the gas outlets, the electrolyser can simply be allowed to pressurise itself, although this does mean that replacement water must be injected. Ideally, this would be incorporated with pressurised hydrogen storage, so as to avoid losses due to unnecessary re-pressurisation.

A good deal of the remaining ohmic losses are due to the membrane, as was highlighted by the calculation presented in Equation 6.55 on page 246, especially in zero-gap designs where the electrodes are in contact with the membrane. The surprisingly high resistance measured for a Zirfon membrane in 0.5 M NaOH served to highlight how the resistance of the membrane is not just determined by what *it* is made of, but also by that of the electrolyte inside and on each side of it.

The conductivity of the electrolyte remains the major source of inefficiency in the electrolyser, regardless of its design. This explains the decision to use 10 M KOH at 100 °C by Divisek *et al.* in their long-term experiments in the 1980's. Evidently as a result of good design, their electrolyser was able to sustain perfectly adequate performance for 16,000 hours (22 months) of discontinuous operation[206]. In total, they observed an increase in cell voltage of just 100 mV, from 1.5 V to 1.6 V. This proves that such performance is attainable.

The effects of diffusion and mass-transport resistance are surprisingly low, with the Raney nickel coated electrodes able to sustain low Tafel slopes up to high current densities, as shown in Figure 5.34 on page 196. In essence, this shows how much electricity there is in a relatively small amount of electrolyte, or in other words, how large the Faraday constant is.

It was thought that a method had been developed to measure the resistance of this diffusion within the last few microns of the electrode surface, by looking at the strange and potentially confusing disagreement between the results for EIS and CV at OCP, as presented in Section 3.4 on page 110. By looking back over previous results, a straight-line relationship was discovered between the size of this disagreement, and the size of the double-layer capacitance (C_{DL}) or roughness factor. Eventually, this was explained by performing time-domain simulations of a constant phase element representation of the C_{DL}, and discovering that it could exhibit two time-constants. This unexpected result explained all of the observations.

It is important to keep questioning whether there is adequate incentive to invest in the production of high current density electrolysers if that requires extra cost and complexity both in terms of design and coatings. Certainly, from a performance point of view, this avenue should not be pursued if extra total surface area can be produced cost-effectively. Limiting current density reduces both ohmic and activation losses, provides extra capacity to cope with overload, reduces stress on components and, if it permits the use of a slightly

lower strength electrolyte, could reduce corrosion. However, all of these are conditional on cost, and it is likely that a larger electrolyser will strike a different set of trade-offs to a smaller one.

However, although the electrical efficiency may improve at low current densities, as shown in Figure 6.5 on page 213 the gas safety does not. In a similar fashion, it is also reduced with low strength electrolyte, as reported on page 234. In combination with the risk of overheating, this means that from a safety point of view the electrolyser must be designed to operate within an acceptable *range* of current densities, outside of which it should be shut down. Given the low ignition energy of hydrogen, as discussed in Section 1.2.3 on page 11, it is possible there is not even any safe way that it can be vented. The only alternative to forced shut-down would be some form of gas recombination, such as a Passive Autocatalytic Recombiner, as discussed on page 210.

The TiN coating investigated in Chapter 4 is an unusual material, since it is an electrically conductive ceramic. Combined with the high quality of the coatings that can be deposited by commercial Physical Vapour Deposition, it was certainly an interesting candidate for investigation. It is also renowned for its mechanical hardness, and thereby might have constituted a method of increasing the longevity of stainless-steel under long term electrolysis. However, its electrical performance (as shown in Figure 4.8b on page 147) for hydrogen evolution was very poor, and it could not be used for oxygen evolution at all. Also, although it showed a marked increase in performance after long-term ageing, it is likely this was due to electrode breakdown, and the subsequent migration of Cu. However, the investigation did provide an opportunity to develop the dependable experimental systems and procedures that would be used later on.

All of the long-term ageing experiments were based on the principle of intermittency, so as to better emulate the stop-start nature of renewable energy generation, and particularly the diurnal cycle. There is good evidence that this poses particular challenges regarding the corrosion of electrodes within electrolysers, as discussed in Section 5.1.1 on page 167.

This would be of greater relevance to the Raney nickel coatings investigated in Chapter 5, since they contain a greater range of elements, including some with greater electronegativity such as Zn. Despite the possibility for enhanced corrosion, both versions of the Raney nickel coating coped well, as demonstrated in Section 5.3.1 on page 179. However, the large increases in surface area are a source for concern, since the surface area can only increase so far before the coating falls to pieces. It is possible that the ageing experiments in Section 5.3.1 on page 179 were simply not long enough, but the author was not at liberty to match the exploits of Divisek *et al*. It is also possible that the coating would age less quickly in KOH, since nickel is less prone to the formation of hydrides than it is in NaOH, and this may well be the key mechanism of cathodic destruction[169].

In any case, it is worth questioning whether it is better to simply remove and recoat the

electrodes at regular service intervals, especially if the coating can be reapplied in a facile procedure, which (as described in Section 5.2 on page 168) Raney nickel clearly can. To decide, it must be known how performance is traded-off against longevity. Certainly it was one of the aims of this thesis to be able to answer that question, but the Raney coating proved itself comfortably able to withstand all of the punishment it was subjected to. This is not a bad result, but it is an inconclusive one.

What is certain is that the performance of the Raney2 coating is a step up over the already high-performing Raney1 coating, and is a very practical proposition for use as a commercial coating. The finding that a sacrificial counter electrode radically improves the morphology was an unconventional, but entirely repeatable discovery. It is likely that the improvements derive from the effect on the deposition of Cr, as partially proven in Figure 5.32b on page 194. In this respect, it is possible that the improvement is similar to that observed for NiMo, which was shown by Shalenbach to be due to an increase in surface area, not an improvement in catalysis [254]. However, it cannot be exactly the same, since according to the XPS, no molybdenum was present in the coating. In any case, an increase in surface area is no bad thing, since as stated in Section 1.3.3 on page 20, within limits it is completely equivalent to improved catalysis.

Much of the writing up phase of this thesis was conducted under the lock-down conditions of a global coronavirus pandemic. Within weeks skies all over the world cleared not just of aeroplanes, but also of dust, smog and pollution. The roads cleared of traffic, and briefly at least, it seemed as if an alternative way of life was revealed. As a consequence, there have been many calls to make a 'green new deal' part of the economic recovery plan, once the pandemic subsides, so that this alternative vision might not be lost. It is tempting to think that green technology can solve any problem, but on its own, it cannot. Despite a microscopic blip in CO_2 emissions, climate change continues almost completely unabated, inexorably and irreversibly. As is known by anyone who can add, it constitutes a far larger threat than the pandemic.

Perhaps it is most appropriate that the last word should go to the family of Greta Thunberg, who are scathing in their condemnation of the belief that global business and lifestyles can continue as normal, so long as sufficient green technology is incorporated into existing systems. Their assertion is that for too many business leaders, politicians and those in the media it is *global warming* that is treated as the problem, not the unsustainable lifestyles that have caused it:

> The connection between growing economic prosperity, increased emissions and lost biological diversity is as clear as day. But that connection doesn't reach us. It gets drowned along the way.
>
> quoted from *'Our House is on Fire'* [255]

If green technology is simply incorporated as part of the same old infinite growth within a finite environment, the end result is just the same.

Appendix A

Appendix A

A.1 Zero-gap Electrolysers

A.1.1 Measurements

The electrolyser area was 40 cm^2. The measurement datasets were as presented in Tables A.1, A.2, A.3 and A.4.

Pump Voltage V	Current Density A m^{-2}	Target Temperature °C	Actual Temperature °C	Average Voltage V
6	25	30	30.2	1.7885
6	50	30	30.2	1.898
6	125	30	30	2.12
6	250	30	30.2	2.455
6	375	30	30	2.815
6	500	30	30	3.165
6	25	50	49.2	1.689
6	50	50	49	1.778
6	125	50	49	1.9665
6	250	50	48.8	2.205
6	375	50	48.8	2.495
6	500	50	48.8	2.745
6	25	70	70	1.5955
6	50	70	70	1.674
6	125	70	70	1.83
6	250	70	70	2.05
6	375	70	70	2.27
6	500	70	70	2.495
8	25	30	30	1.7845
8	50	30	30.2	1.8825
8	125	30	30.2	2.105
8	250	30	30.2	2.435
8	375	30	30.2	2.745
8	500	30	30.2	3.035
8	25	50	50.2	1.679
8	50	50	50.2	1.7665
8	125	50	50.2	1.9545
8	250	50	50.2	2.2
8	375	50	50.2	2.445
8	500	50	50.2	2.765
8	25	70	70	1.5935
8	50	70	70	1.668
8	125	70	70	1.8335
8	250	70	70	2.045
8	375	70	70	2.26
8	500	70	70	2.47
10	25	30	30.2	1.7805
10	50	30	30	1.877
10	125	30	30	2.11
10	250	30	30	2.4
10	375	30	30	2.715
10	500	30	30	3.01
10	25	50	50.2	1.6695
10	50	50	50.2	1.7555
10	125	50	50	1.9435
10	250	50	50	2.175
10	375	50	50	2.42
10	500	50	50.4	2.655
10	25	70	70	1.592
10	50	70	70	1.666
10	125	70	70	1.815
10	250	70	70	2.035
10	375	70	70	2.245
10	500	70	70	2.44

Table A.1: Electrolyser voltage measurements for Electrolyser ZGE-A.

Pump Voltage V	Current Density A m^{-2}	Target Temperature °C	Actual Temperature °C	Average Voltage V
6	250	30	30.6	1.6845
6	500	30	30.6	1.8495
6	1250	30	30.2	2.255
6	2500	30	30.4	2.915
6	3750	30	31	3.55
6	5000	30	30.5	4.265
6	250	50	50.6	1.6225
6	500	50	50.4	1.753
6	1250	50	50.4	2.07
6	2500	50	50	2.585
6	3750	50	50.2	3.11
6	5000	50	51	3.615
6	250	70	70	1.568
6	500	70	70	1.689
6	1250	70	70	1.9755
6	2500	70	69.8	2.43
6	3750	70	69.4	2.875
6	5000	70	69.6	3.335
8	250	30	30	1.6955
8	500	30	30	1.853
8	1250	30	29.6	2.24
8	2500	30	30	2.875
8	3750	30	30	3.54
8	5000	30	30	4.205
8	250	50	50	1.632
8	500	50	50	1.77
8	1250	50	50	2.085
8	2500	50	50	2.585
8	3750	50	50.4	3.08
8	5000	50	50.2	3.6
8	250	70	70	1.5735
8	500	70	70	1.6965
8	1250	70	70	1.982
8	2500	70	70	2.405
8	3750	70	70	2.855
8	5000	70	70	3.285
10	250	30	30	1.6985
10	500	30	30	1.855
10	1250	30	30	2.25
10	2500	30	30	2.895
10	3750	30	30	3.605
10	5000	30	30	4.16
10	250	50	50	1.629
10	500	50	50	1.7605
10	1250	50	50.4	2.075
10	2500	50	50.4	2.575
10	3750	50	50.2	3.065
10	5000	50	50	3.585
10	250	70	70.2	1.5675
10	500	70	70.2	1.6875
10	1250	70	70	1.9695
10	2500	70	70	2.37
10	3750	70	70	2.795
10	5000	70	70.2	3.215

Table A.2: Electrolyser voltage measurements for Electrolyser ZGE-B.

Pump Voltage V	Current Density A m^{-2}	Target Temperature °C	Actual Temperature °C	Average Voltage V
6	250	30	30.6	1.81
6	500	30	30.6	1.945
6	1250	30	30.4	2.175
6	2500	30	30.2	2.52
6	3750	30	30	2.835
6	5000	30	30.8	3.135
6	250	50	49	1.7375
6	500	50	49.2	1.845
6	1250	50	49.4	2.08
6	2500	50	49.8	2.38
6	3750	50	49.6	2.675
6	5000	50	49.8	2.96
6	250	70	69	1.639
6	500	70	69	1.7465
6	1250	70	69.2	1.9515
6	2500	70	69.4	2.26
6	3750	70	70	2.505
6	5000	70	70	2.755
8	250	30	30.2	1.83
8	500	30	30.4	1.95
8	1250	30	30.6	2.215
8	2500	30	30.6	2.54
8	3750	30	30.2	2.865
8	5000	30	30.2	3.18
8	250	50	49	1.738
8	500	50	49	1.85
8	1250	50	49.6	2.08
8	2500	50	49.8	2.405
8	3750	50	49.8	2.71
8	5000	50	49.8	2.97
8	250	70	69.2	1.631
8	500	70	69.2	1.7315
8	1250	70	69.4	1.935
8	2500	70	69.8	2.21
8	3750	70	69.8	2.455
8	5000	70	69.8	2.715
10	250	30	30.6	1.81
10	500	30	30	1.945
10	1250	30	30.4	2.175
10	2500	30	30.4	2.52
10	3750	30	30	2.835
10	5000	30	30.2	3.135
10	250	50	49.4	1.7385
10	500	50	49	1.845
10	1250	50	49.4	2.095
10	2500	50	49.6	2.42
10	3750	50	49.8	2.69
10	5000	50	49.6	2.965
10	250	70	70	1.6205
10	500	70	69.6	1.72
10	1250	70	69.8	1.91
10	2500	70	69.4	2.185
10	3750	70	69	2.43
10	5000	70	69.2	2.66

Table A.3: Electrolyser voltage measurements for Electrolyser ZGE-C.

Pump Voltage V	Current Density A m^{-2}	Target Temperature °C	Actual Temperature °C	Average Voltage V
6	250	30	30.4	1.628
6	500	30	30	1.7195
6	1250	30	29.8	1.922
6	2500	30	29.8	2.22
6	3750	30	30	2.49
6	5000	30	30.4	2.805
6	250	50	50	1.586
6	500	50	50	1.661
6	1250	50	49.8	1.855
6	2500	50	49.8	2.14
6	3750	50	49.6	2.4
6	5000	50	49.8	2.665
6	250	70	69.8	1.563
6	500	70	70	1.634
6	1250	70	70.2	1.803
6	2500	70	70	2.06
6	3750	70	69.8	2.335
6	5000	70	69.6	2.61
8	250	30	30.6	1.6255
8	500	30	30.6	1.704
8	1250	30	30.6	1.9095
8	2500	30	30.6	2.185
8	3750	30	31	2.485
8	5000	30	30.4	2.74
8	250	50	49.8	1.5905
8	500	50	50.2	1.658
8	1250	50	50.2	1.83
8	2500	50	50.2	2.085
8	3750	50	50.2	2.34
8	5000	50	50.2	2.595
8	250	70	69	1.5555
8	500	70	69	1.619
8	1250	70	69.8	1.774
8	2500	70	69.6	2.02
8	3750	70	69	2.27
8	5000	70	69.4	2.53
10	250	30	30.6	1.6285
10	500	30	30.4	1.7075
10	1250	30	30.2	1.9105
10	2500	30	30	2.175
10	3750	30	30	2.45
10	5000	30	30.6	2.7
10	250	50	49.6	1.5835
10	500	50	49.4	1.658
10	1250	50	49.2	1.8275
10	2500	50	49	2.065
10	3750	50	49	2.305
10	5000	50	49.4	2.565
10	250	70	69	1.5475
10	500	70	69	1.604
10	1250	70	69.2	1.755
10	2500	70	69.2	1.975
10	3750	70	69.4	2.205
10	5000	70	69.2	2.42

Table A.4: Electrolyser voltage measurements for Electrolyser ZGE-D.

A.2 Software

Listing A.1: PHP code to simulate the transient response of an RQ network to a voltage ramp.

```
#!/usr/bin/php
<?php
$fp = fopen('cpe-euler.csv', 'w');
fwrite($fp, "t,vTotal,vCpe,i\n");
fwrite($fp, "sec,V,V,A\n");

$qmag = 0.001; // The magnitude of the CPE, in pseudo-Farads
$alpha = 0.7; // The argument of the CPE, between 0 and 1
$r = 10; // Series resistance value, in ohms
$step = 0.001; // The basic time step, in seconds
$writeEvery = 10; // How often to write to file
$ramp = 0.01; // Voltage ramp rate, in volts per second
$tend = 10; // The simulation end time
$gamma = gamma($alpha);
$convu = array(); // The convolution array
$qstepu = array();

$q = 0; // The amount of electrical charge that has flowed
$write = 0;
for ($tloop = 0; $tloop <= $tend / $step; $tloop++) {
  $t = $tloop * $step;
  $convu[$tloop] = ($tloop > 0) ? pow($t, $alpha - 1) : 0;
  $vTotal = $t * $ramp;
  $vCpe = cpe($alpha, $tloop, $t);
  $i = ($vTotal - $vCpe) / $r;
  $qstepu[$tloop] = $i * $step;
  if ($write <= 1) {
    fwrite($fp, "$t,$vTotal,$vCpe,$i\n");
    $write = $writeEvery;
  } else {
    $write--;
  }
  $q = $q + $i * $step;
}
fclose($fp);

function cpe($alpha, $tloop, $t) {
  global $gamma, $step, $qmag, $qstepu, $convu;
  $total = 0;
  for($uloop = 0; $uloop < $tloop; $uloop++) {
    $total += $convu[$tloop - $uloop] * $qstepu[$uloop];
  }
  return $total / $qmag / $gamma;
}

function gamma($x) {
  // https://rosettacode.org/wiki/Gamma_function#Procedural
  $a = array(1.0, 0.5772156649015329, -0.6558780715202539,
             -0.04200263503409524, 0.16653861138229148,
             -0.04219773455554433, -0.009621971527876973,
             0.0072189432466631, -0.0011651675918590652,
             -0.00021524167411495098, 0.0001280502823881162,
```

```
53              -2.013485478078824e-05, -1.25049348214267e-06,
54              1.1330272319817e-06, -2.0563384169776e-07,
55              6.11609510448e-09, 5.00200764447e-09,
56              -1.18127457049e-09, 1.0434267117e-10,
57              7.78226344e-12, -3.69680562e-12, 5.1003703e-13,
58              -2.058326e-14, -5.34812e-15, 1.22678e-15,
59              -1.1813e-16, 1.19e-18, 1.41e-18, -2.3e-19, 2e-20);
60    $y = $x - 1.0;
61    $counta = count($a);
62    $sum = $a[$counta - 1];
63    for ($n = $counta - 2; $n >= 0; $n--) {
64      $sum = $sum * $y + $a[$n];
65    }
66    return 1.0 / $sum;
67  }
```

Bibliography

1. Steffen, W. *et al.* Trajectories of the Earth System in the Anthropocene. *Proceedings of the National Academy of Sciences* **115,** 8252–8259. ISSN: 0027-8424. http://www.pnas.org/lookup/doi/10.1073/pnas.1810141115 (2018).
2. Zeebe, R. E., Dickens, G. R., Ridgwell, A., Sluijs, A. & Thomas, E. Onset of carbon isotope excursion at the Paleocene-Eocene thermal maximum took millennia, not 13 years. *Proceedings of the National Academy of Sciences* **111,** E1062–E1063. ISSN: 0027-8424. http://www.pnas.org/cgi/doi/10.1073/pnas.1321177111 (2014).
3. Zachos, J. C. Rapid Acidification of the Ocean During the Paleocene-Eocene Thermal Maximum. *Science* **308,** 1611–1615. ISSN: 0036-8075. https://www.sciencemag.org/lookup/doi/10.1126/science.1109004 (2005).
4. Dudley, B. B. *BP Energy Outlook 2019 edition* 2019. https://www.bp.com/content/dam/bp/business-sites/en/global/corporate/pdfs/energy-economics/energy-outlook/bp-energy-outlook-2019.pdf.
5. Buchal, C., Karl, H.-d. & Sinn, H.-w. Kohlemotoren, Windmotoren und Dieselmotoren: Was zeigt die CO2-Bilanz? *Ifo Schnelldienst* **25,** 40–54. https://www.econstor.eu/handle/10419/198746 (2019).
6. Rohden, M., Sorge, A., Timme, M. & Witthaut, D. Self-Organized Synchronization in Decentralized Power Grids. *Physical Review Letters* **109,** 064101. ISSN: 0031-9007. https://link.aps.org/doi/10.1103/PhysRevLett.109.064101 (2012).
7. Pala, M. G. *et al.* Transport Inefficiency in Branched-Out Mesoscopic Networks: An Analog of the Braess Paradox. *Physical Review Letters* **108,** 076802. ISSN: 0031-9007. https://link.aps.org/doi/10.1103/PhysRevLett.108.076802 (2012).
8. Witthaut, D. & Timme, M. Braess's paradox in oscillator networks, desynchronization and power outage. *New Journal of Physics* **14,** 083036. ISSN: 1367-2630. https://iopscience.iop.org/article/10.1088/1367-2630/14/8/083036 (2012).
9. Wilde, S. *9 August 2019 power outage report* tech. rep. (Ofgem, 2020). https://www.ofgem.gov.uk/system/files/docs/2020/01/9_august_2019_power_outage_report.pdf.

10. Hesse, H., Schimpe, M., Kucevic, D. & Jossen, A. Lithium-Ion Battery Storage for the Grid—A Review of Stationary Battery Storage System Design Tailored for Applications in Modern Power Grids. *Energies* **10,** 2107. ISSN: 1996-1073. http://www.mdpi.com/1996-1073/10/12/2107 (2017).

11. Falter, C., Batteiger, V. & Sizmann, A. Climate Impact and Economic Feasibility of Solar Thermochemical Jet Fuel Production. *Environmental Science & Technology* **50,** 470–477. https://pubs.acs.org/doi/10.1021/acs.est.5b03515 (2016).

12. Seiler, J. M., Hohwiller, C., Imbach, J. & Luciani, J. F. Technical and economical evaluation of enhanced biomass to liquid fuel processes. *Energy* **35,** 3587–3592. ISSN: 03605442. http://dx.doi.org/10.1016/j.energy.2010.04.048 (2010).

13. Jung, K. A., Lim, S.-R., Kim, Y. & Park, J. M. Opportunity and challenge of seaweed bioethanol based on life cycle CO 2 assessment. *Environmental Progress & Sustainable Energy* **36,** 200–207. http://doi.wiley.com/10.1002/ep.12446 (2017).

14. Park, H. R., Jung, K. A., Lim, S.-R. & Park, J. M. Quantitative Sustainability Assessment of Seaweed Biomass as Bioethanol Feedstock. *BioEnergy Research* **7,** 974–985. http://link.springer.com/10.1007/s12155-014-9430-z (2014).

15. Doddathimmaiah, A. & Andrews, J. Theory, modelling and performance measurement of unitised regenerative fuel cells. *International Journal of Hydrogen Energy* **34,** 8157–8170. ISSN: 03603199. http://dx.doi.org/10.1016/j.ijhydene.2009.07.116 (2009).

16. Passas, G. & Dunnill, C. W. Water Splitting Test Cell for Renewable Energy Storage as Hydrogen Gas. *Fundamentals of Renewable Energy and Applications* **5,** 3–8. https://www.longdom.org/open-access/water-splitting-test-cell-for-renewable-energy-storage-as-hydrogen-gas-2090-4541-1000188.pdf (2015).

17. Phillips, R. & Dunnill, C. W. Zero gap alkaline electrolysis cell design for renewable energy storage as hydrogen gas. *RSC Advances* **6,** 100643–100651. ISSN: 2046-2069. http://xlink.rsc.org/?DOI=C6RA22242K (2016).

18. Romare, M. & Dahllöf, L. *The Life Cycle Energy Consumption and Greenhouse Gas Emissions from Lithium-Ion Batteries* tech. rep. C (IVL Swedish Environmental Research Institute, 2017), 58. http://www.hpv.popol.eu/co2report.pdf.

19. Sharma, S. & Ghoshal, S. K. Hydrogen the future transportation fuel: From production to applications. *Renewable and Sustainable Energy Reviews* **43,** 1151–1158. ISSN: 13640321. http://dx.doi.org/10.1016/j.rser.2014.11.093 (2015).

20. *European temperature for winter 2019 / 20 : Long-term context* tech. rep. (Copernicus Climate Change Service, 2020). https://climate.copernicus.eu/sites/default/files/2020-03/Supplementarytextforwinter2019_2020_0.pdf.

21. EASAC. *Extreme weather events in Europe. Preparing for climate change adaptation: an update on EASAC's 2013 study* tech. rep. March (EASAC, 2018), 1–8. https://easac.eu/publications/details/extreme-weather-events-in-europe/.

22. Gutiérrez-Martín, F., Confente, D. & Guerra, I. Management of variable electricity loads in wind – Hydrogen systems: The case of a Spanish wind farm. *International Journal of Hydrogen Energy* **35,** 7329–7336. https://linkinghub.elsevier.com/retrieve/pii/S0360319910009328 (2010).

23. Kuhn, A. T. & Booth, J. S. Electrical leakage currents in bipolar cell stacks. *Journal of Applied Electrochemistry* **10,** 233–237. http://link.springer.com/10.1007/BF00726091 (1980).

24. Hydrogenics. *Hydrogenics Selected References* tech. rep. (2013). https://pdf.directindustry.com/pdf/hydrogen-systems/hydrogenics-selected-references/14703-788503.html.

25. Baschuk, J. J. & Li, X. Carbon monoxide poisoning of proton exchange membrane fuel cells. *International Journal of Energy Research* **25,** 695–713. http://doi.wiley.com/10.1002/er.713 (2001).

26. Butler, M. S., Moran, C. W., Sunderland, P. B. & Axelbaum, R. L. Limits for hydrogen leaks that can support stable flames. *International Journal of Hydrogen Energy* **34,** 5174–5182. ISSN: 0360-3199. http://dx.doi.org/10.1016/j.ijhydene.2009.04.012 (2009).

27. Belles, F. Detonability and chemical kinetics: Prediction of limits of detonability of hydrogen. *Symposium (International) on Combustion* **7,** 745–751. ISSN: 00820784. https://linkinghub.elsevier.com/retrieve/pii/S0082078458801150 (1958).

28. Mazloomi, K. & Gomes, C. Hydrogen as an energy carrier: Prospects and challenges. *Renewable and Sustainable Energy Reviews* **16,** 3024–3033. https://linkinghub.elsevier.com/retrieve/pii/S1364032112001220 (2012).

29. He, L. & Clavin, P. Premixed hydrogen-oxygen flames. Part I: Flame structure near the flammability limits. *Combustion and Flame* **93,** 391–407. https://linkinghub.elsevier.com/retrieve/pii/001021809390140X (1993).

30. Abdel-Aal, H., Sadik, M, Bassyouni, M & Shalabi, M. A new approach to utilize Hydrogen as a safe fuel. *International Journal of Hydrogen Energy* **30,** 1511–1514. https://linkinghub.elsevier.com/retrieve/pii/S0360319905002521 (2005).

31. Cullis, C. F. & Hinshelwood, C. N. The mechanism of the hydrogen-oxygen reaction - IV. The activation energy of the initiating process. *Proceedings of the Royal Society of London. Series A. Mathematical and Physical Sciences* **186,** 462–469. https://royalsocietypublishing.org/doi/10.1098/rspa.1946.0057 (1946).

32. Brokaw, R. S. *Rate of Reaction between Molecular Hydrogen and Molecular Oxygen* tech. rep. (NASA, 1973). https://ntrs.nasa.gov/citations/19730008201.

33. Hollander, J. *Hydrogen Gas Safety* tech. rep. (Los Alamos National Laboratory (https://bit.ly/2Hx3JkN), 2000). https://miningquiz.com/pdf/Mine_Gases/hydrogengassafety.pdf.

34. Hoyes, J. & Ivings, M. CFD modelling of hydrogen stratification in enclosures: Model validation and application to PAR performance. *Nuclear Engineering and Design* **310,** 142–153. https://linkinghub.elsevier.com/retrieve/pii/S0029549316303089 (2016).

35. Hirsch, F. G. *Effects of Overpressure on the Ear - A Review* tech. rep. (Lovelace Foundation for Medical Education and Research (https://apps.dtic.mil/dtic/tr/fulltext/u2/653129.pdf), 1966). https://apps.dtic.mil/dtic/tr/fulltext/u2/653129.pdf.

36. Houf, W. & Schefer, R. Predicting radiative heat fluxes and flammability envelopes from unintended releases of hydrogen. *International Journal of Hydrogen Energy* **32,** 136–151. https://linkinghub.elsevier.com/retrieve/pii/S0360319906001704 (2007).

37. Colli, A. N., Girault, H. H. & Battistel, A. Non-Precious Electrodes for Practical Alkaline Water Electrolysis. *Materials* **12,** 1336. https://www.mdpi.com/1996-1944/12/8/1336 (2019).

38. Brett, C. M. A. & Brett, A. M. O. *Electrochemistry: Principles, methods, and applications* (Oxford University Press, 1993).

39. Koper, M. T. M. Thermodynamic theory of multi-electron transfer reactions: Implications for electrocatalysis. *Journal of Electroanalytical Chemistry* **660,** 254–260. ISSN: 15726657. http://dx.doi.org/10.1016/j.jelechem.2010.10.004 (2011).

40. Dau, H. *et al.* The Mechanism of Water Oxidation: From Electrolysis via Homogeneous to Biological Catalysis. *ChemCatChem* **2,** 724–761. http://doi.wiley.com/10.1002/cctc.201000126 (2010).

41. Safizadeh, F., Ghali, E. & Houlachi, G. Electrocatalysis developments for hydrogen evolution reaction in alkaline solutions - A Review. *International Journal of Hydrogen Energy* **40,** 256–274. ISSN: 03603199. http://dx.doi.org/10.1016/j.ijhydene.2014.10.109 (2015).

42. Shinagawa, T., Garcia-Esparza, A. T. & Takanabe, K. Insight on Tafel slopes from a microkinetic analysis of aqueous electrocatalysis for energy conversion. *Scientific Reports* **5,** 13801. ISSN: 2045-2322. http://www.nature.com/articles/srep13801 (2015).

43. Su, H.-Y. *et al.* Identifying active surface phases for metal oxide electrocatalysts: a study of manganese oxide bi-functional catalysts for oxygen reduction and water oxidation catalysis. *Physical Chemistry Chemical Physics* **14,** 14010. http://xlink.rsc.org/?DOI=c2cp40841d (2012).

44. Fabbri, E., Habereder, A., Waltar, K., Kötz, R. & Schmidt, T. J. Developments and perspectives of oxide-based catalysts for the oxygen evolution reaction. *Catal. Sci. Technol.* **4,** 3800–3821. http://xlink.rsc.org/?DOI=C4CY00669K (2014).

45. Diaz-Morales, O., Ferrus-Suspedra, D. & Koper, M. T. M. The importance of nickel oxyhydroxide deprotonation on its activity towards electrochemical water oxidation. *Chemical Science* **7,** 2639–2645. http://xlink.rsc.org/?DOI=C5SC04486C (2016).

46. Trześniewski, B. J. *et al.* In Situ Observation of Active Oxygen Species in Fe-Containing Ni-Based Oxygen Evolution Catalysts: The Effect of pH on Electrochemical Activity. *Journal of the American Chemical Society* **137,** 15112–15121. https://pubs.acs.org/doi/10.1021/jacs.5b06814 (2015).

47. Takashima, T., Hashimoto, K. & Nakamura, R. Mechanisms of pH-dependent activity for water oxidation to molecular oxygen by MnO2 electrocatalysts. *Journal of the American Chemical Society* **134,** 1519–27. ISSN: 1520-5126. http://www.ncbi.nlm.nih.gov/pubmed/22206433 (2012).

48. Grimaud, A. *et al.* Activating lattice oxygen redox reactions in metal oxides to catalyse oxygen evolution. *Nature Chemistry* **9,** 457–465. ISSN: 1755-4330. http://www.nature.com/doifinder/10.1038/nchem.2695 (2017).

49. Fierro, S., Nagel, T., Baltruschat, H. & Comninellis, C. Investigation of the oxygen evolution reaction on Ti/IrO2 electrodes using isotope labelling and on-line mass spectrometry. *Electrochemistry Communications* **9,** 1969–1974. https://linkinghub.elsevier.com/retrieve/pii/S1388248107001932 (2007).

50. Macounova, K., Makarova, M. & Krtil, P. Oxygen evolution on nanocrystalline RuO2 and Ru0.9Ni0.1O2-δ electrodes - DEMS approach to reaction mechanism determination. *Electrochemistry Communications* **11,** 1865–1868. ISSN: 13882481. http://dx.doi.org/10.1016/j.elecom.2009.08.004 (2009).

51. Rong, X., Parolin, J. & Kolpak, A. M. A Fundamental Relationship between Reaction Mechanism and Stability in Metal Oxide Catalysts for Oxygen Evolution. *ACS Catalysis* **6,** 1153–1158. ISSN: 2155-5435. https://pubs.acs.org/doi/10.1021/acscatal.5b02432 (2016).

52. Rossmeisl, J., Qu, Z.-W., Zhu, H., Kroes, G.-J. & Nørskov, J. Electrolysis of water on oxide surfaces. *Journal of Electroanalytical Chemistry* **607,** 83–89. https://linkinghub.elsevier.com/retrieve/pii/S0022072806006371 (2007).

53. Diaz-Morales, O., Ledezma-Yanez, I., Koper, M. T. M. & Calle-Vallejo, F. Guidelines for the Rational Design of Ni-Based Double Hydroxide Electrocatalysts for the Oxygen Evolution Reaction. *ACS Catalysis* **5,** 5380–5387. https://pubs.acs.org/doi/10.1021/acscatal.5b01638 (2015).

54. Jones, G., Bligaard, T., Abild-Pedersen, F. & Nørskov, J. K. Using scaling relations to understand trends in the catalytic activity of transition metals. *Journal of Physics: Condensed Matter* **20,** 064239. https://iopscience.iop.org/article/10.1088/0953-8984/20/6/064239 (2008).

55. Calle-Vallejo, F., Díaz-Morales, O. A., Kolb, M. J. & Koper, M. T. M. Why Is Bulk Thermochemistry a Good Descriptor for the Electrocatalytic Activity of Transition Metal Oxides? *ACS Catalysis* **5,** 869–873. https://pubs.acs.org/doi/10.1021/cs5016657 (2015).

56. Friebel, D. *et al.* Identification of Highly Active Fe Sites in (Ni,Fe)OOH for Electrocatalytic Water Splitting. *Journal of the American Chemical Society* **137,** 1305–1313. https://pubs.acs.org/doi/10.1021/ja511559d (2015).

57. Halck, N. B., Petrykin, V., Krtil, P. & Rossmeisl, J. Beyond the volcano limitations in electrocatalysis – oxygen evolution reaction. *Phys. Chem. Chem. Phys.* **16,** 13682–13688. http://xlink.rsc.org/?DOI=c4cp00571f (2014).

58. Cook, T. R. *et al.* Solar Energy Supply and Storage for the Legacy and Nonlegacy Worlds. *Chemical Reviews* **110,** 6474–6502. ISSN: 0009-2665. https://pubs.acs.org/doi/10.1021/cr100246c (2010).

59. Louie, M. W. & Bell, A. T. An Investigation of Thin-Film Ni–Fe Oxide Catalysts for the Electrochemical Evolution of Oxygen. *Journal of the American Chemical Society* **135,** 12329–12337. ISSN: 0002-7863. https://pubs.acs.org/doi/10.1021/ja405351s (2013).

60. Schoeberl, C., Manolova, M. & Freudenberger, R. Sol-gel-deposited cobalt and nickel oxide as an oxygen evolution catalyst in alkaline media. *International Journal of Hydrogen Energy* **40,** 11773–11778. ISSN: 03603199. http://dx.doi.org/10.1016/j.ijhydene.2015.05.046 (2015).

61. Zhu, C. *et al.* Nickel cobalt oxide hollow nanosponges as advanced electrocatalysts for the oxygen evolution reaction. *Chemical Communications* **51,** 7851–7854. http://xlink.rsc.org/?DOI=C5CC01558H (2015).

62. Smith, R. D. L., Prévot, M. S., Fagan, R. D., Trudel, S. & Berlinguette, C. P. Water Oxidation Catalysis: Electrocatalytic Response to Metal Stoichiometry in Amorphous Metal

Oxide Films Containing Iron, Cobalt, and Nickel. *Journal of the American Chemical Society* **135,** 11580–11586. ISSN: 0002-7863. https://pubs.acs.org/doi/10.1021/ja403102j (2013).

63. Fazle Kibria, A. Electrochemical studies of a nickel–copper electrode for the oxygen evolution reaction (OER). *International Journal of Hydrogen Energy* **27,** 879–884. ISSN: 03603199. https://linkinghub.elsevier.com/retrieve/pii/S0360319901001859 (2002).

64. Srirapu, V. K. V. P., Sharma, C. S., Awasthi, R., Singh, R. N. & Sinha, A. S. K. Copper-iron-molybdenum mixed oxides as efficient oxygen evolution electrocatalysts. *Physical chemistry chemical physics : PCCP* **16,** 7385–93. ISSN: 1463-9084. http://www.ncbi.nlm.nih.gov/pubmed/24623197 (2014).

65. Kumar, M., Awasthi, R., Pramanick, A. K. & Singh, R. N. New ternary mixed oxides of Fe, Ni and Mo for enhanced oxygen evolution. *International Journal of Hydrogen Energy* **36,** 12698–12705. ISSN: 03603199. http://dx.doi.org/10.1016/j.ijhydene.2011.07.029 (2011).

66. Song, X., Yang, T., Du, H., Dong, W. & Liang, Z. New binary Mn and Cr mixed oxide electrocatalysts for the oxygen evolution reaction. *Journal of Electroanalytical Chemistry* **760,** 59–63. ISSN: 15726657. http://dx.doi.org/10.1016/j.jelechem.2015.11.044 (2016).

67. Singh, R. N., Madhu, Awasthi, R. & Tiwari, S. K. Iron molybdates as electrocatalysts for O2 evolution reaction in alkaline solutions. *International Journal of Hydrogen Energy* **34,** 4693–4700. ISSN: 03603199. http://dx.doi.org/10.1016/j.ijhydene.2009.04.006 (2009).

68. Zhang, Q. *et al.* Copper-doped cobalt oxide electrodes for oxygen evolution reaction prepared by magnetron sputtering. *International Journal of Hydrogen Energy* **37,** 822–830. https://linkinghub.elsevier.com/retrieve/pii/S0360319911008822 (2012).

69. Zhang, B. *et al.* Homogeneously dispersed multimetal oxygen-evolving catalysts. *Science* **352,** 333–337. ISSN: 0036-8075. https://www.sciencemag.org/lookup/doi/10.1126/science.aaf1525 (2016).

70. Barwe, S., Andronescu, C., Vasile, E., Masa, J. & Schuhmann, W. Influence of Ni to Co ratio in mixed Co and Ni phosphides on their electrocatalytic oxygen evolution activity. *Electrochemistry Communications* **79,** 41–45. ISSN: 13882481. http://dx.doi.org/10.1016/j.elecom.2017.04.014 (2017).

71. Yan, F. *et al.* Highly Stable Three-Dimensional Porous Nickel-Iron Nitride Nanosheets for Full Water Splitting at High Current Densities. *Chemistry - A European Journal.* ISSN: 09476539. http://doi.wiley.com/10.1002/chem.201701662 (2017).

72. Wang, Z. *et al.* Porous Nickel–Iron Selenide Nanosheets as Highly Efficient Electrocatalysts for Oxygen Evolution Reaction. *ACS Applied Materials & Interfaces* **8,** 19386–19392. https://pubs.acs.org/doi/10.1021/acsami.6b03392 (2016).

73. Yeo, B. S. & Bell, A. T. Enhanced Activity of Gold-Supported Cobalt Oxide for the Electrochemical Evolution of Oxygen. *Journal of the American Chemical Society* **133,** 5587–5593. https://pubs.acs.org/doi/10.1021/ja200559j (2011).

74. Sanchez Casalongue, H. G. *et al.* In Situ Observation of Surface Species on Iridium Oxide Nanoparticles during the Oxygen Evolution Reaction. *Angewandte Chemie (International ed. in English)* **53,** 7169–72. ISSN: 1521-3773. http://www.ncbi.nlm.nih.gov/pubmed/24889896 (2014).

75. Nørskov, J. K., Bligaard, T, Rossmeisl, J & Christensen, C. H. Towards the computational design of solid catalysts. *Nature Chemistry* **1,** 37–46. http://www.nature.com/articles/nchem.121 (2009).

76. Suntivich, J., May, K. J., Gasteiger, H. A., Goodenough, J. B. & Shao-Horn, Y. A Perovskite Oxide Optimized for Oxygen Evolution Catalysis from Molecular Orbital Principles. *Science* **334,** 1383–1385. ISSN: 0036-8075. https://www.sciencemag.org/lookup/doi/10.1126/science.1212858 (2011).

77. Murphy, J. J. & Melchiorre, P. Light opens pathways for nickel catalysis. *Nature* **524,** 297–298. http://www.nature.com/articles/nature15200 (2015).

78. Busch, M., Ahlberg, E. & Panas, I. Hydroxide oxidation and peroxide formation at embedded binuclear transition metal sites; TM = Cr, Mn, Fe, Co. *Physical Chemistry Chemical Physics* **13,** 15062. ISSN: 1463-9076. http://xlink.rsc.org/?DOI=c1cp20487d (2011).

79. Doyle, R. L. & Lyons, M. E. G. in *Photoelectrochemical Solar Fuel Production* (eds Giménez, S. & Bisquert, J.) 41–104 (Springer International Publishing, Cham, 2016). http://link.springer.com/10.1007/978-3-319-29641-8_2.

80. Wang, M., Wang, Z., Yu, X. & Guo, Z. Facile one-step electrodeposition preparation of porous NiMo film as electrocatalyst for hydrogen evolution reaction. *International Journal of Hydrogen Energy* **40,** 2173–2181. ISSN: 03603199. http://dx.doi.org/10.1016/j.ijhydene.2014.12.022 (2015).

81. Zhang, J. *et al.* Efficient hydrogen production on MoNi 4 electrocatalysts with fast water dissociation kinetics. *Nature Communications* **8,** 1–8. ISSN: 20411723. http://dx.doi.org/10.1038/ncomms15437 (2017).

82. Gannon, W. J. & Dunnill, C. W. Raney Nickel 2.0: Development of a high-performance bifunctional electrocatalyst. *Electrochimica Acta* **322,** 134687. ISSN: 00134686. https://doi.org/10.1016/j.electacta.2019.134687 (2019).

83. Solmaz, R. Gold-supported activated NiZn coatings: hydrogen evolution and corrosion studies. *International Journal of Energy Research* **41,** 1452–1459. ISSN: 0363907X. http://doi.wiley.com/10.1002/er.3724 (2017).

84. Wang, Y. *et al.* A 3D Nanoporous Ni-Mo Electrocatalyst with Negligible Overpotential for Alkaline Hydrogen Evolution. *ChemElectroChem* **1,** 1138–1144. http://doi.wiley.com/10.1002/celc.201402089 (2014).

85. Zhang, T. *et al.* Nanometric Ni 5 P 4 Clusters Nested on NiCo 2 O 4 for Efficient Hydrogen Production via Alkaline Water Electrolysis. *Advanced Energy Materials* **8,** 1801690. http://doi.wiley.com/10.1002/aenm.201801690 (2018).

86. Chen, W. *et al.* Nickel phosphide based hydrogen producing catalyst with low overpotential and stability at high current density. *Electrochimica Acta* **299,** 756–761. ISSN: 00134686. https://doi.org/10.1016/j.electacta.2019.01.049 (2019).

87. Xiang, R. *et al.* Three-dimensional Core@Shell Co@CoMoO4 nanowire arrays as efficient alkaline hydrogen evolution electro-catalysts. *Applied Catalysis B: Environmental* **246,** 41–49. ISSN: 09263373. https://doi.org/10.1016/j.apcatb.2019.01.035 (2019).

88. Gao, M. Y. *et al.* Facile electrochemical preparation of self-supported porous Ni–Mo alloy microsphere films as efficient bifunctional electrocatalysts for water splitting. *Journal of Materials Chemistry A* **5,** 5797–5805. http://xlink.rsc.org/?DOI=C6TA10812A (2017).

89. Men, Y. *et al.* Tailoring the Electronic Structure of Co 2 P by N Doping for Boosting Hydrogen Evolution Reaction at All pH Values. *ACS Catalysis* **9,** 3744–3752. https://pubs.acs.org/doi/10.1021/acscatal.9b00407 (2019).

90. Huang, Y. *et al.* Atomically engineering activation sites onto metallic 1T-MoS 2 catalysts for enhanced electrochemical hydrogen evolution. *Nature Communications* **10,** 1–11. ISSN: 20411723. http://dx.doi.org/10.1038/s41467-019-08877-9 (2019).

91. Herraiz-Cardona, I., Ortega, E., Vázquez-Gómez, L. & Pérez-Herranz, V. Double-template fabrication of three-dimensional porous nickel electrodes for hydrogen evolution reaction. *International Journal of Hydrogen Energy* **37,** 2147–2156. https://linkinghub.elsevier.com/retrieve/pii/S0360319911024372 (2012).

92. Liu, C. *et al.* Engineering Ni2P-NiSe2 heterostructure interface for highly efficient alkaline hydrogen evolution. *Applied Catalysis B: Environmental* **262,** 118245. https://linkinghub.elsevier.com/retrieve/pii/S0926337319309920 (2020).

93. Shi, Z. *et al.* Porous nanoMoC@graphite shell derived from a MOFs-directed strategy: An efficient electrocatalyst for the hydrogen evolution reaction. *Journal of Materials Chemistry A* **4,** 6006–6013. ISSN: 20507496. http://dx.doi.org/10.1039/C6TA01900E (2016).

94. Liang, H.-W. *et al.* Molecular metal–Nx centres in porous carbon for electrocatalytic hydrogen evolution. *Nature Communications* **6,** 7992. http://www.nature.com/articles/ncomms8992 (2015).

95. Zhu, Y. *et al.* Operando Unraveling of the Structural and Chemical Stability of P-Substituted CoSe 2 Electrocatalysts toward Hydrogen and Oxygen Evolution Reactions in Alkaline Electrolyte. *ACS Energy Letters* **4,** 987–994. https://pubs.acs.org/doi/10.1021/acsenergylett.9b00382 (2019).

96. Lai, F. *et al.* Energy level engineering in transition-metal doped spinel-structured nanosheets for efficient overall water splitting. *Journal of Materials Chemistry A* **7,** 827–833. http://xlink.rsc.org/?DOI=C8TA10162K (2019).

97. Haque, F. *et al.* Ordered intracrystalline pores in planar molybdenum oxide for enhanced alkaline hydrogen evolution. *Journal of Materials Chemistry A* **7,** 257–268. http://xlink.rsc.org/?DOI=C8TA08330D (2019).

98. Zhu, W. *et al.* Nickel sulfide microsphere film on Ni foam as an efficient bifunctional electrocatalyst for overall water splitting. *Chemical Communications* **52,** 1486–1489. http://xlink.rsc.org/?DOI=C5CC08064A (2016).

99. Feng, Y., Yu, X. Y. & Paik, U. Nickel cobalt phosphides quasi-hollow nanocubes as an efficient electrocatalyst for hydrogen evolution in alkaline solution. *Chemical Communications* **52,** 1633–1636. ISSN: 1364548X. http://dx.doi.org/10.1039/C5CC08991C (2016).

100. Xing, Z., Li, Q., Wang, D., Yang, X. & Sun, X. Self-supported nickel nitride as an efficient high-performance three-dimensional cathode for the alkaline hydrogen evolution reaction. *Electrochimica Acta* **191,** 841–845. ISSN: 00134686. http://dx.doi.org/10.1016/j.electacta.2015.12.174 (2016).

101. Xu, X., Song, F. & Hu, X. A nickel iron diselenide-derived efficient oxygen-evolution catalyst. *Nature Communications* **7,** 12324. http://www.nature.com/articles/ncomms12324 (2016).

102. Lu, X. & Zhao, C. Electrodeposition of hierarchically structured three-dimensional nickel–iron electrodes for efficient oxygen evolution at high current densities. *Nature Communications* **6,** 1–7. ISSN: 2041-1723. http://dx.doi.org/10.1038/ncomms7616 (2015).

103. Chi, J. *et al.* Construction of orderly hierarchical FeOOH/NiFe layered double hydroxides supported on cobaltous carbonate hydroxide nanowire arrays for a highly efficient oxygen evolution reaction. *Journal of Materials Chemistry A* **6,** 3397–3401. ISSN: 20507496. http://dx.doi.org/10.1039/C7TA10747A (2018).

104. Liu, R., Wang, Y., Liu, D., Zou, Y. & Wang, S. Water-Plasma-Enabled Exfoliation of Ultrathin Layered Double Hydroxide Nanosheets with Multivacancies for Water Oxidation. *Advanced Materials* **29,** 1701546. http://doi.wiley.com/10.1002/adma.201701546 (2017).

105. Nai, J., Lu, Y., Yu, L., Wang, X. & Lou, X. W. D. Formation of Ni-Fe Mixed Diselenide Nanocages as a Superior Oxygen Evolution Electrocatalyst. *Advanced Materials* **29,** 1703870. http://doi.wiley.com/10.1002/adma.201703870 (2017).

106. Lu, X.-F. *et al.* Bimetal-Organic Framework Derived CoFe 2 O 4 /C Porous Hybrid Nanorod Arrays as High-Performance Electrocatalysts for Oxygen Evolution Reaction. *Advanced Materials* **29,** 1604437. http://doi.wiley.com/10.1002/adma.201604437 (2017).

107. Gong, M. *et al.* An Advanced Ni–Fe Layered Double Hydroxide Electrocatalyst for Water Oxidation. *Journal of the American Chemical Society* **135,** 8452–8455. https://pubs.acs.org/doi/10.1021/ja4027715 (2013).

108. Lu, Z. *et al.* Three-dimensional NiFe layered double hydroxide film for high-efficiency oxygen evolution reaction. *Chemical Communications* **50,** 6479. ISSN: 1359-7345. http://xlink.rsc.org/?DOI=c4cc01625d (2014).

109. Zhang, H., Zhou, W., Dong, J., Lu, X. F. & Lou, X. W. D. Intramolecular electronic coupling in porous iron cobalt (oxy)phosphide nanoboxes enhances the electrocatalytic activity for oxygen evolution. *Energy & Environmental Science* **12,** 3348–3355. http://xlink.rsc.org/?DOI=C9EE02787D (2019).

110. Xu, Y. *et al.* Nickel Nanoparticles Encapsulated in Few-Layer Nitrogen-Doped Graphene Derived from Metal-Organic Frameworks as Efficient Bifunctional Electrocatalysts for Overall Water Splitting. *Advanced Materials* **29,** 1605957. http://doi.wiley.com/10.1002/adma.201605957 (2017).

111. Anantharaj, S., Reddy, P. N. & Kundu, S. Core-Oxidized Amorphous Cobalt Phosphide Nanostructures: An Advanced and Highly Efficient Oxygen Evolution Catalyst. *Inorganic Chemistry* **56,** 1742–1756. https://pubs.acs.org/doi/10.1021/acs.inorgchem.6b02929 (2017).

112. Zhu, Y.-P., Liu, Y.-P., Ren, T.-Z. & Yuan, Z.-Y. Self-Supported Cobalt Phosphide Mesoporous Nanorod Arrays: A Flexible and Bifunctional Electrode for Highly Active Electrocatalytic Water Reduction and Oxidation. *Advanced Functional Materials* **25,** 7337–7347. http://doi.wiley.com/10.1002/adfm.201503666 (2015).

113. Wang, H. *et al.* Double Perovskite LaFe x Ni 1- x O 3 Nanorods Enable Efficient Oxygen Evolution Electrocatalysis. *Angewandte Chemie International Edition* **58,** 2316–2320. https://onlinelibrary.wiley.com/doi/abs/10.1002/anie.201812545 (2019).

114. Zhang, H. *et al.* Unveiling the Activity Origin of Electrocatalytic Oxygen Evolution over Isolated Ni Atoms Supported on a N-Doped Carbon Matrix. *Advanced Materials* **31,** 1904548. https://onlinelibrary.wiley.com/doi/abs/10.1002/adma.201904548 (2019).

115. Song, F. & Hu, X. Ultrathin Cobalt–Manganese Layered Double Hydroxide Is an Efficient Oxygen Evolution Catalyst. *Journal of the American Chemical Society* **136,** 16481–16484. ISSN: 0002-7863. https://pubs.acs.org/doi/10.1021/ja5096733 (2014).

116. Liu, G., Wang, K., Gao, X., He, D. & Li, J. Fabrication of mesoporous NiFe2O4 nanorods as efficient oxygen evolution catalyst for water splitting. *Electrochimica Acta* **211,** 871–878. ISSN: 00134686. http://dx.doi.org/10.1016/j.electacta.2016.06.113 (2016).

117. Bikkarolla, S. K. & Papakonstantinou, P. CuCo 2 O 4 nanoparticles on nitrogenated graphene as highly efficient oxygen evolution catalyst. *Journal of Power Sources* **281,** 243–251. https://linkinghub.elsevier.com/retrieve/pii/S0378775315002232 (2015).

118. Jiang, J., Zhang, A., Li, L. & Ai, L. Nickel-cobalt layered double hydroxide nanosheets as high-performance electrocatalyst for oxygen evolution reaction. *Journal of Power Sources* **278,** 445–451. ISSN: 03787753. http://dx.doi.org/10.1016/j.jpowsour.2014.12.085 (2015).

119. McCrory, C. C. L. *et al.* Benchmarking Hydrogen Evolving Reaction and Oxygen Evolving Reaction Electrocatalysts for Solar Water Splitting Devices. *Journal of the American Chemical Society* **137,** 4347–4357. ISSN: 0002-7863. https://pubs.acs.org/doi/10.1021/ja510442p (2015).

120. Bergmann, A. *et al.* Reversible amorphization and the catalytically active state of crystalline Co3O4 during oxygen evolution. *Nature Communications* **6,** 8625. http://www.nature.com/articles/ncomms9625 (2015).

121. Frydendal, R. *et al.* Benchmarking the Stability of Oxygen Evolution Reaction Catalysts: The Importance of Monitoring Mass Losses. *ChemElectroChem* **1,** 2075–2081. http://doi.wiley.com/10.1002/celc.201402262 (2014).

122. Douglas, T. G., Cruden, A. & Infield, D. Development of an ambient temperature alkaline electrolyser for dynamic operation with renewable energy sources. *International Journal of Hydrogen Energy* **38,** 723–739. ISSN: 03603199. http://dx.doi.org/10.1016/j.ijhydene.2012.10.071 (2013).

123. Bernier, E., Hamelin, J., Agbossou, K. & Bose, T. K. Electric round-trip efficiency of hydrogen and oxygen-based energy storage. *International Journal of Hydrogen Energy* **30,** 105–111. https://linkinghub.elsevier.com/retrieve/pii/S0360319904001788 (2005).

124. Yamaguchi, A. *et al.* Regulating proton-coupled electron transfer for efficient water splitting by manganese oxides at neutral pH. *Nature Communications* **5,** 4256. http://www.nature.com/articles/ncomms5256 (2014).

125. Stevens, M. B. *et al.* Measurement Techniques for the Study of Thin Film Heterogeneous Water Oxidation Electrocatalysts. *Chemistry of Materials*, acs.chemmater.6b02796. ISSN: 0897-4756. http://pubs.acs.org/doi/abs/10.1021/acs.chemmater.6b02796 (2016).

126. De Jonge, R, Barendrecht, E, Janssen, L & van Stralen, S. Gas bubble behaviour and electrolyte resistance during water electrolysis. *International Journal of Hydrogen Energy* **7,** 883–894. ISSN: 03603199. https://linkinghub.elsevier.com/retrieve/pii/0360319982900076 (1982).

127. Herraiz-Cardona, I., Ortega, E. & Pérez-Herranz, V. Impedance study of hydrogen evolution on Ni/Zn and Ni–Co/Zn stainless steel based electrodeposits. *Electrochimica Acta* **56,** 1308–1315. https://linkinghub.elsevier.com/retrieve/pii/S0013468610015045 (2011).

128. Pérez-Alonso, F., Adán, C, Rojas, S, Peña, M. & Fierro, J. Ni/Fe electrodes prepared by electrodeposition method over different substrates for oxygen evolution reaction in alkaline medium. *International Journal of Hydrogen Energy* **39,** 5204–5212. ISSN: 03603199. https://linkinghub.elsevier.com/retrieve/pii/S0360319913031789 (2014).

129. Balej, J. Electrocatalysts for oxygen evolution in advanced water electrolysis. *International Journal of Hydrogen Energy* **10,** 89–99. ISSN: 03603199. https://linkinghub.elsevier.com/retrieve/pii/0360319985900412 (1985).

130. Soares, D. M. Hydride Effect on the Kinetics of the Hydrogen Evolution Reaction on Nickel Cathodes in Alkaline Media. *Journal of The Electrochemical Society* **139,** 98. ISSN: 00134651. http://jes.ecsdl.org/cgi/doi/10.1149/1.2069207 (1992).

131. Divisek, J., Schmitz, H. & Steffen, B. Electrocatalyst materials for hydrogen evolution. *Electrochimica Acta* **39,** 1723–1731. ISSN: 00134686. https://linkinghub.elsevier.com/retrieve/pii/0013468694851573 (1994).

132. Rausch, S. & Wendt, H. Morphology and Utilization of Smooth Hydrogen-Evolving Raney Nickel Cathode Coatings and Porous Sintered-Nickel Cathodes. *Journal of The Electrochemical Society* **143,** 2852–2862. https://iopscience.iop.org/article/10.1149/1.1837118 (1996).

133. Trotochaud, L., Young, S. L., Ranney, J. K. & Boettcher, S. W. Nickel–Iron Oxyhydroxide Oxygen-Evolution Electrocatalysts: The Role of Intentional and Incidental Iron Incorporation. *Journal of the American Chemical Society* **136,** 6744–6753. https://pubs.acs.org/doi/10.1021/ja502379c (2014).

134. Swierk, J. R., Klaus, S., Trotochaud, L., Bell, A. T. & Tilley, T. D. Electrochemical Study of the Energetics of the Oxygen Evolution Reaction at Nickel Iron (Oxy)Hydroxide Catalysts. *The Journal of Physical Chemistry C* **119,** 19022–19029. https://pubs.acs.org/doi/10.1021/acs.jpcc.5b05861 (2015).

135. Peterson, P. *Fitting EIS Data - Diffusion Elements - Warburg* 2014. http://www.consultrsr.net/resources/eis/diffusion.htm (2020).

136. Brightman, E., Hinds, G. & O'Malley, R. In situ measurement of active catalyst surface area in fuel cell stacks. *Journal of Power Sources* **242,** 244–254. ISSN: 03787753. http://dx.doi.org/10.1016/j.jpowsour.2013.05.046 (2013).

137. Reid, O., Saleh, F. S. & Easton, E. B. Determining electrochemically active surface area in PEM fuel cell electrodes with electrochemical impedance spectroscopy and its application to catalyst durability. *Electrochimica Acta* **114,** 278–284. ISSN: 00134686. http://dx.doi.org/10.1016/j.electacta.2013.10.050 (2013).

138. Pletcher, D. & Li, X. Prospects for alkaline zero gap water electrolysers for hydrogen production. *International Journal of Hydrogen Energy* **36,** 15089–15104. https://linkinghub.elsevier.com/retrieve/pii/S0360319911020015 (2011).

139. Zeng, K. & Zhang, D. Recent progress in alkaline water electrolysis for hydrogen production and applications. *Progress in Energy and Combustion Science* **36,** 307–326. ISSN: 03601285. http://dx.doi.org/10.1016/j.pecs.2009.11.002 (2010).

140. Kötz, E. R. & Stucki, S. Ruthenium dioxide as a hydrogen-evolving cathode. *Journal of Applied Electrochemistry* **17,** 1190–1197. ISSN: 0021-891X. http://link.springer.com/10.1007/BF01023602 (1987).

141. Calegaro, M., Santos, M., Miwa, D. & Machado, S. Microgravimetric and voltammetric study of Zn underpotential deposition on platinum in alkaline medium. *Surface Science* **579,** 58–64. https://linkinghub.elsevier.com/retrieve/pii/S0039602805001007 (2005).

142. Phillips, R., Edwards, A., Rome, B., Jones, D. R. & Dunnill, C. W. Minimising the ohmic resistance of an alkaline electrolysis cell through effective cell design. *International Journal of Hydrogen Energy* **42,** 23986–23994. https://linkinghub.elsevier.com/retrieve/pii/S0360319917330203 (2017).

143. Phillips, R. *Minimising the Ohmic Resistance of an Alkaline Electrolysis Cell* PhD thesis (Swansea University, 2019).

144. Lee, C.-Y. & Huang, J.-C. Novel Design for Constant-Pressure Water-Displacement Gas Collector. *Journal of Environmental Engineering* **121,** 727–729. ISSN: 0733-9372. http://ascelibrary.org/doi/10.1061/%28ASCE%290733-9372%281995%29121%3A10%28727%29 (1995).

145. Dong, H. *et al.* Electrochemical performance of porous Ni3Al electrodes for hydrogen evolution reaction. *International Journal of Hydrogen Energy* **36,** 12112–12120. https://linkinghub.elsevier.com/retrieve/pii/S0360319911015874 (2011).

146. Gu, L., Wang, L., Xun, J., Ottova-Leitmannova, A. & Tien, H. A new method for the determination of electrical properties of supported bilayer lipid membranes by cyclic voltammetry. *Bioelectrochemistry and Bioenergetics* **39,** 275–283. https://linkinghub.elsevier.com/retrieve/pii/0302459895050353 (1996).

147. Ehrensberger, M. T. & Gilbert, J. L. A time-based potential step analysis of electrochemical impedance incorporating a constant phase element: A study of commercially pure titanium in phosphate buffered saline. *Journal of Biomedical Materials Research Part A* **9999A,** NA–NA. http://doi.wiley.com/10.1002/jbm.a.32550 (2009).

148. Hassanein, A., Glass, G. & Buenfeld, N. The use of small electrochemical perturbations to assess the corrosion of steel in concrete. *NDT & E International* **31,** 265–272. ISSN: 09638695. https://linkinghub.elsevier.com/retrieve/pii/S0963869598000103 (1998).

149. Krstajić, N. *et al.* Electrodeposition of Ni–Mo alloy coatings and their characterization as cathodes for hydrogen evolution in sodium hydroxide solution. *International Journal of Hydrogen Energy* **33,** 3676–3687. https://linkinghub.elsevier.com/retrieve/pii/S0360319908004680 (2008).

150. González-Buch, C., Herraiz-Cardona, I., Ortega, E., García-Antón, J. & Pérez-Herranz, V. Synthesis and characterization of macroporous Ni, Co and Ni–Co electrocatalytic deposits for hydrogen evolution reaction in alkaline media. *International Journal of Hydrogen Energy* **38,** 10157–10169. https://linkinghub.elsevier.com/retrieve/pii/S0360319913014559 (2013).

151. Tozar, A. & Karahan, I. H. Structural and corrosion protection properties of electrochemically deposited nano-sized Zn-Ni alloy coatings. *Applied Surface Science* **318,** 15–23. ISSN: 01694332. http://dx.doi.org/10.1016/j.apsusc.2013.12.020 (2014).

152. Huang, Z. *et al.* Ni 12 P 5 Nanoparticles as an Efficient Catalyst for Hydrogen Generation via Electrolysis and Photoelectrolysis. *ACS Nano* **8,** 8121–8129. https://pubs.acs.org/doi/10.1021/nn5022204 (2014).

153. Solmaz, R., Salcı, A., Yüksel, H., Doğrubaş, M. & Kardaş, G. Preparation and characterization of Pd-modified Raney-type NiZn coatings and their application for alkaline water electrolysis. *International Journal of Hydrogen Energy* **42,** 2464–2475. https://linkinghub.elsevier.com/retrieve/pii/S0360319916307443 (2017).

154. Yang, T. *et al.* An efficient approach for prediction of Warburg-type resistance under working currents. *International Journal of Hydrogen Energy* **43,** 15445–15456. ISSN: 03603199. https://doi.org/10.1016/j.ijhydene.2018.06.076 (2018).

155. Brug, G., van den Eeden, A., Sluyters-Rehbach, M. & Sluyters, J. The analysis of electrode impedances complicated by the presence of a constant phase element. *Journal of Electroanalytical Chemistry and Interfacial Electrochemistry* **176,** 275–295. https://linkinghub.elsevier.com/retrieve/pii/S0022072884803241 (1984).

156. Hsu, C. H & Mansfeld, F. Technical Note: Concerning the Conversion of the Constant Phase Element Parameter Y 0 into a Capacitance. *CORROSION* **57,** 747–748. ISSN: 0010-9312. http://corrosionjournal.org/doi/10.5006/1.3280607 (2001).

157. Jovic, V. *Determination of the correct value of Cdl from the impedance results fitted by the commercially available software* tech. rep. (University of Belgrade, Belgrade, 2003). http://www.egmont.com.pl/gamry/prasa/jovic.pdf.

158. Barzilai, J. & Borwein, J. M. Two-Point Step Size Gradient Methods. *IMA Journal of Numerical Analysis* **8,** 141–148. ISSN: 0272-4979. https://academic.oup.com/imajna/article-lookup/doi/10.1093/imanum/8.1.141 (1988).

159. Gannon, W. J. & Dunnill, C. W. Apparent disagreement between cyclic voltammetry and electrochemical impedance spectroscopy explained by time-domain simulation of constant phase elements. *International Journal of Hydrogen Energy* **45,** 22383–22393. ISSN: 03603199. https://linkinghub.elsevier.com/retrieve/pii/S0360319920321662 (2020).

160. Athanasiou, V. & Konkoli, Z. On the efficient simulation of electrical circuits with constant phase elements: The Warburg element as a test case. *International Journal of Circuit Theory and Applications* **46,** 1072–1090. http://doi.wiley.com/10.1002/cta.2474 (2018).

161. Valsa, J. & Vlach, J. RC models of a constant phase element. *International Journal of Circuit Theory and Applications* **41,** 59–67. ISSN: 00989886. https://onlinelibrary.wiley.com/doi/full/10.1002/cta.785 (2013).

162. Gannon, W., Jones, D. & Dunnill, C. Enhanced Lifetime Cathode for Alkaline Electrolysis Using Standard Commercial Titanium Nitride Coatings. *Processes* **7,** 112. http://www.mdpi.com/2227-9717/7/2/112 (2019).

163. Delbari, S. A., Nayebi, B., Ghasali, E., Shokouhimehr, M. & Shahedi Asl, M. Spark plasma sintering of TiN ceramics codoped with SiC and CNT. *Ceramics International* **45,** 3207–3216. ISSN: 02728842. https://doi.org/10.1016/j.ceramint.2018.10.223 (2019).

164. Prokudina, V. K. *Titanium Nitride* 398–401. ISBN: 9780128041734. http://dx.doi.org/10.1016/B978-0-12-804173-4.00160-5 (Elsevier Inc., 2017).

165. Azuma, M., Nakato, Y. & Tsubomura, H. Oxygen and chlorine evolution on niobium-, zirconium- and other metal-nitride amorphous thin film electrodes prepared by the reactive RF sputtering technique. *Journal of Electroanalytical Chemistry and Interfacial Electrochemistry* **255,** 179–198. https://linkinghub.elsevier.com/retrieve/pii/0022072888800135 (1988).

166. Gebauer, C. *et al.* Performance of titanium oxynitrides in the electrocatalytic oxygen evolution reaction. *Nano Energy* **29,** 136–148. ISSN: 22112855. http://dx.doi.org/10.1016/j.nanoen.2016.05.034 (2016).

167. Wirth, S., Harnisch, F., Weinmann, M. & Schröder, U. Comparative study of IVB-VIB transition metal compound electrocatalysts for the hydrogen evolution reaction. *Applied Catalysis B: Environmental* **126,** 225–230. ISSN: 09263373. http://dx.doi.org/10.1016/j.apcatb.2012.07.023 (2012).

168. Carta, R., Dernini, S., Polcaro, A., Ricci, P. & Tola, G. The influence of sulphide environment on hydrogen evolution at a stainless steel cathode in alkaline solution. *Journal of Electroanalytical Chemistry and Interfacial Electrochemistry* **257,** 257–268. https://linkinghub.elsevier.com/retrieve/pii/0022072888870463 (1988).

169. Olivares-Ramírez, J., Campos-Cornelio, M., Uribe Godínez, J., Borja-Arco, E & Castellanos, R. Studies on the hydrogen evolution reaction on different stainless steels. *International Journal of Hydrogen Energy* **32,** 3170–3173. ISSN: 03603199. https://linkinghub.elsevier.com/retrieve/pii/S036031990700064X (2007).

170. Schäfer, H. *et al.* Surface Oxidation of Stainless Steel: Oxygen Evolution Electrocatalysts with High Catalytic Activity. *ACS Catalysis* **5,** 2671–2680. https://pubs.acs.org/doi/10.1021/acscatal.5b00221 (2015).

171. Devia, D. M., Restrepo-Parra, E. & Arango, P. J. Comparative study of titanium carbide and nitride coatings grown by cathodic vacuum arc technique. *Applied Surface Science* **258,** 1164–1174. ISSN: 01694332. http://dx.doi.org/10.1016/j.apsusc.2011.09.061 (2011).

172. Cho, E. A., Jeon, U.-S., Hong, S.-A., Oh, I.-H. & Kang, S.-G. Performance of a 1kW-class PEMFC stack using TiN-coated 316 stainless steel bipolar plates. *Journal of Power Sources* **142,** 177–183. ISSN: 03787753. http://linkinghub.elsevier.com/retrieve/pii/S0378775304011000 (2005).

173. *WallworkHT Commercial Coatings (PVD)* 2019. https://www.wallworkht.co.uk/content/commercial_coatings/ (2019).

174. Milošev, I., Strehblow, H.-H & Navinšek, B. Comparison of TiN, ZrN and CrN hard nitride coatings: Electrochemical and thermal oxidation. *Thin Solid Films* **303,** 246–254. ISSN: 00406090. https://linkinghub.elsevier.com/retrieve/pii/S0040609097000692 (1997).

175. Kao, C.-T., Ding, S.-J., Chen, Y.-C. & Huang, T.-H. The anticorrosion ability of titanium nitride (TiN) plating on an orthodontic metal bracket and its biocompatibility. *Journal of Biomedical Materials Research* **63,** 786–792. http://doi.wiley.com/10.1002/jbm.10484 (2002).

176. *XPS Interpretation of Titanium* https://xpssimplified.com/elements/titanium.php (2018).

177. Shimada, S. & Hasegawa, M. Preparation of Titanium Nitride Films from Amide Precursors Synthesized by Electrolysis. *Journal of the American Ceramic Society* **86,** 177–179. http://doi.wiley.com/10.1111/j.1151-2916.2003.tb03298.x (2003).

178. Wang, W., Savadogo, O. & Ma, Z. F. Preparation of new titanium oxy nitride based electro catalysts using an anhydrous sol-gel method for water electrolysis in acid medium. *International Journal of Hydrogen Energy* **37,** 7405–7417. ISSN: 03603199. http://dx.doi.org/10.1016/j.ijhydene.2012.02.025 (2012).

179. Chappé, J.-M. *et al.* Titanium oxynitride thin films sputter deposited by the reactive gas pulsing process. *Applied Surface Science* **253,** 5312–5316. https://linkinghub.elsevier.com/retrieve/pii/S0169433206015273 (2007).

180. Dunnill, C. W. & Parkin, I. P. N-Doped Titania Thin Films Prepared by Atmospheric Pressure CVD using t -Butylamine as the Nitrogen Source: Enhanced Photocatalytic Activity under Visible Light. *Chemical Vapor Deposition* **15,** 171–174. https://onlinelibrary.wiley.com/doi/abs/10.1002/cvde.200806274 (2009).

181. Dunnill, C. W., Aiken, Z. A., Pratten, J., Wilson, M. & Parkin, I. P. Sulfur- and Nitrogen-Doped Titania Biomaterials via APCVD. *Chemical Vapor Deposition* **16,** 50–54. http://doi.wiley.com/10.1002/cvde.200906836 (2010).

182. Dunnill, C. W. *et al.* Visible light photocatalysts—N-doped TiO2 by sol–gel, enhanced with surface bound silver nanoparticle islands. *Journal of Materials Chemistry* **21,** 11854. ISSN: 0959-9428. http://xlink.rsc.org/?DOI=c1jm11557j (2011).

183. Chim, Y. C., Ding, X. Z., Zeng, X. T. & Zhang, S. Oxidation resistance of TiN, CrN, TiAlN and CrAlN coatings deposited by lateral rotating cathode arc. *Thin Solid Films* **517,** 4845–4849. ISSN: 00406090. http://dx.doi.org/10.1016/j.tsf.2009.03.038 (2009).

184. Medford, A. J. *et al.* From the Sabatier principle to a predictive theory of transition-metal heterogeneous catalysis. *Journal of Catalysis* **328,** 36–42. ISSN: 10902694. http://dx.doi.org/10.1016/j.jcat.2014.12.033 (2015).

185. Eftekhari, A. Electrocatalysts for hydrogen evolution reaction. *International Journal of Hydrogen Energy* **42,** 11053–11077. ISSN: 03603199. http://dx.doi.org/10.1016/j.ijhydene.2017.02.125 (2017).

186. Nørskov, J. K. *et al.* Trends in the Exchange Current for Hydrogen Evolution. *Journal of The Electrochemical Society* **152,** J23. https://iopscience.iop.org/article/10.1149/1.1856988 (2005).

187. Schiller, G., Henne, R., Mohr, P. & Peinecke, V. High performance electrodes for an advanced intermittently operated 10-kW alkaline water electrolyzer. *International Journal of Hydrogen Energy* **23,** 761–765. ISSN: 03603199. https://linkinghub.elsevier.com/retrieve/pii/S0360319997001225 (1998).

188. Smith, A. J. & Trimm, D. L. The Preparation of Skeletal Catalysts. *Annual Review of Materials Research* **35,** 127–142. ISSN: 1531-7331. http://www.annualreviews.org/doi/10.1146/annurev.matsci.35.102303.140758 (2005).

189. Endoh, E, Otouma, H, Morimoto, T & Oda, Y. New Raney nickel composite-coated electrode for hydrogen evolution. *International Journal of Hydrogen Energy* **12,** 473–479. https://linkinghub.elsevier.com/retrieve/pii/0360319987900449 (1987).

190. Balej, J., Divisek, J., Schmitz, H. & Mergel, J. Preparation and properties of raney nickel electrodes on Ni-Zn base for H2 and O2 evolution from alkaline solutions Part I: electrodeposition of Ni-Zn alloys from chloride solutions. *Journal of Applied Electrochemistry* **22,** 705–710. http://link.springer.com/10.1007/BF01027497 (1992).

191. De Giz, M. J., Machado, S. A. S., Avaca, L. A. & Gonzalez, E. R. High area Ni-Zn and Ni-Co-Zn codeposits as hydrogen electrodes in alkaline solutions. *Journal of Applied Electrochemistry* **22,** 973–977. http://link.springer.com/10.1007/BF01024146 (1992).

192. Marozzi, C. & Chialvo, A. Development of electrode morphologies of interest in electrocatalysis. Part 1: Electrodeposited porous nickel electrodes. *Electrochimica Acta* **45,** 2111–2120. https://linkinghub.elsevier.com/retrieve/pii/S0013468699004223 (2000).

193. Birry, L & Lasia, A. Studies of the Hydrogen Evolution Reaction on Raney Nickel-Molybdenum Electrodes. *Journal of Applied Electrochemistry* **34,** 735–749. ISSN: 0021-891X. http://link.springer.com/10.1023/B:JACH.0000031161.26544.6a (2004).

194. Chade, D. *et al.* Evaluation of Raney nickel electrodes prepared by atmospheric plasma spraying for alkaline water electrolysers. *International Journal of Hydrogen Energy* **38,** 14380–14390. ISSN: 03603199. http://dx.doi.org/10.1016/j.ijhydene.2013.09.012 (2013).

195. Divisek, J, Malinowski, P, Mergel, J & Schmitz, H. Improved components for advanced alkaline water electrolysis. *International Journal of Hydrogen Energy* **13,** 141–150. https://linkinghub.elsevier.com/retrieve/pii/0360319988900146 (1988).

196. Sheela, G., Pushpavanam, M. & Pushpavanam, S. Zinc–nickel alloy electrodeposits for water electrolysis. *International Journal of Hydrogen Energy* **27,** 627–633. https://linkinghub.elsevier.com/retrieve/pii/S0360319901001707 (2002).

197. Herraiz-Cardona, I., Ortega, E., Vázquez-Gómez, L. & Pérez-Herranz, V. Electrochemical characterization of a NiCo/Zn cathode for hydrogen generation. *International Journal of Hydrogen Energy* **36,** 11578–11587. https://linkinghub.elsevier.com/retrieve/pii/S0360319911015394 (2011).

198. Herraiz-Cardona, I., González-Buch, C., Valero-Vidal, C., Ortega, E. & Pérez-Herranz, V. Co-modification of Ni-based type Raney electrodeposits for hydrogen evolution reaction in alkaline media. *Journal of Power Sources* **240,** 698–704. https://linkinghub.elsevier.com/retrieve/pii/S0378775313008197 (2013).

199. Solmaz, R., Döner, A. & Kardas, G. Preparation, characterization and application of alkaline leached CuNiZn ternary coatings for long-term electrolysis in alkaline solution. *International Journal of Hydrogen Energy* **35,** 10045–10049. https://linkinghub.elsevier.com/retrieve/pii/S0360319910015338 (2010).

200. Solmaz, R. Electrochemical Preparation, Characterization, and Application of a Novel Cathode Material, Mild Steel/Ni/NiZn-Pt, for Alkaline Water Electrolysis. *Energy Sources, Part A: Recovery, Utilization, and Environmental Effects* **36,** 1212–1218. http://www.tandfonline.com/doi/abs/10.1080/15567036.2010.545804 (2014).

201. Solmaz, R., Döner, A., Doğrubaş, M., Erdoğan, I. Y. & Kardaş, G. Enhancement of electrochemical activity of Raney-type NiZn coatings by modifying with PtRu binary deposits: Application for alkaline water electrolysis. *International Journal of Hydrogen Energy* **41,** 1432–1440. https://linkinghub.elsevier.com/retrieve/pii/S0360319915310028 (2016).

202. Bates, M. K., Jia, Q., Doan, H., Liang, W. & Mukerjee, S. Charge-Transfer Effects in Ni–Fe and Ni–Fe–Co Mixed-Metal Oxides for the Alkaline Oxygen Evolution Reaction. *ACS Catalysis* **6,** 155–161. https://pubs.acs.org/doi/10.1021/acscatal.5b01481 (2016).

203. Sapountzi, F. M., Gracia, J. M., Weststrate, C. K.-J., Fredriksson, H. O. & Niemantsverdriet, J. H. Electrocatalysts for the generation of hydrogen, oxygen and synthesis gas. *Progress in Energy and Combustion Science* **58,** 1–35. https://linkinghub.elsevier.com/retrieve/pii/S0360128516300260 (2017).

204. Rose, I. & Whittington, C. *Ni-plating Handbook* tech. rep. (Nickel Institute, 2014). https://nickelinstitute.org/media/2323/nph_141015.pdf.

205. Bourasseau, C. & Guinot, B. in *Hydrogen Production* (ed Godula-Jopek, A.) 311–382 (Wiley, 2015). ISBN: 978-3-527-33343-4.

206. Divisek, J, Mergel, J & Schmitz, H. Advanced water electrolysis and catalyst stability under discontinuous operation. *International Journal of Hydrogen Energy* **15,** 105–114. ISSN: 03603199. https://linkinghub.elsevier.com/retrieve/pii/036031999090032T (1990).

207. Marceta Kaninski, M. P., Nikolic, V. M., Tasic, G. S. & Rakocevic, Z. L. Electrocatalytic activation of Ni electrode for hydrogen production by electrodeposition of Co and V species. *International Journal of Hydrogen Energy* **34,** 703–709. ISSN: 03603199. http://dx.doi.org/10.1016/j.ijhydene.2008.09.024 (2009).

208. Lyons, M. E. G., Doyle, R. L., Godwin, I., O'Brien, M. & Russell, L. Hydrous Nickel Oxide: Redox Switching and the Oxygen Evolution Reaction in Aqueous Alkaline Solution. *Journal of The Electrochemical Society* **159,** H932–H944. https://iopscience.iop.org/article/10.1149/2.078212jes (2012).

209. Takano, N. & Kaida, S. Crack Initiation by Cathodic Hydrogen Charging in Nickel Single Crystal. *ISIJ International* **52,** 263–266. http://joi.jlc.jst.go.jp/JST.JSTAGE/isijinternational/52.263?from=CrossRef (2012).

210. Divisek, J, Steffen, B & Schmitz, H. Theoretical analysis and evaluation of the operating data of a bipolar water electrolyser. *International Journal of Hydrogen Energy* **19,** 579–586. ISSN: 03603199. https://linkinghub.elsevier.com/retrieve/pii/0360319994902151 (1994).

211. Park, B.-O., Lokhande, C., Park, H.-S., Jung, K.-D. & Joo, O.-S. Performance of supercapacitor with electrodeposited ruthenium oxide film electrodes—effect of film thickness. *Journal of Power Sources* **134,** 148–152. https://linkinghub.elsevier.com/retrieve/pii/S0378775304003489 (2004).

212. Ye, J.-M., He, D.-H., Li, F., Li, Y.-L. & He, J.-B. Roles of soluble species in the alkaline oxygen evolution reaction on a nickel anode. *Chemical Communications* **54,** 10116–10119. http://xlink.rsc.org/?DOI=C8CC05896B (2018).

213. Smith, A. M., Trotochaud, L., Burke, M. S. & Boettcher, S. W. Contributions to activity enhancement via Fe incorporation in Ni-(oxy)hydroxide/borate catalysts for near-neutral pH oxygen evolution. *Chemical Communications* **51,** 5261–5263. http://xlink.rsc.org/?DOI=C4CC08670H (2015).

214. Burke, M. S. *et al.* Revised Oxygen Evolution Reaction Activity Trends for First-Row Transition-Metal (Oxy)hydroxides in Alkaline Media. *The Journal of Physical Chemistry Letters* **6,** 3737–3742. https://pubs.acs.org/doi/10.1021/acs.jpclett.5b01650 (2015).

215. Yu, F. *et al.* High-performance bifunctional porous non-noble metal phosphide catalyst for overall water splitting. *Nature Communications* **9,** 2551. ISSN: 2041-1723. http://www.nature.com/articles/s41467-018-04746-z (2018).

216. Jiang, N., You, B., Sheng, M. & Sun, Y. Electrodeposited Cobalt-Phosphorous-Derived Films as Competent Bifunctional Catalysts for Overall Water Splitting. *Angewandte Chemie International Edition* **54,** 6251–6254. http://doi.wiley.com/10.1002/anie.201501616 (2015).

217. Wang, H. *et al.* Bifunctional non-noble metal oxide nanoparticle electrocatalysts through lithium-induced conversion for overall water splitting. *Nature Communications* **6,** 1–8. ISSN: 20411723. http://dx.doi.org/10.1038/ncomms8261 (2015).

218. Jiao, L., Zhou, Y.-X. & Jiang, H.-L. Metal–organic framework-based CoP/reduced graphene oxide: high-performance bifunctional electrocatalyst for overall water splitting. *Chemical Science* **7,** 1690–1695. http://xlink.rsc.org/?DOI=C5SC04425A (2016).

219. Li, Y. *et al.* Ternary NiCoP nanosheet arrays: An excellent bifunctional catalyst for alkaline overall water splitting. *Nano Research* **9,** 2251–2259. http://link.springer.com/10.1007/s12274-016-1112-z (2016).

220. Tang, C., Cheng, N., Pu, Z., Xing, W. & Sun, X. NiSe Nanowire Film Supported on Nickel Foam: An Efficient and Stable 3D Bifunctional Electrode for Full Water Splitting. *Angewandte Chemie International Edition* **54,** 9351–9355. http://doi.wiley.com/10.1002/anie.201503407 (2015).

221. Herraiz-Cardona, I., Ortega, E., Antón, J. G. & Pérez-Herranz, V. Assessment of the roughness factor effect and the intrinsic catalytic activity for hydrogen evolution reaction on Ni-based electrodeposits. *International Journal of Hydrogen Energy* **36,** 9428–9438. https://linkinghub.elsevier.com/retrieve/pii/S0360319911012067 (2011).

222. Delahaye-Vidal, A. & Figlarz, M. Textural and structural studies on nickel hydroxide electrodes. II. Turbostratic nickel (II) hydroxide submitted to electrochemical redox cycling. *Journal of Applied Electrochemistry* **17,** 589–599. http://link.springer.com/10.1007/BF01084134 (1987).

223. Teramura, Y. & Takai, M. in *Compendium of Surface and Interface Analysis* 11 Suppl, 509–520 (Springer Singapore, Singapore, 2018). http://link.springer.com/10.1007/978-981-10-6156-1_83.

224. Ngamlerdpokin, K. & Tantavichet, N. Electrodeposition of nickel–copper alloys to use as a cathode for hydrogen evolution in an alkaline media. *International Journal of Hydrogen Energy* **39,** 2505–2515. https://linkinghub.elsevier.com/retrieve/pii/S036031991302911X (2014).

225. Janssen, L., Sillen, C., Barendrecht, E. & van Stralen, S. Bubble behaviour during oxygen and hydrogen evolution at transparent electrodes in KOH solution. *Electrochimica Acta* **29,** 633–642. https://linkinghub.elsevier.com/retrieve/pii/0013468684871224 (1984).

226. Chandran, P., Bakshi, S. & Chatterjee, D. Study on the characteristics of hydrogen bubble formation and its transport during electrolysis of water. *Chemical Engineering Science* **138,** 99–109. ISSN: 00092509. http://dx.doi.org/10.1016/j.ces.2015.07.041 (2015).

227. Lee, G. C. *et al.* The role of surface energy in heterogeneous bubble growth on ideal surface. *International Journal of Heat and Mass Transfer* **108,** 1901–1909. ISSN: 00179310. http://dx.doi.org/10.1016/j.ijheatmasstransfer.2016.10.005 (2017).

228. Newman, J. *Resistance for Flow of Current To a Disk* tech. rep. (Lawrence Berkeley National Laboratory, 1965). https://escholarship.org/uc/item/96z6t5r3.

229. Tobias, C. W. Effect of Gas Evolution on Current Distribution and Ohmic Resistance in Electrolyzers. *Journal of The Electrochemical Society* **106,** 833. https://iopscience.iop.org/article/10.1149/1.2427506 (1959).

230. Mandin, P., Derhoumi, Z., Roustan, H. & Rolf, W. Bubble over-potential during two-phase alkaline water electrolysis. *Electrochimica Acta* **128,** 248–258. ISSN: 00134686. http://dx.doi.org/10.1016/j.electacta.2013.11.068 (2014).

231. Abdin, Z., Webb, C. & Gray, E. Modelling and simulation of an alkaline electrolyser cell. *Energy* **138,** 316–331. https://linkinghub.elsevier.com/retrieve/pii/S0360544217312288 (2017).

232. Vogt, H. A hydrodynamic model for the ohmic interelectrode resistance of cells with vertical gas evolving electrodes. *Electrochimica Acta* **26,** 1311–1317. https://linkinghub.elsevier.com/retrieve/pii/0013468681851158 (1981).

233. Nagai, N. Existence of optimum space between electrodes on hydrogen production by water electrolysis. *International Journal of Hydrogen Energy* **28,** 35–41. https://linkinghub.elsevier.com/retrieve/pii/S0360319902000277 (2003).

234. Badino, G. The legend of carbon dioxide heaviness. *Journal of Cave and Karst Studies* **71,** 100–107. ISSN: 10906924. https://www.academia.edu/download/33785013/legend_carbon_dioxide.pdf (2009).

235. Bachellerie, E. *et al.* Generic approach for designing and implementing a passive autocatalytic recombiner PAR-system in nuclear power plant containments. *Nuclear Engineering and Design* **221,** 151–165. https://linkinghub.elsevier.com/retrieve/pii/S0029549302003308 (2003).

236. K. Blanchat, T. & Malliakos, A. Analysis of hydrogen depletion using a scaled passive autocatalytic recombiner. *Nuclear Engineering and Design* **187,** 229–239. https://linkinghub.elsevier.com/retrieve/pii/S0029549398002830 (1999).

237. Hug, W, Divisek, J, Mergel, J, Seeger, W & Steeb, H. Highly efficient advanced alkaline electrolyzer for solar operation. *International Journal of Hydrogen Energy* **17,** 699–705. https://linkinghub.elsevier.com/retrieve/pii/036031992900090J (1992).

238. Ulleberg, O. Modeling of advanced alkaline electrolyzers: a system simulation approach. *International Journal of Hydrogen Energy* **28,** 21–33. ISSN: 03603199. https://linkinghub.elsevier.com/retrieve/pii/S0360319902000332 (2003).

239. Sánchez, M., Amores, E., Rodríguez, L. & Clemente-Jul, C. Semi-empirical model and experimental validation for the performance evaluation of a 15 kW alkaline water electrolyzer. *International Journal of Hydrogen Energy* **43,** 20332–20345. https://linkinghub.elsevier.com/retrieve/pii/S0360319918328751 (2018).

240. Gilliam, R, Graydon, J, Kirk, D & Thorpe, S. A review of specific conductivities of potassium hydroxide solutions for various concentrations and temperatures. *International Journal of Hydrogen Energy* **32,** 359–364. https://linkinghub.elsevier.com/retrieve/pii/S0360319906005428 (2007).

241. Millet, P. in *Hydrogen Production* (ed Godula-Jopek, A.) 33 –62 (Wiley, 2015). ISBN: 978-3-527-33342-4.

242. Ismael, T., Yun, S. B. & Ulugbek, F. Radiator Heat Dissipation Performance. *Journal of Electronics Cooling and Thermal Control* **06,** 88–96. http://www.scirp.org/journal/doi.aspx?DOI=10.4236/jectc.2016.62008 (2016).

243. Gannon, W. J. F., Warwick, M. E. A. & Dunnill, C. W. Woven Stainless-Steel Mesh as a Gas Separation Membrane for Alkaline Water-Splitting Electrolysis. *Membranes* **10,** 109. ISSN: 2077-0375. https://www.mdpi.com/2077-0375/10/5/109 (2020).

244. Vermeiren, P., Adriansens, W., Moreels, J. P. & Leysen, R. in *Hydrogen Power: Theoretical and Engineering Solutions* 179–184 (Springer Netherlands, Dordrecht, 1998). http://link.springer.com/10.1007/978-94-015-9054-9_21.

245. Maksimov, V. G. & Varrik, N. M. Zirconium Oxide Fibers for Cell Separators of Alkaline Storage Batteries. *Glass and Ceramics* **74,** 288–294. http://link.springer.com/10.1007/s10717-017-9981-5 (2017).

246. Rodríguez *et al.* Simple and Precise Approach for Determination of Ohmic Contribution of Diaphragms in Alkaline Water Electrolysis. *Membranes* **9,** 129. https://www.mdpi.com/2077-0375/9/10/129 (2019).

247. Liu, Z. *et al.* The effect of membrane on an alkaline water electrolyzer. *International Journal of Hydrogen Energy* **42,** 29661–29665. ISSN: 03603199. https://doi.org/10.1016/j.ijhydene.2017.10.050 (2017).

248. Jansson, R. E. W., Marshall, R. J. & Rizzo, J. E. The rotating electrolyser. I. The velocity field. *Journal of Applied Electrochemistry* **8,** 281–285. http://link.springer.com/10.1007/BF00612680 (1978).

249. Gillespie, M. I., van der Merwe, F. & Kriek, R. J. Performance evaluation of a membraneless divergent electrode-flow-through (DEFT) alkaline electrolyser based on optimisation of electrolytic flow and electrode gap. *Journal of Power Sources* **293,** 228–235. ISSN: 03787753. http://linkinghub.elsevier.com/retrieve/pii/S0378775315009684 (2015).

250. Subramanian, B. & Ismail, S. Production and use of HHO gas in IC engines. *International Journal of Hydrogen Energy* **43,** 7140–7154. ISSN: 03603199. https://doi.org/10.1016/j.ijhydene.2018.02.120 (2018).

251. Vermeiren, P, Adriansens, W., Morells, J. & Leysen, R. Evaluation of the ZirfonS separator for use in alkaline water electrolysis and Ni-H2 batteries. *International Journal of Hydrogen Energy* **23,** 321–324. ISSN: 03603199. https://linkinghub.elsevier.com/retrieve/pii/S0360319997000694 (1998).

252. Długołęcki, P. *et al.* On the resistances of membrane, diffusion boundary layer and double layer in ion exchange membrane transport. *Journal of Membrane Science* **349,** 369–379. https://linkinghub.elsevier.com/retrieve/pii/S0376738809008849 (2010).

253. Ursúa, A., San Martín, I., Barrios, E. L. & Sanchis, P. Stand-alone operation of an alkaline water electrolyser fed by wind and photovoltaic systems. *International Journal of Hydrogen Energy* **38,** 14952–14967. https://linkinghub.elsevier.com/retrieve/pii/S0360319913023082 (2013).

254. Schalenbach, M. *et al.* Nickel-molybdenum alloy catalysts for the hydrogen evolution reaction: Activity and stability revised. *Electrochimica Acta* **259,** 1154–1161. ISSN: 00134686. https://doi.org/10.1016/j.electacta.2017.11.069 (2017).

255. Ernmann, M., Beata, E., Thunberg, S. & Thunberg, G. *Our House is on Fire* (Penguin Random House, 2020).